



FREEDAM-PLUS

Valorisation of knowledge for FREE from DAMage steel connections

Grant Agreement Number:899321-2020

Seismic Design of Steel Structures with FREE from DAMage joints

Part I: Informative Documents

Authors:

Vincenzo Piluso (Coordinator), Gianvittorio Rizzano, Massimo Latour, Antonella Bianca Francavilla, Sabatino Di Benedetto

University of Salerno, Italy

Raffaele Landolfo, Mario D'Aniello

University of Naples, Italy

Luis Simões da Silva, Aldina Santiago, Ana Francisca Santos

University of Coimbra, Portugal

Jean-Pierre Jaspart, Jean-Francois Demonceau

University of Liege, Belgium



31/12/2020

TABLE OF CONTENTS

TABLE OF CONTENTS	II
LIST OF FIGURES	V
LIST OF TABLES	XI
CHAPTER 1	1
1.1 INTRODUCTION	1
1.2 DRAWBACKS OF TRADITIONAL CONNECTIONS.....	5
1.3 SMART CONNECTIONS.....	9
1.3.1 Smart connections with hysteretic dampers.....	10
1.3.2 Smart connections with BRB.....	13
1.3.3 Smart connections with friction dampers	16
1.4 SELF-CENTERING CONNECTIONS	21
1.5 REFERENCES	23
CHAPTER 2	29
2.1 INTRODUCTION	29
2.2 SELECTION OF MATERIALS FOR FRICTION PADS DEVELOPMENT.....	33
2.2.1 Basic friction theories.....	33
2.2.2 Friction materials tested during the research project FREEDAM.....	35
2.3 BEHAVIOUR UNDER CYCLIC LOADING CONDITIONS	38
2.3.1 Layout for low-velocity tests	39
2.3.2 Layout for high-velocity tests.....	41
2.3.3 Summary of the test results	42
2.3.3.1 Influence of the type of coating: “Hard” Materials (M6-M8)	43
2.3.3.2 Influence of the type of coating: “Soft” Materials (M1-M5)	45
2.3.3.3 Influence of the clamping force	46
2.3.3.4 Influence of the Disk Springs Configuration	50
2.3.3.5 Influence of Randomness.....	51
2.3.3.6 Influence of velocity	53
2.4 PRELOADING LOSSES DURING THE SERVICE LIFE.....	56
2.4.1 Introduction	56
2.4.2 Short-term loss of preloading	59
2.4.3 Mid-term loss of preloading	61
2.4.4 Long-term loss of preloading.....	62
2.5 DESIGN AND ADVANCED MODELLING OF FRICTION DAMPERS	63
2.5.1 Design values of the friction coefficient and regression models.....	63
2.6 REFERENCES	67
CHAPTER 3	71
3.1 INTRODUCTION	71
3.2 EXPERIMENTAL TESTS ON EXTERNAL JOINTS	73
3.2.1 Description of the test setup.....	73
3.2.2 Results of the experimental tests.....	78

3.3	EXPERIMENTAL TESTS ON INTERNAL JOINTS	84
3.3.1	<i>Test setup and experimental programme</i>	84
3.3.2	<i>Results of the experimental tests</i>	87
3.4	CONCLUSIONS	90
3.5	REFERENCES	91
CHAPTER 4	95
4.1	INTRODUCTION	95
4.2	FE MODELLING OF FREEDAM DAMPERS	96
4.2.1	<i>Modelling assumptions</i>	96
4.2.2	<i>Validation and discussion of results</i>	100
4.3	FE MODELLING OF FREEDAM CONNECTIONS	104
4.3.1	<i>Modelling assumptions</i>	105
4.3.2	<i>Validation and discussion of results: external joints</i>	106
4.3.3	<i>Validation and discussion of results: internal joints</i>	109
4.4	SUMMARY OF NEW INFORMATIONS FOR DESIGN PROVISIONS	110
4.4.1	<i>Shear force in the T and L stub connections</i>	110
4.4.2	<i>Influence of clamping force</i>	114
4.4.3	<i>Influence of Friction Coefficient</i>	116
4.5	REFERENCES	118
CHAPTER 5	121
5.1	INTRODUCTION	121
5.2	FREEDAM DAMPERS UNDER IMPACT LOADING	122
5.2.1	<i>DESCRIPTION OF THE TESTED SPECIMENS AND EXPERIMENTAL PROGRAMME</i>	122
5.2.2	<i>DESCRIPTION OF THE TEST SETUP</i>	124
5.2.3	<i>RESULTS OF THE EXPERIMENTAL TESTS</i>	125
5.2.4	<i>SIMULATION OF THE TESTS' RESULTS</i>	127
5.2	FREEDAM CONNECTIONS UNDER IMPACT LOADING	128
5.4	REFERENCES	143
CHAPTER 6	147
	SEISMIC SIMULATION BY PSEUDO-DYNAMIC TESTING	147
6.1	INTRODUCTION	147
6.2	MOCK-UP BUILDING	147
6.3	PSEUDO-DYNAMIC TESTING OF THE MOCK-UP BUILDING WITH RBS CONNECTIONS.....	151
6.3.1	<i>Imperial Valley (PGA = 1.10g)</i>	151
6.3.2	<i>Spitak (PGA = 0.80g)</i>	152
6.3.3	<i>Artificial record (PGA = 0.50g)</i>	153
6.3.4	<i>Santa Barbara (PGA = 0.80g)</i>	153
6.3.5	<i>Coalinga (PGA = 0.80g)</i>	154
6.4	PD TESTING OF THE MOCK-UP WITH FREEDAM CONNECTIONS	156
6.4.1	<i>Imperial Valley (PGA = 1.10g)</i>	157
6.4.2	<i>Spitak (PGA = 0.80g)</i>	158
6.4.3	<i>Artificial record (PGA = 0.50g)</i>	159

6.4.4	<i>Santa Barbara (PGA = 0.80g)</i>	160
6.4.5	<i>Coalinga (PGA = 0.80g)</i>	160
6.5	NUMERICAL SIMULATION OF THE SEISMIC RESPONSE.....	162
6.5.1	<i>Structure with RBS connections</i>	162
6.5.2	<i>Structure with FREEDAM connections</i>	167
6.6	COMPARISON OF SEISMIC PERFORMANCES	171
6.7	REFERENCES	175

LIST OF FIGURES

Figure 1.1: Comparison between different design strategies	4
Figure 1.2: Behaviour of the components of the connection designed	6
Figure 1.3: Moment-rotation cyclic response of the connection designed	7
Figure 1.4: Moment-rotation cyclic response of RBS connection [25]	7
Figure 1.5: Moment-rotation cyclic response of a DST connection designed	8
Figure 1.6: Beam-to-column connection equipped with a slit damper [28].....	10
Figure 1.7: Design criterion for connections equipped with slit dampers	11
Figure 1.8: Experimental test results on connections equipped with slit dampers	12
Figure 1.9: Beam-to-column connections equipped with buckling restrained braces [29].....	12
Figure 1.10: Structural detail of the “all steel” BRB used as hysteretic damper [29].....	13
Figure 1.11: Force distribution in beam-to-column joints equipped with top and bottom BRBs [29]	14
Figure 1.12: Force distribution in beam-to-column joints equipped with bottom BRBs [29] ...	15
Figure 1.13: Moment-rotation cyclic response of beam-to-column joints equipped with BRBs [29]	15
Figure 1.14: Conception and ideal force-displacement behaviour of a symmetric friction connection	16
Figure 1.15: Conception and ideal force-displacement behaviour of	17
Figure 1.16: Bolt shank behaviour in double curvature	17
Figure 1.17: Sliding hinge joint with asymmetric friction connections [36, 43]	18
Figure 1.18: Cyclic behaviour of sliding hinge joints with asymmetric friction connections [43]	19
Figure 1.19: a) Configuration with horizontal damper;	19
Figure 1.20: Testing of a connection equipped with the friction damper	20
Figure 1.21: Testing of a connection equipped with the friction damper	21
Figure 1.22: Self-centering connections equipped with friction dampers [48, 54].....	22
Figure 1.23: Components of a sel-centering connection with friction dampers (left)	22
Figure 2.1 – Examples of displacement and velocity activated dissipative bracings	29
Figure 2.2 – Dampers after testing	30
Figure 2.3 – First Japanese patent on anti-seismic friction device [11].....	31
Figure 2.4 – Concept of sliding hinge joint with symmetric friction devices [12]	31
Figure 2.5 – Basic concepts of tribology.....	31
Figure 2.6 – FREE from Damage joint	32
Figure 2.7 – Cyclic slip tests on steel.....	35
Figure 2.8 – Tests on rubber	36

Figure 2.9 – Tests on thermal spray Aluminium.....	37
Figure 2.10 – Thermal spray techniques	38
Figure 2.11 – Cyclic slip test on a lap shear joint	39
Figure 2.12 – Tightening of the bolts	40
Figure 2.13 – Specimens' layout for high-velocity tests.....	40
Figure 2.14 – Test machine	43
Figure 2.15 – Hysteretic behaviour of hard shims	43
Figure 2.16 – Damage of hard shims	44
Figure 2.17 – Actual friction coefficient and bolt forces evolution	44
Figure 2.18 - Hysteretic behaviour of soft shims	45
Figure 2.19 – Actual friction coefficient and bolt forces evolution	46
Figure 2.20 – Damage after the tests.....	46
Figure 2.21 – Effect of preload	47
Figure 2.22 – Bolt forces and energy dissipation degradation	48
Figure 2.23 – Influence of the preload	48
Figure 2.24 – Effect of Belleville washers	49
Figure 2.25 – Effect of the number of disk springs employed.....	50
Figure 2.26 – Effective damping degradation and bolt forces degradation	51
Figure 2.27 – Effect of random variability.....	52
Figure 2.28 – Influence of the velocity – M4 shims	53
Figure 2.29 – Influence of velocity on the initial value of the friction coefficient.....	53
Figure 2.30 – Dependence of the FC degradation on velocity.....	54
Figure 2.31 – Dependence of the FC degradation on velocity up to 400 mm	55
Figure 2.32 – Evolution of the preload in time	56
Figure 2.33 – Test layouts	57
Figure 2.34 – Belleville washers considered.....	58
Figure 2.35 – Configurations of washers examined.....	58
Figure 2.36 – Short-term test results.....	59
Figure 2.37 – Mid-term test results.....	61
Figure 2.38 – Long-term test results	63
Figure 2.39 – Design values of the friction coefficients for the materials examined.....	66
Figure 3.1– Layouts of friction connections with SFDs	72
Figure 3.2 – Tested specimens (external joints): a) configuration with horizontal damper; b) configuration with vertical damper	74
Figure 3.3 – Experimental layout: a) FJ-CYC01-FJ-CYC04; b) FJ-CYC05-FJ-CYC08	74
Figure 3.4 – Structural scheme: a) action in an external joint due to the seismic loads;	75
Figure 3.5 – Structural scheme: a) action in an external joint due to the seismic loads;	76

Figure 3.6 – Position of the LVDTs: a) FREEDAM-CYC01; b) FREEDAM-CYC02.....	77
Figure 3.7 – Hysteretic curves.....	79
Figure 3.8 – Specimens in the deformed configuration: a) FJ-CYC01; b) FJ-CYC02; c) FJ-CYC03; d) FJ-CYC04.....	80
Figure 3.9 – Position of the instruments - FREEDAM-CYC01	81
Figure 3.10 – Position of the instruments - FREEDAM-CYC02	81
Figure 3.11 – Slip force vs displacement curve of the friction dampers FREEDAM-CYC01 (left) and FREEDAM-CYC02 (right)	82
Figure 3.12 – Local measurements FREEDAM-CYC01 – T-stub and L-stubs.....	82
Figure 3.13 – Local measurements FREEDAM-CYC02 – T-stub and L-stubs.....	83
Figure 3.14 – Preload force in the bolts of the friction damper FREEDAM-CYC01 (left) and FREEDAM-CYC02 (right).....	83
Figure 3.15 – FREEDAM-CYC02 specimen in the deformed configuration at the end of the test	84
Figure 3.16 – Tested specimens (internal joints)	85
Figure 3.17 – Test layout for internal joints (dimensions in mm).....	86
Figure 3.18 – Scheme for the calculation of the constraint reactions in the test layout.....	86
Figure 3.19 – Instrumentation	87
Figure 3.20 – Moment rotation curves – Specimens with smaller beam	88
Figure 3.21 – Moment rotation curves – Specimens with IPE 450 beam.....	89
Figure 3.22 – Deformation of T-stub and L-stubs	90
Figure 3.23 – Bolt forces.....	90
Figure 4.1 - Generated FE models of lap shear specimens: a) example of mesh; b-i) sub-assemblies with different number of disc springs	97
Figure 4.2 - True stress – strain nonlinear properties.....	97
Figure 4.3 – Displacement history of series UT-NV	98
Figure 4.4 - Experimental vs both Implicit and Explicit Force-Displacement curves.....	99
Figure 4.5 – Sliding vs displacement response of Models NV-21-22-23-24.....	100
Figure 4.6 – Simulated vs test response of lap shear joints with M6 material [NV-21-22-23-24]	101
Figure 4.7 – The friction coefficient curves for lap shear joints with material M4 [NV-17-18-19-20].....	102
Figure 4.8 – The friction coefficient curves for lap shear joints with material M4 [NV-17-18-19-20].....	102
Figure 4.9 – Contact area vs. Pressure.	103
Figure 4.10 – Contact Area Percentages for Different Preload Torques.	104
Figure 4.11 –Contact Pressures for Different Preload Torques.	104
Figure 4.12 – Features of FE model of beam-to-column joints with FREEDAM dampers	105

Figure 4.13 – average stress-strain curve of steel S355	106
Figure 4.14 – Experimental vs numerical results in terms of Bending Moment – Connection rotation	107
Figure 4.15 – Experimental vs. numerical models after cyclic test up to 5%	108
Figure 4.16 – Equivalent plastic damage (PEEQ) in the damper bolts.....	108
Figure 4.17 – Comparison between T and X joints with haunched damper	109
Figure 4.18 – Comparison between T and X joints with vertical rib damper	110
Figure 4.19 Shear force transferred by different components.....	111
Figure 4.20 Shear force at the connection face	112
Figure 4.21 Distribution of shear in the connected elements at 0.04 rad damper rotation	112
Figure 4.22 PEEQ Distribution at the end of the cyclic analysis for large joint assemblies....	113
Figure 4.23 Normalised disipated energy a) Friction energy and b) Plastic energy	114
Figure 4.24 Influence of the clamping force on the bending moment capacity	115
Figure 4.25 Configuration 1 vs Configuration 2	117
Figure 5.1 - FREEDAM specimen: Lateral view	122
Figure 5.2 - Tested specimens: Front view (dimensions in mm).....	123
Figure 5.3 -Sketch of the experimental layout used for impact tests – Friction damper tests .	124
Figure 5.4 - Types of impact tests – Force history scheme.....	125
Figure 5.5 - Experimental force versus displacement curves (Group A, M1)	125
Figure 5.6 - Numerical model of friction damper: Geometry and boundary conditions	127
Figure 5.7- Experimental tests vs numerical simulations	128
Figure 5.8 - Influence of velocity on the behaviour of the friction damper	128
Figure 5.9 - External connection tested (University of Coimbra).....	129
Figure 5.10 - Main components of the internal connections (University of Liege).....	129
Figure 5.11 - Experimental layout.....	130
Figure 5.12 - Experimental rotational connection behaviour: quasi-static vs impact tests.....	131
Figure 5.13 - Connection after failure: T-stub	131
Figure 5.14 - FEM models: Boundary conditions.....	132
Figure 5.15- M16 HV Bolt modelling.....	132
Figure 5.16 - FEM vs Experimental tests.....	133
Figure 5.17 - Parametric FEM results	133
Figure 5.18 - Impact test configuration (half of the specimen) with.....	133
Figure 5.19 Test nomenclature.....	134
Figure 5.20 Impact test layout: Mass M1 (211kg) (b) and M2 (460 kg) (c).....	135
Figure 5.21 force vs. vertical displacment and moment vs. rotation curves obtained through the static test.....	135

Figure 5.22 Impact test results – examples of point displacement vs. time measurements for the point 10C	136
Figure 5.23. FEM detail and energy comparison	139
Figure 5.24. Comparison between an implicit and explicit simulation of the static test	140
Figure 5.25 Experimental tests vs FE modelling	140
Figure 6.1 – The mock-up and its connections	148
Figure 6.2 – Building mock-up (with RBS connections).....	149
Figure 6.3 – Reference scheme adopted for the design of the tested MRFs	150
Figure 6.4 – Displacements (left) and reaction forces (right) histories for test 1	151
Figure 6.5 – RBSs hysteretic curves (left) and global dissipated energy (right) for Test 1 (MRF-1).....	152
Figure 6.6 – Displacements histories (left) and moment-rotation curves (right)	153
Figure 6.7 – Displacements histories (left) and moment-rotation curves (right).....	153
Figure 6.8 – Displacements histories (left) and moment-rotation curves (right).....	154
Figure 6.9 – Hysteretic curves of the collapsed RBSs (top) and corresponding damage patterns (bottom).....	154
Figure 6.10 – Hysteretic curves of the collapsed RBSs (top) and corresponding damage patterns	155
Figure 6.11 – Floor displacements (left) and actuators forces (right) of Test 5.....	156
Figure 6.12 – Test 1: floor displacements (left) and reaction forces (right)	157
Figure 6.13 – Test 2: floor displacements (left) and reaction forces recorded by actuators (right)	158
Figure 6.14 – Test 2: moment-rotation curves related to FREEDAM connections belonging to MRF-1	158
Figure 6.15 – Test 3: floor displacements (left) and reaction forces recorded by actuators (right)	159
Figure 6.16 – Test 3: moment-rotation curves related to FREEDAM connections belonging to MRF-1).....	159
Figure 6.17 – Test 4: floor displacements (left) and reaction forces recorded by actuators (right)	160
Figure 6.18 – Test 4: moment-rotation curves related to FREEDAM connections belonging to MRF-1	160
Figure 6.19 – Test 5: floor displacements (left) and reaction forces recorded by actuators (right)	161
Figure 6.20 – Test 5: moment-rotation curves related to FREEDAM connections belonging to MRF-1	161
Figure 6.21 – FREEDAM connection 1A at the end of the second experimental campaign...	161
Figure 6.22 – 3D model of the mock-up with RBS connections	162
Figure 6.23 – Experimental and numerical moment-rotation response of the RBS	163

Figure 6.24 – FE model of the RBS beam-joint system	163
Figure 6.25 – Comparison of the hysteretic loops for RBS-1A	165
Figure 6.26 – FE model of the structure.....	167
Figure 6.27 – FE model of the beam-to-column connection (refined model).....	168
Figure 6.28 – Uniaxial Hysteretic material: parameters	168
Figure 6.29 – Roof displacements: Test 1 (left) and Test 3 (right).....	170
Figure 6.30 – Base: Test 1 (left) and Test 2 (right).....	170
Figure 6.31 – Hysteretic curves (connection 1A): Test 2 (left) and Test 5 (right).....	171
Figure 6.32 – Comparison between the second level floor displacements and the base shear	173
Figure 6.33 – Connection 1A: hysteretic curves and dissipated energy	174

LIST OF TABLES

Table 2.1: Short-term relaxation configuration FW	60
Table 2.2: Short-term relaxation configuration BW	60
Table 2.3: Short-term relaxation configuration 3DS	60
Table 2.4: Short-term relaxation configuration 3DSps	60
Table 2.5: Mid-term tests summary	61
Table 2.6: Results of the regression study	64
Table 2.7: Static friction coefficient statistical variation	65
Table 2.8: Design values of the friction coefficients	66
Table 3.1: Loading displacement hystory	76
Table 3.2: Comparison between experimental and design values of friction moments.....	78
Table 3.3: Experimental programme.....	85
Table 4.1: Comparison between implicit and explicit analysis.....	99
Table 4.2: ID of specimens with disk springs	99
Table 4.3: Friction material properties	106
Table 4.4 Bending moments for model FD 1-2-DS considering the variation of clamping force	116
Table 4.5 Bending moments for model FD 2-2-DS considering the variation of clamping force	116
Table 4.6 Bending moments for model FD 1-2 considering the friction coefficient variation	116
Table 4.7 Bending moments for model FD 2-2 considering the friction coefficient variation	116
Table 5.1 - Experimental programme	123
Table 5.2 - Summary of the values of the friction dynamic factors and.....	126
Table 5.3. Summary of the values of the Dynamic factors after the occurrence of slippage...	126
Table 5.4. Experimental programme.....	130
Table 5.5. Impact test labels and main properties	134
Table 5.6. Impact Tests results.....	137
Table 5.7. DIF calculation.....	138
Table 5.8. Comparison of FEM experimental.....	141
Table 5.9. Impact force estimation and DIF.....	141
Table 6.1: Accelerograms used to perform the tests	150
Table 6.2: Main experimental results (structure with RBS connections)	151
Table 6.3: Main experimental results (structure with FREEDAM connections).....	157
Table 6.4: Experimental versus analytical comparison of base shear,.....	164
Table 6.5: Comparisons concerning connection 1A	166
Table 6.6: Uniaxial Hysteretic material: parameters.....	168

Table 6.7: Experimental versus numerical comparison of actuators' forces and floor displacements	169
Table 6.8: Experimental versus numerical comparison of connection 1A (PsD tests vs Sim. 2)	171
Table 6.9: Comparison between the experimental campaigns in terms of floor displacements and base shear	172

CHAPTER 1

SMART CONNECTIONS FOR SEISMIC-RESISTANT FRAMES: A BRIEF OVERVIEW

1.1 INTRODUCTION

Recent experimental research on beam-to-column connections for seismic-resistant steel structures is more and more focusing on smart connections with the aim of reducing the structural damage occurring under destructive seismic events. For this reason, the attention of many researchers is devoted to beam-to-column connections equipped with seismic dampers. Such dampers provide the dissipation of the earthquake input energy and, therefore, they practically substitute the dissipative zones of traditional moment-resisting frames, i.e. the beam ends where the development of plastic hinges is typically expected. In principle, any seismic damper typology can be applied: hysteretic dampers, buckling restrained braces, lead extrusion dampers, shape memory alloy dampers, viscous dampers, friction dampers. Such dampers are not only able to provide wide and stable hysteresis loops but can also be quite easily substituted after destructive seismic events. For this reason, beam-to-column connections equipped with seismic dampers can be referred as “smart connections”.

Moreover, reparability of structures after severe ground motions is mainly related to the amount of permanent deformations. For this reason, a modern topic in the research activity on smart connections is related to the possibility of building self-centering, thus avoiding out-of-plumb after major seismic events.

This Chapter provides a brief overview on smart connections, testifying the vitality of the research activity on seismic-resistant steel structures which is becoming more and more also an art of structural detailing, with a wide number of smart solutions which concrete structures are not able to provide.

It is well known that the different strategies for the design of seismic-resistant structures can be framed in view of energy balance. According to the traditional strategy for the seismic design of building structures [1-4], in case of frequent and occasional seismic events whose return period is comparable with the life cycle of structures, the earthquake input energy has to be completely dissipated by means of viscous damping. Therefore, the hysteretic energy is equal to zero because, for such seismic events, the structure has to be designed to remain in the elastic range. Conversely, in case of rare and very rare seismic events whose return period is about 500 years and even more, most of the earthquake input energy is dissipated by hysteresis, but leading to severe plastic excursions and related structural damage. Such structural damage has to be compatible with the ductility and the energy dissipation capacity of structures because, even though structural damage is accepted, collapse prevention has to be assured and the safeguard of human lives has to be guaranteed.

Within the above framework, with reference to steel Moment Resisting Frames (MRFs), there is the need to provide the structure with sufficient lateral strength and stiffness in order to remain in the elastic range under frequent and occasional seismic events. In particular, adequate lateral stiffness is needed to reduce the damage to non-structural components which is a fundamental requirement for the check against serviceability limit states. Conversely, in case of destructive earthquakes, MRFs have to be designed in order to dissipate the earthquake input energy at the beam ends where cyclic plastic bending has to occur. To this aim, it is recommended that beam-to-column connections are designed with sufficient over-strength [5-7] with respect to the connected beams, accounting for random material variability [6] and the occurrence of strain-hardening, to guarantee the full development of the ultimate flexural resistance of plastic hinges [7]. In addition, aiming to promote the plastic engagement of the greatest number of dissipative zones by properly controlling the failure mode, modern seismic codes, such as Eurocode 8, require the application of hierarchy criteria to promote the yielding of beam ends rather than column ends. To date, the classical design philosophy based on “weak beam”-“strong joint”-“strong column” hierarchy has been widely applied in practical seismic design [1-4] and surely provides some advantages, such as the development of quite stable hysteresis loops of dissipative zones and the prevention of soft-storey mechanisms which, as well known, have to be absolutely avoided because of their poor energy dissipation capacity. However, on the other hand, the traditional design approach provides also several drawbacks [8-10].

With reference to severe seismic events, the main drawback of the traditional strategy is intrinsic in the strategy itself. In fact, on one hand, even if structural damage is essential to dissipate the earthquake input energy, on the other hand, such structural damage is the main source of direct and indirect losses which are becoming more and more intolerable in case of industrialised countries, as testified by the amount of economical losses occurred during recent seismic events. Another drawback, which is specific to the case of steel MRFs, is that the use of full-strength beam-to-column joints with the code required over-strength is not cost-effective and constitute an important burden when there is an ongoing competition with structural solutions adopting other materials such as, in particular, reinforced concrete. In fact, in order to guarantee the desired connection performance levels, a significant over-sizing is needed leading to the use of supplementary web plates, additional reinforcing ribs or cover plates or, even, the use of haunched beams.

In order to reduce the main drawback of the traditional design strategy, i.e. the occurrence of structural damage, in past decades several strategies have been proposed. In particular, a strategy well suited for application to steel structures is the so-called strategy of supplementary energy dissipation, or passive control [11-15], where the earthquake input energy is dissipated by viscous damping or hysteretic damping by means of the introduction of energy absorbers generally located between couples of points of the structure where high relative displacements or velocities are expected [12]. Among the different strategies included in the framework of passive control systems, also the use of friction dampers has been proposed in past research activities aimed to reduce lateral displacements for serviceability limit state requirements and to reduce structural damage to fulfil ultimate limit state requirements.

Friction dampers present high potential at a low cost and they are easy to install and maintain. Therefore, in past, several devices for friction damping have been experimentally tested [16-18]

and some of these have been used in buildings around the world. The most widely adopted system for installing such friction dampers consists in the introduction of a bracing system which is integrated with friction dampers [16, 19, 20]. Several researchers worked on this structural configuration proposing design procedures to optimize the slip force of the bracing system.

With reference to the drawbacks deriving, in the traditional design strategy, from the need to design beam-to-column joints with high over-strength with respect to the connected beams, an alternative to the “weak beam”-“strong joint”-“strong column” approach has been proposed. The alternative philosophy of “strong column”-“weak joint”-“strong beam” can be applied, because Eurocode 8 has opened the door to the use of partial strength joints, provided that they are able to provide sufficient plastic rotation capacity (typically 0.035 rad for high seismicity zones) to be checked by means of experimental tests. With such design approach, even in the case of big beam sections like those occurring in case of long spans or high gravity loads, the adoption of partial strength joints allows to control the bending moment transferred to the column which, in this way, can be prevented from an excessive over-sizing resulting from the application of beam-column hierarchy criterion. In addition, the structural detail of beam-to-column joints can be significantly simplified by improving the overall cost-effectiveness of the structural scheme, by overcoming the economical drawbacks resulting in case of connections designed to attain high overstrength.

The growing interest of the scientific community to the design of dissipative semi-continuous frames with partial-strength joints [5, 21-27] in MRFs is also reflected in the last version of Eurocode 8, but the actual application of this technique is still strongly limited in practice, because the actual dissipative capacities of the joints have to be demonstrated by means of experimental testing which is generally out of the possibilities of common designers. In addition, even though the application of partial-strength joints can lead, on one hand, to a more economical design, on the other hand, it can provide also some disadvantages such as the reduction of the frame lateral stiffness and, generally, of the energy dissipation capacity at the beam end.

Starting from the background briefly summarized above, in order to overcome the drawbacks of the described design strategies, many researchers have focused their efforts on the possibility to conceive and design “smart connections” which are able to concentrate the dissipation of the earthquake input energy in specifically designed dissipaters, i.e. damping devices which are smartly located within the components of the connection itself. Therefore, the goal is the design of connections able to withstand almost without any damage not only frequent and occasional seismic events, but also destructive earthquakes such as those corresponding to rare and very rare events.

The basic idea of these research works is inspired by the strategy of supplementary energy dissipation, but it is based on the use of the damping devices under a new perspective. In fact, while passive control strategies have been commonly based on the integration of the energy dissipation capacity of the primary structure by means of a supplementary dissipation coming from damping devices; conversely, the new design strategy, which could be named “Substitution Strategy”, is based on the use of dampers conceived in such a way to substitute the traditional dissipative zones of MRFs, i.e. the beam ends.

From the technological point of view, the innovation regards the conception of beam-to-column connections which are equipped with dampers. These dampers can be located either at the bottom

flange level or at the levels of both flanges and, in addition, can belong to different typologies: viscous dampers, lead extrusion dampers, hysteretic dampers, friction dampers, shape memory alloy (SMA) dampers, buckling restrained braces (BRB).

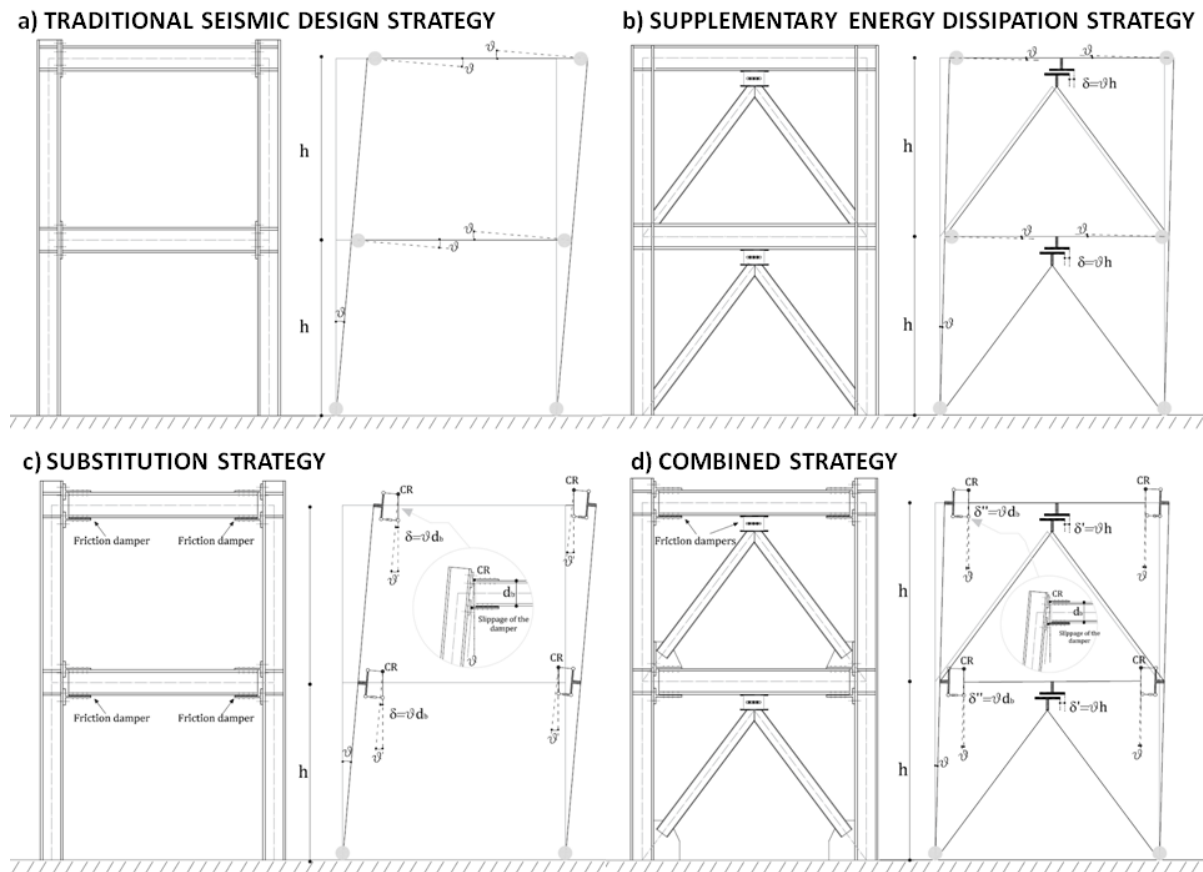


Figure 1.1: Comparison between different design strategies

In order to well clarify the differences with respect to either traditional seismic design or supplementary energy dissipation strategy, the different schemes are analysed in Figure 1.1 where the use of friction dampers is proposed [10]. In particular, Figure 1.1a points out that dissipative zones of traditional MRFs are located at the beam ends where plastic hinges have to be developed. The seismic demand is usually expressed in terms of maximum inter-storey drift (ϑ in the figure) which governs the plastic rotation expected in dissipative zones. The supplementary energy dissipation strategy (Figure 1.1b) is aimed to the reduction of the seismic demand by introducing seismic dampers which have to be located, for their effectiveness, between couple of points subjected to high relative displacements. The supplementary energy dissipation provided by such devices allows the reduction of the drift ϑ and, as a consequence, the reduction of the structural damage occurring at the beam ends. Conversely, the substitution strategy (Figure 1.1c) allows the prevention of the structural damage, because all the dissipative zones are substituted by means of connections equipped with friction dampers. The expected drift demand does not reduce when comparison is made with traditional structures (Figure 1.1a), but this drift leads to very limited structural damage in some joint components, because the rotation of the beam-to-column connections is accommodated by properly calibrating the stroke

of the friction dampers (Figure 1.1c). The maximum rotation allowed is practically given by the ratio between the damper stroke and the lever arm, i.e. its distance from the centre of rotation CR. However, it is useful to note that the relative displacement occurring between the ends of the friction damper ($\delta = \vartheta d_b$, being d_b the beam depth) is significantly less than the one ($\delta = \vartheta h$, being h the inter-storey height) occurring when the supplementary energy dissipation strategy is applied (Figure 1.1b). This is the main reason why cases a) and c) are expected to provide similar drift demands. Finally, a further improvement of seismic performances is obtained by combining the substitution strategy with the supplementary energy dissipation strategy. Such combined strategy (Figure 1.1d) leads both to the reduction of the drift demands expected in case of destructive seismic events and, in addition, to the prevention of significant damage in beam-to-column connections. Obviously, the drift reduction is also an important benefit to reduce damage to the building non-structural components.

The use of beam-to-column connections equipped with dampers is an effective tool to reduce the damage in the structural components by addressing the energy dissipation towards specifically designed components which, if needed, can be substituted after one or more seismic events. However, an important drawback which is common to the traditional design strategies still remains. In fact, both in case of traditional connections and in case of connections equipped with seismic dampers, after destructive seismic events, the structure is subjected to permanent overall deformations resulting into an out-of-plumb whose magnitude governs the possibility to effectively repair the building. For this reason, research efforts are also devoted to the possibility of equipping the connections with self-centering devices which are often constituted by a post-tensioning system.

The following Sections provide a brief overview on “smart connections” equipped with seismic dampers belonging to different typologies. The main results coming from the technical literature and research projects currently in progress are briefly presented and an attempt of classification is made. A brief presentation of connections equipped with self-centering systems is also made. The sprightliness of the research on these topics shows that the future of steel constructions can be really shining because of the variety of structural solutions and enormity of advantages that steel construction technologies are able to provide, compared to reinforced concrete structures, when the formidable task of seismic safety has to be addressed. It is a responsibility of the steel industry to be able to promote the use of steel in seismic prone countries by making designers and customers completely aware of steel potentialities in reducing direct and indirect losses typically occurring after destructive seismic events.

1.2 DRAWBACKS OF TRADITIONAL CONNECTIONS

A quick overview of the rotational response of traditional beam-to-column connections can be obtained from the analysis of the results presented in [25] where the results of an experimental program dealing with the ultimate behaviour of bolted beam-to-column connections under cyclic actions are presented. In particular, different connections constituted by the same beam and the same column were designed and tested. The design was aimed to assure the same flexural resistance of the connections, but changing for each connection the weakest component. Therefore, it was pointed out how the ultimate behaviour can be governed by properly

strengthening the components whose yielding has to be prevented. To this scope, the component approach was adopted as a design tool for component hierarchy criteria. Moreover, the actual possibility of extending the component approach to the prediction of the cyclic response of beam-to-column joints was outlined, so that the results obtained testified that the component approach can be a powerful tool also for the seismic design of connections.

In Figure 1.2 [25], the behaviour of an extended end-plate connection designed to obtain the panel zone in shear as the weakest component is shown. In particular, the cyclic response of the main connection components is pointed out. The use of the component method has allowed the control of the component providing the main source of energy dissipation which actually was constituted by the panel zone in shear as it is evident from the moment versus shear distortion cyclic response of the panel zone. However, because of significant strain hardening of the panel zone, the resulting over-strength gives rise also to the yielding of the end-plate in bending so that the fracture of the weld connecting the end-plate to the beam flange governs the collapse of the connection.

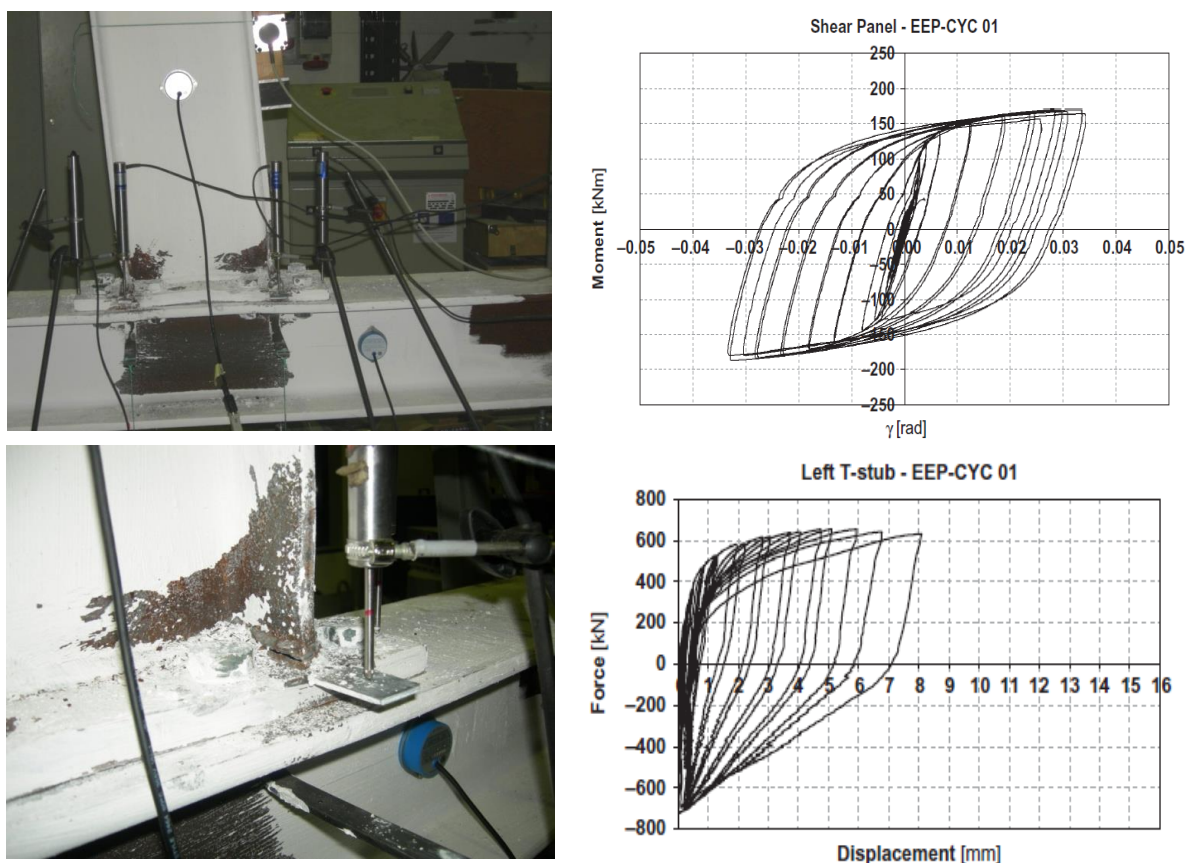


Figure 1.2: Behaviour of the components of the connection designed with the panel zone in shear as weakest joint component [25]

The moment-rotation cyclic response of the connection is shown in Figure 1.3 [25]. It points out that, when the yielding of the connection mainly involves the panel zone in shear, wide and stable hysteresis loops are obtained. In particular, the plastic rotation supply of the connection is well beyond the values which are typically needed to withstand destructive seismic events. However, even though the concentration of yielding in the panel zone is able to assure adequate plastic

rotation supply and energy dissipation capacity, the structural damage is difficult to be repaired. In addition, non-linear structural analysis aimed at seismic performance assessment should be carried out by properly modelling the panel zone. Moreover, significant second-order effects in plastic range can occur. For this reason, it is the author opinion that, despite the high energy dissipation provided, beam-to-column joints with panel zone yielding should be avoided.

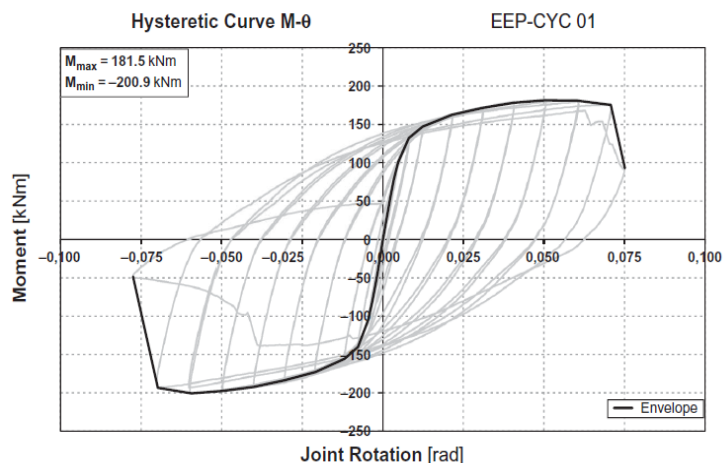


Figure 1.3: Moment-rotation cyclic response of the connection designed with the panel zone in shear as weakest joint component [25]

The behaviour of full-strength beam-to-column connection is governed by the yielding of the beam-end. Therefore, the corresponding cyclic behaviour is governed by the local buckling of the plate elements constituting the member section. Flange and web local buckling govern, depending on their width-to-thickness ratios, the strength degradation occurring under cyclic loading conditions. This is typically also the case of RBS (reduced beam section) connections. Figure 1.4 [25] shows the moment-rotation cyclic response of an extended end-plate connection with RBS. The connection has the same column and the same beam of Figure 1.2 and the RBS was calibrated to obtain almost the same flexural resistance.

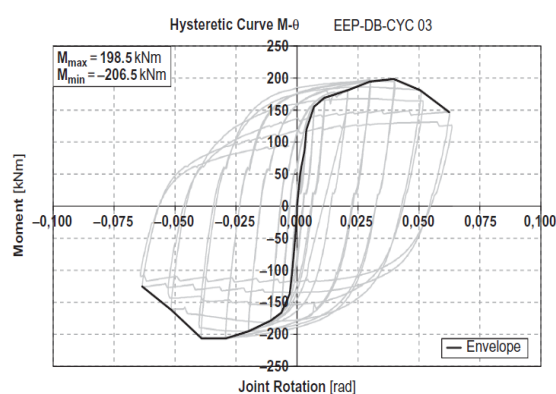
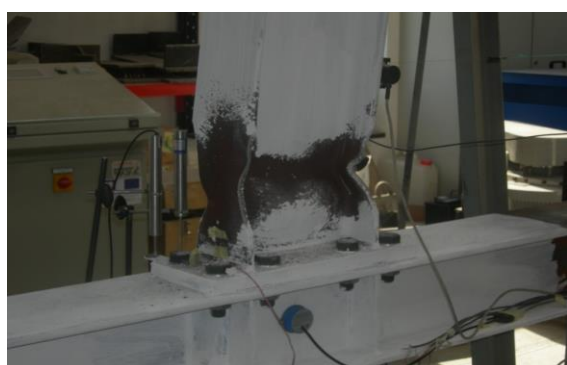


Figure 1.4: Moment-rotation cyclic response of RBS connection [25]

The real configuration of the plastic hinge is evidently the result of local buckling involving cyclically the two flanges and, because of kinematic compatibility requirements, the web. Also in this case the plastic rotation supply is well beyond the values typically needed to survive under destructive seismic events, but also the main drawback of traditional design philosophy is evident. The price of energy dissipation is the structural damage occurring at the beam ends. The

plastic deformation gives rise to a permanent building drift whose magnitude governs the possibility to effectively repair the building after destructive seismic events.

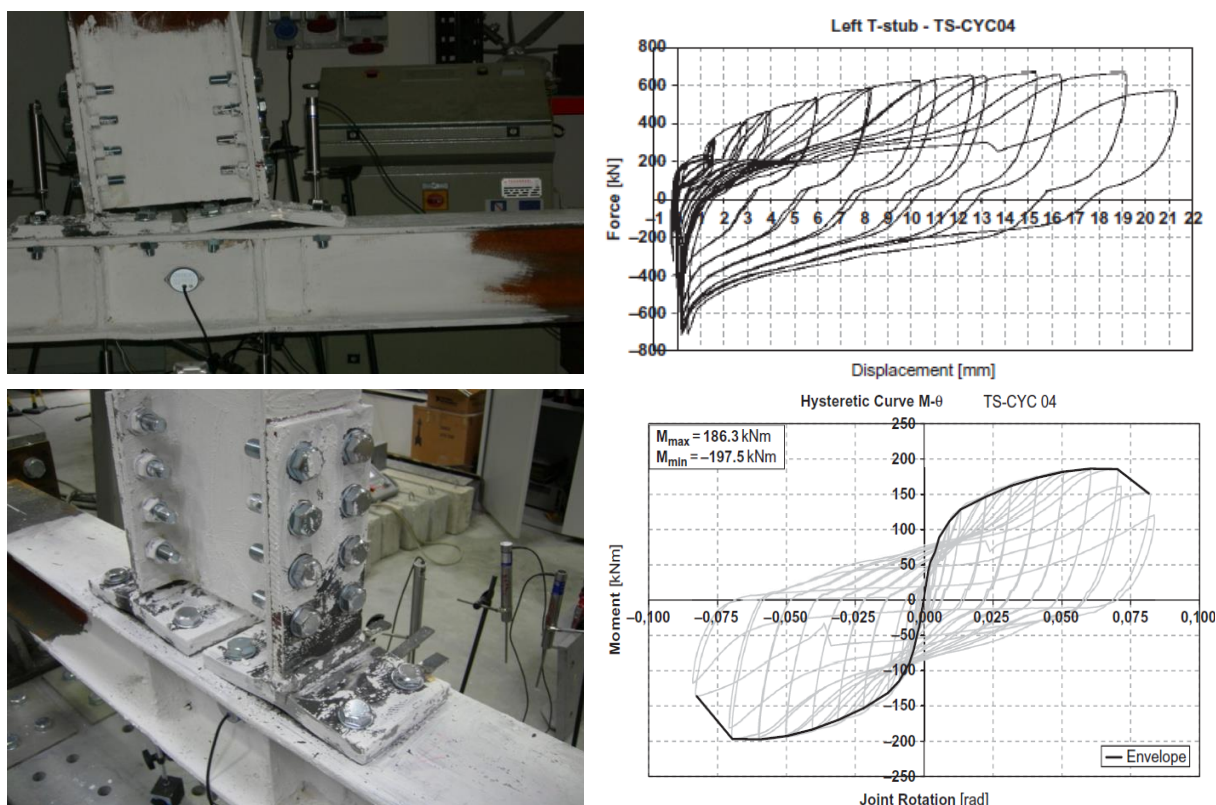


Figure 1.5: Moment-rotation cyclic response of a DST connection designed with bolted T-stubs as the weakest joint component [25]

Figure 1.5 shows the cyclic response of a double split tee connection [25]. The beam and the column sections are the same of the connections examined in Figures 1.2 and 1.4. The bolted T-stubs were designed as the weakest joint component and, in addition, to obtain a beam-to-column joint having almost the same flexural resistance of the joints previously examined. Therefore, the influence of the choice of the weakest joint component is pointed out. The force versus displacement of the weakest joint component, i.e. the bolted T-stub, is also depicted in Figure 1.5 (for the left T-stub). As expected, the failure of the connection was governed by the bolted T-stub with the formation of yield lines in the T-stub flanges. In particular, a crack occurred at the yield line close to the T-stub web, initially in its central part, and progressively developed up to the complete fracture of the T-stub flange. Properly designed [25] bolted T-stubs are able to provide a plastic rotation supply well beyond the value needed to withstand severe seismic events. However, the hysteresis loops are not stable because they are characterized by a pinching phenomenon progressively increasing. The main advantage of such traditional connection typology is that the bolted T-stubs can be easily substituted, so that they could be regarded as hysteretic dampers equipping the connection. On the other hand, the flexural deformability of the connection can be significant so that it has to be considered in the structural design. As a consequence, the lateral deformability of the structure has to be properly controlled. Starting from the brief overview of the cyclic rotational response of traditional beam-to-column

connections given above, the following considerations can be carried out concerning the advantages and the disadvantages of traditional connections.

Traditional full-strength beam-to-column connections generally exhibit the following advantages:

- the dissipative zones are constituted by the beam ends which are able to provide adequate values of the plastic rotation supply, well beyond the benchmark value, equal to 0.035 rad, typically required for high ductility structures. This is assured by limiting the width-to-thickness ratios of the plate elements constituting the member section;
- the hysteresis loops are wide, while their stability is related to the strength degradation as affected by the width-to-thickness ratios of the plate elements constituting the member section.

The main disadvantages can be recognised as follows:

- the dissipative zones belong to the primary structural system which, as a consequence, is damaged following severe seismic events and, therefore, need to be repaired;
- the repairing of the yielded beam ends is not easy when compared with other connection components (such as bolted T-stubs);
- after destructive seismic events, the building structure remains out-of-plumb. Therefore, recentering is a major concern for reparability;
- direct and indirect losses occur under severe seismic events.

Conversely, with reference to traditional connections designed as partial-strength connections, the following advantages can be pointed out:

- if the yielding of the panel zone in shear is excluded, the dissipative components are typically constituted by the plate elements constituting the fastening elements which in many cases can be easily substituted (such as bolted T-stubs and angles);
- the beams, i.e. the members belonging to the primary structural system, remain in the elastic range;

On the other hand, the following disadvantages occur:

- the structural design is highly complicated when using partial-strength connections because the designer has to be able to account for and to control not only the flexural resistance of the connection but also the rotational stiffness and the plastic rotation supply;
- the fastening elements subjected to yielding have to be repaired or substituted;
- after destructive seismic events, the building structure remains out-of-plumb. Therefore, recentering is a major concern for reparability;
- direct and indirect losses occur under severe seismic events.

1.3 SMART CONNECTIONS

Smart connections constitute an answer to many of the drawbacks exhibited by traditional connections, either full-strength or partial-strength connections, in case of buildings subjected to destructive seismic events. Smart connections can be conceived in order to reach one or more of the following goals:

- to assure that the primary structural system remain in elastic range (like in case of partial-strength connections where beams remain undamaged);

- to dissipate the earthquake input energy in specifically designed components which can be easily substituted after destructive seismic events;
- to reduce the permanent overall deformations, i.e. the out-of-plumb, occurring after destructive seismic events.

In order to achieve one or more of the above goals, smart connections can be designed according to the following strategies:

- by equipping the connections with seismic dampers which can belong to different typologies (hysteretic dampers, lead extrusion dampers, dampers constituted by buckling restrained braces, friction dampers, dampers based on shape memory alloys);
- by equipping the connections with recentering systems;
- by equipping the connections with seismic dampers and recentering systems.

In the following, some proposals of smart connection systems belonging to different typologies are briefly presented.

1.3.1 Smart connections with hysteretic dampers

An innovative connection system with slit dampers was developed by Oh et al. [28], which could not only provide good seismic performance but could also be quickly repaired after a heavy earthquake. The beam-to-column connection is equipped with a slit damper located at the bottom flange (Figure 1.6) where plastic deformations are concentrated. The centre of rotation is fixed at the level of the top flange using a bolted T-stub. The location of the centre of rotation has the aim of preventing the damage of the concrete slab usually located on the top flange of the beam. The yield flexural resistance and the ultimate flexural resistance of the connection is governed by the yield and ultimate resistance values of the slit damper and by the lever arm.

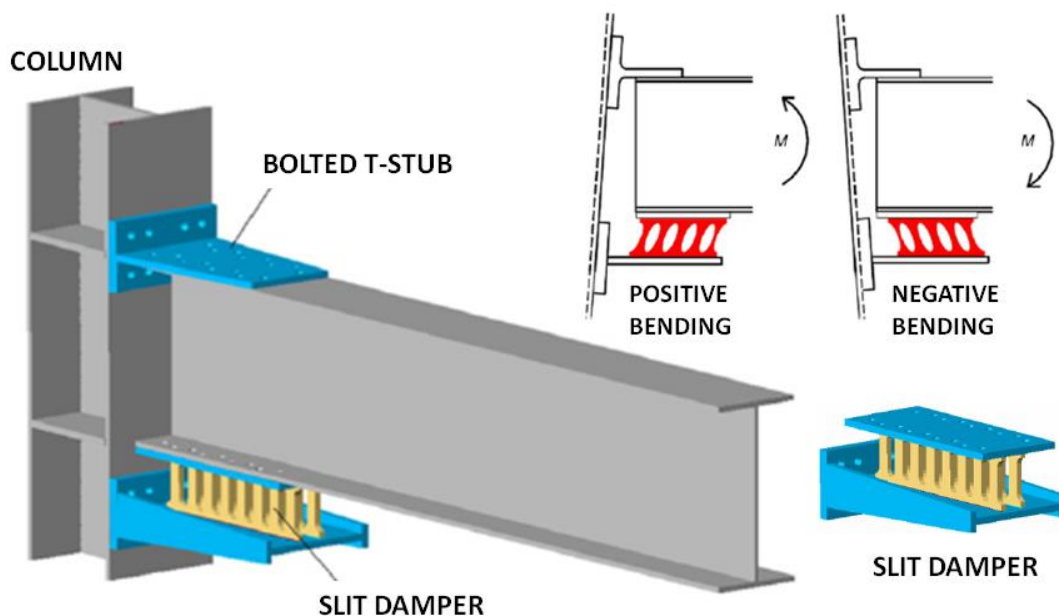


Figure 1.6: Beam-to-column connection equipped with a slit damper [28]

According to the notation given in Figure 1.7, the yield resistance of the slit damper is given by:

$$P_y = \min \left\{ n \frac{f_y t B^2}{2H'} ; n \frac{2f_y t B}{3\sqrt{3}} \right\} \quad (1.1)$$

where n is the number of the struts of the slit damper, t is the thickness, B is the width of the struts, H' is the equivalent height and f_y is the yield stress; the ultimate resistance is given by:

$$P_u = \min \left\{ n \frac{f_u t B^2}{2H'} ; n \frac{2f_u t B}{3\sqrt{3}} \right\} \quad \text{with} \quad H' = H + 2 \frac{r^2}{H_T} \quad (1.2)$$

where H_T is the total height of the struts of the slit damper and f_u is the ultimate stress. The first yielding displacement of the slit damper is given by:

$$\delta_y = \frac{1.5P_y H_T}{n E t B} \left[\left(\frac{H'}{B} \right)^2 + 2.6 \right] \quad (1.3)$$

where E is the Young modulus.

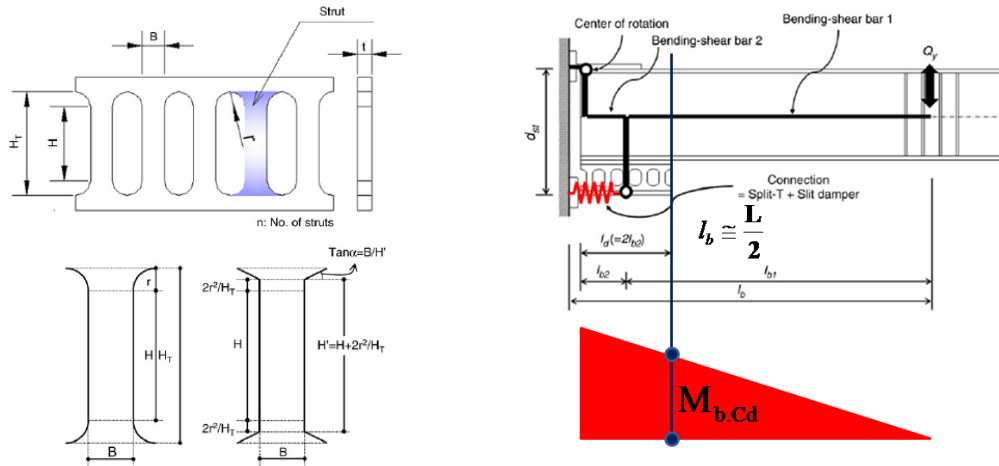


Figure 1.7: Design criterion for connections equipped with slit dampers

As the aim of smart connections is to prevent the yielding of the connected beams, a design criterion can be easily derived by properly applying the second principle of capacity design with reference to the connection components. According to this principle, the non-dissipative components have to be designed considering the maximum internal actions that the dissipative components yielded and strain-hardened up to their ultimate conditions are able to transmit. In this case, the dissipative component is constituted by the slit damper whose ultimate resistance is given by Eq. (1.2). Therefore, the bending moment corresponding to the capacity of the slit damper is given by (Figure 1.7):

$$M_{b,Cd} = \frac{P_u d_{st}}{(l_{b1} + l_{b2})} (l_{b1} - l_{b2}) \quad (1.4)$$

Therefore, the beam section, i.e. the primary non-dissipative zone whose yielding has to be prevented, has to satisfy the following design requirement:

$$M_{b,Cd} \leq M_{b,Rd} \quad (1.5)$$

being $M_{b,Rd}$ the design resistance of the beam.

The design of the beam section by exploiting Eqns. (1.2), (1.4) and (1.5) assures that beam yielding is prevented. In order to assure that energy dissipation is concentrated in the slit damper only, also all the other joint components have to be designed according to the second principle

of capacity design. It means that the bolted T-stub located at the top flange has to be designed to transmit a force equal to P_u . Similarly, also the column web in compression, the column web in tension and the panel zone in shear have to be checked considering the maximum force P_u which the slit damper is able to transmit.

Because of the use of a hysteretic damper specifically designed to assure adequate displacement capacity and energy dissipation, connections equipped with slit dampers are able to assure stable hysteresis loops (Figure 1.8) with a plastic rotation capacity beyond the benchmark value required by code provisions and to prevent the yielding of the connected beam. Therefore, after a destructive seismic event, only the substitution of the slit damper could be needed.

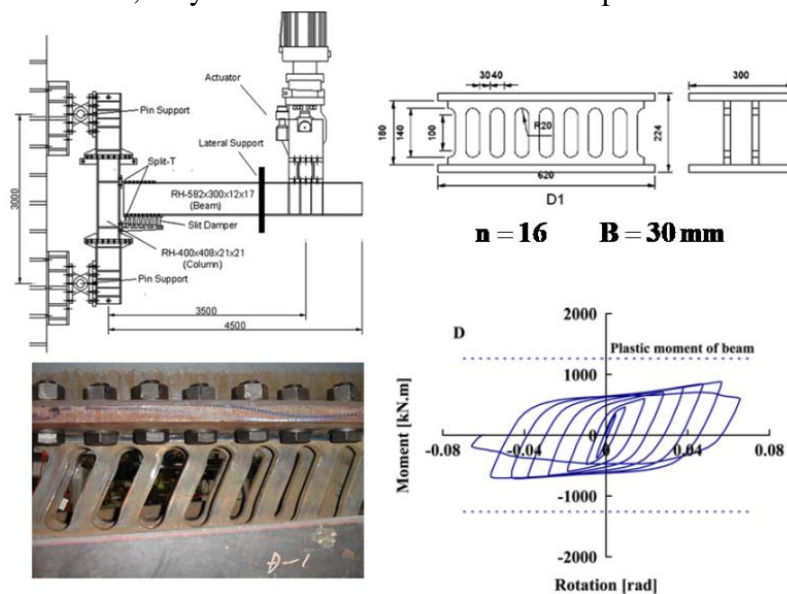


Figure 1.8: Experimental test results on connections equipped with slit dampers

Test results [28] indicated that properly designed connections equipped with slit dampers showed an excellent hysteretic behaviour. In addition, the energy dissipation and plastic deformation in this system were concentrated only in the slit dampers, while the inelastic behaviour of beams and columns is prevented through appropriate capacity design.

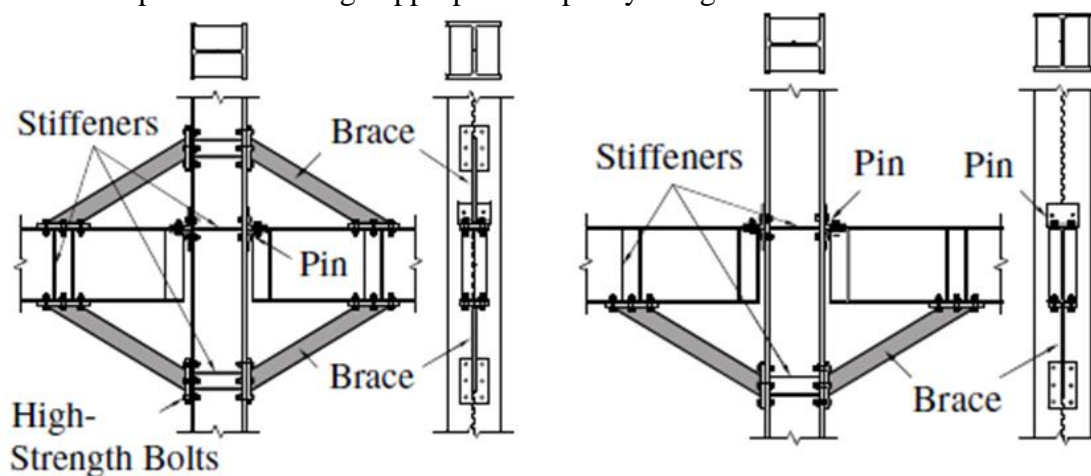


Figure 1.9: Beam-to-column connections equipped with buckling restrained braces [29]

1.3.2 Smart connections with BRB

It is well known that Buckling Restrained Braces (BRBs) are constituted by a central core subjected to tension/compression representing the dissipative component. The buckling of the core in compression is prevented using a properly designed external case. Therefore, BRBs can be regarded as a particular type of hysteretic dampers which are typically used as bracing members in concentrically braced frames. However, as soon as they are recognised as a typology of hysteretic dampers, it is evident that their use can be extended to many structural configurations. In particular, the use of BRBs for equipping beam-to-column joints with hysteretic dampers has been proposed in [29] (Figure 1.9) where two configurations have been investigated. The first configuration corresponds to the use of buckling restrained braces connecting both the top flange and the bottom flange. In the second configuration, BRBs are connected to the bottom flange only. In both cases, the top flange is connected to the column also using a bolted T-stub which practically establishes the location of the centre of rotation.

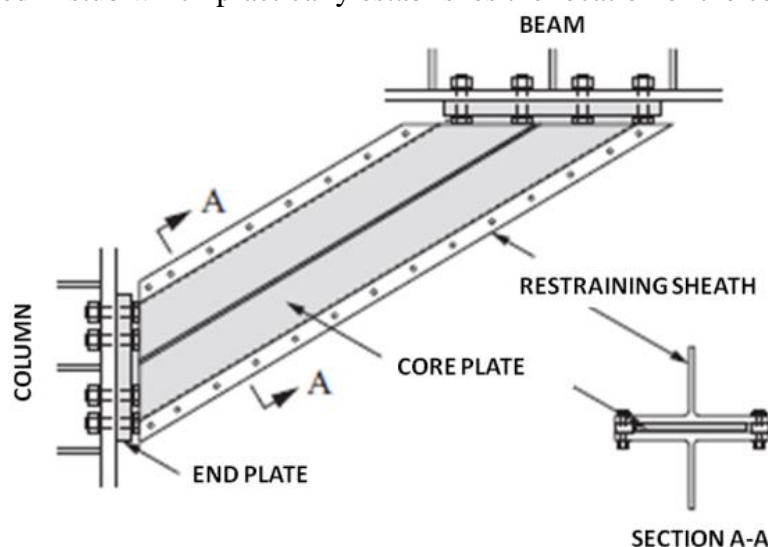


Figure 1.10: Structural detail of the “all steel” BRB used as hysteretic damper [29]

The hysteretic damper is constituted by a core plate whose buckling in compression is prevented by an external case formed by two bolted T elements. Therefore, the damper is an “all steel” BRB (Figure 1.10).

The primary aim of smart connections is the prevention of the beam yielding and the concentration of the energy dissipation in the seismic dampers. Therefore, also in this case, the design of the structural detail has to be based on the application of capacity design principles at the component level. Starting from the yielding condition of the core plate $N = N_y$, the beam shear action $Q_b = Q_{bp}$ leading to the yielding condition can be easily evaluated (Figure 11). In fact, as an example, concerning the configuration with BRBs connecting both the top flange and the bottom flange, the vertical equilibrium equation provides:

$$V = Q_{bp} - 2N_y \sin \alpha \tag{1.6}$$

the horizontal equilibrium equation provides $H = 0$ and, finally, the rotation equilibrium around the centre of rotation B gives:

$$Q_{bp} = \frac{2N_y \cos\alpha}{2l_b - d_c} [d_b + \text{tg}\alpha(2\xi l_b - d_c)] \quad (1.7)$$

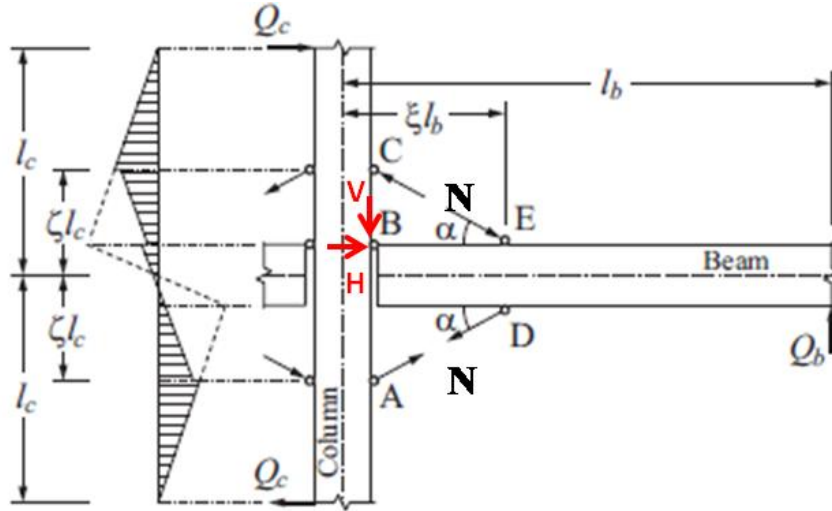


Figure 1.11: Force distribution in beam-to-column joints equipped with top and bottom BRBs [29]

Therefore, taking into account that:

$$\text{tg}\alpha = \frac{\zeta l_c - \frac{d_b}{2}}{\xi l_b - \frac{d_c}{2}} \quad (1.8)$$

the beam shear action corresponding to the yielding of the BRB core plate is given by:

$$Q_{bp} = \frac{4\zeta l_c}{2l_b - d_c} N_y \cos\alpha \quad (1.9)$$

The maximum bending moment, occurring in the beam when the BRB is yielded, develops at section ED. According to the second principle of capacity design, it is given by:

$$M_{b,Cd} = Q_{bp}(1-\xi)l_b = \frac{4\zeta l_c}{2l_b - d_c} N_y \cos\alpha (1-\xi)l_b \quad (1.10)$$

In order to prevent the yielding of the beam, the following condition has to be satisfied:

$$M_{b,Cd} \leq M_{b,Rd} = \frac{Z_b f_y}{\gamma_{M0}} \quad (1.11)$$

Therefore, combining Eq. (1.11) and Eq. (1.10), a relation to design the core plate of the BRB, given the beam sections, is easily derived:

$$A_{core} \leq \frac{1}{f_y} \frac{M_{b,Rd} \left(1 - \frac{d_c}{2l_b}\right)}{2\zeta l_c (1-\xi) \cos\alpha} \quad (1.12)$$

As soon as the core plate of the BRBs has been designed to prevent the beam yielding, all the other joint components have to be dimensioned considering the maximum forces transmitted when the core plate is yielded, i.e, when $N = N_y$ occurs.

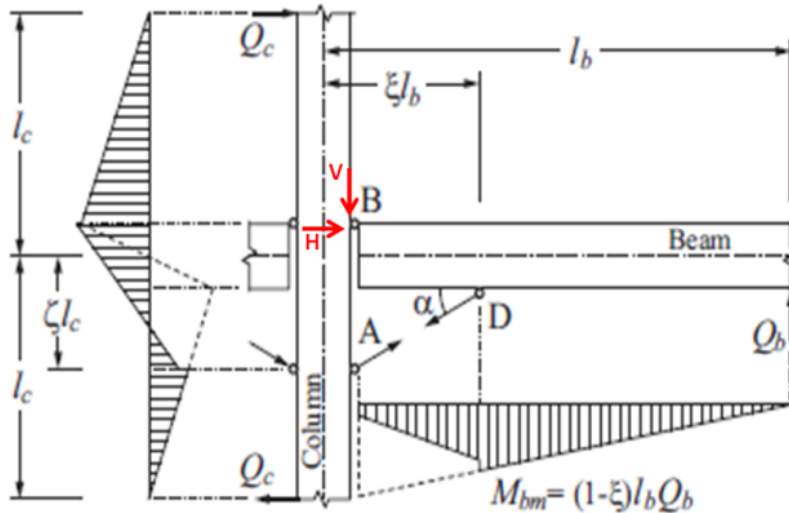


Figure 1.12: Force distribution in beam-to-column joints equipped with bottom BRBs [29]

By applying the same procedure to the case of beam-to-column joints equipped with BRBs located at the bottom flange only (Figure 1.12), the following relation for designing the core plate is obtained:

$$A_{\text{core}} \leq \frac{1}{f_y} \frac{M_{b,Rd} \left(1 - \frac{d_c}{2l_b} \right)}{\zeta l_c (1 - \xi) \left(1 + \frac{d_b}{2\zeta l_c} \right) \cos \alpha} \quad (1.13)$$

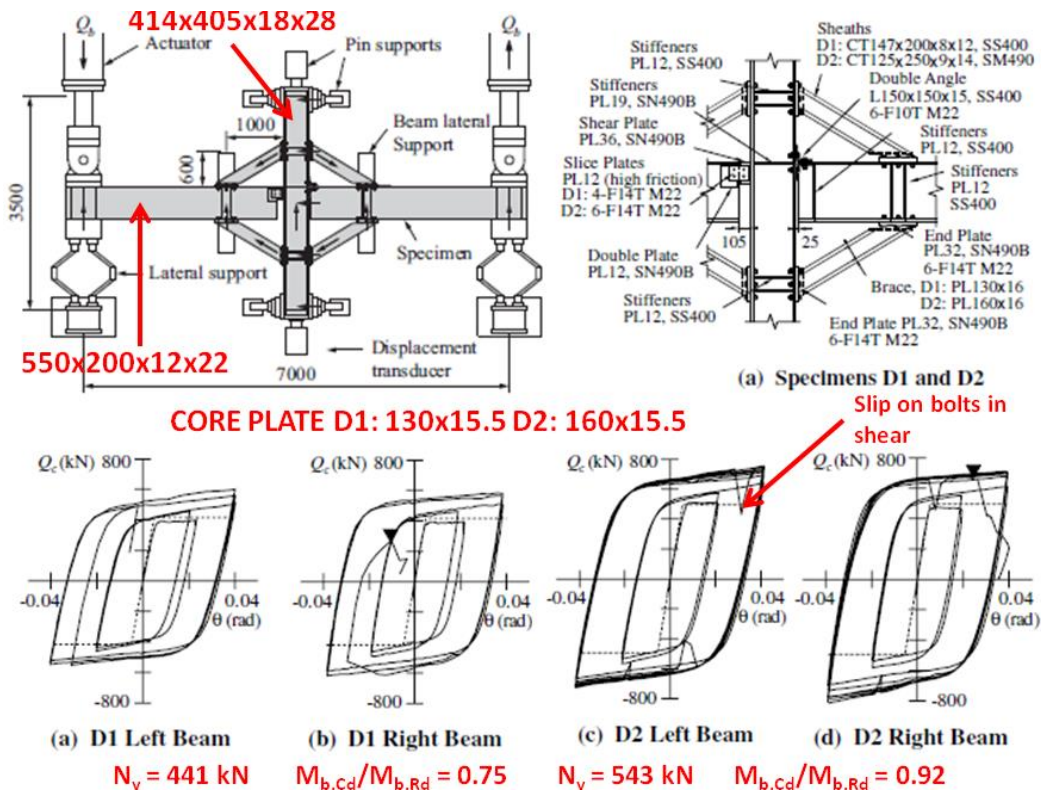


Figure 1.13: Moment-rotation cyclic response of beam-to-column joints equipped with BRBs [29]

Test results [29] indicated that properly designed connections equipped with buckling restrained braces, adopted as hysteretic dampers, showed an excellent hysteretic behaviour (Fig. 13). The energy dissipation and plastic deformation were concentrated only in the BRBs, while the inelastic behaviour of beams and columns is prevented through appropriate capacity design.

1.3.3 Smart connections with friction dampers

Even though beam-to-column joints equipped with friction dampers were proposed for the first time in 1995 by Popov and Yang [30], the research activity on this innovative connection typology has received a boost only recently, mainly in New Zeland [31-35], where the first applications to real buildings have been also made in the “Te Puni Village Buildings” [36], and Italy [9, 10, 37-39].

The friction dampers currently proposed for equipping beam-to-column joints can be divided into two categories: 1) dampers based on Symmetric Friction Connections (SFC) and 2) dampers based on Asymmetric Friction Connections (AFC).

The symmetric friction connections are typically constituted by two external plates bolted with normal holes to an internal plate with long slotted hole in the direction of the applied force. Moreover, friction pads are located between the external plates and the internal plate (Figure 1.14). The friction pads can be constituted by a plate of a specifically selected material or by steel plates properly coated. In both case, either the friction pad material or the coating of the steel plates need to be accurately selected to provide adequate values of the friction coefficient and to reduce the loss of bolt preloading due to the wearing of the contact surfaces with the aim of assuring the stability of the hysteresis loops [40, 42]. The normal washers are often substituted by means of Belleville washers, i.e. disk springs, to reduce the bolt preloading losses.

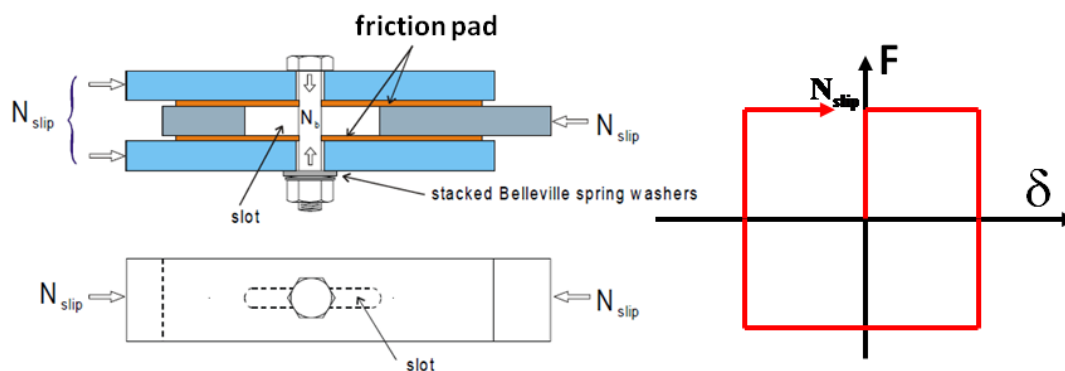


Figure 1.14: Conception and ideal force-displacement behaviour of a symmetric friction connection

The theoretical force-displacement behaviour of a symmetric friction connection corresponds to the ideal rigid-perfectly plastic model where the plateau is actually due to the slip resistance of the connection which can be computed as:

$$N_{slip} = n_b n_s \mu N_b \quad (1.14)$$

being n_b the number of bolts, n_s the number of contact surfaces, μ the coefficient of friction and N_b the bolt preloading. Also the asymmetric friction connections (Figure 1.15) are constituted by two external plates bolted with normal holes to an internal plate with long slotted holes in the direction of the applied force, but the force is transmitted to the device by only one

external plate. The second external plate, so-called cap plate, is not subjected to external forces. Moreover, two shims or friction pads are located between the external plates and the internal plate.

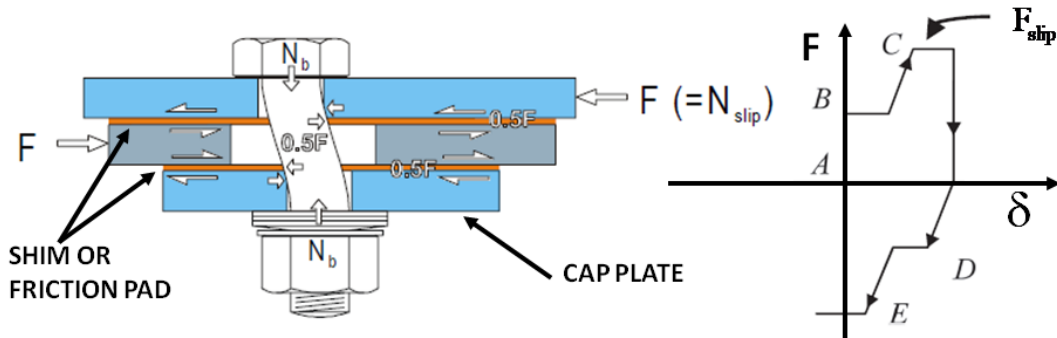


Figure 1.15: Conception and ideal force-displacement behaviour of an asymmetric friction connection

There are two sliding surfaces in the AFC: 1) the interface between the upper shim and the external plate transmitting the applied force, and 2) the interface between the lower shim and the internal plate. The idealised force-displacement behaviour of AFCs is characterised by two slip resistance levels. As the seismic demand exceeds the frictional resistance of the AFC, sliding first occurs on the first interface for a slip resistance level corresponding to point B. Further increases in seismic demand forces the second interface to slide, which is represented by slip level C. At this stage, the bolt is in double curvature with bending moment distribution shown in Figure 1.16. Upon load reversal, sliding occurs on the first interface (D), followed by the second interface (E).

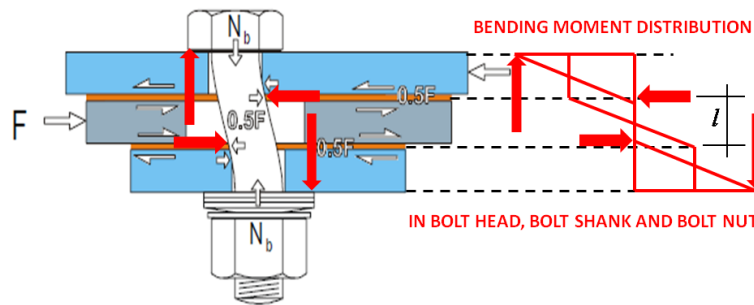


Figure 1.16: Bolt shank behaviour in double curvature

The maximum bending moment in the bolt shank is given by:

$$M = \frac{Vl}{2} = \frac{\mu Nl}{2} \tag{1.15}$$

The design flexural resistance of the bolt shank, reduced due to the contemporary tension force N due to bolt preloading, is given by:

$$M_{\text{bolt.Rd}} = Z_b \left(1 - \frac{N}{N_{b,\text{Rd}}} \right) f_{ub} \cong 0.1655d_b^3 \left(1 - \frac{N}{0.56d_b^2 f_{ub}} \right) f_{ub} \tag{1.16}$$

The design shear resistance of the bolt shank is given by:

$$V_{\text{bolt.Rd}} \cong 0.62f_{ub} 0.56d_b^2 \tag{1.17}$$

As the bolt is contemporaneously subjected to bending moment and shear, M-V interaction is taken into account using the following domain:

$$\frac{M}{M_{\text{bolt.Rd}}} + \frac{V}{V_{\text{bolt.Rd}}} = 1 \quad (1.18)$$

Taking into account that $V = \mu N$, combining equations (1.15-1.18) and solving with respect to N , the slip resistance due to a single bolt is evaluated as:

$$F_{\text{slip}} = 2\mu N \quad (1.19)$$

It is useful to note that the main disadvantage of AFCs compared to SFCs is due to M-N-V interaction in the bolt shank which, given the coefficient of friction and the bolt diameter, leads to a reduction of the force transmitted by friction. In fact, the value of N corresponding to the bolt yielding condition is less than N_b , so that AFCs are able to transmit a lower force compared to SFCs. On the other hand, the authors of AFCs claim for some recentering effect due to the shape of the hysteresis loop.

Beam-to-column joints equipped with asymmetric friction dampers are also referred as sliding hinge joints (Figure 1.17) [31-35]. The beam end is placed to leave a “beam clearance” away from the column face. The beam top flange is connected to the column flange using a cover plate welded to the column and bolted to the beam. The end of the cover plate, welded to the column, establishes the location of the centre of rotation. The location of the centre of rotation is aimed to minimize the slab damage. The shear force in the beam is carried by the top web bolts. Horizontally slotted holes are provided in the bottom flange plate and in the bottom holes of the column web plate to allow significant rotations of the beam end relative to the column face. A gap is provided between the end of the beam bottom flange and the column face. This gap is required to be large enough to accommodate the rotation demands expected under severe seismic events. Below the bottom flange plate is the bottom flange cap plate. It is a floating plate because it has no physical connection to the rest of the joint apart from through the bolts. A web cap plate is similarly placed on the outside of the web plate. On all surfaces where sliding may possibly occur, shims are placed. These shims may be manufactured of steel, brass or other materials. These have standard sized holes so sliding occurs on the side of the shim in contact with the bottom flange plate or web plate.

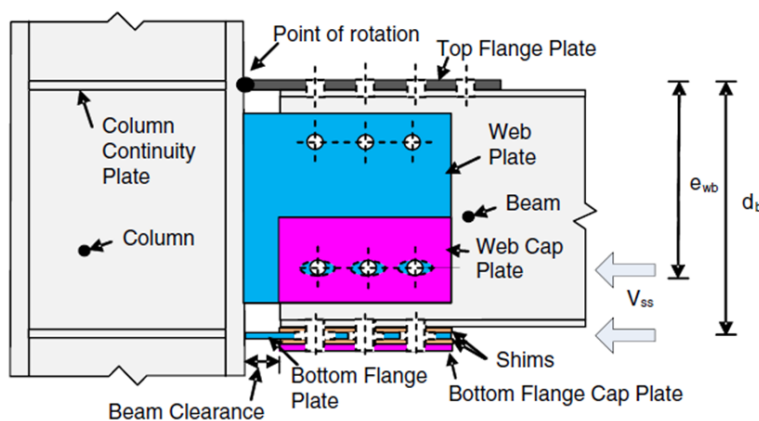


Figure 1.17: Sliding hinge joint with asymmetric friction connections [36, 43]

The cyclic behavior of sliding hinge joints equipped with asymmetric friction connections is shown in Figure 1.18. It can be pointed out that the hysteretic loop shape is not that of a traditional friction device (i.e. rectangular) but it is like a smeared out version.

This connection typology is referred by the authors as a low damage connection because yielding is limited to the development of a yield line in the top flange plate and in the bottom flange plate welded to the column flange, due to the bending of these plates resulting from the connection rotation, and to yielding of the bolts due to the M-N-V interaction typically occurring in AFCs. It means that, after a severe seismic events, bolts have to be substituted.

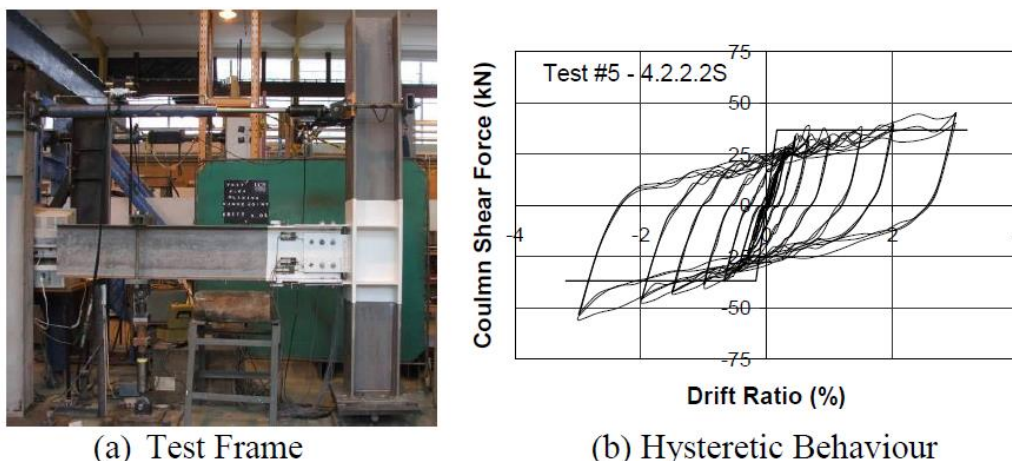


Figure 1.18: Cyclic behaviour of sliding hinge joints with asymmetric friction connections [43]

A wide experimental analysis on beam-to-column connections equipped with symmetric friction connections has been carried at Salerno University within the framework of the European RFCS Research Project FREEDAM [44]. The connection is conceived to allow the use of a friction damper completely prefabricated and assembled on shop to assure the maximum control of the tightening of the bolts and, as a consequence, of the bolt preloading level governing the slip resistance of the friction damper. Therefore, the prefabricated and pre-assembled friction damper is successively bolted on site to the column flange and to the beam flange. In addition, the prefabricated friction damper gives rise to the increase of the lever arm and, therefore, to the increase of the bending moment corresponding to the slip (Figure 1.19). The experimental program leading to the development of the friction damper is presented in Chapter 2 while the testing of complete beam-to-column joints sub-assemblages is presented in Chapter 3.

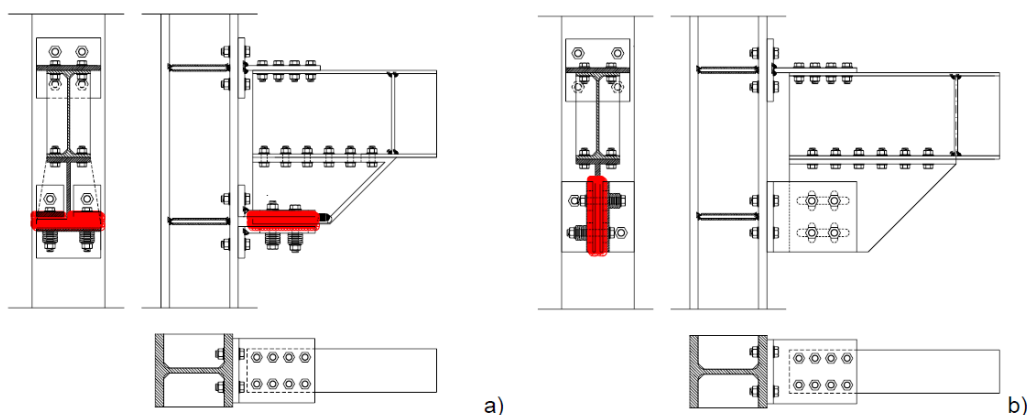


Figure 1.19: a) Configuration with horizontal damper;
b) Configuration with vertical damper

Eight external beam-to-column connections have been tested. The main objective of the tests is, on one hand, the validation of the design procedure developed within the project and, on the

other hand, the assessment of the proposed system in terms of energy dissipation and prevention of connection damage.

The tests have regarded eight beam-to-column joints, considering two different sizes of the beam (IPE 270 and IPE 450) and two different configurations of the friction damper (horizontal and vertical) equipping the joints (Figure 1.19). For each damper configuration the test has been executed twice, once using disc springs and another time using simple flat washers for the bolt assemblies [44, 45].

The specimens have been designed exploiting, for all the joint components, except the friction pad, the models already proposed by Eurocode 3 part 1-8 and, for the new component, i.e. the friction damper, the results coming from the experimental tests specifically devoted to the friction damper have been exploited. The design procedure for beam-to-column joints equipped with FREEDAM dampers is presented in Chapter 7 belonging to Part II (“Design Handbook”).

As an example the testing of a beam-to-column joint equipped with the friction damper in the horizontal configuration is shown in Figure 1.20. The cyclic behaviour of the joint is also presented showing the relation between the bending moment, evaluated at the column flange, and the connection rotation. The shape of the hysteresis loops is due to the bending of the stem of fixed T-stub and to the bending of the angles, due to the connection rotation, giving rise to a pressure distribution on the friction pads (cockpit effect) different from that occurring in simple axial tests typically carried out for the experimental investigation of the friction damper alone.

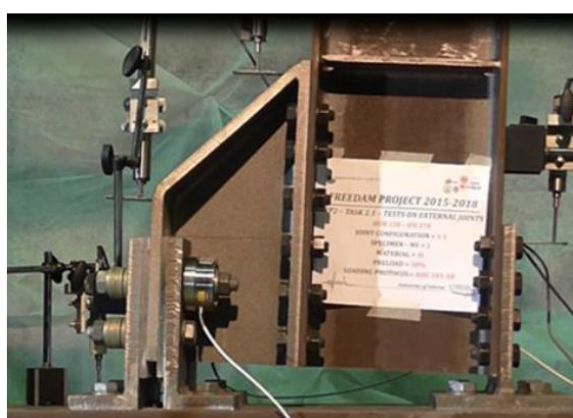
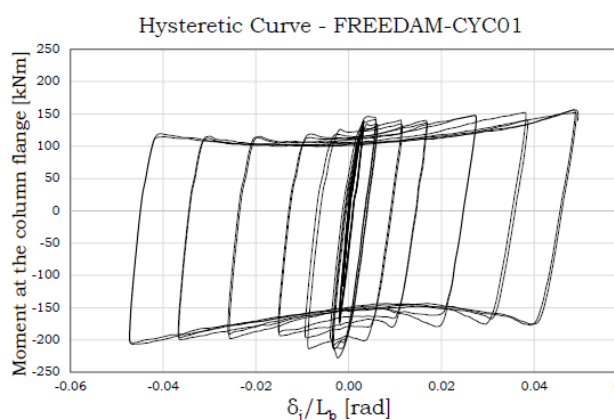


Figure 1.20: Testing of a connection equipped with the friction damper in the horizontal configuration



Some minor yielding is limited to the stem of the fixed T-stub and to the stems of the angles due to their bending because of the cockpit effect. The connections can easily accommodate any desired value of the rotation by simply designing the stroke of the long slotted holes of the friction dampers. The beam-to-column joint equipped with the friction damper in the vertical configuration has been conceived in order to avoid the cockpit effect and, as a consequence, to improve the shape of the hysteresis loops. Also in this case, the friction damper is conceived to be completely prefabricated and assembled on shop and, successively, bolted on site to the column flange and to the beam flange.

As an example the testing of a beam-to-column joint equipped with the friction damper in the vertical configuration is shown in Figure 1.21. The cyclic behaviour of the joint is also presented

showing the relation between the bending moment, evaluated at the column flange, and the connection rotation. The shape of the hysteresis loops is very close to the ideal rectangular shape. Also the stability of the loops is excellent with only minor degradation of the slip resistance due to the wearing of the contact surfaces of the friction pads. This is due to the coating process specifically designed for the friction pads [44].

In addition, in this case minor yielding is limited to the stem of the fixed T-stub, subjected to the bending due to the connection rotation, used to locate the centre of rotation. The centre of rotation is obviously located at the top flange supporting the concrete slab. Such choice of the centre of rotation is aimed to prevent the damage of the concrete slab in building structures.

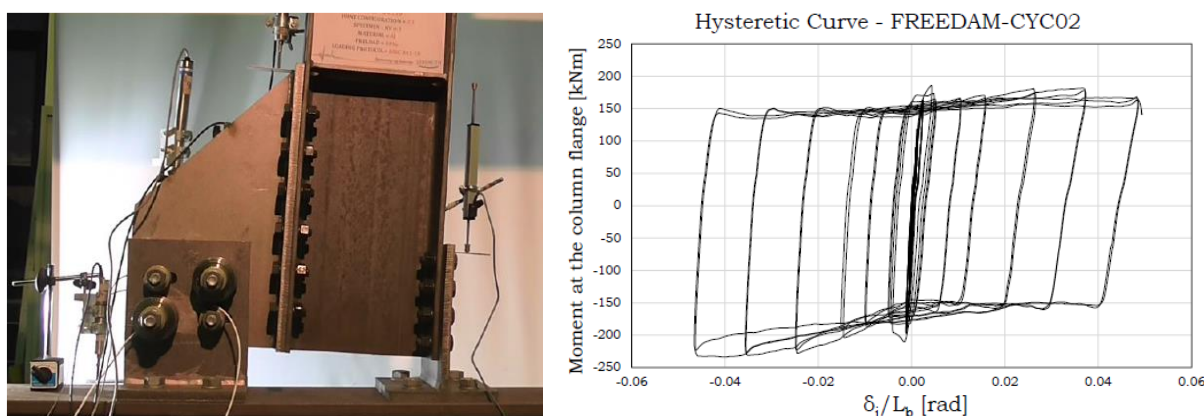


Figure 1.21: Testing of a connection equipped with the friction damper in the vertical configuration

1.4 SELF-CENTERING CONNECTIONS

Self-centering dissipative connections (SC-DC) for moment-resisting frames have also been recently proposed [46-54]. They are constituted by a re-centering system based on post-tensioned (PT) strands which is combined with a dissipative connection. Even though SC-DCs proposed by different researchers are equipped with hysteretic dampers or friction dampers, in principle the dissipative connection in SC-DCs can be equipped with any typology of passive seismic dampers.

As an example, a self-centering dissipative connection equipped with passive friction dampers is shown in Figure 1.22. The self-centering system is typically constituted by PT strands running parallel to the beams across multiple bays through the columns. Such strands are anchored outside the connection region as depicted in Figure 1.23. The high strength steel strands are post-tensioned after the friction devices are installed. The beam flanges are compressed against the column flanges because of the initial post-tensioning force applied to the strands. In order to prevent premature yielding or buckling of the beam flanges due to excessive compression under the combined action of axial force, due to post-tensioning, and bending, reinforcing plates are needed. Such reinforcing plates are typically welded on the outside faces of the beam flanges. Shim plates are placed between the column flange and the beam flanges so that only the beam flanges and reinforcing plates are in contact with the column. This enables good contact to be

maintained between the beam flanges and column face, while protecting the beam web from yielding under bearing.

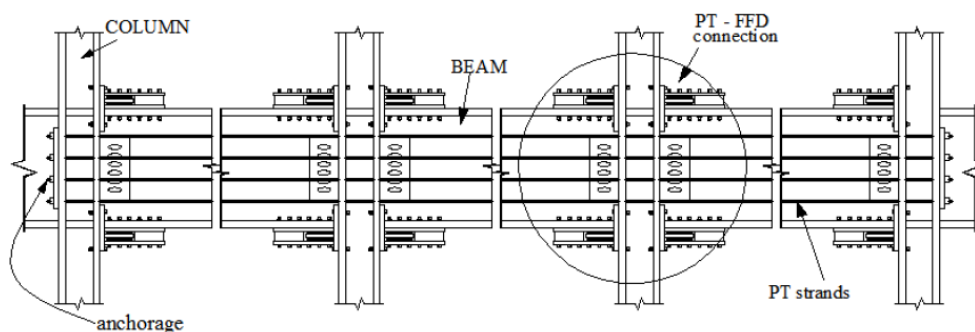


Figure 1.22: Self-centering connections equipped with friction dampers [48, 54]

The friction devices are located at the beam flanges and are composed by an internal plate (friction plate) sandwiched between two brass shim plates constituting the friction pads. The friction pads are in contact with such internal plate and either the beam flange reinforcing plate or an outer plate. All plates are bolted to the beam flanges. Long slotted holes are drilled on the internal plate to accommodate the stroke of the friction damper during gap opening and closing of the connections. Friction is generated when the beam flanges and outer plate slide against the internal plate when the beam rotates about the centre of rotation located at the mid-depth of the reinforcing plates. A shear tab with slotted holes is bolted to the beam web and welded to the column flange to transmit the shear forces.

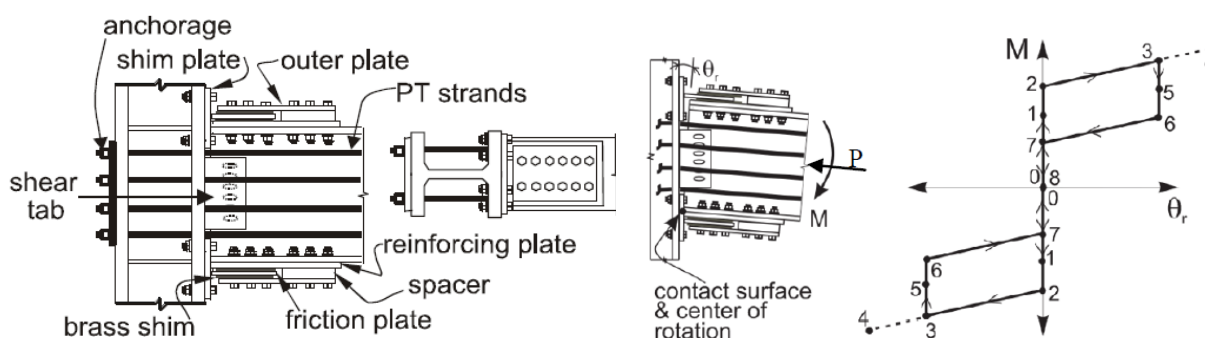


Figure 1.23: Components of a self-centering connection with friction dampers (left) and resulting cyclic response (right) [48, 54]

The moment-rotation behaviour of such connection typology when subjected to cyclic loading is schematically shown in Figure 1.23. The behavior is characterized by a gap opening and closing at the beam-column interface. The total moment resistance of the connection is provided by the moment due to the initial post-tensioning force in the strands, friction force, and an additional force developed due to elongation of the strands. The friction forces act at the mid-depth of top and bottom friction plates.

Under applied moment, the connection initially behaves as a rigid connection and the relative rotation is equal to zero (events 0 to 2 in Figure 1.23). Once the magnitude of the applied moment reaches the moment resistance due to the initial post-tensioning force in the strands,

decompression of the beam from the column face occurs. The corresponding moment (event 1) is called the decompression moment. The applied moment continues to increase between events 1 and 2 as the rotation of the beam is still restrained by the resistance of the friction dampers. At event 1 the friction force is minimal and increases gradually up to its maximum value at point 2, which is the point of incipient rotation.

After gap opening, the elastic axial stiffness of the post-tensioned strands provides the residual stiffness of the connection. In this phase, the elongation of the strands produce an additional force contributing to resist the total applied moment. Yielding of the strands eventually may occur at event 4. When unloading occurs (event 3), the relative rotation remains constant. At event 5, the friction force is again equal to zero. Between events 5 and 6 the friction force changes direction and progressively increases until its maximum value is obtained again at event 6. Between events 6 and 7, the beam rotates until the beam top flange is back in contact with the shim plate, but not compressed. Between events 7 and 8 the value of the friction force decreases with the beam being compressed against the shim plates and M equal to zero at event 8. A complete reversal in the applied moment will result in a similar connection behavior occurring in the opposite direction of loading, as shown in Fig. 23.

It is easy to recognize that, in order to obtain a self-centering behaviour, it is of primary importance that the strands remain in elastic range and, in addition, also the beam flanges have to be strengthened to prevent yielding. If these conditions are assured the post-tensioning force is preserved and the connection will self-center upon unloading. It means that the relative rotation returns to zero upon removal of the connection moment and the structure returns to its pre-earthquake position provided that the columns are designed to prevent their yielding. The cyclic moment-rotation behaviour of the connection is characterized by a flag-shaped hysteresis loop where the energy dissipation capacity is related to the force developed between the friction surfaces.

1.5 REFERENCES

- [1] Mazzolani F.M., Piluso V.: “Theory and Design of Seismic Resistant Steel Frames”, E & FN Spon, An imprint of Chapman & Hall, First Edition, 1996. ISBN 0-419-18760-X.
- [2] Mazzolani F.M., (Editor): “Moment Resistant Connections of Steel Frames in Seismic Areas, Design and Reliability”, E&FN Spon, 2000.
- [3] Elghazouli A.Y.: “Seismic Design of Steel Frames with Bolted Beam-to-Column Connections”, Elnashai, A. S. and Dowling, P. J. (Editors.), ICP (pubs.), (2000).
- [4] Bruneau M., Uang C., Wittaker A. W.: “Ductile Design of Steel Structures”, McGraw Hill, 1998.
- [5] Faella C., Piluso V., Rizzano G.: “Structural Steel Semirigid Connections”, CRC Press, Boca Raton, Ann Arbor, London, Tokyo, 1999. ISBN 0-8493-7433-2.
- [6] Piluso V., G. Rizzano G.: “Random Material Variability Effects on Full-Strength End-Plate Connections”, Journal of Constructional Steel Research, Volume 63, Issue 5, pp. 658-666, 2007.

-
- [7] Piluso V., G. Rizzano, M. Latour M., Francavilla A.B.: “Progettazione Sismica dei Collegamenti Flangiati Trave-Colonna a Completo Ripristino di Resistenza e Duttilità”, Centro Stampa Università di Salerno, ISBN: 978-88-940089-2-0, Ottobre 2015.
- [8] Piluso V., Montuori R., Troisi M.: “Innovative structural details in MR-frames for free from damage structures”, *Mechanics Research Communications*, Vol. 58 (2014), pp. 146–156.
- [9] Latour M., Piluso V., Rizzano G.: “Free from damage beam-to-column joints: Testing and design of DST connections with friction pads”, *Engineering Structures*, Vol. 85, pp. 219-233, 2015
- [10] Latour M., Piluso V., Rizzano G.: “Experimental analysis of beam-to-column joints equipped with sprayed aluminium friction dampers”, *Engineering Structures*, Vol. 146, pp. 33-48, 2018.
- [11] Aiken I.D., Clark P.W., Kelly J.M.: “Design and Ultimate-Level Earthquake Tests of a 1/2.5 Scale Base-Isolated Reinforced-Concrete Building.” *Proceedings of ATC-17-1 Seminar on seismic Isolation, Passive Energy Dissipation and Active Control*. San Francisco. California. 1993
- [12] Constantinou M.C., Soong T.T., Dargush G.F.: “Passive Energy Dissipation Systems for Structural Design and Retrofit.” *Multidisciplinary Center for Earthquake Engineering Research, University at Buffalo, State of New York*, 1998.
- [13] Christopoulos C., Filiatrault A.: “Principles of Passive Supplemental Damping and Seismic Isolation”, IUSS PRESS, 2000, Pavia. Italy
- [14] Yang T-S., Popov E.P.: “Experimental and Analytical Studies of Steel Connections and Energy Dissipators”, Report No. UCB/EERC-95/13, University of California, Berkeley, 1995.
- [15] Kelly J.M.: “Aseismic Base Isolation: A review. *Proceedings, 2nd U.S. National Conference on Earthquake Engineering, Stanford, CA, 823-837, 1979*
- [16] Pall A.S., Marsh C.: “Response of Friction Damped Braced Frames”, *Journal of Structural Division, ASCE, Vol. 108, No. ST6, June, pp. 1313-1323, 1982*
- [17] Marsh C., Pall A.S.: “Friction Devices to Control Seismic Response”, *Proceedings Second ASCE/EMD Specialty Conference on Dynamic Response of Structures, Atlanta, U.S.A., January, pp. 809-818, 1981.*
- [18] Pall A.S., Marsh C., Fazio P.: “Limited Slip Bolted Joints for Large Panel Structures”, *Proceedings, Symposium on Behavior of Building Systems and Building Components, Nashville, U.S.A., March, pp. 385-494, 1979.*
- [19] Mualla I., Belev B.: “Seismic Response of Steel Frames Equiped with a New Friction Damper Device Under Earthquake Excitation”, *Engineering Structures*, 24(3), pp.365-71, 2002.
- [20] Kelly J., Skinner R., Heine A.: “Mechanisms of Energy Absorption in Special Devices for Use in Earthquake Resistant Structures”, *Bullettin of the New Zealand Society for Earthquake Engineering*, 5(3), pp.63-88, 1972.
- [21] Calado L., De Matteis G., Landolfo R.: “Experimental response of top and seat angle semi-rigid steel frame connections”. *Material and Structures*, Vol.33, 2000, pp.499-510.
- [22] De Matteis G., Landolfo R., Calado L.: “Cyclic Behaviour of Semi-Rigid Angle Connections: a Comparative Study of Tests and Modelling”. *Proc. of Third International*

- Conference "Behaviour of Steel Structures in Seismic Areas", Montreal (Canada), August, 2000, Balkema pp.165-174.
- [23] Elnashai A.S., Elghazouli A.Y.: "Seismic Behaviour of Semi-Rigid Steel Frames: Experimental and Analytical Investigations", *Journal of Constructional Steel Research*, 29, pp. 149-174, 1994.
- [24] Elnashai A.S., Elghazouli A.Y, Danish-Ashtiani F.A.: "Response of Semi-Rigid Steel Frames to Cyclic and Earthquake Loads", *Journal of Structural Engineering, ASCE*, 124(8), pp. 857-867, 1998.
- [25] Iannone F., Latour M., Piluso V., Rizzano G.: "Experimental Analysis of Bolted Steel Beam-to-Column Connections: Component Identification". *Journal of Earthquake Engineering*, 15(2), pp. 214-44, 2011.
- [26] Latour M., Piluso V., Rizzano G.: "Cyclic Modeling of Bolted Beam-to-Column Connections: Component Approach", *Journal of Earthquake Engineering*, 15(4), pp.537-63, 2011.
- [27] Latour M., Rizzano G.: "Experimental Behavior and Mechanical Modeling of Dissipative T-Stub Connections", *Journal of Structural Engineering*, 138(2), pp.170-82, 2012.
- [28] Oh S.H., Kim Y.J., Ryu H.S.: "Seismic performance of steel structures with slit dampers", *Engineering Structures*, vol. 31, pp. 1997-2008, 2009.
- [29] Inoue K., Suita K., Takeuchi I., Chusilp P., Nakashima M., Zhou F.: "Seismic-Resistant Weld-Free Steel Frame Buildings with Mechanical Joints and Hysteretic Dampers", *Journal of Structural Engineering, ASCE*, Vol. 132, No. 6, June 1, pp. 864-872, 2006
- [30] Yang T.S., Popov E.P.: "Experimental and analytical studies of steel connections and energy dissipators", Berkeley: Earthquake Engineering Research Center, UCB/EERC-95/13, 1995.
- [31] Khoo H., Clifton G.C., MacRae G., Ramhormozian S.: "Proposed design models for the asymmetric friction connection", *Earthquake Engineering and Structural Dynamics*. December 2014;44(8):1309-1324.
- [32] Borzouie J., MacRae G., Chase J.: "Cyclic Performance of Asymmetric Friction Connections with Grade 10.9 Bolts. *The Bridge and Structural Engineer*. March 2015; 45(1).
- [33] Yeung S., Zhou H., Khoo H., Clifton G.C., MacRae G.: "Sliding shear capacities of the Asymmetric Friction Connection", 2013 NZSEE Conference, April 26-28, Wellington, 2013. Paper n. 27
- [34] Butterworth J.W., Clifton G.C.: "Performance of Hierarchical Friction Dissipating Joints in Moment Resisting Steel Frames", 12 World Conference on Earthquake Engineering, Paper N. 718, 2000
- [35] Golondrino J.C., MacRae G., Chase J., Rodgers G., Clifton G.C.: "Velocity effects on the behavior of asymmetrical friction connections (AFC)", 8th STESSA Conference, Shanghai, China, July 1-3, 2015
- [36] MacRae G., Clifton G.C.: "Low Damage Design of Steel Structures", *Steel Innovations 2013*, Workshop, 21-22 February 2013, Christchurch.
- [37] Latour M., Piluso V., Rizzano G.: "Experimental Analysis of Innovative Dissipative Bolted Double Split Tee Beam-to-column Connections", DOI: 10.1002 /stco.201110009, *Steel Construction*, Volume 4, Issue 2, pages 53–64, June, 2011.

- [38] Latour M., Piluso V., Rizzano G.: “Experimental Behaviour of Friction T-stub Joints under Cyclic Loads”, *Steel Construction*, Volume 6, Issue 1, pages 11–18, 2013.
- [39] D’Aniello M., Zimbru M., Latour M., Francavilla A. B., Landolfo R., Piluso V., Rizzano G.: “Development and Validation of Design Criteria for Free from Damage Steel Joints”, *EUROSTEEL 2017*, September 13–15, 2017, Copenhagen, Denmark.
- [40] Ferrante Cavallaro G., Latour M., Francavilla A.B., Piluso V., Rizzano G.: “Standardised friction damper bolt assemblies time-related relaxation and installed tension variability”, *Journal of Constructional Steel Research*, 141, pp. 145-155, 2018.
- [41] Ferrante Cavallaro G., Francavilla A.B., Latour M., Piluso V., Rizzano G.: “Experimental behaviour of innovative thermal spray coating materials for FREEDAM joints”, *Composites Part B: Engineering* 115, pp. 289-299, 2017.
- [42] Latour M., Piluso V., Rizzano G.: “Experimental analysis on friction materials for supplemental damping devices”, *Construction and Building Materials* 65, pp. 159-176, 2014.
- [43] MacRae G., Clifton G.C.: “New Technology Applications, Recent Developments and Research Directions for Seismic Steel Structures in New Zealand”, *Asian Conference on Earthquake Engineering*, Bangkok, Thailand, December, 2010.
- [44] Piluso V., Rizzano G., Latour M., Francavilla A.B., Ferrante Cavallaro G., Nastri, da Silva L.S., Santiago A., Santos A.F., Castellano M.G., Di Fusco D., Jaspert J.P., Demonceau J.F., D’Antimo M., Landolfo R., D’Aniello M., Zimbru M., Silva J.M., Guerra I.: “FREEDAM - FREE from DAMage Steel Connections”, Grant Agreement RFSR-CT-2015-00022, Mid-term Report: 1st July 2015 – 31st December 2016 (Coordinator: V. Piluso).
- [45] Piluso V., Latour M., Francavilla A.B., Rizzano G.: “Experimental tests on FREEDAM connections subjected to cyclic loading conditions: Test Report”, *FREEDAM - FREE from DAMage Steel Connections*, Grant Agreement RFSR-CT-2015-00022, Deliverable D5-WP2T2.1 “Test Report”, Task 2.1 – Tests on external beam-to-column joints, 31 March 2016.
- [46] Ricles J.M., Sause R., Garlock M., Zhao C.: “Posttensioned Seismic-Resistant Connections for Steel Frames”, *Journal of Structural Engineering*, Vol. 127, No. 2, February, pp. 113-121, 2001.
- [47] Christopoulos C., Filiatrault A., Uang C-M., Folz B.: “Posttensioned Energy Dissipating Connections for Moment-Resisting Steel Frames”, *Journal of Structural Engineering*, Vol. 128, No. 9, September 1, pp. 1111-1120, 2002.
- [48] Rojas P., Ricles J.M., Sause R.: “Seismic Response and Design of Post-Tensioned Steel Moment Resisting Frames with Friction Components”, *13th World Conference on Earthquake Engineering*, Vancouver, B.C., Canada, August 1-6, Paper No. 1603, 2004.
- [49] Garlock M., Ricles J.M., Sause R.: “Experimental Studies of Full-Scale Posttensioned Steel Connections”, *Journal of Structural Engineering*, Vol. 131, No. 3, March 1, pp. 438-448, 2005.
- [50] Chou C-C., Chen J-H., Chen Y-C, Tsai K-C: “Evaluating performance of post-tensioned steel connections with strands and reduced flange plates”, *Earthquake Engineering and Structural Dynamics*, 35, pp. 1167–1185, 2006.

-
- [51] Garlock M., Sause R., Ricles J.M.: “Behavior and Design of Posttensioned Steel Frame Systems”, *Journal of Structural Engineering*, Vol. 133, No. 3, March 1, pp. 389-399, 2007.
 - [52] Garlock M, Li J.: “Steel self-centering moment frames with collector beam floor diaphragms”, *Journal of Constructional Steel Research*, 64, pp. 526–538, 2008.
 - [53] Wolski M., Ricles J.M., Sause R.: “Experimental Study of a Self-Centering Beam–Column Connection with Bottom Flange Friction Device”, *Journal of Structural Engineering*, Vol. 135, No. 5, May 1, pp. 479-488, 2009.
 - [54] Rojas P., Suárez D.C., Ricles J.M., Sause R.: “Seismic evaluation of an eight story building with self- centering steel moment resisting frames and flange friction devices”, *15th World Conference on Earthquake Engineering*, Lisboa, Paper No. 3002, 2012

CHAPTER 2

DEVELOPMENT OF FREEDAM DAMPERS

2.1 INTRODUCTION

The development of supplemental damping devices started in New Zealand about 50 years ago thanks to an improved understanding of the seismic response of constructions based on the physical interpretation of the structural dynamics in terms of energy balance [1]-[4]. In fact, as already discussed, the seismic input energy is usually transformed in kinetic energy, viscous and hysteretic damping, and elastic strain energy. The addition of a passive energy dissipation systems in specific points of a construction changes the structural properties and, specifically, it modifies the energy balance during the seismic event, providing benefits in terms of reduction of the sway displacements and damage. Additionally, maximizing the energy dissipation in specific fuses through the adoption of proper design strategies allows improving the structural reparability in case of severe seismic events because of the opportunity to easily replace the damaged devices. Owing to these benefits, in the past few decades, the development of supplemental damping systems has received great attention of academics and engineers leading to the development of a large number of dissipative devices [5]-[10]. Many of these systems have been installed in buildings and bridges worldwide, both for seismic retrofit and for new constructions (Figure 2.1-Figure 2.2).



a) Viscous dampers applied in the Rion-Antirion Bridge (Greece) - (Courtesy: FIPMEC srl)

b) Buckling restrained braces installed in a precast r.c. structure in Ancona (Italy) - (Courtesy: FIPMEC srl)

Figure 2.1 – Examples of displacement and velocity activated dissipative bracings

In general, passive energy dissipation systems may be divided according to three categories: *i) displacement activated; ii) velocity activated; iii) motion activated*. The first category regards the devices which dissipate energy due to the relative displacement occurring between two points of the structure. These dampers have features which are not dependent on the frequency of motion and provide forces which are in phase with the internal actions arising in the structure. Typical examples of systems belonging to this category are all the typologies of metallic yielding dampers. The second category regards dampers which dissipate the seismic input energy through relative velocities occurring between connected points of the structure. The features of these dampers depend on the earthquake frequency and, typically, the maximum forces generated in the dampers are not in phase with the structural response. This means that the maximum

resistance exhibited by velocity activated dampers is not contemporaneous to the peak structural response in terms of displacements and forces. Typical examples of velocity-dependent systems are viscous and visco-elastic dampers.



a) ADAS device after testing



b) Pall devices installed in a single-diagonal brace at Boeing Commercial Airplane Factory Everett, USA - (Ref: Dr Pall)

Figure 2.2 – Dampers after testing

Finally, motion-activated devices are those modifying the structural response through a secondary system. A typical example of a motion-activated device is the tuned-mass damper which consists of a mass-spring-dashpot system able to disturb the flow of energy, reducing the structural response. A wide category of supplemental dampers is based on dry friction for dissipating the earthquake input energy. In these elements, the energy is dissipated by means of the slippage between two surfaces in contact, which are clamped through the application of hydraulic pressures, electromagnetic forces or, in the simplest case, by means of high strength bolts. This last clamping method is, due to its simplicity, probably the most applied in civil engineering practice. In fact, by adopting high strength bolts, it is possible to apply a constant force on one or more surfaces in contact by simply governing the value of the tightening torque and the number and diameter of bolts. Friction dampers usually fall into the category of displacement activated dampers, because their sliding force is considered only slightly dependent on the velocity and frequency content of the excitation. Nevertheless, while on the one hand the initial sliding force of friction dampers is in many cases negligibly affected by velocity, on the other hand, wearing and degradation of the friction resistance is, indeed, largely dependent on velocity. The cyclic behaviour of friction dampers can be usually described by means of a rigid-plastic response.

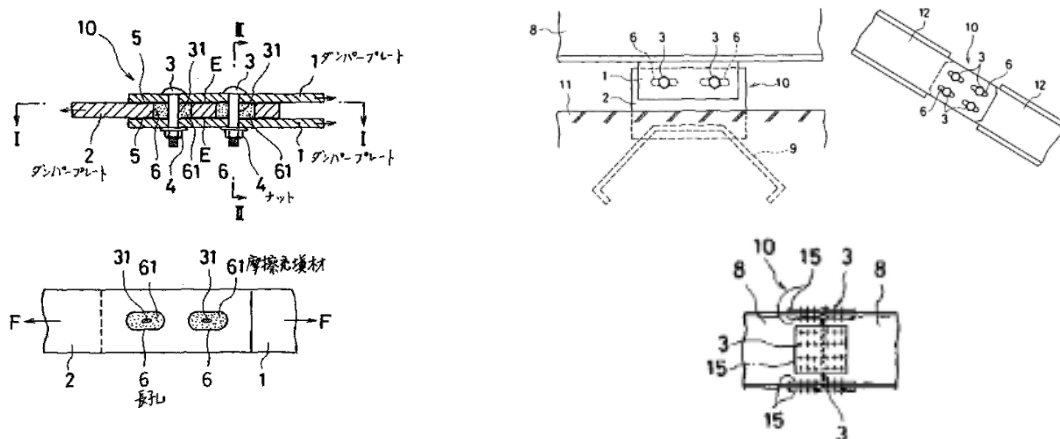
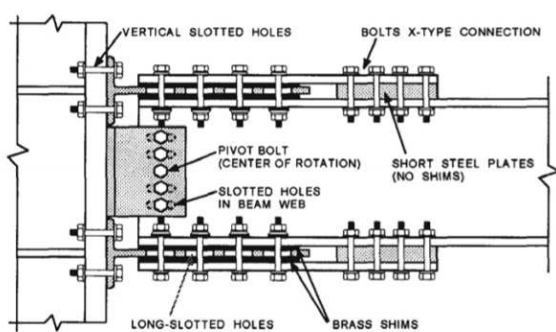


Figure 2.3 – First Japanese patent on anti-seismic friction device [11]



a) Concept of sliding hinge joint with symmetric friction devices [12]

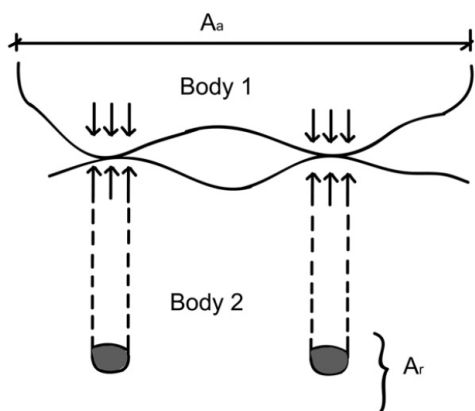


b) Sliding hinge joint with asymmetric friction dampers of the award-winning Te Puni Village of Wellington - [13]

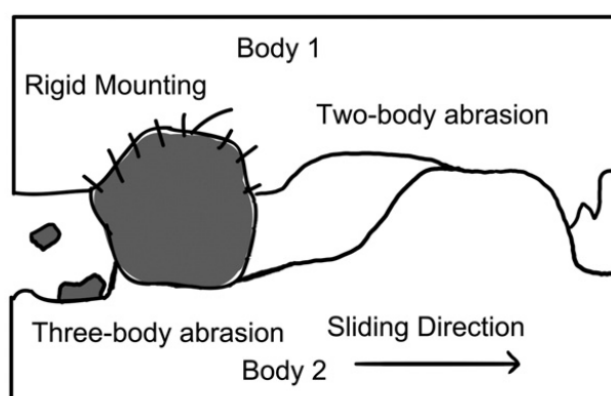
Figure 2.4 – Concept of sliding hinge joint with symmetric friction devices [12]

Therefore, the only parameter needed by the designer is the slip force which, in turn, depends on the value of the load normal to the surfaces in contact and on the friction coefficient which is an intrinsic characteristic of the sliding interface. A great advantage of friction devices is that they can be used to work as displacement reducers under service conditions while they can dissipate the seismic input energy under severe seismic actions.

The friction coefficient depends on different phenomena, such as adhesion, ploughing and the presence of contaminants. The modelling of these phenomena is usually studied in tribology where, in order to develop theories for predicting slip forces under static and dynamic loads, the surfaces' topography, materials' hardness, mechanical properties and the effects of interface layers are physically modelled (Figure 2.5). Conversely, in structural engineering, the properties of friction materials are typically studied by following the experimental approach which, for seismic engineering scopes is usually considered sufficient to provide the information needed for designing such devices.



a) Difference between real and apparent contact areas [14]



b) Abrasive wear [14]

Figure 2.5 – Basic concepts of tribology

In technical literature, several works are concerned with the characterisation of the hysteretic behaviour of sliding metallic surfaces with different superficial treatments clamped by means of high strength friction grip bolts. This case is particularly significant for civil engineering purposes because the greatest part of friction dampers developed since the 70s' to be used for

dissipative braces or links adopts this approach. The first devices of such a type were developed by [15] introducing friction dampers at the intersection of braces, which adopted asbestos brake lining pads between the steel sliding surfaces. One of the simplest forms of friction damper has been proposed by [16] who adopted simple bolted slotted plates located at the end of a conventional bracing member. The brace-to-frame connection was designed to slip before yielding or buckling of the brace. Another friction damper for chevron braces was proposed by [17]. Recent applications of friction dampers are related to the concept of low damage systems, which can dissipate the input energy suffering only negligible damage. Low damage semi-rigid beam-to-column connections have been recently investigated. Slotted bolted connections have proved to be a promising alternative to the traditional connection typologies. Indeed, slotted bolted connections have been primarily investigated by Grigorian et al. [12] and, based on these studies, Sliding Hinge Joints (SHJs) with Asymmetric friction connections (AFCs) located at the bottom beam flange, have been developed by Clifton [18][21] (Figure 2.4). After these initial studies, other similar solutions have been proposed in the last years. In [23]-[24] the friction damper has been realised with angles, and a haunch bolted both to the bottom beam flange and to the column. The main benefit of this configuration is the possibility of prefabricating the damper, assuring a better control of the friction material employed and of the correct application of the bolt tightening procedures. Moreover, the main difference with the solution proposed by Clifton is the adoption of Symmetrical Friction Connections (SFCs) in place of Asymmetrical Friction Connections (AFCs). For both solutions, the presence of the slab concentrates plasticity at the bottom beam flange level, and, accordingly, the damage is confined in the device leaving the connection undamaged (Figure 2.6).

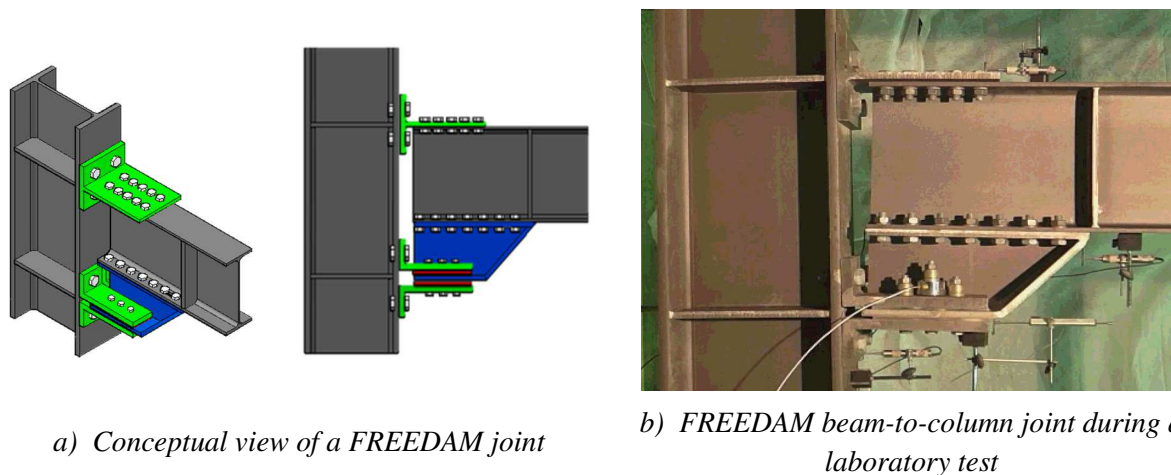


Figure 2.6 – FREE from Damage joint

In all the applications previously reported, it is clear that the development of a reliable friction damper able to provide wide and stable hysteresis loops is of paramount importance. Within the research project FREEDAM, this issue has been widely investigated proposing solutions with low cost and easy to apply in practice, also providing simple tools for the design and modelling of the developed slotted bolted friction dampers. The slippage force of a friction damper is the result of the product of the friction coefficient multiplied by the number of friction interfaces, the bolt number, and the bolt preloading force. Therefore, in order to govern the slippage resistance of a friction damper, it is necessary to control the preloading force applied with the bolts and to characterise accurately the value of the friction coefficient of the material employed

to realise the friction interface. The bolt preloading force can be controlled by applying one of the methods suggested by EN1090-2 EUROCODE 0. Basis of structural design. CEN, 2010.

[27] (i.e., combined, torque, DTI washers), which are conceived to assure the minimum 95% reliability on the tightening required by EN1990 [26]. Conversely, the value of the friction coefficient that a determined interface is able to develop is something that needs to be characterised experimentally and depends on a plurality of factors. In particular, as already demonstrated in past experimental works, the friction coefficient of an interface strongly depends on the materials employed to realise the friction device and on its main tribological properties, such as the superficial finishing, micro and macro hardness, shear resistance of the materials and roughness. This topic is addressed in the next paragraphs where the behaviour of the friction dampers developed during the research project FREEDAM. Specifically, the response of the dampers under cyclic loading conditions (low and high velocity) is presented. Subsequently, the long-term response of friction dampers is considered, and relevant information for the design of the friction dampers of the FREEDAM joint is given.

2.2 SELECTION OF MATERIALS FOR FRICTION PADS DEVELOPMENT

2.2.1 Basic friction theories

From the historical standpoint, the major part of past tribology studies has been addressed to the investigation of friction properties of metals, recognising that there are two main sources of friction between sliding bodies: adhesion and ploughing. The adhesion component arises because when two surfaces are loaded against each other, asperities deform plastically leading to the formation of the so-called “cold-weld” junctions. Because of the intimate contact of these junctions, the shearing of the adhesive ties requires a certain sliding load. Regarding ploughing, it is due to the natural surfaces’ roughness, so that the relative movement between the surfaces in contact requires that one body must lift over the other. The simplest theory to mathematically explain the origin of the adhesion component is due to [28] who states that being adhesion-dependent on the shear resistance of the cold-weld junctions, it has to be proportional to the real contact area which, for metals with ideal elastic-plastic behaviour, can be assumed equal to $A = N/\sigma_0$, where A is the real area of contact, σ_0 is the material penetration hardness and N is the load normal to the surfaces. The total friction force due to adhesion (F_A) can be expressed as:

$$F_A = As = \frac{N}{\sigma_0} s \quad (2.1)$$

being s the force per unit of area needed to shear cold-weld junctions. As already stated, ploughing is the friction force caused by the asperities of a hard metal penetrating in a softer metal. According to Bowden and Tabor theory, this contribution can be estimated as follows:

$$F_P = nrh\sigma_0 \quad (2.2)$$

where n is the number of asperities, r is the half-width of the asperity, and h is the height of the asperity. Therefore, the total sliding force (F) due to adhesion and ploughing is given by:

$$F = F_A + F_P = \frac{N}{\sigma_0} s + nrh\sigma_0 \quad (2.3)$$

The ploughing component is very important during the abrasion process, but, in the case of metals, it has been demonstrated that such contribution is negligible compared to adhesion. Therefore, Eq.(2.1) explains a very important property for metals, stating that the ratio between the frictional force and the normal applied load is a constant value which does not depend on the apparent area of contact. Practically, Bowden and Tabor's theory explains two of the three postulates of the classical theory of dry friction, stating that:

- the total frictional force is independent of the apparent surface area of contact;
- the total frictional force that can be developed is proportional to the normally applied action;
- in case of slow sliding velocities, the total frictional force is independent on the sliding velocity.

The first two postulates are often known as Amontons' laws, after the French engineer who presented them in 1699, while the third one, is due to Coulomb [29]-[30]. During slippage, the classical relationship to compute the tangential force acting at the sliding interface in the direction opposed to the motion is the well-known Coulomb friction equation $F=\mu N$, where F is the sliding force, N is the normal action and μ is the friction coefficient. The force of friction is always opposed to the movement (in case of kinetic friction) or potential movement (in case of static friction). According to Eq.(2.1), the following relationship can be obtained:

$$\mu = \frac{s_0}{\sigma_0} \quad (2.4)$$

where s_0 is the critical shear stress of the weakest material and σ_0 is the hardness of the softest material. Eq.(2.4) provides a reasonable estimate of the friction coefficient for metals, but in general, the friction coefficient depends on the other three effects: the contact pressure (P), the sliding speed (v), and the temperature (T). Therefore, in general, the coefficient of friction of an interface should be expressed as $\mu=\mu(P, v, T)$.

In the case of rubber-based materials, the structure of the material influences its frictional characteristics. In fact, rubber has a low elastic modulus, and its real contact area is strongly affected by the magnitude of the normal load because the material adapts to the shape of the surface asperities of the hardest material [31]. The behaviour of polymeric materials deviates from the classical friction theory. In fact, tribology of polymers is influenced by the adhesive junctions, the shear resistance of the rubbing material in contact and the real contact area [32]. The coefficient of friction of polymers, depending on the considered range of applied normal load and on the type of polymer, may be represented by means of constant or decreasing relationships [33]-[35]. In particular, several mathematical relationships have been proposed to model the friction coefficient of steel-rubber interfaces, by expressing μ as a function of the contact pressure (P) and of the material elastic modulus (E). Some of them are herein reported:

$$[36]: \frac{1}{\mu} = a + b \left(\frac{P}{E} \right) \quad (2.5)$$

where a and b are empirical parameters to be found by means of experimental testing;

$$[32]: \mu = K \left(\frac{P}{E} \right)^{-1/n} \quad (2.6)$$

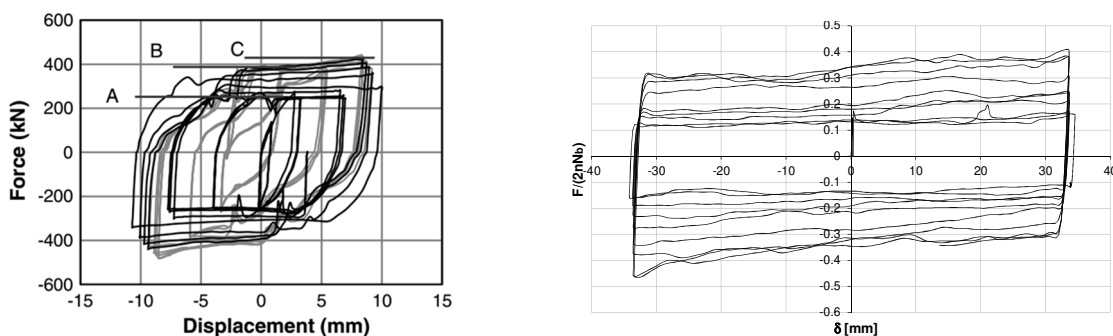
where the value of K and n have to be experimentally found;

$$[37]: \mu = \mu_{\infty} + a(P)^{-h} \quad (2.7)$$

where μ_{∞} is the value of the friction coefficient when the pressure is infinite, a is an experimental constant and h is the Shore hardness divided by 100. Finally, in the case of rubber, another important deviation from the classical friction theory must be pointed out. In fact, in the case of polymeric materials, the friction force can be significantly dependent on the sliding velocity. This behaviour is due to the viscoelastic behaviour of polymers. Notwithstanding, usually for many polymeric materials, the influence of velocity is small within a limited range of speeds (0.01-1 cm/s).

2.2.2 Friction materials tested during the research project FREEDAM

To date, several studies have already been devoted to the analysis of friction materials for seismic devices and friction joints. Mainly, past studies have been focused on the analysis of friction materials, especially for application to supplemental energy dissipation devices [38]-[40] but, more recently, similar studies have also been developed for the application of friction dampers in connections or for the development of particular types of friction joints with finger plates for tubular steel towers. In particular, significant works dealing with the characterisation of the behaviour of friction interfaces have recently been performed within the activities of the HISTWIN project in [41]-[42] (where static friction connections for application in steel wind towers have been studied), and by the research group of the University of Auckland [18]-[21] that has already performed a number of cyclic tests both on elementary connections and joints equipped with asymmetric friction dampers. In addition, other works dealing with the characterisation of the friction coefficient of interfaces have also already been developed in [43]. Within the FREEDAM research project, all these works have been used as a reference to provide a rational selection of materials to be tested for the application in FREEDAM connections.



a) Test on Mild Steel [14] 4 bolts – Preload level of each bolt 210 kN - 1 contact surface

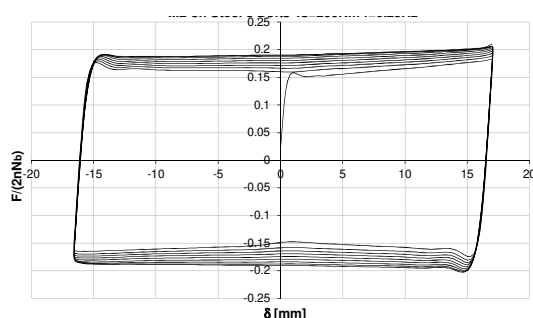
b) Test on Mild Steel [43] 4 bolts – Preload level of each bolt 50 kN - 2 contact surfaces

Figure 2.7 – Cyclic slip tests on steel

Additionally, the selection of the interfaces to be used for the friction dampers has been driven by some principles coming out from classical theoretical studies devoted to the assessment of

the response of damping devices to be used in seismic engineering applications. From Eq.(2.4) it can be easily recognized that, in the case of metallic interfaces, high values of the friction coefficient can be normally achieved only by coupling materials with a big difference of the superficial hardness. There are several possibilities to obtain this difference, but the materials mainly employed for realising friction interfaces in combination with steel are normally metals, rubbers or carbide alloys. Some of these categories of materials have already been widely investigated by several authors, such as high-strength tempered steels, brass, or phenolic rubbers. Examples of experimental works already carried out are that performed by [14] on normal and abrasion-resistant steels and the work performed by [43] on mild steel, brass, sprayed aluminium and different types of rubbers. These analyses have evidenced that interfaces constituted by mild steel can develop only low values of the friction coefficient (0.1-0.25) and in addition, when subjected to a cyclic loading history, provide a significant strain-hardening behaviour due to the damage occurring in the surfaces and the increase of the ploughing component of the friction coefficient (Figure 2.7).

Obviously, an initial value of the friction coefficient very low and the strain-hardening response shown under cyclic loading conditions are features not appropriate for the application of these materials to friction dampers. In fact, a low value of the initial friction coefficient represents a strong limitation for the development of friction connections with a low cost because employing a material of such a type would require the employment of many bolts in the damper and, as a consequence, the adoption of devices of big size and high cost. In addition, also the strain-hardening behaviour is not an advantageous feature for the application because, if the friction devices are subjected to strain-hardening, then it is required that all the other elements of the connections and the columns have to be over-strengthened with respect to the increased values of the forces, leading to a strong oversizing of all the elements of the frame. For all these reasons, interfaces with mild steel are usually not considered suitable for seismic dampers and, for similar reasons, also high-strength steels and abrasion-resistant steels already proposed in [14] provide limitations. Friction shims made of abrasion-resistant steel, even though they can develop a higher value of the friction coefficient (about 0.4), are still characterized by some strain-hardening. Other materials considered in past experimental works are brass, sprayed aluminium and different types of rubber [43].

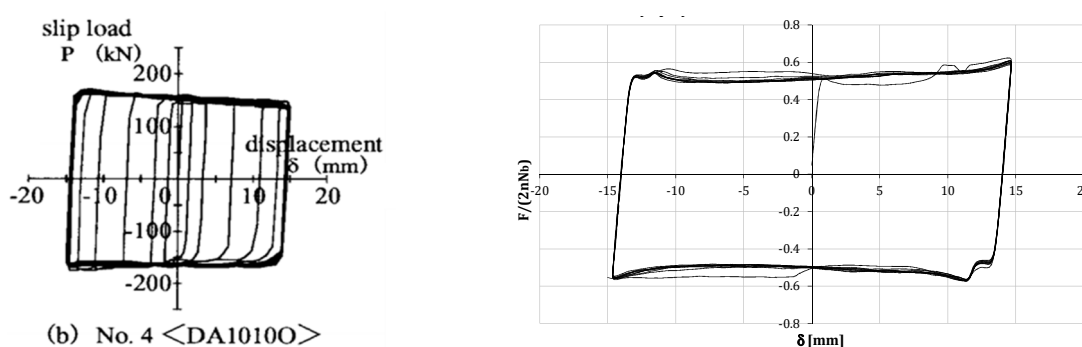


a) Test on Rubber M2 [43] 4 bolts – Preload level of each bolt 50 kN - 2 contact surfaces) b) Brittle failure of rubber friction shims along the net section [43]

Figure 2.8 – Tests on rubber

From past experience, rubbers normally used for application in braking systems (which are mainly constituted by phenolic resins) have demonstrated to provide a stable response but a pretty low value of the friction coefficient (ranging from 0.15 to 0.25). In addition, as reported

in [43], these materials are typically characterized by a low value of the tensile resistance, and this makes them not appropriate for application in friction connections unless they are glued to the steel plates. In fact, they can easily undergo brittle failures in holed sections under the actions normally arising in friction connections (Figure 2.8). Therefore, due to these drawbacks, rubber materials have not been considered for further testing in the project FREEDAM. Brass has been the topic of several studies devoted to characterizing its friction behavior [38], [39], [43] or testing its application in friction devices. In particular, in work performed by Voiculescu & Dalban [39], it has been pointed out, by means of tests on simple lap shear connections, that the friction coefficient of brass is approximately equal to 0.3. In [43], brass has also been studied by means of tests on splice connections and, also, in this case, it has been pointed out that the initial value of the friction coefficient is very low (about 0.1) even though it tends to increase with the increase of the ploughing arising on the interface under cyclic loading conditions.



a) Test on thermal spray Aluminium [40] 1 bolt -2 contact surfaces- Friction Coefficient provided by authors: 0.71
 b) Behaviour of thermal spray Aluminium [43] 4 bolts - Preload level of each bolt 50 kN - 2 contact surfaces

Figure 2.9 – Tests on thermal spray Aluminium

Promising tests on thermally sprayed aluminium have been provided by [40] and [43]. These experimental analyses have pointed out that the tribological response of thermally sprayed aluminium, is characterised by the development of values of the friction coefficient higher than 0.4 and by a stable response under cyclic loading conditions (Figure 2.9). Aside from the specific application, these studies have shown that, in general, thermal spray coatings are also characterised by a high potential for industrial application due to their low cost. On the base of this consideration, during the research project FREEDAM, materials that can be applied by means of thermal spray techniques have been selected for the development of friction dampers. Thermal spray is an industrial procedure to apply coatings by means of special devices/systems through which melted or molten metals are propelled at high speed on cleaned and prepared component surfaces. In this procedure, the coating material is melted by a heat source, and then it is propelled by means of gases on a base material, where it solidifies, forming a solid layer (Figure 2.10).

As already mentioned before, the difference between the superficial hardness of the plates in contact it is a fundamental feature because the friction coefficient of a metal interface is governed by the ratio between the shear resistance of the weakest material (s_0) and the superficial hardness of the softest material (σ_0) [28]. Therefore, based on the previous observation, it is clear that to obtain a high value of the friction coefficient, the requirements are: i) a big difference of the

superficial hardness of the materials in contact; ii) a high value of the shear resistance of the weakest material; iii) a very low value of the superficial hardness of the softest material is needed. To avoid corrosion phenomena, FREEDAM friction dampers are constituted by internal stainless steel plated made of 1.4301 (equivalent to AISI 304) steel grade, which is characterized by a superficial hardness of about 130 HV. Therefore, the material of the friction shims to be coupled with the stainless steel plates has been selected to be characterised by a much lower or much higher value of the superficial hardness in order to develop high values of the friction coefficient. In order to reach this scope, the materials' selection has been carried out by checking among all the materials or alloys commercially available those characterised by values of the superficial hardness significantly far from 130 HV. Therefore, two classes of materials have been tested: the so-called “hard” materials and the so-called “soft” materials. In the class of soft materials, pure metals applied by means of thermal spray, characterized by an HV ranging from 5 to 30, have been tested (labelled from M1 to M5 in the subsequent paragraphs). Conversely, in the class of hard materials, carbide alloys produced as powder blends and also the electroless nickel friction shims produced by 3M Deutschland GmbH have been individuated as coating materials characterised by high values of the superficial hardness and, therefore, appropriate to realise a friction interface for the coating of the dampers' friction shims (labelled from M6 to M8 in the subsequent paragraphs). The superficial hardness of the selected carbide alloys varies from 550 to 1200 HV. Conversely, the friction shims produced by 3M are Electroless Nickel has diamond powder additions to obtain a high value of the superficial hardness (600/900 HV).

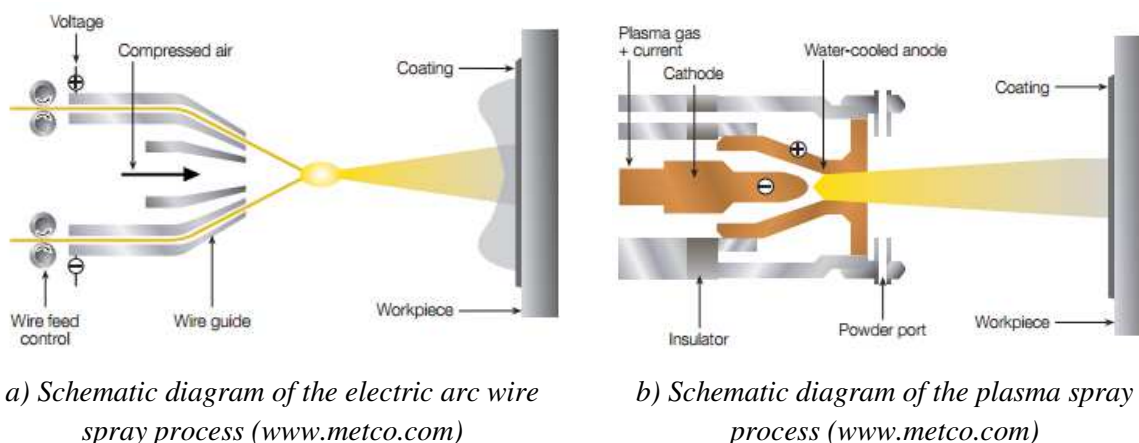


Figure 2.10 – Thermal spray techniques

It is useful to note that when stainless steel is combined with harder materials, the consumption of the steel plate is promoted and, therefore, the friction coefficient obtained is mainly governed by the ratio between the shear resistance and superficial hardness of the steel plate. Conversely, when steel is combined with a softer material, the wearing of the interface is due essentially to the consumption of the friction shims, and the friction coefficient mainly depends on the ratio between the shear resistance and the superficial hardness of the material employed to coat the friction shim.

2.3 BEHAVIOUR UNDER CYCLIC LOADING CONDITIONS

In order to characterise the friction coefficient of the dampers used in the FREEDAM joints, a wide experimental campaign on elementary friction dampers has been undertaken both at the

University of Salerno and at the facilities of FIP Industriale SpA. The experimental work has considered a number of variables, namely: i) the type of friction material employed; ii) the effect of the bolts clamping force; iii) the effect of the typology of adopted bolt assembly; iv) the random material variability evaluated in terms of friction coefficient; v) the speed of application of the loads. The main results and the applied test procedures are hereinafter briefly reported.

2.3.1 Layout for low-velocity tests

The typical specimen realised to evaluate the value of the friction coefficient of the interfaces analysed during the research project FREEDAM is composed by a system of steel plates assembled in order to test the uni-axial behaviour of friction interfaces resulting from the coupling of a stainless steel plate with friction shims coated with one of the eight materials previously described.

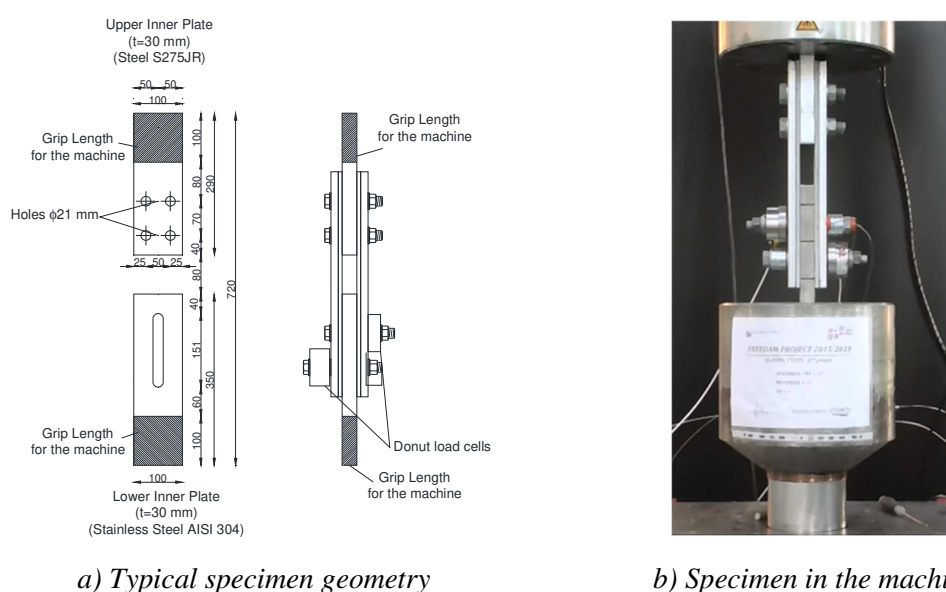


Figure 2.11 – Cyclic slip test on a lap shear joint

The tested sub-assembly is inspired by the specimens' layout provided for slip tests by EN1090-2 [27]. In particular, it is constituted by a slotted steel plate realised in 1.4301 Stainless Steel [45] equivalent to AISI 304 steel, a steel plate with normal holes used to connect the specimen to the testing machine and external steel plates and friction shims pre-stressed with M20 class 10.9 HV bolts [46] (Figure 2.11). The tested specimen aims to simulate the same conditions that are expected in the friction damper of FREEDAM beam-to-column connections. In particular, the stainless steel plate with slotted holes simulates the internal plate of a haunch that can be easily prefabricated and attached to the lower beam flange directly in the construction site in order to realize the friction damper, while the external steel plates aim to simulate the stems of the angles used to fasten the friction damper to the face of the column.

In order to determine the value of the initial slippage force and its degradation, all the specimens have been tested under cyclic loading conditions following the loading protocol provided by EN15129 (2009) [47], which is the only code currently available devoted to the testing of displacement dependent dissipative devices. Such a code requires to perform the tests under cyclic loading conditions aiming to reproduce the actual working conditions on the devices. To

this scope, it suggests applying to the damper increasing amplitude cycles at 25%, 50% and 100% of the maximum design displacement of the device.

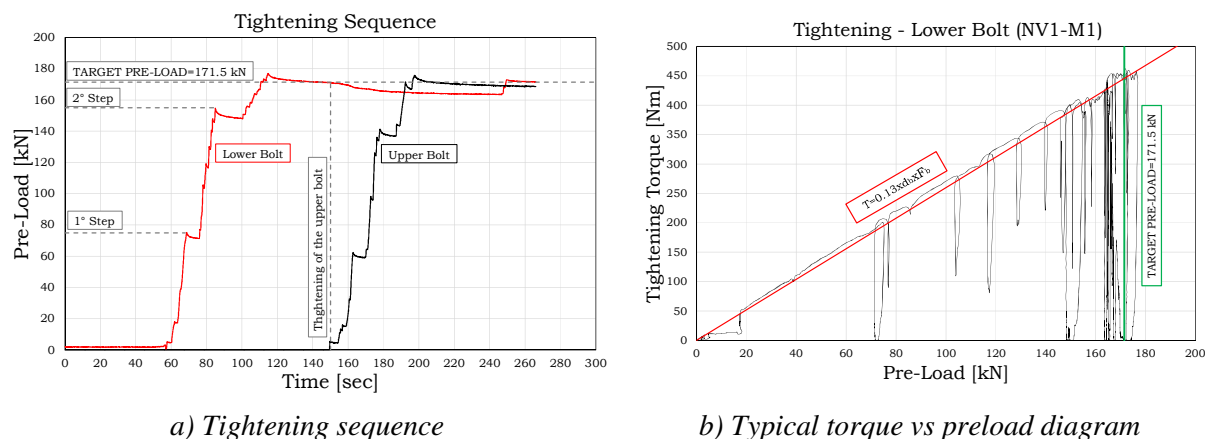


Figure 2.12 – Tightening of the bolts

The maximum amplitude was defined by estimating the displacement demand arising at the friction damper level in real applications. Therefore, considering a reference value of the lever arm, i.e., the distance between the upper T-stub of the FREEDAM connection and the mid-center of the friction damper, equal to 600 mm and a maximum rotation of 40 mrad (greater than the minimum value required by EC8 equal to 35 mrad for DCH frames), the design displacement demand at the level of the damper has been calculated as $0.04 \times 600 = 24$ mm, which has been rounded up to 25 mm. The cycles were executed at increasing values of the speed that were defined in order to remain in a quasi-static range and according to the capabilities of the available equipment. In the tests hereinafter presented, the velocity of the cycle varied from 1 mm/s for the first 10 cycles to 5 mm/s for the cycles at the maximum amplitude. In each test, both the upper and lower M20 high strength bolts have been tightened by means of a torque wrench in order to reach the test preload, monitoring it through donut load cells.

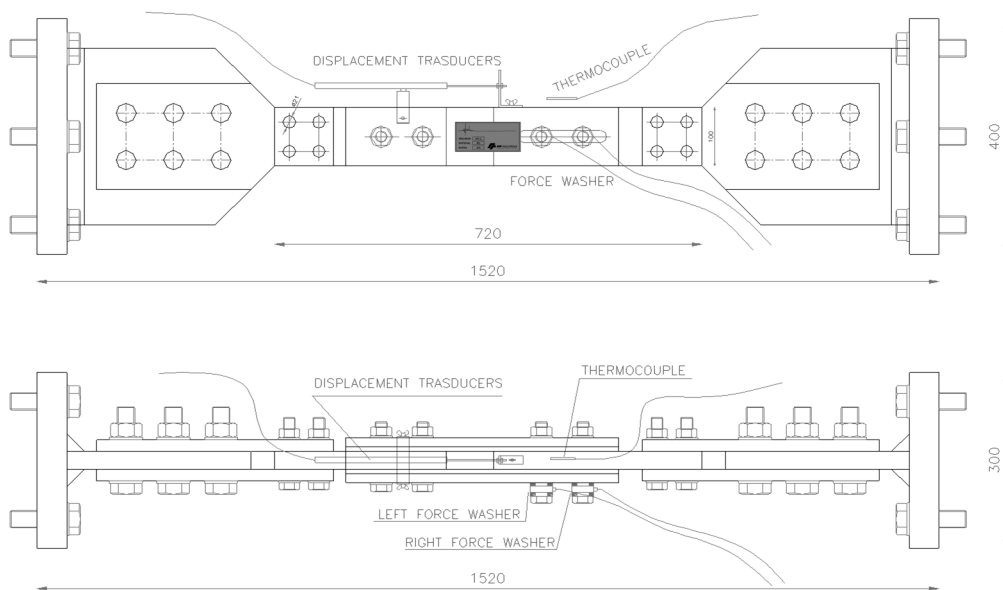


Figure 2.13 – Specimens' layout for high-velocity tests

The low-velocity tests have been carried out employing a universal testing machine Schenck Hydropuls S56 (Figure 2.11). Such a machine is constituted by a hydraulic piston with loading

capacity equal to ± 630 kN, maximum stroke equal to ± 125 mm and a self-balanced steel frame used to counteract the axial load. Different sensors have been used before and during the test to control the bolt force, the slippage load, the tightening torque, and the displacement continuously. The axial displacements of the device have been read directly from the transducer of the testing machine and, in the same way, the slippage force has been controlled directly exploiting the load cell of the machine. Before the test, the tightening torque has been applied through a hand torque wrench and monitored by means of a torque sensor Futek TAT430 with a maximum capacity equal to 680 Nm. At the same time, the pretension applied to the bolts has been monitored before and during the test by means of donut load cells Futek LTH500 with a maximum capacity of 222 kN. Before every test, the force has been applied to the bolts by means of a torque wrench, monitoring the tightening torque applied and the preloading force in the bolt. In particular, the adopted bolts had an average value of the k-factor equal to 0.13. The value of the tightening torque applied to the bolts in each test was varying from a maximum equal to $0.13 \times 171.5 \times 20 = 446$ Nm (100% of the proof preload) and a minimum equal to $0.40 \times 0.13 \times 171.5 \times 20 = 178$ Nm (40% of the proof preload).

2.3.2 Layout for high-velocity tests

In order to investigate the behaviour of friction materials under high velocities, a specific experimental campaign on sub-assemblages equipped with friction pads has been planned and developed at the facilities of FIP Industriale S.p.a. The specimens (Figure 2.13) are almost identical to those used for the tests at low velocity, apart from the attachment system to the testing rig. The specimens are constituted by two friction pads that slide on an AISI 304 plate. The bolts that apply the preload on the friction pads are two M20 HV 10.9; the force on them is measured through two force washers. Figure 2.14 shows the machine adopted for performing the tests. It is composed of a very stiff frame and an actuator with a maximum axial force equal to 2000 kN, piston stroke equal to ± 300 mm, and maximum velocity, at the maximum force, equal to 300 mm/s. The tests have been carried out under displacement control, applying for the tests of the first phase of analysis a sinusoidal input with a frequency of 1.27 Hz, variable amplitude (up to ± 25 mm), and maximum velocity of 200 mm/s.



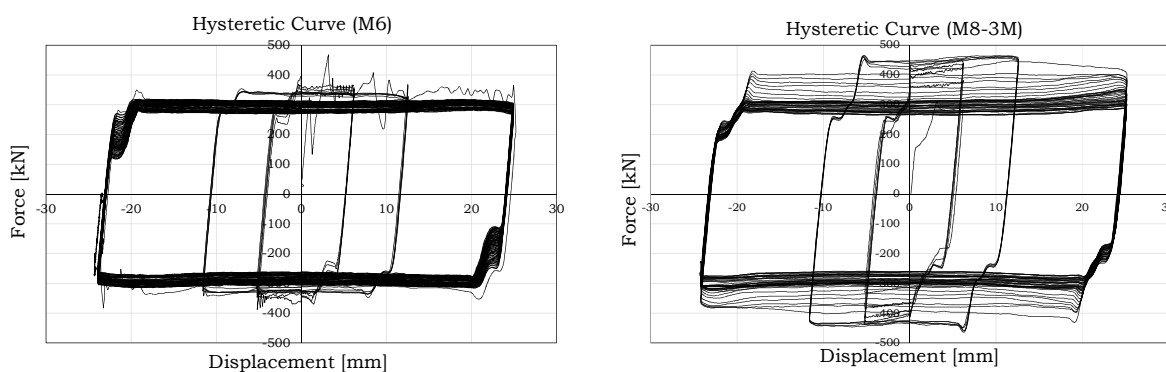
Figure 2.14 – Test machine

Aside from the shape of the input signal, the testing protocol is the same used in the low-velocity tests. Obviously, the speed of application of the load has been varied case by case in order to investigate the role played by the velocity over the friction coefficient.

2.3.3 Summary of the test results

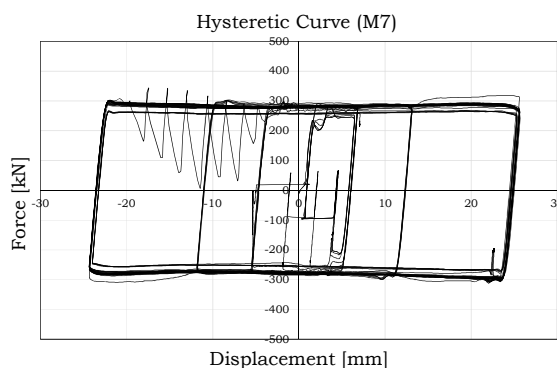
As previously mentioned, in the low-velocity tests, the cyclic loading protocol has been applied following the loading procedure suggested by EN15129 [47], and for each test, the sequences of cycles have been applied at the following velocities:

- 5 cycles at 6.25 mm at 1 mm/s;
- 5 cycles at 12,5 mm at 4/5 mm/s;
- 40 cycles at 25 mm at 4/5 mm/s.



a) Hysteretic behaviour of M6 shims

b) Hysteretic behaviour of 3M shims



c) Hysteretic behaviour of M7 shims

Figure 2.15 – Hysteretic behaviour of hard shims

For each test, the cyclic response of the interfaces has been evaluated by analysing, the initial value of the friction coefficient and its degradation during the cyclic loading history by means of the load sensors applied to the specimen. In particular, in the following diagrams, several quantities have been reported:

- The force-displacement hysteretic represented in terms of slip force ($F_{\text{slip},i}$) and displacement (d_i) acquired from the load cell and the LVDT, respectively, of the testing machine;
- The “effective” (or design) value of the friction coefficient ($\mu_{\text{effective}}$) versus the cumulative displacement (d_{total}). The effective value of the friction coefficient has been calculated as the ratio between the slip force acquired from the load-cell of the testing machine and the sum of the initial preload forces applied by the bolts to the friction interface ($4N_0$);
- The “actual” value of the friction coefficient (μ_{actual}) versus the cumulative displacement (d_{total}). The actual value of the friction coefficient has been calculated as the ratio between

the slip force acquired from the load-cell of the testing machine and the sum of the actual values of the preloading forces applied by the bolts to the friction interface acquired directly from the load cells during the test ($2N_{\text{cell},1}+2N_{\text{cell},2}$). In the following, a synthesis of the obtained results is reported.

Additionally, the behaviour of the friction device was described evaluating the effective damping degradation as defined by EN 15129 [47]. This parameter represents the energy dissipation degradation normalised with respect to the value of the energy dissipation measured at the 3rd cycle of the set of cycles of maximum amplitude. The main results are summarised in the next sections. Nevertheless, due to the high amount of data, for the detailed test results reference has to be made to the deliverable of Task 1.1 of the FREEDAM research project.

2.3.3.1 Influence of the type of coating: “Hard” Materials (M6-M8)

A synthesis of the results of the tests on the interfaces coupling stainless steel with friction pads coated with the “hard” coatings are delivered in Figure 2.15, where the hysteretic curves of one of the tested materials are reported.

In case of M6 carbide coating, the cyclic response has been characterised by the development of an initial value of the slip force equal to about 350 kN, followed by a progressive degradation that, at the end of the test was of about the 20%. During the tests, the peculiar behavior of this material has been observed. In fact, as it is possible to note from Figure 2.15, the hysteretic curve was affected by an initial stick-slip phase with the development of a first unstable cycle characterised by jumps of the force and sudden releases of energy. Nevertheless, after this first cycle, that probably allows to break the initial interatomic attraction between the surfaces in contact (adhesion component of friction), the slippage occurred regularly leading to a very stable response up to the end of the test. In the case of M7 carbide coating, globally, a similar response was observed. The behaviour, in this case, was characterised by an initial slip force equal to about 250 kN, that after few cycles slightly increased, stabilising at a value of about 300 kN. After reaching this value, all the cycles were characterised by the same slippage force obtaining, also in this case, a stable and dissipative behaviour. Even though the hysteretic behaviour reported in Figure 2.15 appears pretty similar to that observed for material M6, in reality, in this case, in order to perform the test it was necessary to significantly reduce the velocity due to the development of a strong stick and slip behaviour, characterised by sudden releases of energy and vibrations. 3M friction shims were characterised by a response that, as already observed in the past by the same authors with other materials such as brass or some types of phenolic rubbers [43], was characterised by two different phases of the response. A first phase where the interface provided a strain-hardening behavior characterized by an increase of the slippage resistance of about 60%. A second phase characterised by a reduction of the slippage force, which, at the end of the degradation returned to the initial value. In addition, in this case, no stick and slip response has been observed, and all the cycles have been characterized by a stable value of the slippage force. The initial value of the slippage force has been of about 400 kN.

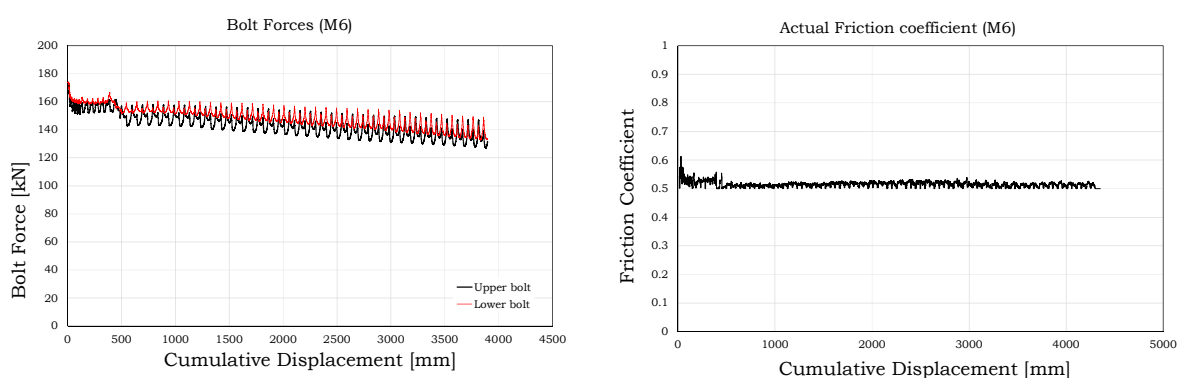


a) Damage of M6 shims

b) Damage of 3M shims

Figure 2.16 – Damage of hard shims

After the tests, the specimens have been opened in order to evaluate the damage of the interfaces. In Figure 2.16 the damage state of the interface is represented for specimens employing M6 and 3M friction shims. As it is possible to observe from this figure, for these materials, due to the higher hardness of the coating layer with respect to stainless steel, the greatest part of the damage was concentrated on the stainless steel plate which at the end of the test had many scratches in the zone located under the bolt head. In Figure 2.17, as an example, the diagram of the bolt forces (monitored by means of the load cells) and of the actual friction coefficient represented versus the cumulative travel of the damper are reported for the specimen with friction pads coated with M6 carbide. From such a figure, it is possible to observe that both bolts, which were initially tightened in order to reach the proof load equal to 171.5 kN, after the first cycle of the loading history, lost about the 7% of the initial preload, and afterwards they uniformly loosened during the test reaching at the end a total loss of about the 20%. Conversely, the “actual” friction coefficient remains constant showing a stable behaviour of the friction shims



a) Typical diagrams of the bolt forces

b) “Actual” friction coefficient vs cumulative travel: M6

Figure 2.17 – Actual friction coefficient and bolt forces evolution

2.3.3.2 Influence of the type of coating: “Soft” Materials (M1-M5)

Similar to what occurred in the case of M7 carbide, also some of the soft materials exhibited a behavior characterized by the stick-slip phenomenon. This is the case of three of the selected non-ferrous metals, namely M2, M3 and M5, whose response was characterised by alternate stops and starts of the motion with strong and sudden releases of energy (Figure 2.18). Therefore,

also in all these cases, the tests have been stopped prematurely in order to prevent damage to the testing equipment. For these materials, after the first sliding, the hysteretic behaviour has been characterised by alternate and continuous jumps of the force from the static to the dynamic values. It is worth noting that, even though the cyclic behaviour of these interfaces is clearly not appropriate for seismic applications, from the results obtained in this experimental analysis it seems that these materials, due to the high value of the friction coefficient, could be still promising for application in friction connections designed for static loads.

M1 and M4 metals have exhibited very similar behavior (Figure 2.18). In particular, their hysteretic response has been characterised by a value of the slippage force higher than the corresponding obtained with the “hard” materials but, on the other hand, they have also provided a more significant degradation due both to the bolt loosening and to the damage occurring in the friction pads. In addition, for both materials, the behavior exhibited in the two identical tests was significantly different, showing a random variability of the behavior of these materials. Such variability was mainly due to the different behavior provided by the bolts in the two tests. As an example, in Figure 2.19 with red and black lines are represented the results expressed in terms of friction coefficient and bolt forces versus the cumulated travel, for the two tests executed on the specimens with M4 friction pads.

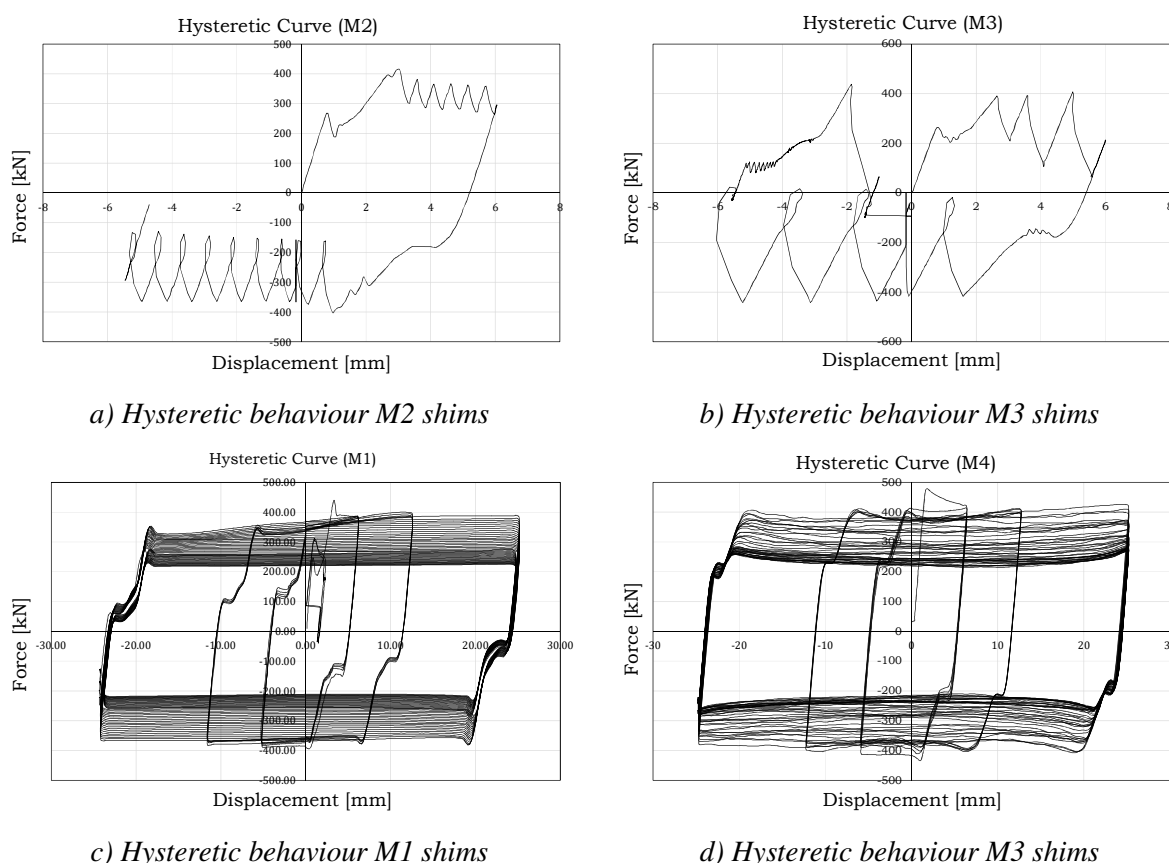


Figure 2.18 - Hysteretic behaviour of soft shims

From these graphs, it is clear that, even though the actual value of the friction coefficient does not vary in the two tests, the bolts provide a significantly different behavior leading, consequently, to a different response of the whole hysteretic response. In particular, in one of the two tests after the first sliding, a sudden loss of pretension in the bolts of about 15% was observed, leading, as a consequence, to a proportional loss of the sliding force. Such a different

response of the specimens can be probably due to the imperfections of the coating applied on the friction shims, which in case of soft coatings is completely manual and leads to a non-uniform spread of the coating metal.

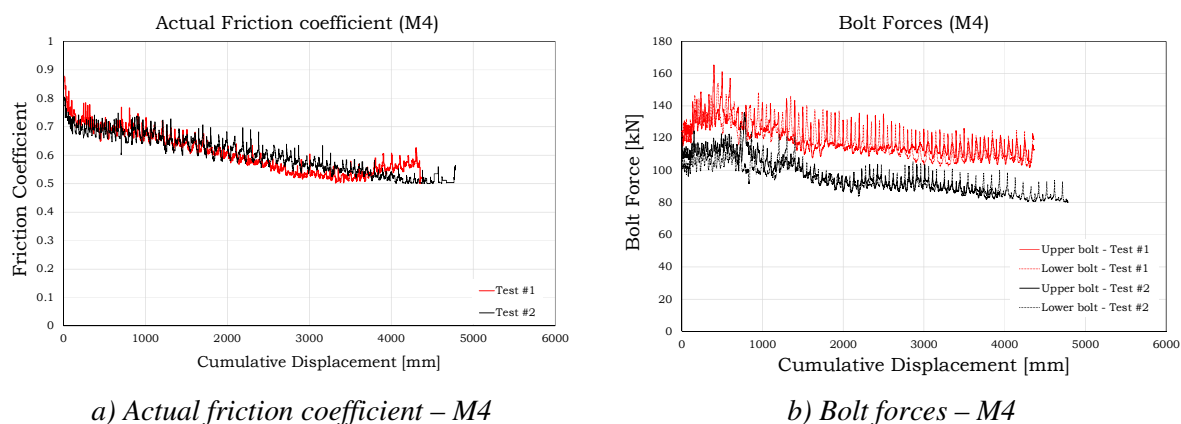


Figure 2.19 – Actual friction coefficient and bolt forces evolution

In the case of material M1, the degradation of the initial slippage force at the end of the tests was 45%, while in the case of material M4, it was about 50%. Nevertheless, both materials provided very high values of the friction coefficient and, in particular, the initial friction coefficient of materials M1 and M4 were equal to about 0.55/0.65 and 0.7/0.9, respectively. As in previous cases, also the specimens realised with soft materials were opened after the test, in order to evaluate the damage of the interfaces. As it is possible to note from Figure 2.20, as expected, in these cases the damage was mainly concentrated in the friction shims, while the stainless steel plates after the test were practically undamaged.

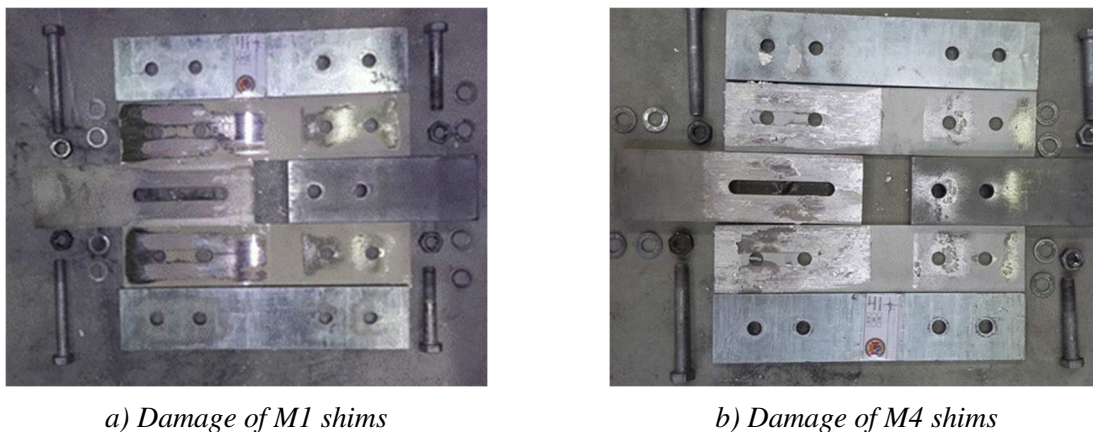


Figure 2.20 – Damage after the tests

2.3.3.3 Influence of the clamping force

To investigate the influence of the parameters affecting the response of the elementary friction dampers, the experimental tests on some materials (M1, M4, M6) have been extended. In particular, for these three materials, the influence of the clamping force, the influence of the disk spring configurations, and the random material variability effects have been examined. In this section, the influence of the clamping force on the hysteretic response of friction dampers is briefly discussed. The representation of the typical force-displacement curves of a set of tests with variable preload is reported, as an example, in Figure 2.21, for one of the three examined materials (M6). The results for the other materials in terms of global behavior is very similar,

and it will not be commented in detail. As expected, the hysteretic response was, in general, characterised by a high initial stiffness until the achievement of the value of the static slip force that, in all the analysed cases, was higher than the stabilised dynamic friction resistance. All the materials exhibited hysteresis loops almost rectangular. In terms of force-displacement response, the only material providing a less stable behaviour was material M6 which, as already explained, is a hard coating whose behaviour is characterised, at high pressures, by a first cycle exhibiting a slight stick-slip response.

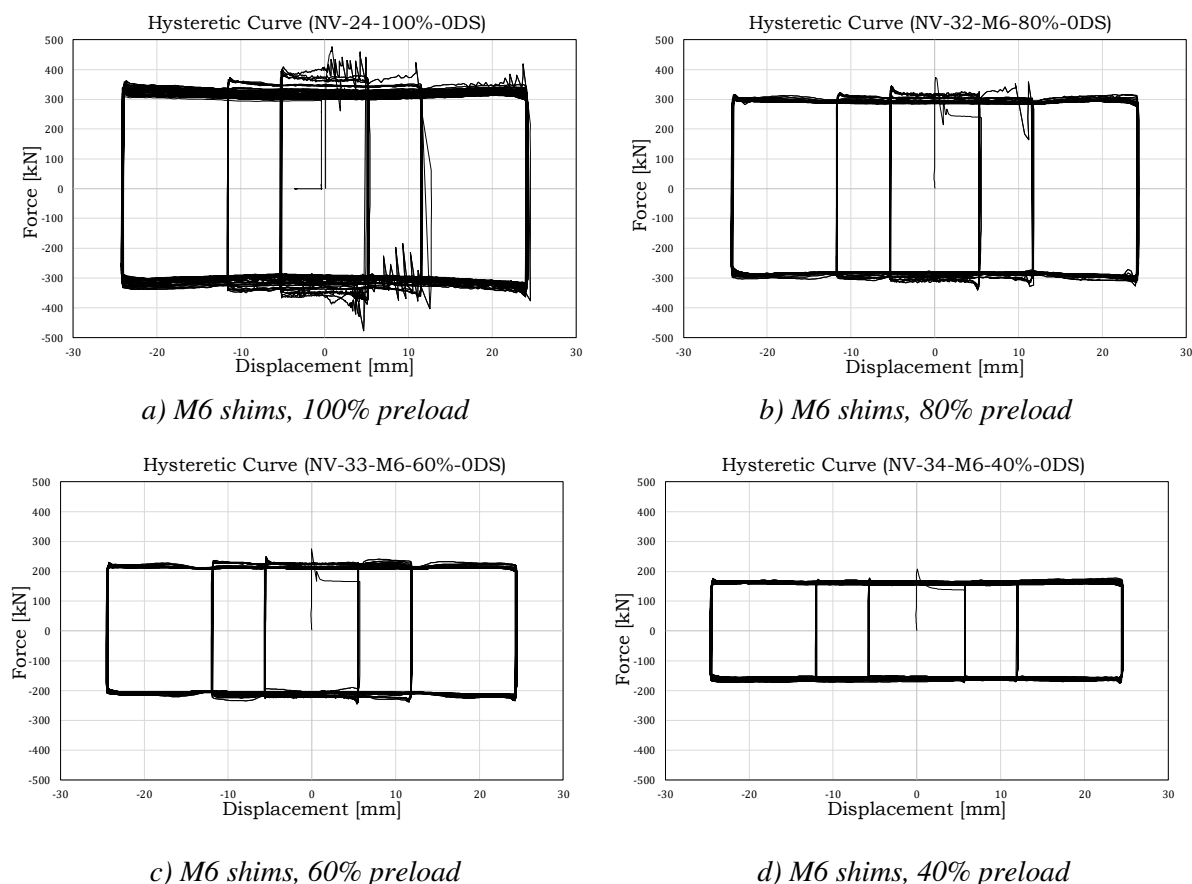
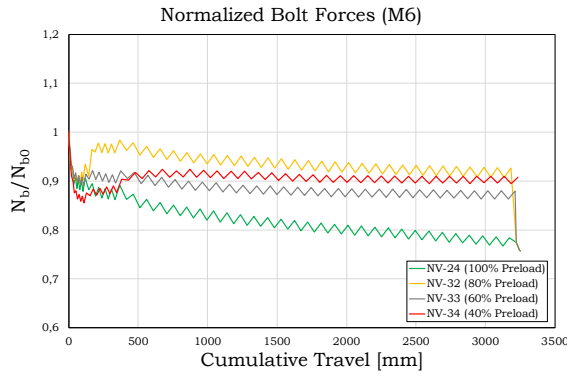
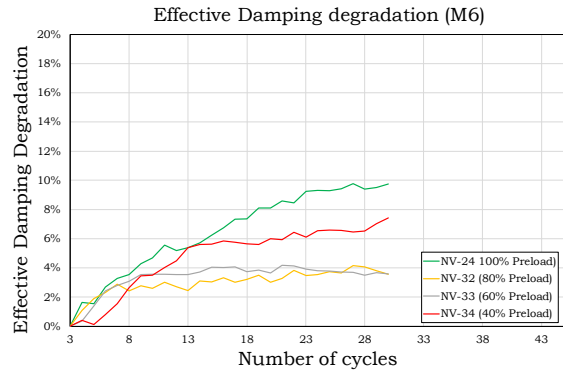


Figure 2.21 – Effect of preload

One of the most important aspects observed in this set of tests is that, for this specific coating material, the stick-slip response disappears reducing the bolts pre-loading, showing that the stick-slip phenomenon strongly depends on the contact pressure generated on the interface. In Figure 2.22, the evolution of the bolt forces during the tests, and the effective damping degradation are represented. The bolt force (N_b) is normalised with respect to the initial value applied at the beginning of the test (N_{b0}), while the effective damping degradation is calculated according to the procedure given in [47].



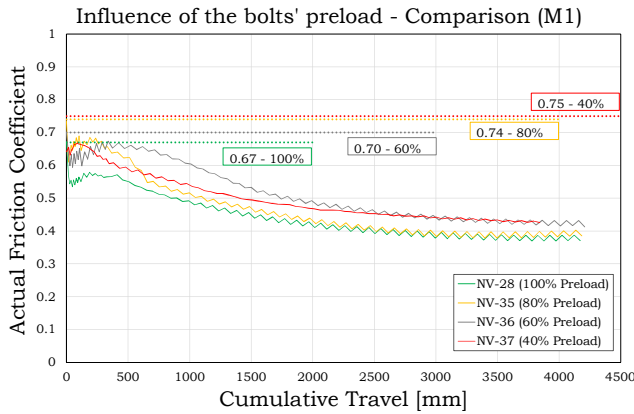
a) Bolt forces degradation (100% to 40% preloads)



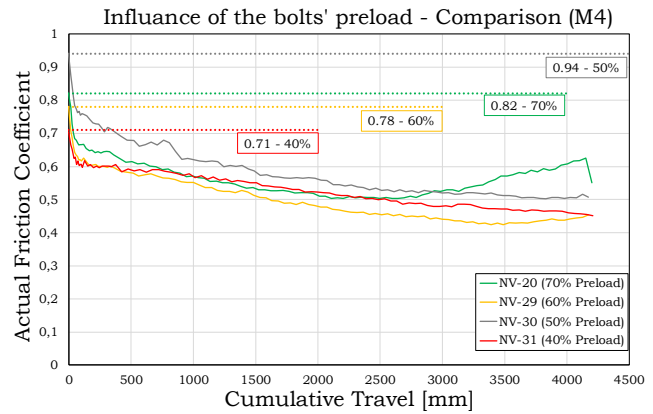
b) Energy dissipation degradation (100% to 40% preloads)

Figure 2.22 – Bolt forces and energy dissipation degradation

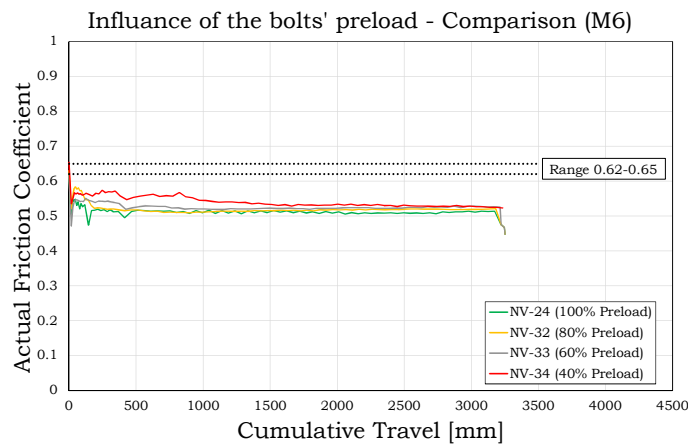
From these charts, it is possible to observe that the reduction of the initial preloading force leads to an improvement of the effective damping degradation. This last parameter expresses mainly the degradation of the energy dissipation capacity of the friction connection.



a) Influence of the preload on the friction coefficient: M1 shims



b) Influence of the preload on the friction coefficient: M4 shims



c) Influence of the preload on the friction coefficient: M6 shims

Figure 2.23 – Influence of the preload

In terms of the initial value of the friction coefficient, as reported in synthesis in Figure 2.23 the three analyzed materials did not show a strong dependence on the preloading, while their

progressive degradation reduced, as far as the initial clamping force was reduced. The variation of the initial value of the friction coefficient observed in these tests was practically within the normal statistical range of variation of the friction coefficient observed for these materials. In particular, the initial value of the friction coefficient for material M1 ranged from 0.67 to 0.75, for material M4 from 0.71 to 0.94 and for material M6 from 0.62 to 0.65 (not showing a clear tendency with respect to the applied preload), while the statistical range of variation of the same parameter is, as demonstrated hereinafter, equal to 0.62-0.81 for material M1, 0.69-0.84 for material M4 and 0.52-0.68 for material M6. Therefore, the tests at variable values of the preloading force did not point out a clear correlation between the static friction coefficient and bolt preloading. Conversely, the representation of the bolt forces, normalised with respect to the initial preload, versus the cumulative travel and the diagrams of the effective damping degradation versus the number of cycles showed that a reduction of the preloading force, as expected, results in a lower loss of bolt preload and lower energy degradation. Additionally, the analysis of all the data revealed that for material M6 the effective damping degradation at the 10th cycle was always lower than the 10% as required by EN15129 [47]. Conversely, for materials M1 and M3 (soft materials), the results showed that this minimum requirement could be met only if the load pressure is limited to 60% of the proof load.

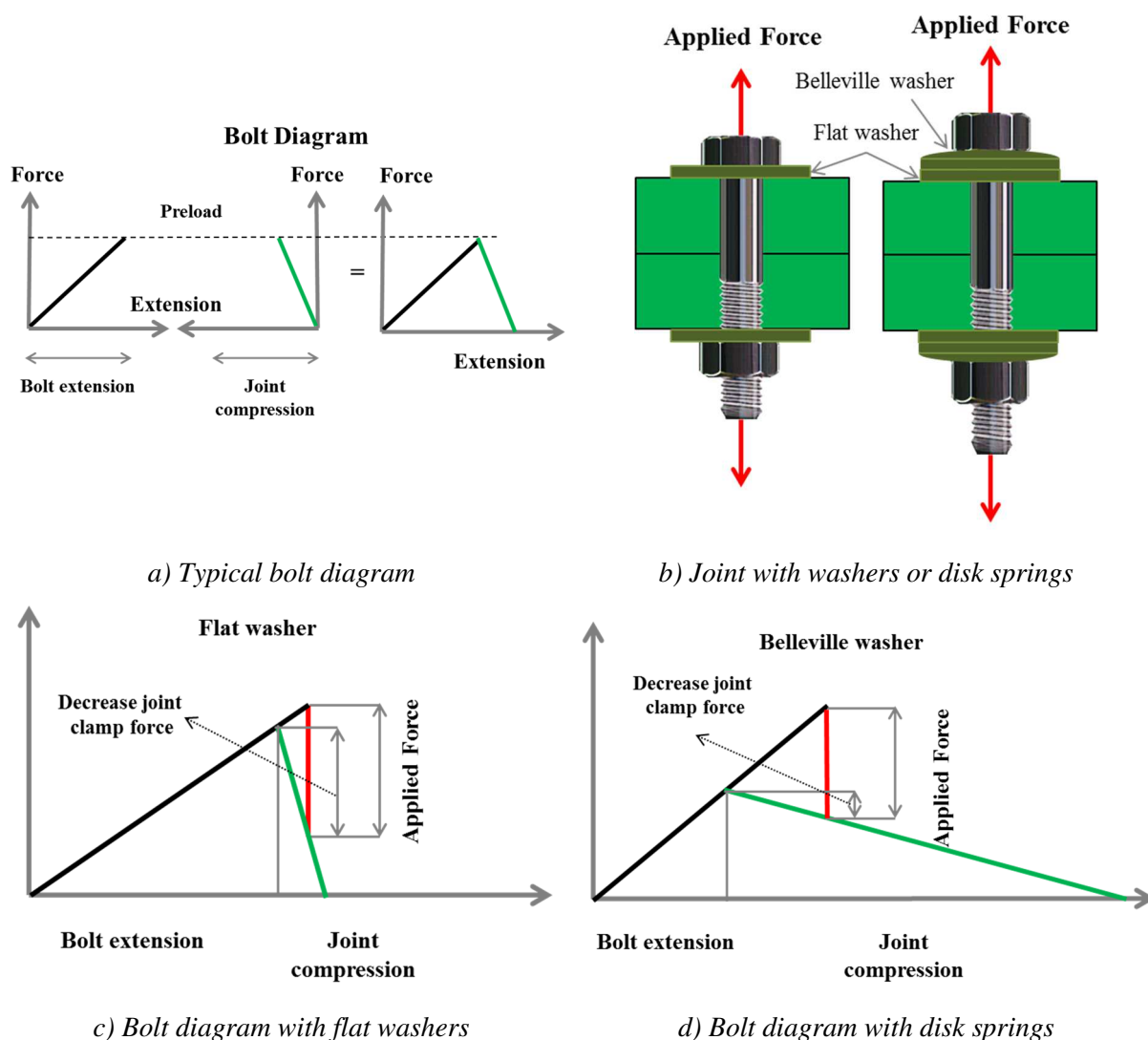


Figure 2.24 – Effect of Belleville washers

2.3.3.4 Influence of the Disk Springs Configuration

Disk springs are a type of conical annular washers, also often referred as Belleville, which can compress elastically (provided that they are properly pre-set [48] until reaching a threshold value beyond which they show a significant increase of stiffness until complete flattening. Their main feature is that they can be arranged one over the other (parallel stack) to double the resistance or back-to-back (series stack) to double the deformability or, again, in combinations of series and parallels in order to obtain a system of washers contemporarily with desired values of stiffness and resistance. Their presence, in technical literature, is usually considered beneficial in all those cases where it is needed to maintain constant the preload in bolts over the lifetime of a connection and especially in the cases where vibrations, creep, or elastic interactions between bolts may be expected. All these phenomena are widely explained in [48].

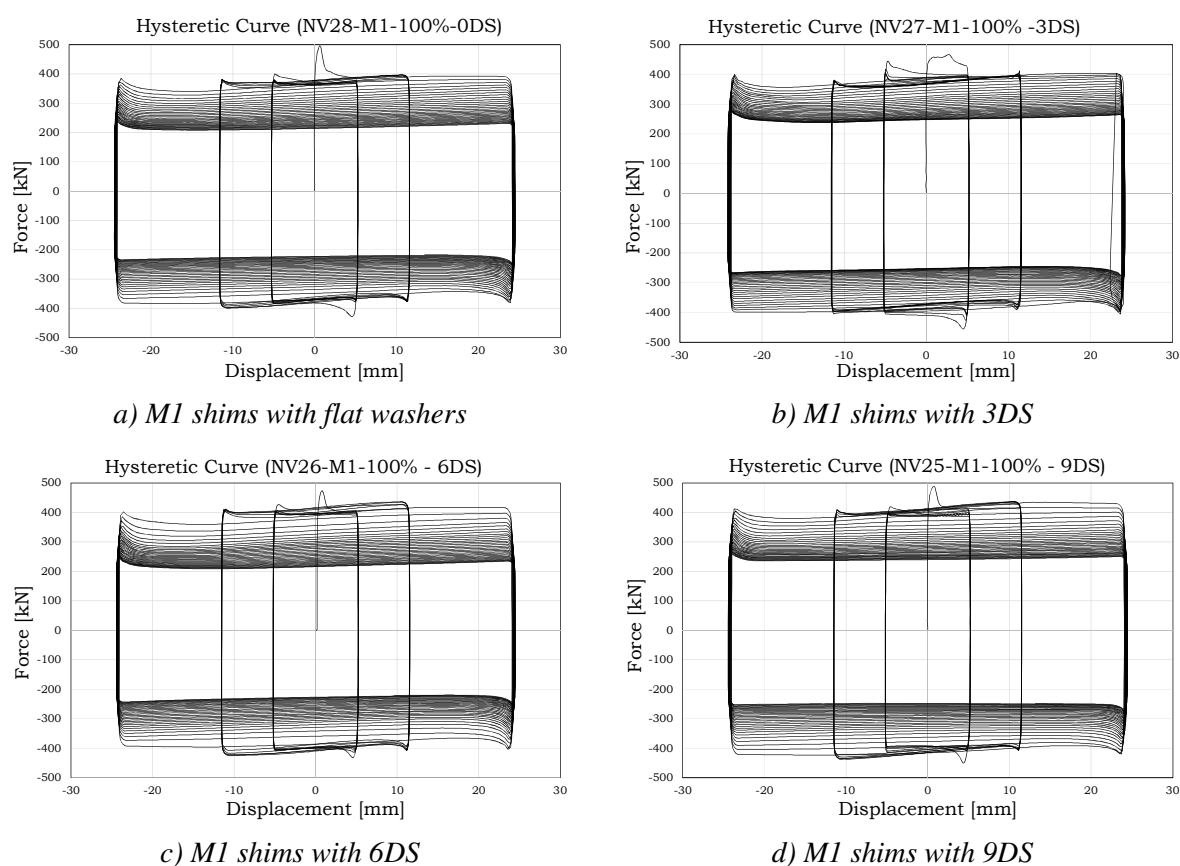


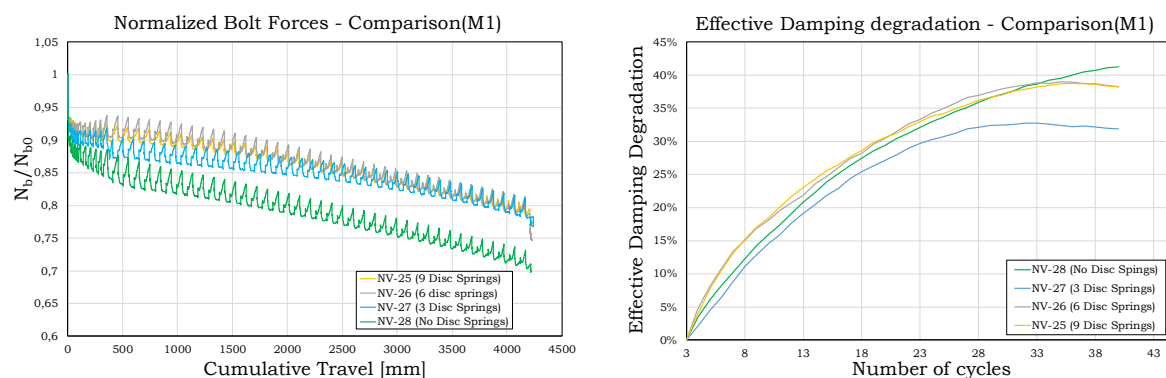
Figure 2.25 – Effect of the number of disk springs employed

Their possible effect is explained briefly in Figure 2.24, where the behavior of a system with normal washers and another with disk springs are compared. The main difference between the two cases, as it is possible to verify easily, is that when in the bolt assembly there is a reduction of the thickness, which may be due to wearing under cyclic loads or to creep of the coating layers, the lower axial stiffness of the assembly helps to compensate the reduction of the clamped thickness which may be due to wearing of the friction material or the squashing of coatings and asperities. In fact, the conical washers act as springs pushing the bolt shank and restoring, at least partially, the loosening. The effect of the disk springs configuration was studied during the FREEDAM project with cyclic tests, considering the employment of four different possible configurations, namely: no disk springs, 3 in parallel, 3 in parallel-2 times in series (6 disk

springs), 3 in parallel-3 times in series (9 disk springs). As before, the test results are summarised, as an example for M1 material, but negligible differences in the behaviour were observed for the other cases and, therefore, the same considerations herein reported can be extended to all the materials examined in this work. The comparison is herein provided with reference to material M1 because it allows highlighting more easily the influence of the disk springs in the cyclic response. Considering material M1, it is possible to observe from Figure 2.25 that the configuration of the disk springs, globally, did not seem to provide a significant influence over the hysteretic response. In fact, all the tests started with an initial slippage force of about 400 kN and ended with a force of about 200 kN and rather, in contrast with the expected response, in the case with the higher number of disk springs, the behavior showed a higher degradation.

This result, from the point of view of the overall hysteretic response, points out the limited efficiency of the European standardized disk springs on the overall response of the damper. This is also evidenced by the representation of the bolt forces during the test and the effective damping degradation diagram (Figure 2.26).

Figure 2.26a reports the bolt forces during the tests showing that higher deformability of the bolt assembly, as expected, results in a lower loss of the initial preload. However, the benefit obtained does not result in an overall improvement of the hysteretic response of the connection, probably due to a higher wearing of the friction material. This is highlighted in the diagrams of the effective damping degradation (Figure 2.26b) which show that the adoption of a different layout of the disk springs does not correspond to a significant improvement of the response.



a) Bolt forces with different configurations of washers

b) Effective damping degradation with different configurations of washers

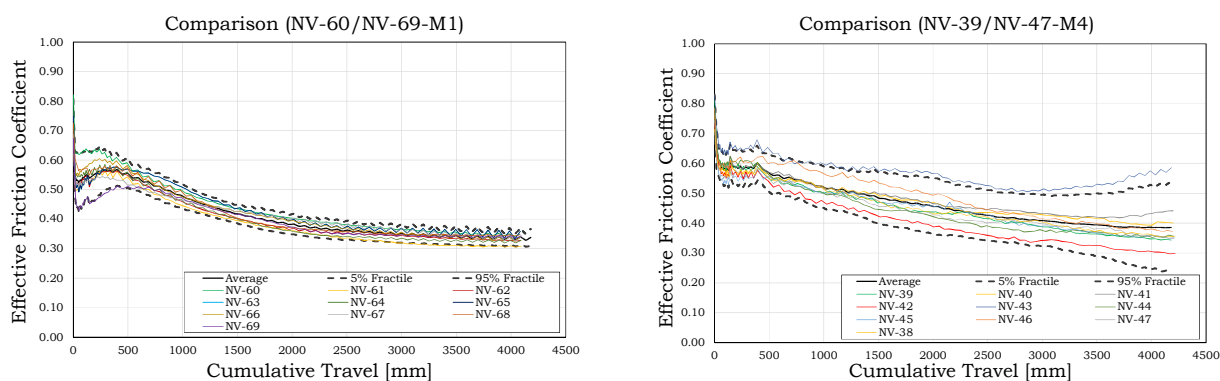
Figure 2.26 – Effective damping degradation and bolt forces degradation

In conclusion, the results of this set of tests demonstrated that the European standardized disk springs might help to keep constant the bolt preload but, overall, they are not able to provide a significant improvement of the cyclic response. Therefore, while their role may be significant to limit other effects, such as those related to the long-term loss of the initial preloading, vibrations or thermal effects, in the same time, their use seems of limited influence on the cyclic behaviour.

2.3.3.5 Influence of Randomness

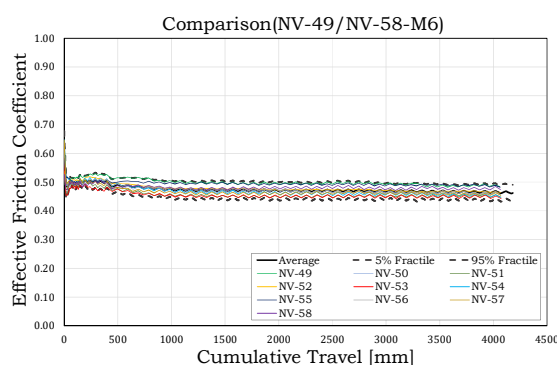
Specific tests of the FREEDAM project were devoted to assess the statistical range of variation of the friction coefficient and to propose values of the friction coefficients to be used in SLS and ULS design. In fact, it is easy to observe also from the previous results that the examined coating materials are affected by a random variation that needs to be accounted for in the design,

especially in view of the application of capacity design principles. In fact, while for SLS checks it is usually needed to adopt the characteristic value of the static friction coefficient, for ULS checks and, in particular, for the application of capacity design principles it is necessary to know both the minimum value of the dynamic friction coefficient (referred to the stabilised cyclic) and the upper bound value of the static friction coefficient.



a) Randomness of the friction coefficient – M1 shims

b) Randomness of the friction coefficient – M4 shims



c) Randomness of the friction coefficient – M6 shims

Figure 2.27 – Effect of random variability

The ratio between these two values obviously affects the over-strength factor, which has to be considered in practice for the design of the non-dissipative parts of the structure. This series of the test has been executed, for each coating material, on ten equal specimens, all preloaded at a preload equal to the 60% of the proof level (maximum value suggested as a result of the FREEDAM project). Even though disk springs are not significantly relevant from a seismic point of view, as already explained previously, considering their possible influence on the long-term response and on vibration and thermal effects, the specimens were arranged to adopt six disk springs, with a set of 2 parallels, 3 times in series. In the diagrams of Figure 2.27, a synthesis of the friction coefficients obtained in all the tests, represented versus the cumulative travel is given, reporting in the same diagrams the mean value (continuous line) and the 5% and 95% fractiles (lower and upper dashed lines) evaluated for each value of the cumulative travel subtracting or adding to the mean value k - times the coefficient of variation. In order to account for the limited number of data (10 specimens for each material), the value of k - has been defined according to the indications given by EC0 in section D7.2 [26], namely it has been assumed equal to 1.92 under the assumption of normal distribution.

2.3.3.6 Influence of velocity

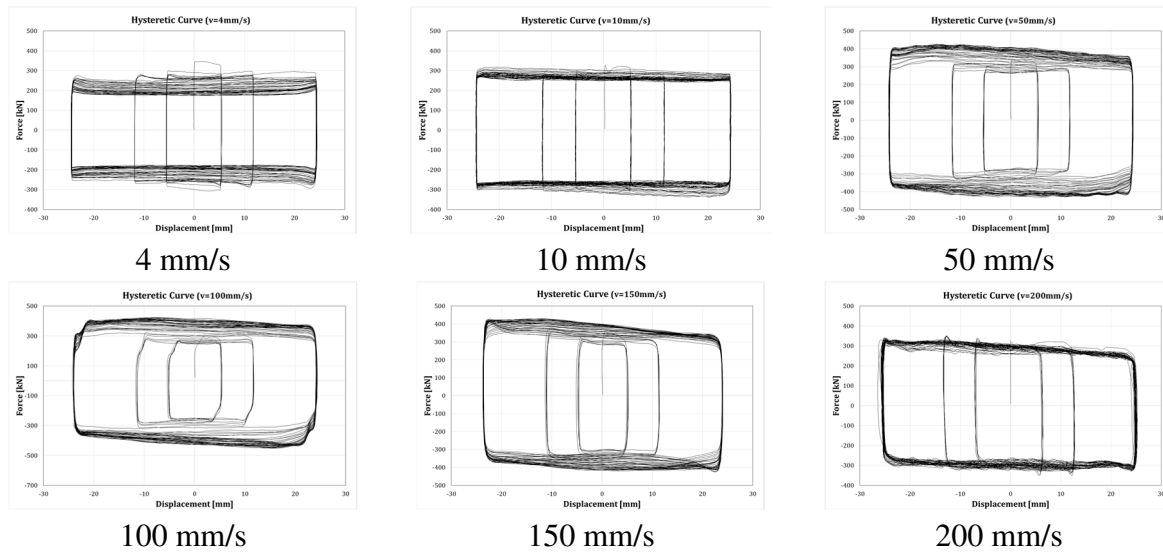
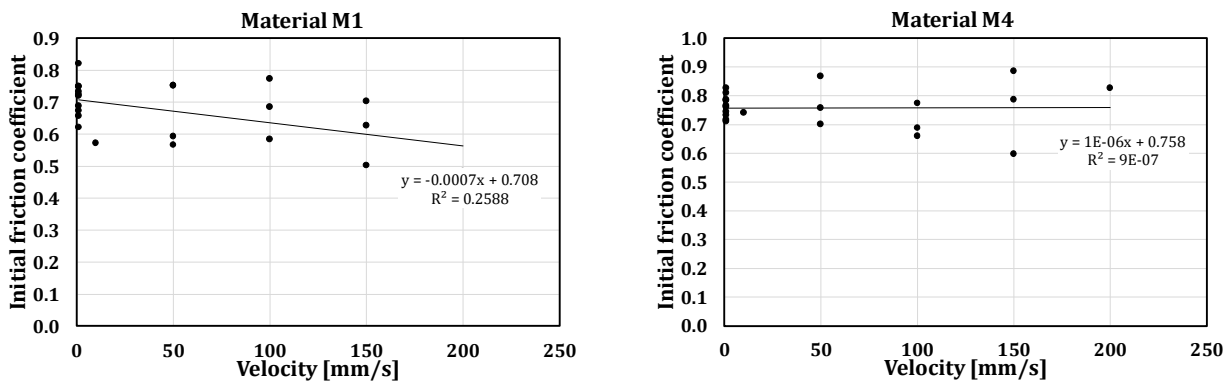


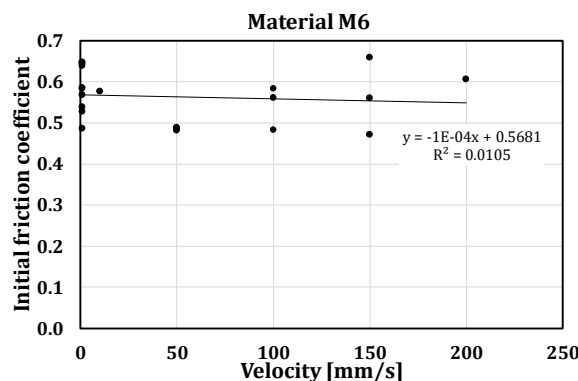
Figure 2.28 – Influence of the velocity – M4 shims

Similarly to the low-velocity tests, also the high-velocity tests have been executed in two separate steps. In the first session, a limited number of tests has been carried out, extending the analysis to eight materials.



a) Influence of velocity – M1 shims

b) Influence of velocity – M4 shims



c) – Influence of velocity on the initial FC – M6 shims

Figure 2.29 – Influence of velocity on the initial value of the friction coefficient

Subsequently, further tests have been carried out only on materials M1, M4, M6. The first phase of testing has regarded 15 high-velocity tests, with friction shims coated with both the five soft

and three hard materials previously mentioned. Conversely, the second phase has regarded 45 high-velocity tests only on three materials (M1, M4 and M6).

The high-velocity tests pointed out a significant dependence of the friction coefficient over the velocity. This is easily recognizable from the test results, which are represented here, as an example, for material M4 only (Figure 2.28). For the other materials similar results have been obtained, even though for material M1 some instability of the hysteretic loops, only for the highest considered velocity (200 mm/s), was observed. Velocity provides a change of the shape of the hysteretic loops, but it does not change the value of the initial sliding force significantly. In fact, as shown in Figure 2.29, the initial value of the friction coefficient observed in all the high-velocity tests ranged in minimum/maximum values, which fall in the normal statistical range of variation of the friction coefficient for the three considered materials. Additionally, a very weak correlation for the three materials was observed drawing a regression line of the initial friction coefficient *vs* the sliding velocity (regression almost horizontal).

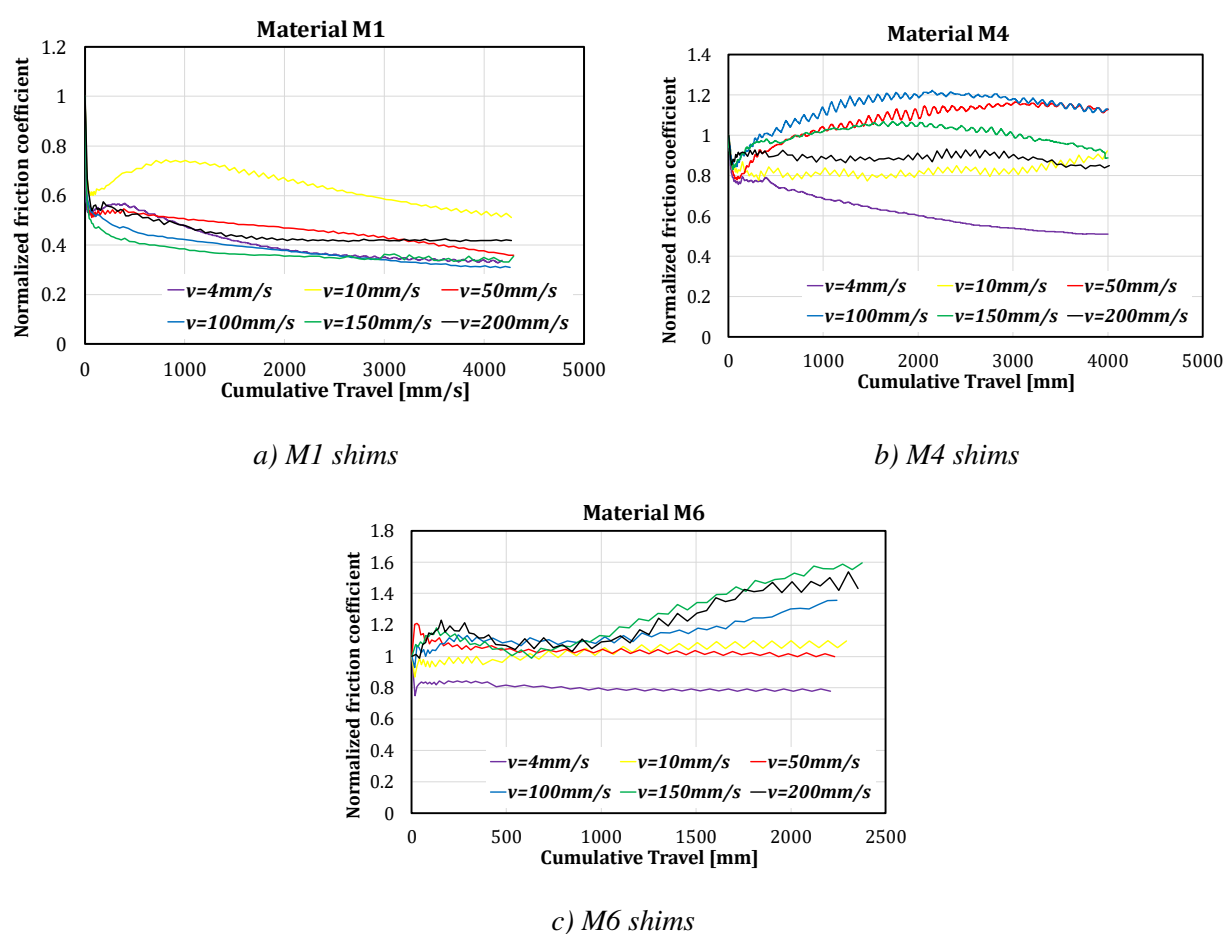


Figure 2.30 – Dependence of the FC degradation on velocity

Nevertheless, the tests highlighted that, while velocity does not affect the values of the initial friction coefficient significantly, it provides a relevant effect on the wearing of the material and bolt forces fluctuation during the tests. In almost all the cyclic tests, it has been observed that the cyclic degradation of the friction coefficient is significantly higher when the sliding velocity is low (quasi-static). Therefore, usually, a conservative estimate of the evolution of the friction coefficient degradation can be obtained with low-velocity tests, which can be normally carried out with simpler layouts. The cyclic degradation of the friction coefficient is not uniformly

varying with the sliding velocity. In fact, for the three materials, different degradation rates were observed depending on the test velocity. For instance, referring to material M4, it was observed that the rate of degradation of the friction coefficient becomes lower increasing the velocity in the range 4-100 mm/s, while increases again in the range of velocities 100-200 mm/s. Similarities were also observed in other cases, but every material has its own degradation properties, and a general rule cannot be defined. Material M1 showed a slight dependence of the degradation of the friction coefficient on velocity. Conversely, material M6 showed a variable response depending on the sliding velocity.

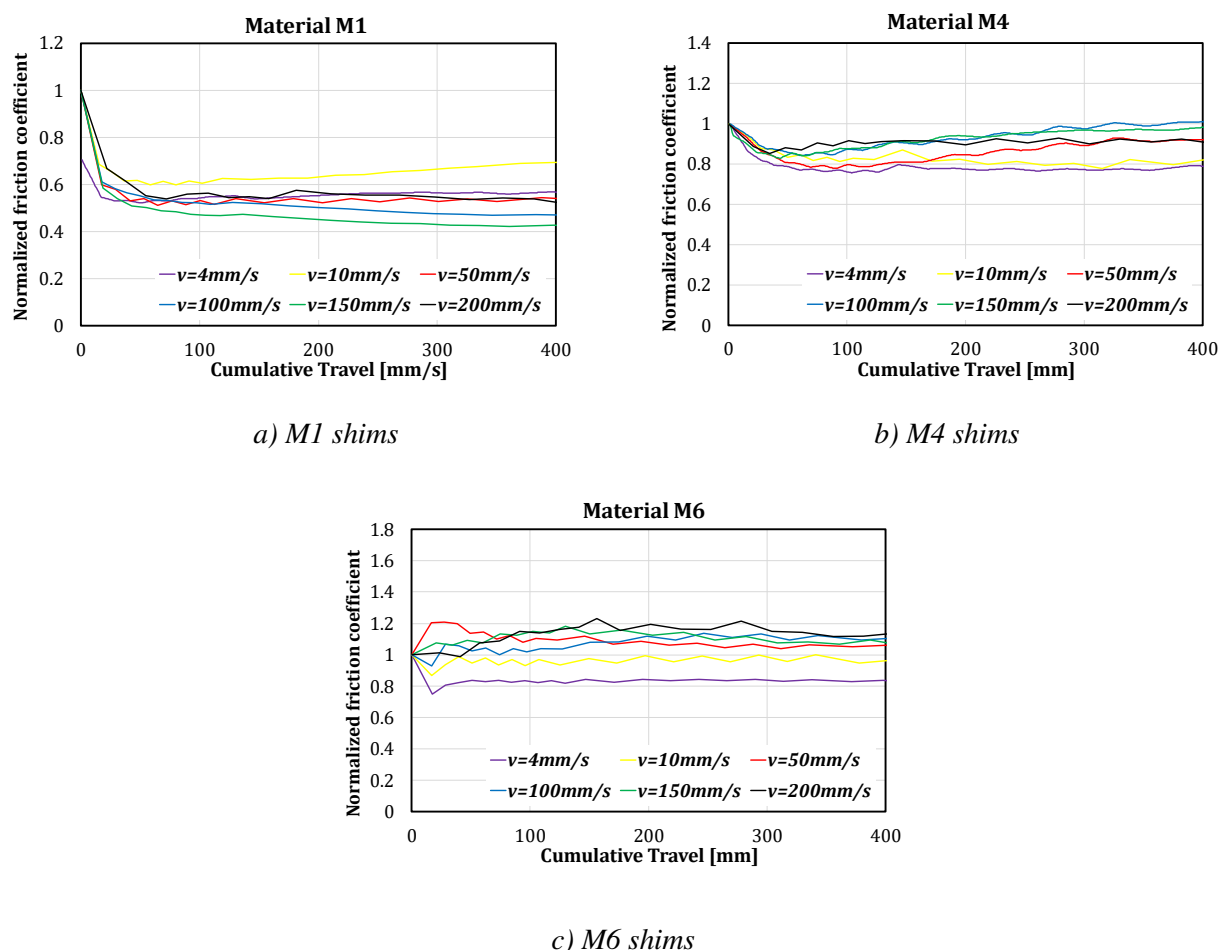


Figure 2.31 – Dependence of the FC degradation on velocity up to 400 mm

Materials M4 and M6 showed a possible increase of the friction coefficient beyond the initial static value, depending on the cumulative travel and sliding velocity. Specifically, material M4 showed a maximum increase of the friction coefficient, compared to the static value, of about 20%. Conversely, material M6 achieved, for very large values of the cumulative travel, increases of the 60%. From the design point of view, this effect may be detrimental for the application of capacity design principles and, therefore, it has to be considered when estimating the damper overstrength for the design of the non-dissipative elements of the structure. Nevertheless, it has to be observed that the high-velocity tests were carried out considering very large values of the cumulative travels, which are certainly beyond the cumulative travel demand occurring in case of realistic seismic events. In practical situations, a truthful estimate of the maximum cumulative travel could be done considering the demand arising from the adoption of the standardised loading protocols which are usually assumed as benchmarks for the characterisation of the joint

behaviour. For instance, it is easy to verify that if the AISC 358 loading protocol for seismic prequalification is considered, the lever arm of a reference joint is fixed, as an example, to 600 mm and the maximum joint rotation is fixed to 40 mrad, the upper bound estimate of the cumulative travel demand in the friction damper is equal to about 400 mm. In Figure 2.31, the same diagrams are re-drawn, fixing the maximum abscissa to 400 mm. This highlights that, within this range, the dynamic over-strength, compared to the initial static value, is equal to about 1 for materials M1 and M4 (soft), while it is equal to about 1.2 for material M6.

2.4 PRELOADING LOSSES DURING THE SERVICE LIFE

2.4.1 Introduction

Several works have examined the influence of preloading techniques, relaxation phenomena, coatings creep, vibration, self-loosening, showing that preloadable bolts always experience a loss of the initial preload [49]-[51]. The loss of preload is usually significant in the first 12h after tightening, and a strong influence on the overall loss is also due to the magnitude of the external loads applied to the connections [52]. Additionally, long-term tests typically show that after the end of the initial effects, the loss of preload is continuous, obeying to a logarithmic evolution law [50]. The loss of initial bolt tension is linked to different phenomena, among which the insufficient initial pretension in the bolts, the self-loosening, relaxation, creep, the use of a non-suitable material and the application of external loads are the most important. A schematic representation of the evolution of the bolt preloading over time is represented in Figure 2.32, where three phases can be distinguished. Immediately after tightening, the bolt experiences an initial loss which is mainly associated with the installation process. This initial loss occurs just after tightening and increases with the magnitude of the applied preload, especially if the bolt is tightened beyond its yield limit [53]. After installation, a so-called mid-term loss appears; different aspects affect the amount of this loss, such as the temperature variations, problems of installation and influence of external loads. Lastly, a long-term loss occurs continuously during the lifetime of the structure, and, after a certain time, the loss-rate becomes stable.

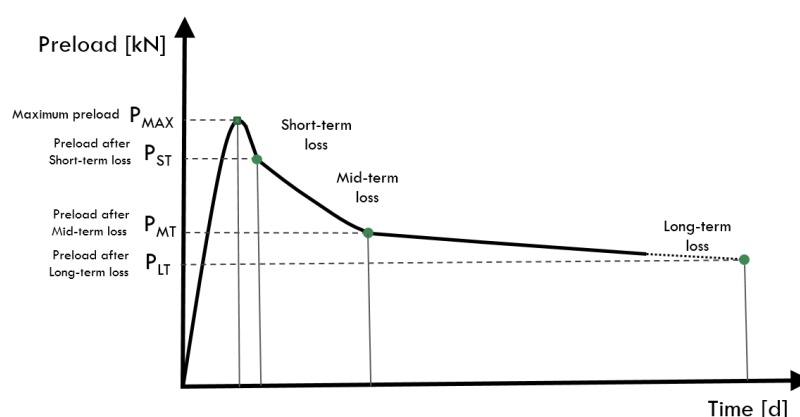


Figure 2.32 – Evolution of the preload in time

In order to characterize the response of preloadable bolts applied in friction devices, experimental tests have been conducted at the University of Salerno and at the University of Liege during the FREEDAM project (Figure 2.33). In order to characterise the loss-of-

preloading, assessing the methodologies to limit such a loss, four typologies of bolted assemblies equipped with different configurations of washers and disk springs have been examined.

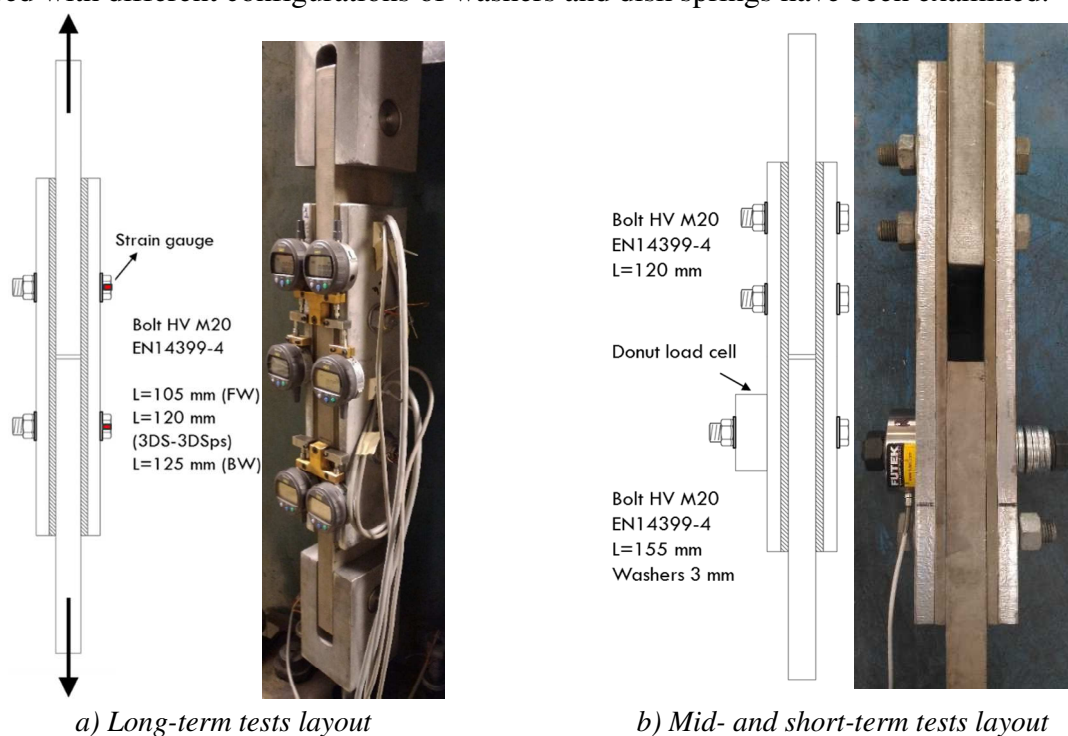


Figure 2.33 – Test layouts

Additionally, in order to assess both the short, mid- and long- term loss, for each configuration of the washer, tests extended for different periods of time have been executed. In order to assess the short- and mid-term relaxation, 20 short-term tests (extended up to 18h) and four mid-term tests (30 days) have been performed. Additionally, for the four different washer configurations, five long-term relaxation tests have been performed monitoring the evolution of the bolt forces over 5 months. The tests have been performed on Symmetrical Friction Connections (SFCs) composed of shims (8 mm) coated with a friction material (material M4), two external hot-dip galvanized plates (15 mm) made of S275JR steel, and an internal slotted plate made of AISI 304 stainless steel. The plates were fastened with M20 10.9 HV bolts. The target bolt preloading for the device was fixed equal to 120 kN, since previous tests on SFCs have shown the beneficial effect provided by the reduction of the bolt stress to a working range limited to about the 30-70% of the proof preload. For all the tests, the bolts were equipped with force measuring devices. In the short- and mid-term tests, the evolution of the preload in the bolts was detected using a donut load cell (FUTEK LYH500 maximum capacity 222.4 kN). For the long-term tests, strain gauges embedded in the bolt shank were used.

In some of the tests, in order to reduce the loss of preloading, Belleville washers having the shape of a conical disk (Figure 2.34) have been employed. To assess the effectiveness of these springs on the reduction of the loss-of-preload, two different types of conical-shaped disk springs have been examined in this work: the standardised European disk springs for M20 bolts (DS DIN 6796 [54]) and a customised type of Belleville washer (Big Washer, BW). The customised disk springs are pre-set in the shop. This means that they are fully flattened in the factory in order to harden the material, assuring a perfectly elastic force-displacement behaviour. Conversely, the European typology of standardised disk spring is typically produced without pre-setting.

Therefore, it has been tested alternatively in the “as delivered” condition (not pre-set), pre-setting it in the laboratory with a universal testing machine.

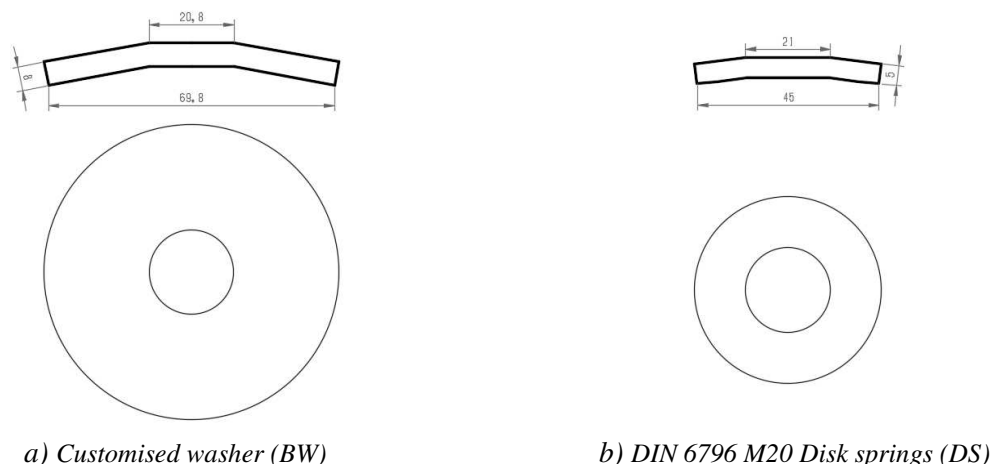


Figure 2.34 – Belleville washers considered

The customised springs carry a force equal to about 120 kN. Conversely, the European disk springs complying with DIN6796 have a flattening load of about 70 kN. As aforesaid, four different configurations of washers have been tested within the present study. The layouts described in Figure 2.35 have been tested: i) a configuration with flat washer (FW) complying with EN14399-6 [55]; ii) a configuration with a couple of pre-set customised Belleville Washers (BW) installed both under the bolt head and under the nut; iii) a stacking of 3 disk springs (3DS) in parallel complying with DIN6796; iv) a stacking of 3 disk springs in parallel complying with DIN6796, pre-set in the laboratory (3DSps).

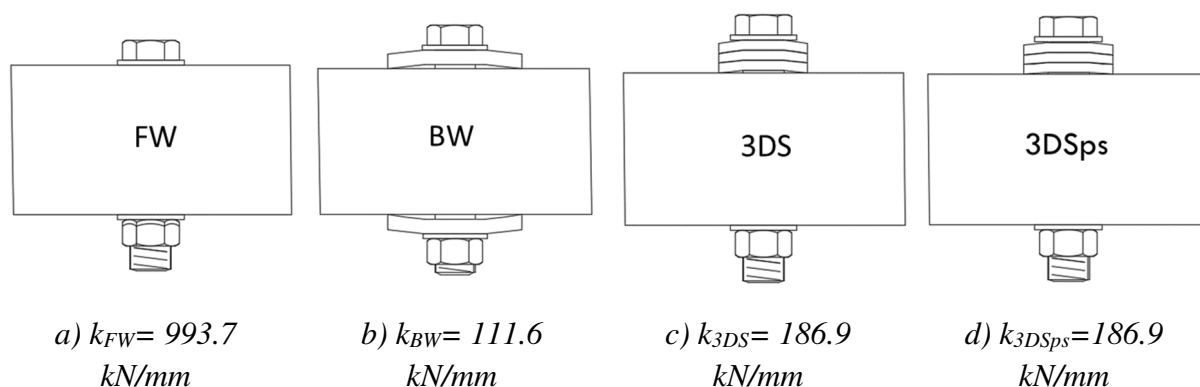


Figure 2.35 – Configurations of washers examined

Three experimental test campaigns to investigate the short-mid- and long-term tests are presented in this section. All the performed tests have been named with acronym strings “ST-FW-TEST #”; where the first two letters indicate the type of test, ST=Short-Term, MT= Mid-term, and LT= Long-term; the second couple of letters individuates the bolt configurations, FW= Flat Washer, BW=Big Washer, 3DS= 3 Disk Springs and 3DSps= 3 Disk Springs Pre-Set and the last number indicates the test number (1, 2, 3...). The same string has been used for the test with the applied external load adding the string EXLOAD (EXternal LOAD) after the bolt configuration. For example, the label “ST-BW-EXLOAD-TEST1” indicates the Short-term (ST) Test 1 (TEST1) on the Big Washer configuration (BW) with an externally applied load (EXLOAD). The external

load applied to the lap shear joints is determined according to EN1090-2 for extended creep tests, and it is equal to 120 kN.

2.4.2 Short-term loss of preloading

In order to assess the short-term relaxation in the proposed bolted connection, 20 tests (extended up to 18h) have been performed on Layout 2 (Figure 2.36). For each configuration, five tests have been performed. The examined configurations of washers are the following: a) the EN14399-6 standard washers without disk springs; b) customised disk spring (BS); c) DIN 6796 washers without pre-setting (3DS); d) DIN 6796 washers with pre-setting (3DSps). Four of the five tests have been executed without external loads in the connection (ST-##-TEST#), and the fifth test has been executed applying an external load equal to 120 kN (ST-##-EXLOAD-TEST#) to the elementary friction damper. This to estimate, separately, the influence of the external tensile load over the loss of preload. All the test results are summarised in Figure 2.36.

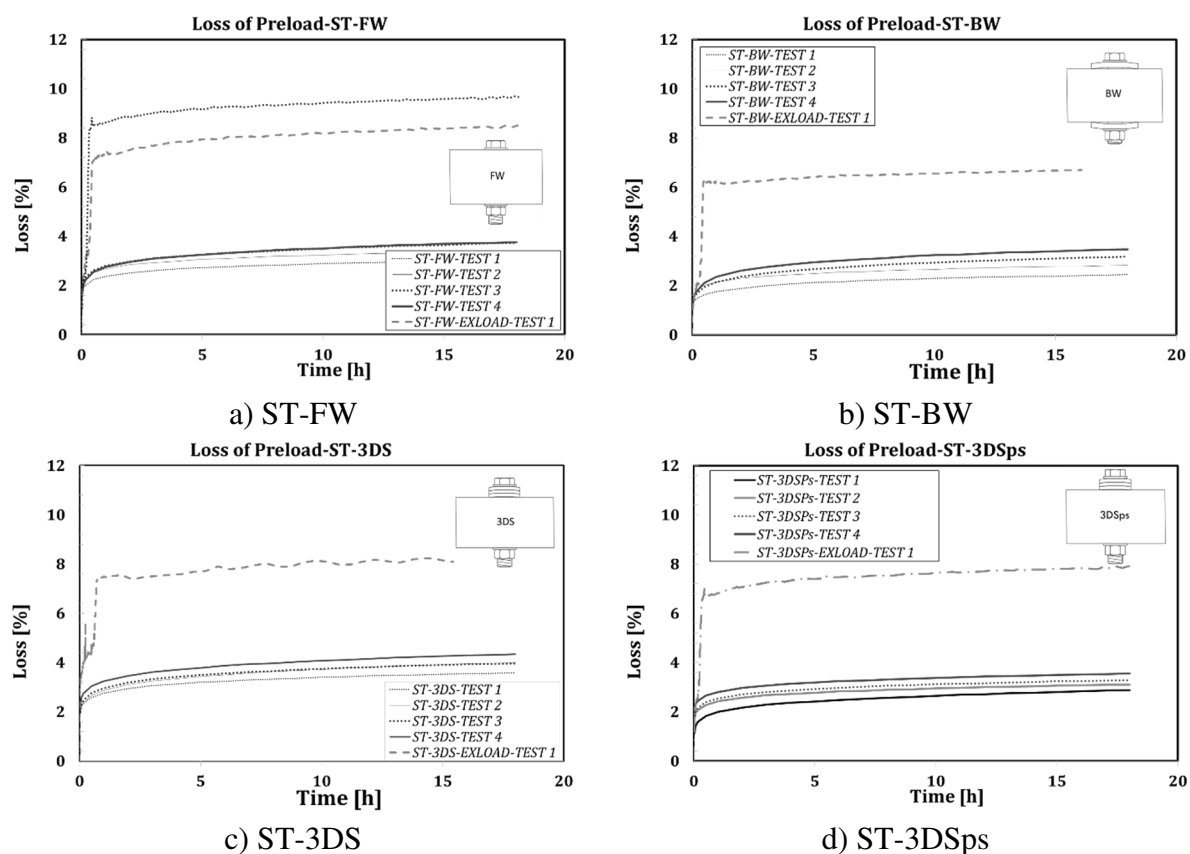


Figure 2.36 – Short-term test results.

When a tensile load is applied to the damper (ST-##-EXLOAD-TEST#), an instantaneous loss of preload occurs. This is due to the settlement of the coatings between the bolt head and nut and of the bolt threads. Mostly, the externally applied load results in a concentrated loss at the end of the loading process. All the tests, in fact, show a shifting of the loss-time curves proportional to the applied load. In Table 2.1-Table 2.4, the loss of preloading occurring in the bolted assemblies is reported in terms of statistical parameters (mean value 5% and 95% fractiles) for time step 1h, 6h, 12h, and 18h. The loss is estimated as a percentage of the initial peak value (120kN). Additionally, the expected loss in 50 years is calculated at each time step with a logarithmic extrapolation of the data up to that time step, according to the procedure given in EN 1090-2. The last two columns of each table report the loss of preload and the 50 years loss

estimation for the test with an applied tensile load; in this case, due to the limited sample tested, statistical evaluation was not possible.

Table 2.1: Short-term relaxation configuration FW

ST-FW TEST 1-4									ST-FW-EXLOAD-TEST1-2	
Time	μ [%]	σ [%]	CV	Fractile 5% [kN]	Fractile 95% [kN]	Loss after 50 years			Loss [%]	Loss in 50 years [%]
						Fractile 5%	μ [%]	Fractile 95%		
1h	2.65%	0.17%	6.39%	2.29%	3.01%	5.24%	6.93%	6.90%	8.15%	12.80%
6h	3.12%	0.15%	4.71%	2.81%	3.44%	5.46%	6.57%	6.68%	8.71%	13.16%
12h	3.34%	0.26%	7.91%	2.78%	3.91%	5.05%	6.45%	7.10%	8.97%	13.13%
18h	3.49%	0.29%	8.40%	2.86%	4.11%	4.98%	6.42%	7.16%	9.16%	13.23%

Table 2.2: Short-term relaxation configuration BW

ST-BW TEST 1-4									ST-BW-EXLOAD-TEST 1	
Time	μ [%]	σ [%]	CV	Fractile 5% [kN]	Fractile 95% [kN]	Loss in 50 years			Loss [%]	Loss in 50 years [%]
						Fractile 5%	μ [%]	Fractile 95%		
1h	2.10%	0.22%	10.35%	1.64%	2.56%	4.28%	5.49%	6.70%	6.17%	6.31%
6h	2.61%	0.31%	12.06%	1.94%	3.28%	4.08%	5.49%	6.90%	6.48%	7.07%
12h	2.84%	0.36%	12.55%	2.08%	3.60%	4.02%	5.49%	6.96%	6.60%	9.91%
18h	2.98%	0.39%	12.96%	2.16%	3.80%	3.97%	5.49%	7.00%	6.76%	9.22%

Table 2.3: Short-term relaxation configuration 3DS

ST-BW TEST 1-4									ST-BW-EXLOAD-TEST 1	
Time	μ [%]	σ [%]	CV	Fractile 5% [kN]	Fractile 95% [kN]	Loss in 50 years			Loss [%]	Loss in 50 years [%]
						Fractile 5%	μ [%]	Fractile 95%		
1h	2.96%	0.18%	6.08%	2.57%	3.34%	6.05%	6.95%	7.85%	7.55%	15.23%
6h	3.54%	0.22%	6.30%	3.07%	4.02%	6.01%	6.94%	7.88%	7.95%	13.38%
12h	3.81%	0.24%	6.39%	3.29%	4.33%	6.00%	6.95%	7.89%	8.12%	12.83%
18h	3.97%	0.27%	6.69%	3.40%	4.54%	5.96%	6.95%	7.94%	8.29%	12.59%

Table 2.4: Short-term relaxation configuration 3DSps

ST-3DSps TEST 1-4									ST-3DSps-EXLOAD-TEST 1	
Time	μ [%]	σ [%]	CV	Fractile 5% [kN]	Fractile 95% [kN]	Loss after 50 years			Loss [%]	Loss in 50 years [%]
						Fractile 5%	μ [%]	Fractile 95%		
1h	2.44%	0.29%	11.98%	1.82%	3.07%	4.13%	5.55%	6.97%	6.87%	12.28%
6h	2.88%	0.28%	9.56%	2.30%	3.47%	2.22%	5.52%	6.65%	7.47%	11.16%
12h	3.07%	0.26%	8.49%	2.52%	3.63%	4.51%	5.51%	6.51%	7.72%	11.18%
18h	3.20%	0.25%	7.76%	2.67%	3.73%	4.59%	5.50%	6.41%	7.85%	11.21%

The short-term loss appears to have a similar magnitude for each studied configuration when external loads are not applied to the assembly (3.4% on average). When the external load is considered, the configuration FW, 3DS, and 3DSps show a comparable level of loss (9.16%, 8.29%, and 7.85% respectively), while the configuration BW shows a slightly smaller loss 6.76%.

2.4.3 Mid-term loss of preloading

Following the same approach adopted for the short-term tests and the same layout, four mid-term relaxation tests have been performed, monitoring the evolution of the bolt force, up to 30 days (720 hours). The mid-term tests have the main goal of identifying the loss appearing in the first hours/days after tightening. However, the tests were extended much longer to have an idea about the stabilising time of the loss. The results given in Figure 2.37 are always compared with the case in which an external tensile load is applied in the specimen (MT-##-EXLOAD-TEST#).

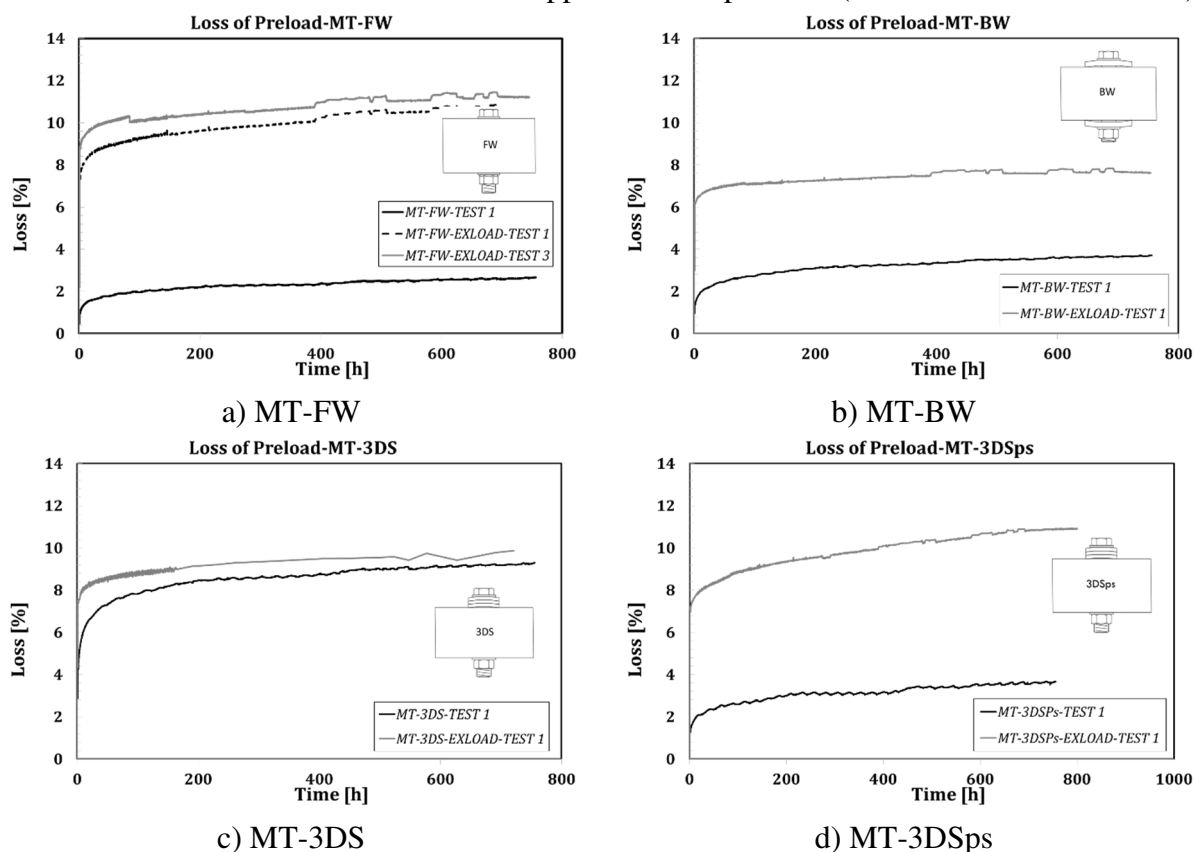


Figure 2.37 – Mid-term test results.

In Table 2.5, results are given for the tests with and without the external loads. For the assembly with FW, with an externally applied load, two tests are available. Hence, the values are referring to the average, using a regression study providing the expected losses in 50 years based on the 30-days relaxation tests. The table is reporting both cases, the one with external load (MT-##-EXLOAD-TEST#) and the one without (MT-##-TEST#).

Globally there is not a significant difference between the loss for the assemblies FW, BW, and 3DSps when no external loads are applied. On the contrary, a higher loss appears for the assembly 3DS (9.21%), which is also rather close to the loss experienced when an external load is applied for the same assembly (9.87%). Nevertheless, due to the limited number of tests, it is rather difficult to generalise the mid-term response of the different assemblies.

Table 2.5: Mid-term tests summary

Time	MT-FW		MT-FW-EXLOAD		MT-BW		MT-BW-EXLOAD		MT-3DS		MT-3DS-EXLOAD		MT-3DSPs		MT-3DSPs-EXLOAD	
	Loss [%]	50y Loss [%]	Loss [%]	50y Loss [%]	Loss [%]	50y Loss [%]	Loss [%]	50y Loss [%]	Loss [%]	50y Loss [%]	Loss [%]	50y Loss [%]	Loss [%]	50y Loss [%]	Loss [%]	50y Loss [%]
1h	0.89	0.9	8.62	12.54	1.22	4.18	6.17	6.31	3.8	13.99	7.55	16.23	1.17	4.12	6.82	12.28
6h	1.31	2.77	9.27	12.82	1.76	4.75	6.48	7.07	5.54	15.81	7.95	13.38	1.69	4.68	7.48	11.17
12h	1.48	3.17	9.49	12.85	1.99	5.00	6.60	9.19	6.17	15.94	8.12	12.84	1.92	4.94	7.73	11.17
18h	1.56	3.43	9.64	12.93	2.13	5.13	6.76	9.22	6.72	15.94	8.29	12.59	2.08	5.18	7.85	11.22
24h	1.6	4.18	9.77	13.00	2.2	5.13	6.81	7.75	6.72	15.82	8.41	12.19	2.10	5.18	8.00	11.48
7d	2.15	4.01	10.31	12.93	2.45	5.78	7.21	8.61	8.27	14.84	9.00	11.73	2.44	5.49	9.22	12.44
15d	2.32	4.19	10.70	12.97	3.29	6.06	7.47	9.11	8.65	14.28	9.35	11.78	3.10	5.87	9.90	15.92
30d	2.59	4.35	11.22	13.61	3.67	6.33	7.65	9.08	9.21	13.92	9.87	11.88	3.60	6.12	10.8	15.97

2.4.4 Long-term loss of preloading

The long-term tests were carried out monitoring the loss of preload over a period of five months. The tests have been executed following the protocol for extended creep tests, according to EN 1090-2. The aim of the codified approach is to individuate the slope of the displacement-log time curve, defining, by extrapolation, the loss occurring in the target time. In the tests presented in this work, the stabilisation occurred after about 2-3 months. This result is consistent with the findings of other authors, which, on similar details, found that the stabilization usually occurs before 4 months [49]. The tests were performed in a temperature-controlled room with a constant temperature of 20 °C for the whole test duration. The objective was to measure the change in strain experienced by the bolts in order to quantify the amount of loss in a long-term period of time accounting for the influence of the service load defined according to EN 1090-2. The gauges measurements were recorded continuously for five months before and after the tensile load application. In order to track the displacements of the plate due to creep, six indicators (Digimatic indicator ID-C112X/1012X) with an accuracy of 0.0025 mm were placed on the specimens. The devices are measuring the relative displacements between the internal plate and the friction pad and the relative displacements between the external plate and the friction pads, which are way below the limitation given in EN1090-2. Six devices were adopted to control both relative and total displacements. Immediately after tightening of the bolts, the assemblies were placed into the machine, and the tensile axial load was applied. The losses of preloading during five months, expressed as a percentage of the initial bolt preloading, are reported in Figure 2.38.

Overall, there is not a remarkable difference between the results for the FW, 3DS, and 3DSPs, which is confirming the results already discussed for short- and mid-term tests. The higher bolt loss can be detected for the configuration with Flat Washers, which are losing 11.9%-12.3%. This is in line with the expected results since there is no possibility for the standard washer to compensate for the loss in the bolt. 3DS assembly is showing a loss of 11.3%, which is still similar to the FW assembly, in this case, the lack of pre-setting of the disk springs makes them less suitable for the current application. However, also the 3DSPs configuration shows similar results (11.6% in 5 months); indeed, a similar preloading loss was registered for this configuration. The result obtained for the 3DSPs (Belleville DIN6796) indicates that, for this

case, the loss of preload is not influenced by the pre-setting procedure. A lower reduction of the loss of preloading is observed with the BW configuration.

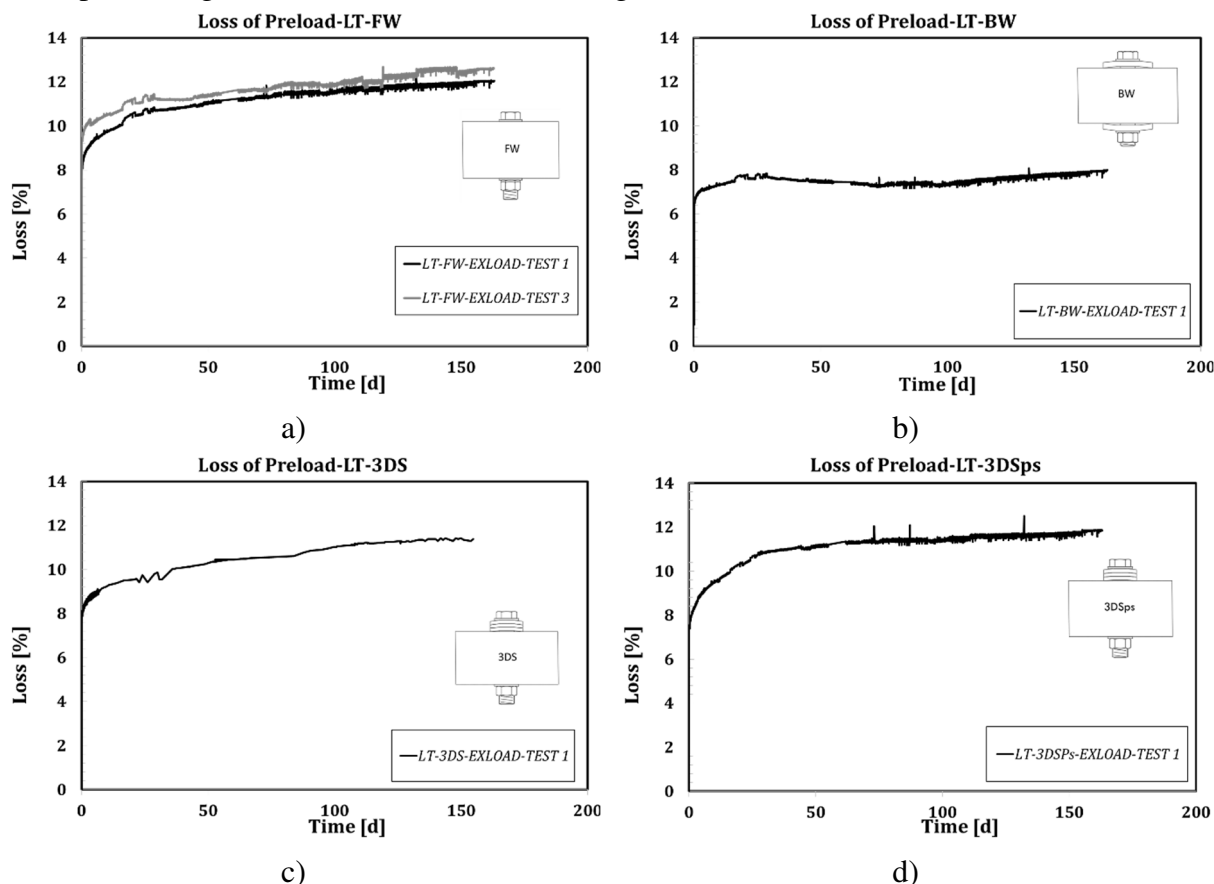


Figure 2.38 – Long-term test results

In fact, the BW assembly shows a smaller loss of preload in 5 months (7.4%). This result is in line with the short-term and mid-term loss presented in the previous paragraphs. However, for this case, the evolution of the loss is slightly different from the other cases. In fact, the slope of the loss is not always positive. This can be the result of relaxation, leading to slow unloading of the washer, which compensates for the tension loss in the bolt. This may require the bolt tension to drop until the slide of the big washers' edge over the underneath plate is allowed. More details on the influence of this kind of washer on the preload can be found in [56]. It has to be highlighted that the experimental tests presented, although in a limited number, are confirming and extending the results obtained in previous tests on similar details [57]-[58]. It is worth noting that in all the examined cases, the bolt loss of initial pretension was never larger than the 16% of the installation preload. From the design point of view, this information is very important because it highlights the need to adopt a partial safety factor related to the bolt loss of pretension, which, on the base of the performed analyses, could be fixed conservatively equal to 1.16. From the practical point of view, it means that to assure that the devices do not slip during the target life of the structure, the bolts have to be initially preloaded with 16% higher tightening torques.

2.5 DESIGN AND ADVANCED MODELLING OF FRICTION DAMPERS

2.5.1 Design values of the friction coefficient and regression models

In order to provide a fast tool for the design or to model the devices with the three coating materials which have been more largely studied during the research project FREEDAM (M1, M4, and M6), a regression analysis of the low-velocity test data (mean and upper/lower bound fractiles) has been carried out. For the sake of simplicity, low-velocity test data are considered because, as previously shown, they provide the most conservative response in terms of cyclic degradation. The results of the regression study are summarised in Table 2.6. The friction coefficient is expressed as a function of the cumulative travel through the following equation:

$$\begin{aligned}\mu_{eff} &= A_0\delta_t^2 + B_0\delta_t + C_0 && \text{if } \delta_t < k \\ \mu_{eff} &= A_1\delta_t^2 + B_1\delta_t + C_1 && \text{if } k < \delta_t < 400 \text{ mm} \\ \mu_{eff} &= A_2\delta_t^2 + B_2\delta_t + C_2 && \text{if } 400 < \delta_t < 1500 \text{ mm} \\ \mu_{eff} &= A_3\delta_t^2 + B_3\delta_t + C_3 && \text{if } 1500 < \delta_t < 4000 \text{ mm}\end{aligned}$$

Table 2.6: Results of the regression study

	Material M1			Material M4			Material M6		
	Fractile 5%	average	Fractile 95%	Fractile 5%	average	Fractile 95%	Fractile 5%	average	Fractile 95%
A_0	0	0	0	$6.35 \cdot 10^{-5}$	$7.34 \cdot 10^{-5}$	$7.934 \cdot 10^{-5}$	$1.2 \cdot 10^{-4}$	9.83 $\cdot 10^{-5}$	$8 \cdot 10^{-5}$
B_0	$-7.2 \cdot 10^{-3}$	$7.6 \cdot 10^{-3}$	$7.9 \cdot 10^{-3}$	$-6.35 \cdot 10^{-3}$	$-7.34 \cdot 10^{-3}$	$-7.934 \cdot 10^{-3}$	$-6.7 \cdot 10^{-3}$	$-6.84 \cdot 10^{-3}$	$-7.1 \cdot 10^{-3}$
C_0	0.61	0.69	0.79	0.69	0.76	0.84	0.52	0.60	0.68
A_1	0	0	0	0	0	0	0	0	0
B_1	$2 \cdot 10^{-4}$	$2 \cdot 10^{-4}$	0	0	0	0	$-4.3 \cdot 10^{-5}$	$-2.11 \cdot 10^{-5}$	$-8.69 \cdot 10^{-7}$
C_1	0.43	0.50	0.59	0.53	0.58	0.64	0.487	0.504	0.521
A_2	0	0	0	0	0	0	0	0	0
B_2	$-1.1 \cdot 10^{-4}$	$-1.6 \cdot 10^{-4}$	$-1.1 \cdot 10^{-4}$	$-1.233 \cdot 10^{-4}$	$-9.096 \cdot 10^{-5}$	$-7.37 \cdot 10^{-5}$	$-3.63 \cdot 10^{-5}$	$-3.01 \cdot 10^{-5}$	$-2.39 \cdot 10^{-5}$
C_2	0.55	0.64	0.63	0.579	0.616	0.669	0.484	0.508	0.532
A_3	0	0	0	0	0	0	0	0	0
B_3	$-4 \cdot 10^{-5}$	$-3 \cdot 10^{-5}$	$-5 \cdot 10^{-5}$	$-5.32 \cdot 10^{-5}$	$-4.41 \cdot 10^{-5}$	$-3.09 \cdot 10^{-5}$	0	0	0
C_3	0.45	0.44	0.54	0.474	0.545	0.604	0.43	0.463	0.496
k		25			50			50	

Additionally, starting from the results obtained in previous sections, the main parameters to be used for the design of the dissipative connections with the three materials described in this paper have been derived. As aforementioned, the design of a friction device requires at least three different values of the friction coefficient. The value to be used for serviceability limit state checks, the value to design the resistance of the dampers and the upper bound value of the friction coefficient to design the non-dissipative parts of the structure (in case of a low-yielding structure they are connections, beams and columns). In particular, dealing with the SLS checks, it is

necessary to assure that the friction connections do not slip under the occurrence of static loading conditions or under the occurrence of moderate seismic events. In all these load combinations, the characteristic value of the static friction coefficient has to be used. Concerning the dampers, in order to guarantee a proper energy dissipation at ULS it is needed to consider the lowest expected value of the dynamic friction coefficient, namely the characteristic value of the dynamic friction coefficient. Additionally, for the ULS design of the non-dissipative parts of the structure, that in this case are represented by the beams, the columns and the connecting elements, the highest expected value of the static friction coefficient has to be considered, namely the 95% fractile of the static friction coefficient. In fact, this is the maximum possible value that, from a statistical point of view, the non-dissipative elements have to withstand before that sliding of the damping devices occurs. With this aim, for any of the three materials, for every set of 10 data, the effective and actual values of the static friction coefficients have been evaluated, summarising the results in Table 2.7.

Table 2.7: Static friction coefficient statistical variation

Material M1				Material M4				Material M6			
TEST n°		$\mu_{0,effective}$	$\mu_{0,actual}$	TEST n°		$\mu_{0,effective}$	$\mu_{0,actual}$	TEST n°		$\mu_{0,effective}$	$\mu_{0,actual}$
NV	60	0.82	0.84	NV	38	0.72	0.74	NV	49	0.64	0.65
NV	61	0.72	0.73	NV	39	0.81	0.85	NV	50	0.63	0.63
NV	62	0.66	0.67	NV	40	0.76	0.81	NV	51	0.57	0.57
NV	63	0.75	0.77	NV	41	0.77	0.80	NV	52	0.54	0.55
NV	64	0.73	0.75	NV	42	0.73	0.76	NV	53	0.59	0.59
NV	65	0.75	0.77	NV	43	0.83	0.86	NV	54	0.65	0.65
NV	66	0.62	0.62	NV	44	0.79	0.82	NV	55	0.58	0.59
NV	67	0.69	0.70	NV	45	0.71	0.74	NV	56	0.64	0.65
NV	68	0.72	0.74	NV	46	0.78	0.81	NV	57	0.65	0.65
NV	69	0.67	0.69	NV	47	0.74	0.77	NV	58	0.53	0.53
MEAN		0.71	0.73	MEAN		0.76	0.79	MEAN		0.60	0.61
DEV ST		0.06	0.061	DEV ST		0.04	0.041	DEV ST		0.05	0.047
CV		0.08	0.084	CV		0.05	0.052	CV		0.08	0.077
Fractile 5%		0.62	0.61	Fractile 5%		0.69	0.72	Fractile 5%		0.52	0.52
Fractile 95%		0.81	0.85	Fractile 95%		0.84	0.87	Fractile 95%		0.68	0.70

As described previously, these values, together with the 5% fractiles of the dynamic friction coefficients evaluated in correspondence of the first stabilized cycle, represent the values needed to design the friction connections.

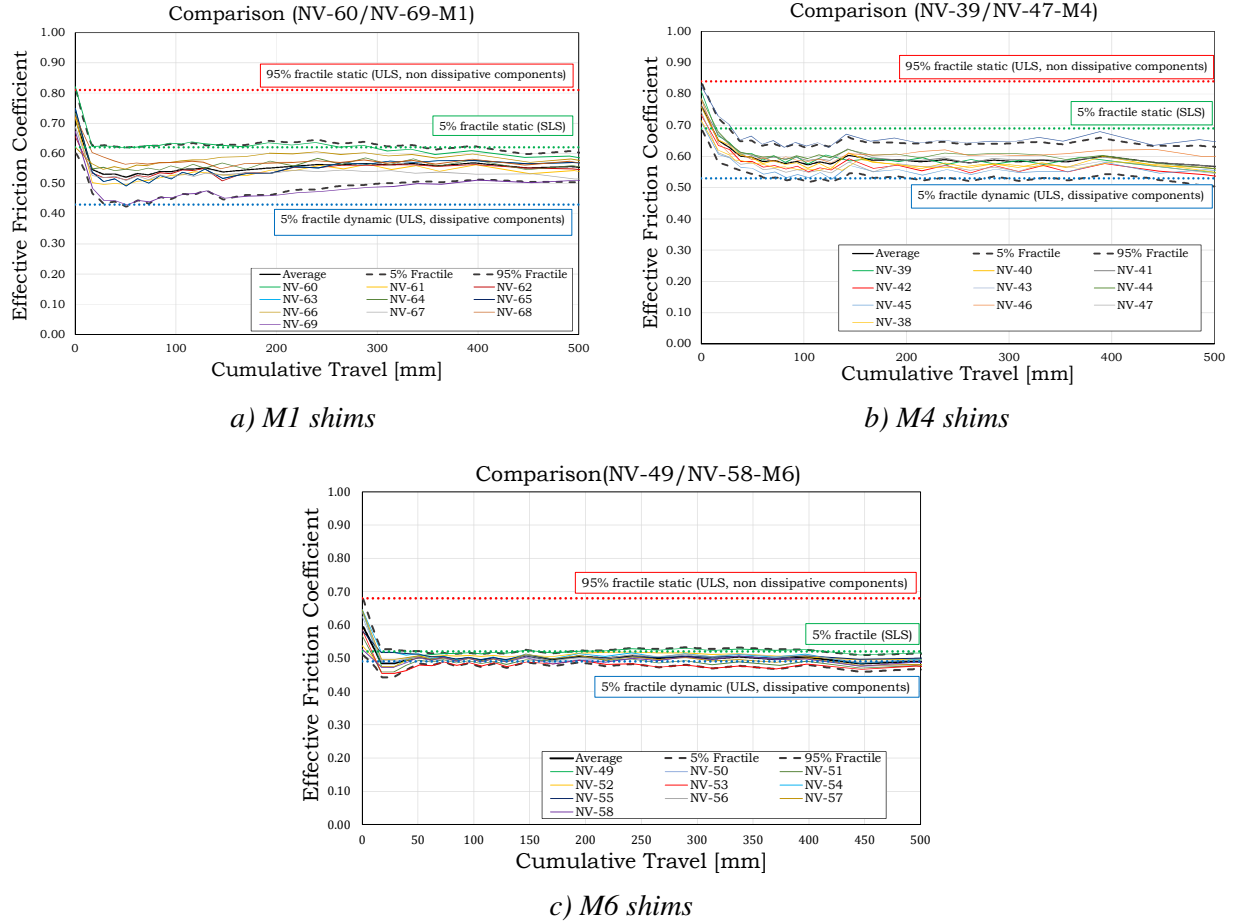


Figure 2.39 – Design values of the friction coefficients for the materials examined

The meanings of these friction coefficients are represented in Figure 2.39, while for the sake of simplicity, they are summarised in Table 2.8.

Table 2.8: Design values of the friction coefficients

Material M1		Material M4		Material M6	
Design FC	$\mu_{0,d}$	Design FC	$\mu_{0,d}$	Design FC	$\mu_{0,d}$
Static 5% fractile	0.62	Static 5% fractile	0.69	Static 5% fractile	0.52
Static 95% fractile	0.81	Static 95% fractile	0.84	Static 95% fractile	0.68
Dynamic 5% fractile	0.43	Dynamic 5%	0.53	Dynamic 5% fractile	0.49

2.6 REFERENCES

- [1] Kelly, J., Skinner, R. & Heine, A., 1972. Mechanisms of Energy Absorption in Special Devices for Use in Earthquake Resistant Structures. *Bulletin of the New Zealand Society for Earthquake Engineering*, 5(3), pp.63-88.
- [2] Skinner, R., Kelly, J. & Heine, A., 1975. Hysteresis Dampers for Earthquake Resistant Structures. *Earthquake Engineering and Structural Dynamics*, 3, pp.287-96.
- [3] Aiken, I., Nims, D., Whittaker, A. & Kelly, J., 1993. Testing of Passive Energy Dissipation Systems. *Earthquake Spectra*, 9(3).
- [4] Christopoulos, C. & Filiatrault, A., 2006. *Principles of Passive Supplemental Damping and Seismic Isolation*. Pavia: IUSS PRESS.
- [5] Soong, T. & Spencer Jr, B., 2002. Supplemental Energy Dissipation: State-of-the-Art and State-of-the-Practice. *Engineering Structures*, 24, pp.243-59.
- [6] Cahis, X., Bozzo, L., Foti, D. & Torres, L., 1997. An Energy Dissipating Device for Seismic Protection of Masonry Walls. In *L'ingegneria Sismica in Italia*. Taormina, Italia, 1997.
- [7] Kobori, T. et al., 1992. Development of Hysteresis Steel Dampers. In *Earthquake Engineering Tenth World Conference*, 1992.
- [8] Nakashima, M., 1995. Strain-Hardening Behavior of Shear Panels made of Low-yield Steel: Test. *Journal of Structural Engineering ASCE*, 121(12), pp.1742-49.
- [9] Whittaker, A., Bertero, V., Alonso, J. & Thompson, C., 1989. UCB/EERC-89/02 Earthquake Simulator Testing of Steel Plate Added Damping and Stiffness Elements. Berkeley: College of Engineering University of California.
- [10] Alonso, J., 1989. *Mechanical Characteristics of X-Plate Energy Dissipators*. Berkeley: University of California.
- [11] Takenaka Komuten KK, 1989. ANTI-SEISMIC DAMPER USING BOLT DRIVE. Patent. Priority JP20211389A·1989-08-03
- [12] Grigorian CE, Yang TS, Popov EP. 1993 “Slotted bolted connection energy dissipators”. *Earthquake Spectra*. Vol.9, No.3, pp.491-504.
- [13] MacRae G.A., Clifton G.C., Mackinven H., Mago N., Butterworth J., Pampanin S. “The sliding hinge joint moment connection.” *Bulletin of New Zealand society for earthquake engineering*, vol.43, n.3, September 2010.
- [14] Khoo, H., Clifton, C. Butterworth, J. MacRae, G. Ferguson, G. 2012. “Influence of steel shim hardness on the sliding hinge joint performance”. *Journal of Constructional Steel Research*, 72, 119-129.
- [15] Pall, A. & Marsh, C., 1981. Response of Friction Damped Braced Frames. *Journal of the Structural Division*, 108(6), pp.1313-23.
- [16] Tremblay, R. & Stiemer, S., 1993. Energy Dissipation through Friction Bolted Connections in Concentrically Braced Steel Frames. *ATC 17-1 Seminar on Seismic Isolation*, 2, pp.557-68.
- [17] Mualla, I. & Belev, B., 2002. Seismic Response of Steel Frames Equipped with a New Friction Damper Device Under Earthquake Excitation. *Engineering Structures*, 24(3), pp.365-71.

-
- [18] Clifton GC, Butterworth JW, (2000). Moment-resisting steel framed seismic-resisting systems with semi-rigid connections 12th WCEE, Auckland, New Zealand.
- [19] G. C. Clifton, J. Butterworth, and J. Weber, "Moment-resisting steel framed seismic-resisting systems with semi-rigid connections", SESOC, vol. 11, no. 2, pp. 21–52, 1988.
- [20] MacRae G.A., Clifton G.C., Mackinven H., Mago N., Butterworth J., Pampanin S. "The sliding hinge joint moment connection." Bulletin of New Zealand society for earthquake engineering, vol.43, n.3, September 2010.
- [21] S. Ramhormozian, G. Clifton, D. Cvitanich, S. Maetzig, and G. Macrae, "Recent Developments on the Sliding Hinge Joint," in The 2016 New Zealand Society for Earthquake Engineering (NZSEE) Annual Technical Conference, 2016.
- [22] S. Kishiki, S. Yamada, T. Takeuchi, K. Suzuki, E. Saeki, A. Wada. 2004. "New ductile steel frames limiting damage to connection elements at bottom flange of beam-ends: part 2 cyclic loading tests of frames with a concrete slab. Proc. 13th WCEE.
- [23] M. Latour, V. Piluso, and G. Rizzano, "Free from damage beam-to-column joints: Testing and design of DST connections with friction pads," Eng. Struct., 2015.
- [24] M. Latour, V. Piluso, and G. Rizzano, "Experimental analysis of innovative dissipative bolted double split tee beam-to-column connections," Steel Constr., 2011.
- [25] Cahis, X., Bozzo, L., Foti, D. & Torres, L., 1997. An Energy Dissipating Device for Seismic Protection of Masonry Walls. In L'ingegneria Sismica in Italia. Taormina, Italia, 1997.
- [26] EUROCODE 0. Basis of structural design. CEN, 2010.
- [27] EN 1090-2. Execution of steel structures and aluminium structures: technical requirements for steel structures. CEN, 2008.
- [28] Bowden, F. & Tabor, D., 1950. The Friction and Lubrication of Solids: part I. Oxford: Oxford University Press.
- [29] Halling, J., 1978. Principles of Tribology. London: Macmillan Education LTD.
- [30] Persson, B., 2000. Sliding Friction. Berlin: Springer.
- [31] Zhang, S., 1998. State-of-the art of Polymer Tribology. Tribology International, 31, pp.49-60.
- [32] Schallamach, A., 1958. Friction and Abrasion of Rubber. Wear, 1, pp.384-417.
- [33] Shooter, K. & Thomas, R., 1952. Frictional Properties of some Plastics. Research, 2, pp.533-39.
- [34] Rees, B., 1957. Static Friction of Bulk Polymers over a Temperature Range. Research, 10, pp.331-38.
- [35] Schallamach, A., 1952. The Load Dependence of Rubber Friction. In Phys Soc., 1952
- [36] Thirion, P., 1948. Les Coefficients d'Adherence du Caoutchouc. Rubber Chemistry and Technology, 21, pp.505-15.
- [37] Ratner, S. & Sokolskaya, V., 1956. The Influence of the Hardness of Rubber on its Coefficient of Static Friction without Lubrication. Rubber Chem. Technol., 29, pp.829-33.
- [38] Mualla, I., 2000. "Experimental evaluation of new friction damper device". 12th WCEE, Auckland, New

- [39] Voiculescu, D., Dalban, C., 1999. “Behaviour of steel concentrically braced frames with friction dissipation devices”. SDSS '99, Timisoara, RomaniaZealand.
- [40] Ono, S., Nakahira, K., Tsujioka, S., Uno, N., 1996. “Energy absorption capacity of thermally sprayed aluminum friction dampers”. *Journal of Thermal Spray Technology*, 5(3), 303-309.
- [41] C. Heistermann, M. Veljkovic, R. Simões, C. Rebelo, L. Simões da Silva. (2013). Design of slip resistant lap joints with long open slotted holes. *Journal of Constructional Steel Research*, Volume 82, March 2013, Pages 223-233
- [42] M.Pavlović, C. Heistermann, M. Veljković, D.I Pak, M. Feldmann, C. Rebelo, L. Simões da Silva. (2015). Friction connection vs. ring flange connection in steel towers for wind converters. *Engineering Structures*, Volume 98, 1 September 2015, Pages 151-162
- [43] Latour M, Piluso V, Rizzano G. (2014). Experimental Analysis of Friction Materials for supplemental damping devices. *Construction and Building Materials*.
- [44] Voiculescu, D., Dalban, C., 1999. “Behaviour of steel concentrically braced frames with friction dissipation devices”. SDSS '99, Timisoara, RomaniaZealand.
- [45] EN10088-1, 2005. Part 1: List of stainless steels
- [46] EN 14399-4 (2006). High-strength structural bolting assemblies for preloading –Part 4: System HV –Hexagon bolt and nut assemblies
- [47] EN 15129, (2009). Anti-seismic devices
- [48] G. P. Davet, “Using Belleville Springs To Maintain Bolt Preload,” 1997.
- [49] C. Heistermann, “Behaviour of Pretensioned Bolts in Friction Connections,” 2011.
- [50] C. Heistermann, M. Veljkovic, R. Simões, C. Rebelo, and L. Simões da Silva, “Design of slip resistant lap joints with long open slotted holes,” *Journal of Constructional Steel Research*, 2013.
- [51] M. Veljkovic, “Achievements of HISTWIN project,” 2015.
- [52] “FINITE ELEMENT ANALYSIS OF LAP JOINTS.” [Online]. Available: https://www.steelconstruct.com//gsPublications/Eurosteel2014-Christine_Heistermann.pdf. [Accessed: 11-Apr-2016].
- [53] C. Heistermann, “Resistance of Friction Connections with Open Slotted Holes in Towers for Wind Turbines,” 2014.
- [54] “DIN 6796. Conical spring washers for bolted connections.”
- [55] CEN, “EN 14399-6. High-strength structural bolting assemblies for preloading - Part 6: Plain chamfered washers,” no. June, 2006.
- [56] S. Ramhormozian, G. C. Clifton, G. A. MacRae, and G. P. Davet, “Stiffness-based approach for Belleville springs use in friction sliding structural connections,” *J. Constr. Steel Res.*, vol. 138, pp. 340–356, Nov. 2017.
- [57] M. D’Antimo, J.-F. Demonceau, M. Latour, G. Rizzano, and J.-P. Jaspert, “Experimental investigation of the creep effect on prestressed bolts used in innovative friction connections,” *Ce/Papers*, vol. 1, no. 2–3, pp. 580–589, 2017.
- [58] G. Ferrante Cavallaro, M. Latour, A. B. Francavilla, V. Piluso, and G. Rizzano, “Standardised friction damper bolt assemblies time-related relaxation and installed tension variability,” *J. Constr. Steel Res.*, vol. 141, pp. 145–155, 2018.

CHAPTER 3

DEVELOPMENT OF FREEDAM CONNECTIONS

3.1 INTRODUCTION

In the last decades, the use of replaceable anti-seismic devices in the beam-to-column joints has received great attention from the scientific community [1-11] due to the high energy dissipation capacity and the consequent reduction of the global and the local ductility demand. To date, a large variety of dampers has been proposed, providing systems based on the activation of simple dissipative mechanisms such as yielding of metals, dry friction, and viscosity of fluids [12,13]. Their application has been mainly suggested within the framework of design strategies based on the supplementary energy dissipation.

Nevertheless, even though the introduction of anti-seismic devices reduces the structural damage, the lateral displacements which are usually needed to activate the dampers lead to the development of damage in the main structural members which may be either difficult or impractical to repair.

For such a reason, recently, new approaches based on the idea of adopting in steel structures connections equipped with dampers that undergo only minimal damage are being proposed. This is the case, for example, of the Sliding Hinge Joint (SHJ) developed at the University of Auckland since 2004 [14-20]. These joints, when used in steel Moment Resisting Frames (MRFs), can accommodate large beam-column inelastic rotations through the sliding of Asymmetric Friction Dampers (AFDs) located at the level of the bottom beam flange [21-24]. Such typology provides many benefits because it is rigid and partial-strength allowing to limit the lateral drifts and, contemporaneously, to protect the beam end from yielding and to reduce the column oversizing deriving from the application of beam-column hierarchy criteria specified by the code provisions.

Recently, similar layouts of beam-to-column connections based on the inclusion of Symmetric Friction Dampers (SFDs) have also been proposed within a comprehensive research work aimed at the development, design and testing of beam-to-column joint equipped with friction dampers [25-35]. Such new connections allow achieving the same benefits provided by the SHJ (rigidity, tuneable resistance, ductility, and high energy dissipation capacity) with the use of an industrialized kit completely manufactured in the shop and bolted to the structural elements (beam and column) directly on site.

The main advantage of the industrialized kit is the precise control of the friction shims quality and the bolts tightening procedure. These issues are, in fact, fundamental for the proper functioning of the friction devices and need to be strictly controlled during the production process. To assure the required disassembly ability to the friction device, the damper is realized with a slotted haunch which is bolted to the beam flange and L-stubs and friction shims clamped with high strength preloadable bolts. Two configurations have been investigated namely HFC-configuration, where the haunch is parallel to the beam flange, and VFC-configuration, where

the haunch is orthogonal to the beam flange (Fig. 3.1). Under bending actions, the joint is forced to rotate around a point located at the base of the upper T-stub web and the energy dissipation supply is provided by the alternate slippage of the haunch on the friction shims. Another advantage of the haunch is the increase of the lever arm which allows reducing the force to be transmitted by the friction devices to fulfil serviceability requirements.

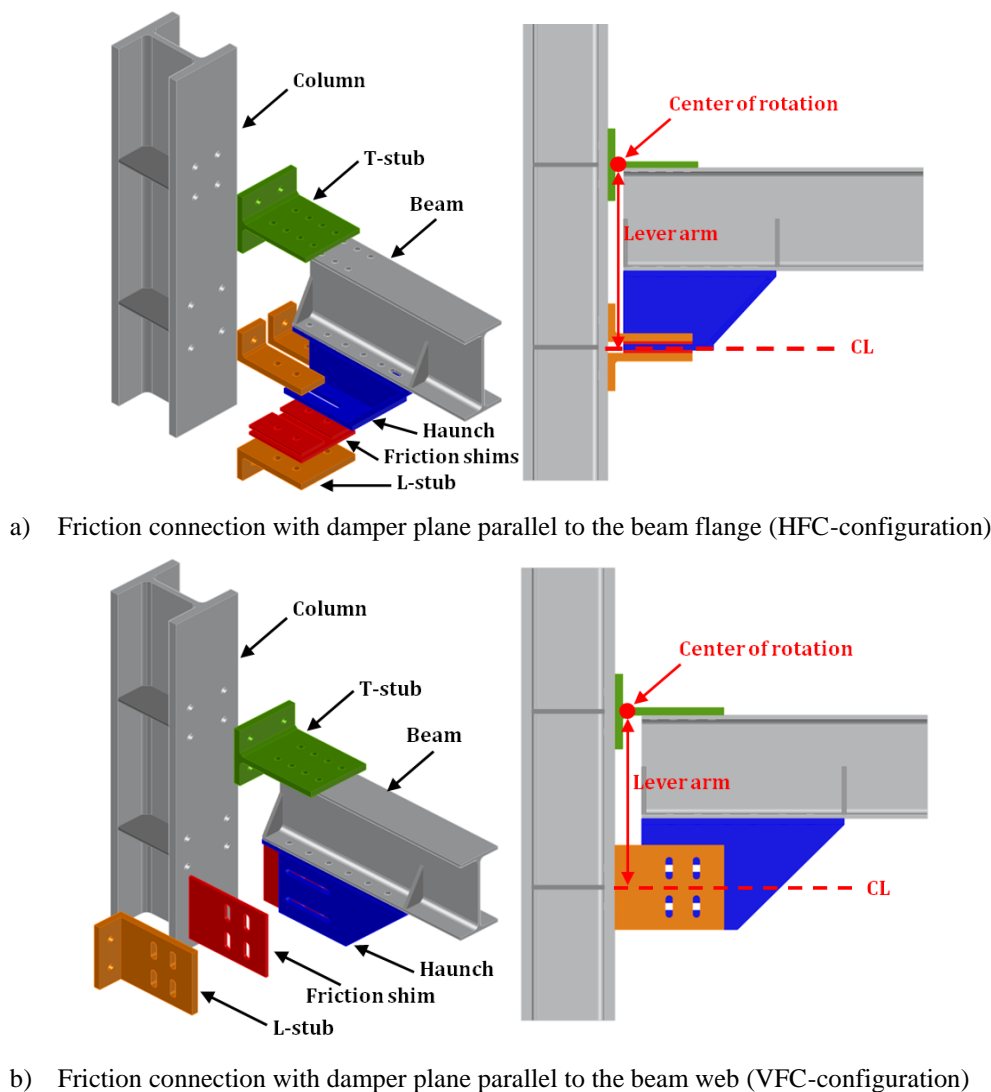


Figure 3.1– Layouts of friction connections with SFDs

Experimental works devoted to this specific connection typology have addressed important aspects of the connection behaviour, such as the response of the friction shims under cyclic loading histories, the behaviour of preloadable bolts at installation and over their service-life, the finite element modelling of beam-to-column joints with friction devices and the impact response of elementary friction dampers [25-36].

Aiming to assess the experimental response of friction joints, a wide experimental campaign has been carried within the research project FREEDAM on sub-assemblages able to represent the behaviour of internal joints and external joints in actual moment-resisting frames. The results of the experimental tests have allowed the validation of the design criteria for friction joints developed during the project and the calibration of FEM models used to perform parametric

studies. In particular, the primary aim of the experimental activity is verifying the ability of the proposed beam-to-column connections to dissipate the earthquake input energy almost without any damage. To this scope, 16 experimental tests have been carried out. In particular, 8 tests on external joints have been performed at the University of Salerno and 8 tests on internal joints have been carried out at the University of Coimbra.

The specimens have been designed exploiting, for all the joint components, except for the friction dampers, the models already proposed by Eurocode 3 part 1-8. Conversely, for the new component, i.e. the friction damper, the results coming from the experimental activities on lap-shear specimens with slotted holes and interposed friction pads have been used. In particular, as described in Chapter 2, the tests on the coating materials for the friction pads have demonstrated that materials M1 and M6 can develop a slight stick and slip behaviour which may induce vibrations. Therefore, even though they can be considered appropriate for the application to the FREEDAM dampers, the tests on the beam-to-column joints have been devoted only to material M4 because it seems to be the most reliable for the application to FREEDAM joints avoiding stick and slip phenomena. The experimental activity has been carried out concerning sixteen beam-to-column connections, eight on joints fastening IPE 270 beams and eight connecting IPE 450 beams. As already stated, two different configurations of the friction damper have been considered, namely horizontal configuration, HFC, and vertical configuration, VFC (Figure 3.1). For each damper configuration, the test has been executed twice. One test has been carried out using disk springs and a second test concerned a specimen using simple flat washers for the bolt assemblies.

3.2 EXPERIMENTAL TESTS ON EXTERNAL JOINTS

3.2.1 Description of the test setup

The experimental activity has regarded the following joints:

- FJ-CYC01: IPE270 beam-HEM220 column, VFC-configuration, M20 HV bolts class 10.9 equipped 6 disk springs (3 groups stacked in series of 2 disk springs stacked in parallel);
- FJ-CYC02: IPE270 beam-HEM220 column, HFC-configuration, M20 HV bolts class 10.9 equipped 6 disk springs (3 groups stacked in series of 2 disk springs stacked in parallel);
- FJ-CYC03: IPE450 beam-HEB500 columns, VFC-configuration, M20 HV bolts class 10.9 equipped 6 disk springs (3 groups stacked in series of 2 disk springs stacked in parallel);
- FJ-CYC04: IPE450 beam-HEB500 columns, HFC-configuration, M20 HV bolts class 10.9 equipped 6 disk springs (3 groups stacked in series of 2 disk springs stacked in parallel);
- FJ-CYC05: IPE270 beam-HEM220 column, VFC-configuration, M20 HV bolts class 10.9 without disk springs;
- FJ-CYC06: IPE270 beam-HEM220 column, HFC-configuration, M20 HV bolts class 10.9 without disk springs;
- FJ-CYC07: IPE450 beam-HEB500 columns, VFC-configuration, M20 HV bolts class 10.9 without disk springs;
- FJ-CYC08: IPE450 beam-HEB500 columns, HFC-configuration, M20 HV bolts class 10.9 without disk springs.

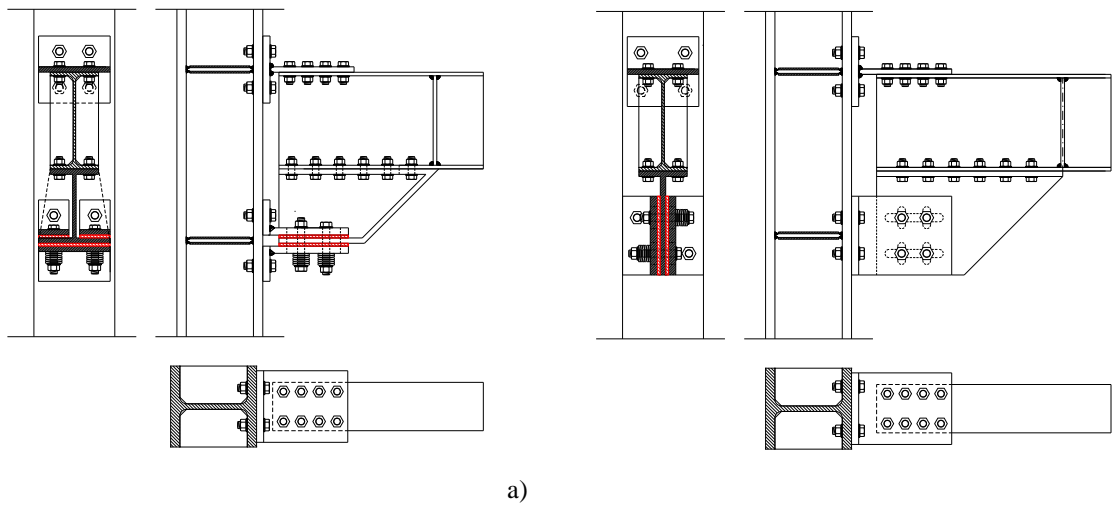


Figure 3.2 – Tested specimens (external joints): a) configuration with horizontal damper; b) configuration with vertical damper

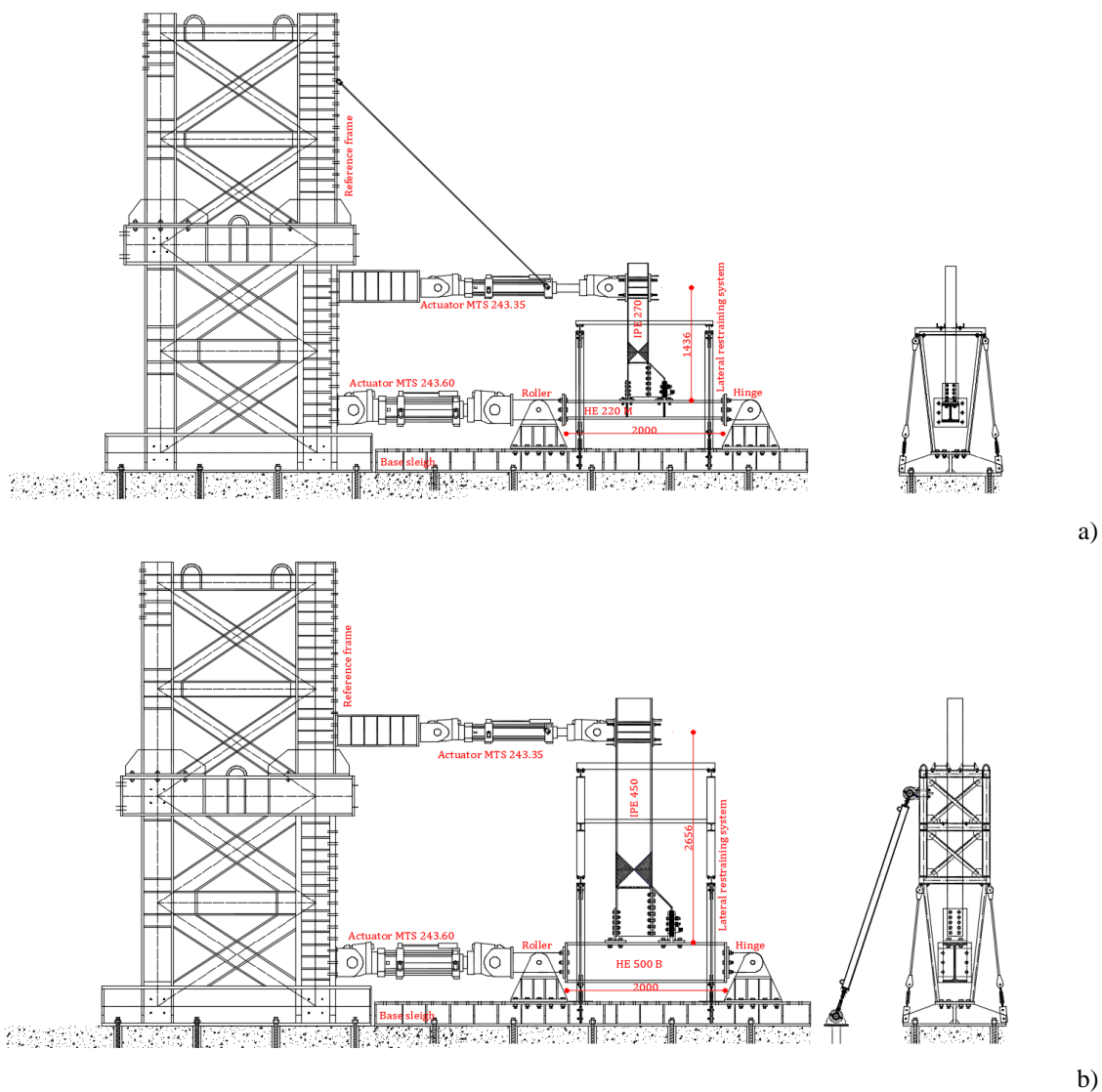


Figure 3.3 – Experimental layout: a) FJ-CYC01-FJ-CYC04; b) FJ-CYC05-FJ-CYC08

All the experimental tests have been executed at the STRENGTH laboratory (STRuctural ENgineering Testing Hall) of the University of Salerno. The tests setup is constituted by instruments and machines that could be divided into three macro-categories: constraining devices, loading machines and measurement instruments. In the STRENGTH laboratory, the main constraining device is represented by the laboratory strong floor having holes (with a diameter of 80 mm and spaced according to 1.0 m x 1.0 m grid) which are used to fix all the testing equipment of the laboratory. This strong floor has been exploited to fasten all the restraints necessary to develop the testing rig for external beam-to-column joints. In this case, to perform the cyclic tests on the joints, some constraining structures have been used: a rigid and strong vertical frame and a horizontal steel rigid restraint, both realized assembling fully welded steel plates and structural members (Fig. 3.3).

Besides, aiming to simulate the point of zero moments occurring in the actual structural scheme (Figure 3.4), two steel hinges have been adopted (Figure 3.3). Such hinges have been designed to resist shear actions up to 2000 kN and bolted to the base steel sleigh. One of the two hinges has been detailed to absorb shear and axial actions using a pin. Calibrated holes have been adopted to minimize the slippage. The second one has been designed to allow the displacement in the horizontal direction and to resist displacements in the orthogonal direction. To this scope, a pin has been used combined with slotted holes to allow the desired displacement.

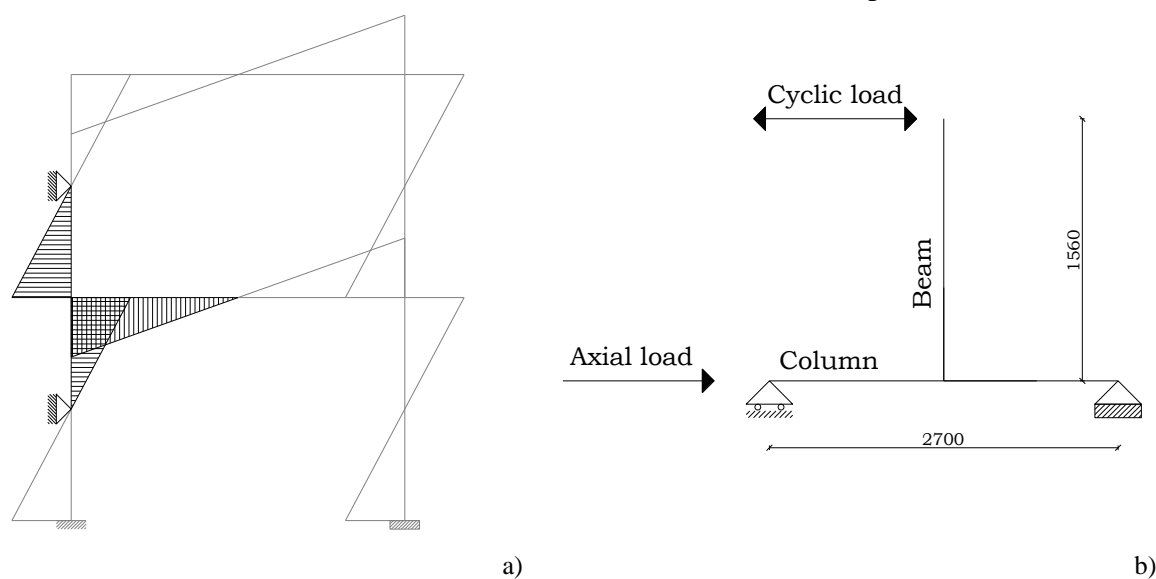


Figure 3.4 – Structural scheme: a) action in an external joint due to the seismic loads;
b) reproduced scheme in the laboratory

Finally, lateral-torsional restraints (Figure 3.3) have been employed to avoid lateral-torsional buckling phenomena of the beam during the experimental tests. Concerning the loading equipment, in the experimental campaign, three different MTS hydraulic actuators have been used. Aiming to apply the axial load in the column, an MTS 243.60 actuator, working under load control, has been used. This actuator has a maximum loading capacity equal to 1000kN in compression and 650 kN in tension with a maximum piston stroke equal to ± 125 mm. To apply the bending action in the connection, two different MTS actuators have been used depending on the size of the beam. The first one, adopted for testing IPE 270 beams, has a maximum load capacity equal to 245 kN with a maximum piston stroke equal to ± 500 mm and the second one,

used for testing IPE 450 beams, has a load capacity equal to 500 kN, and maximum piston stroke equal to +/-500 mm.

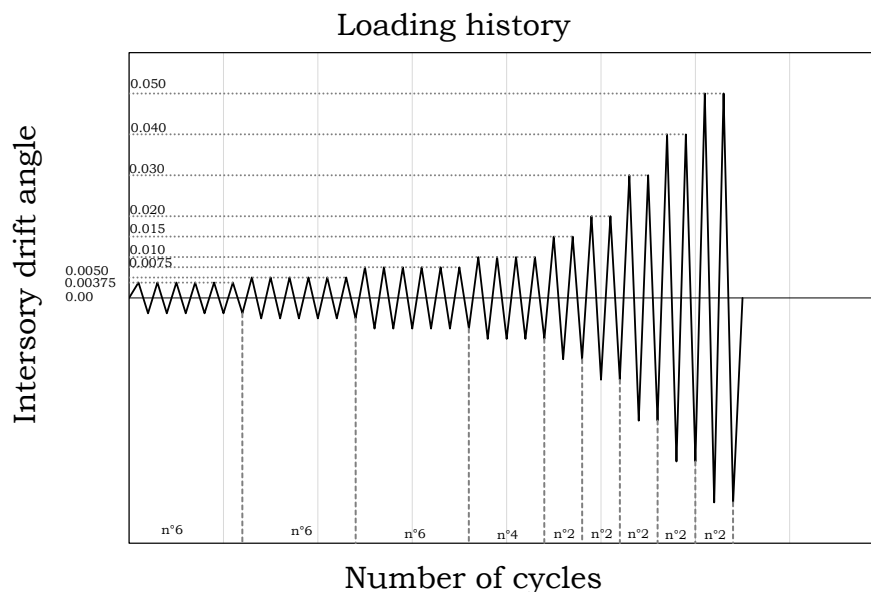


Figure 3.5 – Structural scheme: a) action in an external joint due to the seismic loads;
b) reproduced scheme in the laboratory

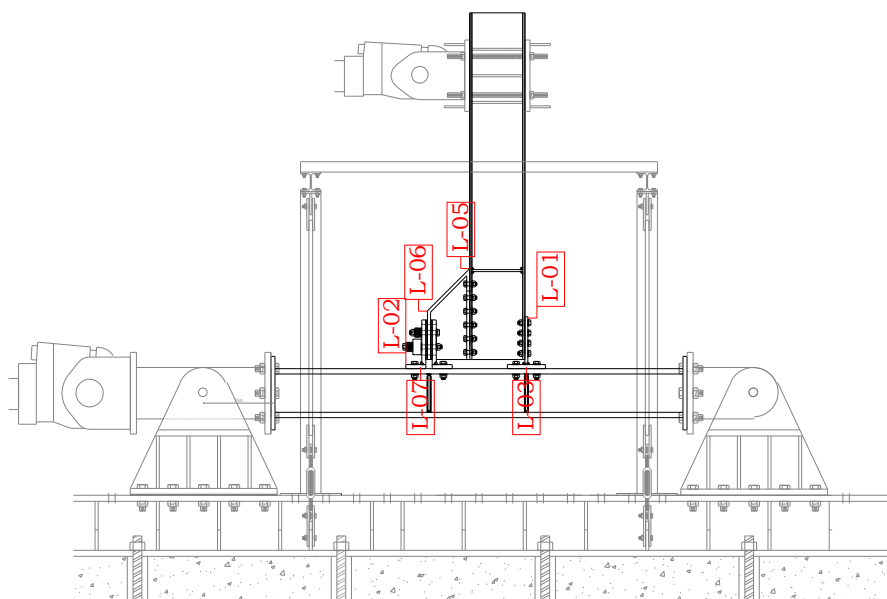
Both of them have been exploited to apply, under displacement control, the desired displacement history at the tip of the beam. The monitoring of the applied displacements on the tested specimens during the tests has been also carried out by using external displacements' transducers. In particular, during the experimental campaign, the displacements of the beam, the column and the elements composing the connection, particularly the friction damper, have been continuously measured using LVDTs. As aforementioned, the experimental tests have been executed using two hydraulic actuators, the bottom actuator has been governed under force control to impose a constant axial compression load equal to 650 kN while the top actuator has been used to impose the desired cyclic displacement history.

Table 3.1: Loading displacement history

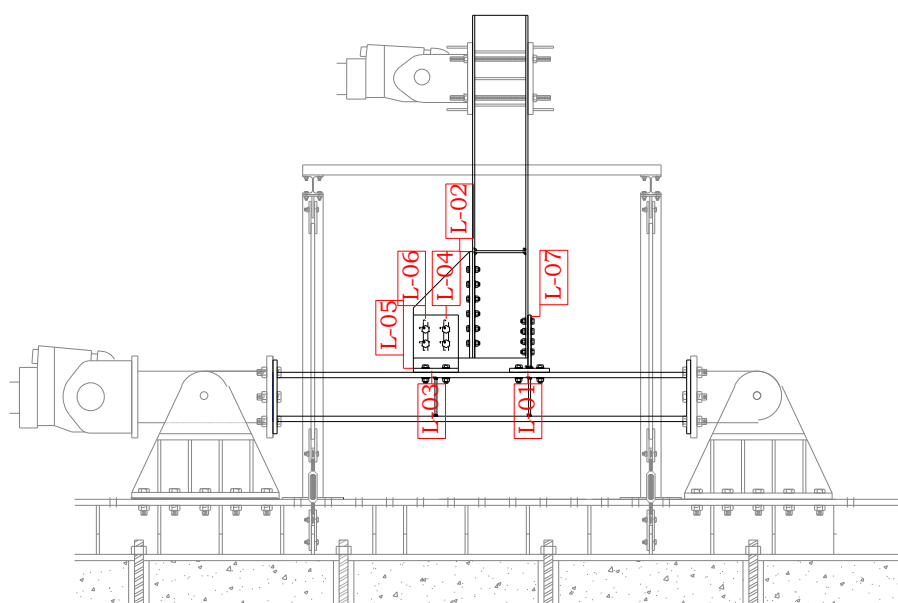
v [mm/s]	step	θ [rad]	# cycles	δ [mm]
0.5	1	0.00375	6	5.835
	2	0.0050	6	7.780
1	3	0.0075	6	11.67
	4	0.010	4	15.56
	5	0.015	2	23.34
2	6	0.020	2	31.12
	7	0.030	2	46.68
4	8	0.040	2	62.24
	9	0.050	2	77.80

In particular, the top actuator has been connected to the tip of the beam to apply a displacement history according to the AISC 346-10 loading protocol [37] (Figure 3.5). This is a loading

protocol devoted specifically to joints, very common in the US practice, and normally used for the prequalification of joints. This loading protocol is the same that was used also in the EQUALJOINTS research project.



a)



b)

Figure 3.6 – Position of the LVDTs: a) FREEDAM-CYC01; b) FREEDAM-CYC02

Therefore, starting from the knowledge of code requirements, it is possible to obtain the displacement history at the top of the beam. The tests have been executed up to a maximum rotation equal to 50 mrad (Table 1.1). It is useful to note that this rotation is far higher than the minimum required by EC8, equal, for DCH frames, to 35 mrad . During the tests, many parameters have been monitored and acquired, to evaluate forces and displacements at the level of the top actuator and the displacements of the different joint components. In all the tests at least six linear displacement transducers have been employed. Examples of the arrangement of the

devices on the two different joint configurations are reported hereinafter for test n°1 and test n°2. For all the other tests similar layouts of the measurement devices have been employed. In particular, in FREEDAM CYC-01 joint the following sensors have been employed (Figure 3.6a):

- LVDTs n.02, 03 and 07 to measure the relative displacement between the T-stub/angles flanges and the column flange;
- LVDT n. 05 to measure the displacements between the haunch and the beam;
- LVDTs n. 06 to measure the displacement of the friction device;
- LVDT n. 01 to evaluate possible slips of the web of the T-stub with respect to the beam flange.

In FREEDAM CYC-02 joint the following sensors have been employed (Figure 3.6b):

- LVDTs n.01, 03 and 05 have been used to measure the relative displacements arising between the T-stub/angles flanges and the column flange;
- LVDT n. 02 to measure the displacements between the rib and the beam flange in the friction connection;
- LVDTs n. 04 and 06 to measure the displacements of the two bolt rows of the friction device;
- LVDT n. 07 to evaluate possible slips of the web of the T-stub with respect to the beam flange.

Besides, in all the experimental tests, the pre-loads applied in the bolts of the friction devices have been monitored before and during the test using donut load cells (Futek LTH500) labelled with numbers RC-01, RC-03 and RC-04. In the tests with IPE 270 beams only two load cells have been employed, while in the tests with IPE 450 beams three load cells have been employed.

3.2.2 Results of the experimental tests

For sake of shortness, only the results obtained for specimens FJ-CYC01 to FJ-CYC04 are herein presented. More information on the whole experimental program can be found in the final report of the whole project.

The experimental tests provided a response in line with the expected behaviour. In fact, as depicted in Figs. 3.7, wide and stable hysteretic cycles have been obtained and, macroscopically, no damage was observed in the non-dissipative components at the end of the tests.

Table 3.2: Comparison between experimental and design values of friction moments

	FJ-CYC01	FJ-CYC02	FJ-CYC03	FJ-CYC04
M_{exp} [kNm]	+185.45	+145.73	+697.48	+556.97
	-210.41	-227.80	-863.04	-782.37
$M_{nd,d}$ [kNm]	226.02	217.85	861.85	861.85
M_{Ed} [kNm]	142.61	137.46	543.79	543.79

The upper bound values of the static resistance adopted for the design of the non-dissipative components (represented in Fig. 3.7 with a dashed line) are practically equal to the maximum bending moments observed during the experimental tests (Table 3.2). Similarly, the dynamic values of the bending resistance, calculated considering the dynamic friction coefficient, are very close to the sliding resistance of the joints. In Table 3.2, a comparison between the experimental strength of the four connections and the specimens' design resistance is reported. For all the

specimens, it is possible to observe that the experimental values of the joints flexural resistance are very close to the range of the design values (between the upper bound static and lower bound dynamic values). The agreement with the design procedure is fully satisfactory.

In the case of joints with the HFC-configuration, a slightly lower sliding resistance was observed under sagging bending moments, mainly due to the higher deformability of the L-stubs in tension which led to a loss of preload higher than expected. Conversely, in the case of joints with VFC-configuration, the sliding resistance of the connection, both under hogging and sagging bending moments, is practically equal to the design resistance. In the case of joints with HFC-configuration, the response of the joint was strongly asymmetric exhibiting significantly different resistance values under positive and negative bending moments. The difference with respect to the maximum resistance was greater than 35% in the case of FJ-CYC 02 specimen. The asymmetry was mainly due to the bending of the T-stubs/L-Stubs plates and the consequent fluctuation of the pressure on the friction pads. The joints with VFC-configuration, exhibited a lower asymmetry of the cyclic behaviour. Nevertheless, during the experimental tests, also owing to the reduction of the bolts clamping forces, a small decrease of the bending moment was observed at large rotations. This effect was more evident for the specimens with the deep beam, for which the cumulative travel at the level of the friction damper is greater, due to the increase of the connection lever arm.

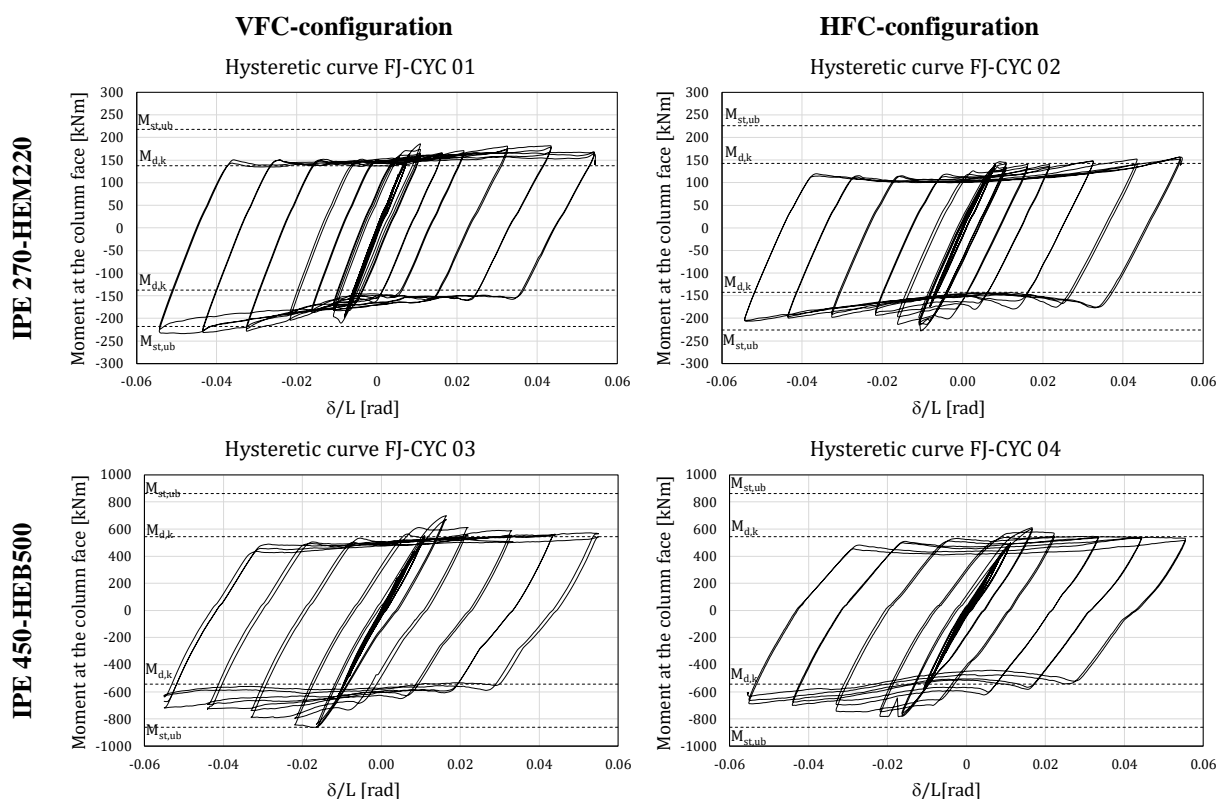


Figure 3.7 – Hysteretic curves

It is also possible to observe from the hysteresis loops that the response was characterized by a first slippage arising at a force value slightly higher than those corresponding to the following cycles. After a few cycles, the slippage force is stabilized and the hysteretic loops are almost always repeated for the whole loading history with the same shape. These results are in line with

the outcomes of the experimental tests on the friction dampers as the shapes of the loops of the joint was perfectly comparable with that of the shear-lap tests executed on the friction dampers, presented in Chapter 2. The first peaks correspond to the static friction coefficient (higher than the dynamic value in the case the soft coating materials), while the stabilized cycle corresponds to a slip force of the damper whose value is mainly related to the dynamic value of the friction coefficient. Additionally, considering the friction coefficients obtained testing the dampers alone (Chapter 2), it is possible to verify that both the static and dynamic values of the slip force observed during the whole loading history were compatible with the predicted range of slip force values based on the tests carried out on the dampers alone. Slight differences are in any case obtained due to the flexibility of the steel L-stubs of the friction damper that caused during the test oscillations (increase and decrease) of the bolt forces under hogging/sagging bending moments.

In Fig. 3.8 the joints in the deformed configuration are depicted pointing out the correct definition of the geometry of the dampers which were able to accommodate the design rotation equal to 50 mrad. The accuracy of the adopted design procedure was demonstrated also by the local measurements executed during the tests. In fact, for all the specimens, the energy dissipation was provided only by the friction dampers leaving at the end of the test all the structural elements practically undamaged. In particular, assuming that the centre of rotation is located in correspondence of the T-stub at the centreline of the top flange of the beam and the damper is subjected to cyclic tension/compression force, the representations of the local measures obtained with the LVDTs are made reporting the measured displacement versus the local force acting in the damper or at the T-stub level.

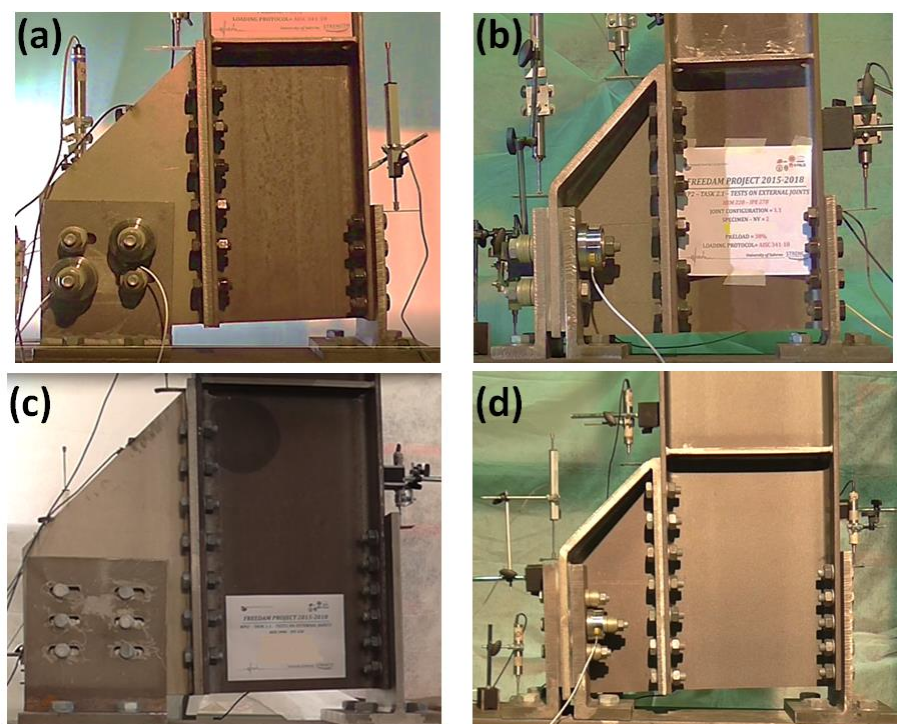


Figure 3.8 – Specimens in the deformed configuration: a) FJ-CYC01; b) FJ-CYC02; c) FJ-CYC03; d) FJ-CYC04

Using the displacements recorded by the LVDT 04 and LVDT 06 (Figure 3.9), in the case of VFC configuration, and the displacements recorded by LVDT 06 (Figure 3.10), in the case of HFC configuration, the force versus displacement of the friction dampers have been determined.

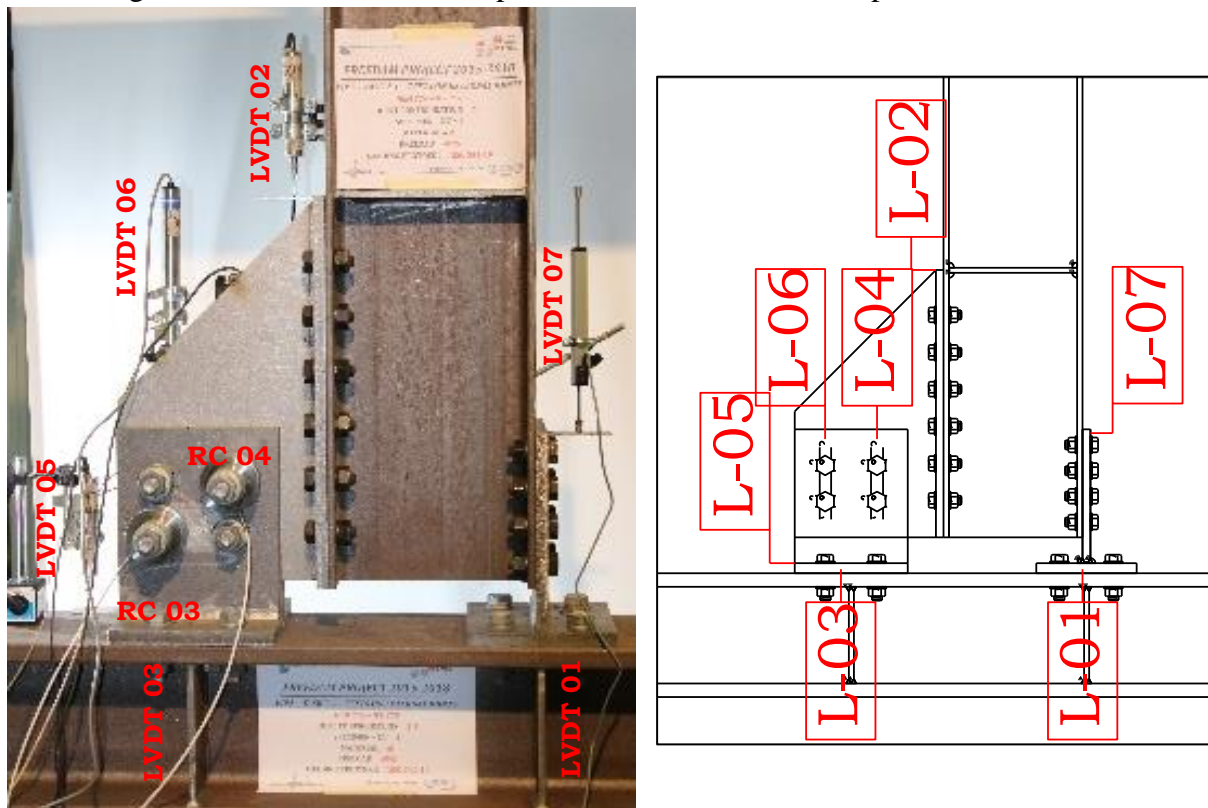


Figure 3.9 – Position of the instruments - FREEDAM-CYC01

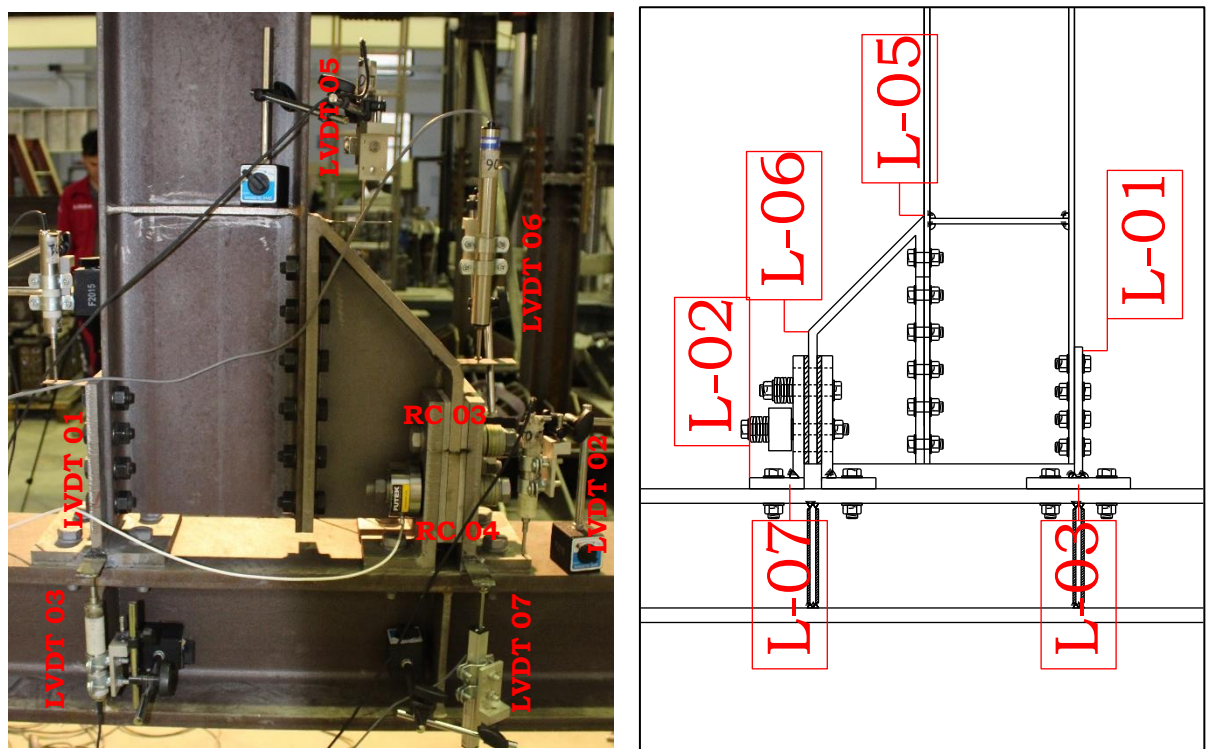


Figure 3.10 – Position of the instruments - FREEDAM-CYC02

It can be easily observed that the hysteretic loops are practically rectangular with a significant energy dissipation capacity and almost no degradation both in terms of stiffness and resistance (Figure 3.11).

The local measurements (Figures 3.12 and 3.13) show that the T-stub and L-stubs remain practically in the elastic range, while the dissipation is given only by the friction damper which provided a stable hysteretic response with high energy dissipation. At the end of the tests, a loss of the bolt clamping force equal to about the 25-30% was observed. This outcome suggests that, even though friction connections are low-damage, after the occurrence of a severe ground motion they need proper maintenance to check the residual resistance of the damper and the magnitude of the loss of preload. In particular, the re-tightening of the bolts to restore the bolt preloading can be required. Nevertheless, it has to be noted that real earthquakes provide a cumulative plastic rotation demand in the joint components which is usually much lower compared to that imposed through the AISC-358 loading protocol. Therefore, the loss of the clamping force observed during these tests has to be considered as an upper bound value which has not a direct correspondence with the loss of preloading occurring after an actual ground motion.

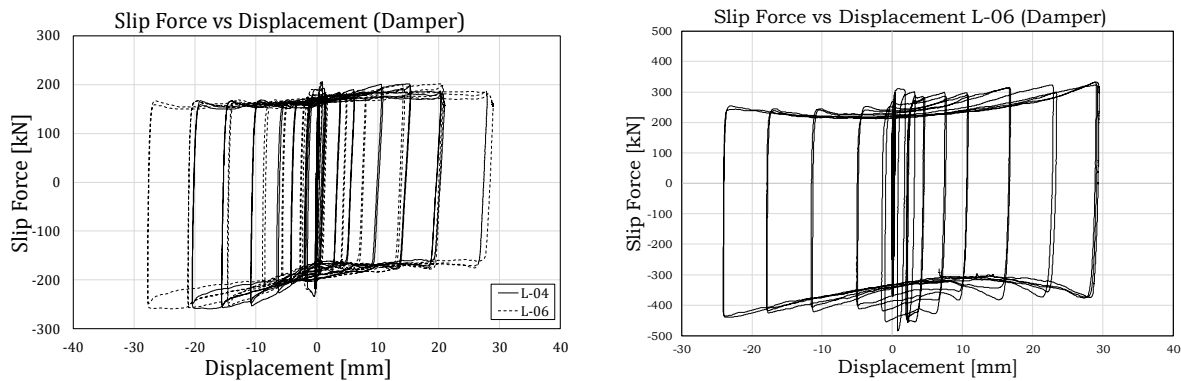


Figure 3.11 – Slip force vs displacement curve of the friction dampers FREEDAM-CYC01 (left) and FREEDAM-CYC02 (right)

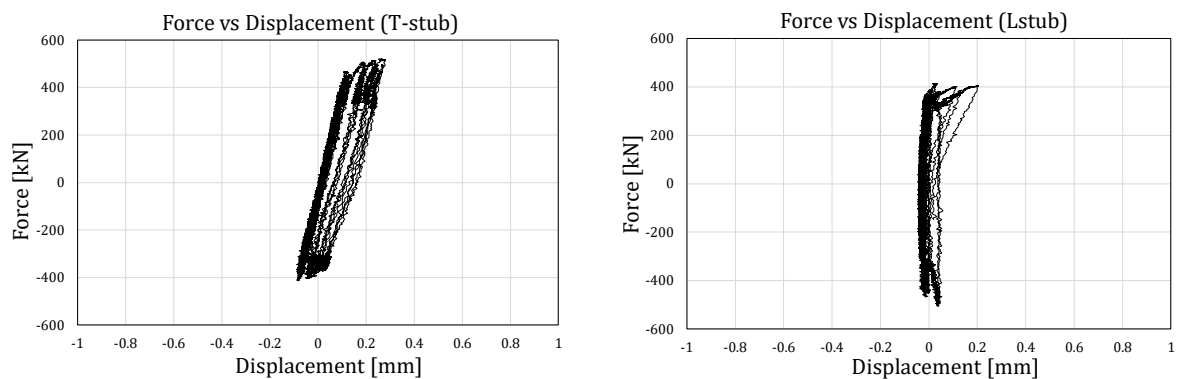


Figure 3.12 – Local measurements FREEDAM-CYC01 – T-stub and L-stubs

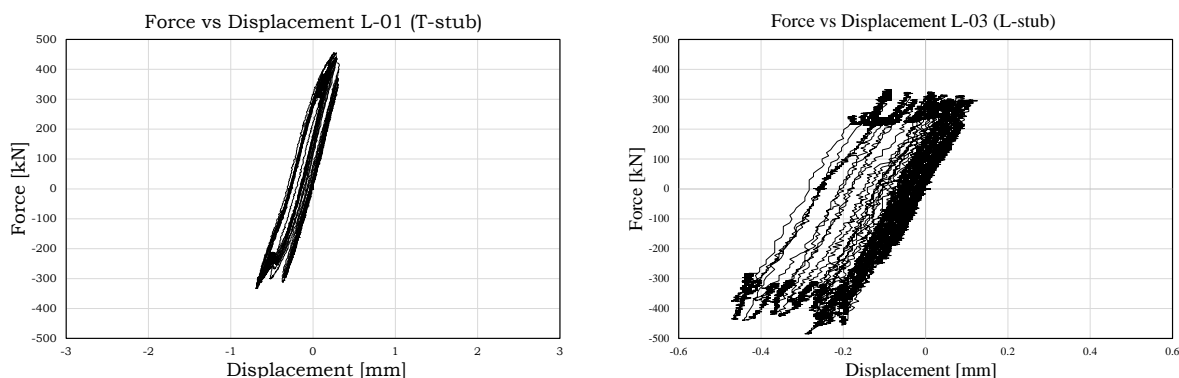


Figure 3.13 – Local measurements FREEDAM-CYC02 – T-stub and L-stubs

The value of the bolts' preload and their variation during the tests has been monitored using two load cells, RC-03 and RC-04, located in correspondence of the two bolt rows of the damper. These results are represented in Figure 3.14. From this figure, it is possible to observe that initially, at first sliding as already detected in the shear lap tests, there is a settlement of the bolts with a loosening that increases as far as the loading cycles increase. This loosening occurs up to the achievement of high displacement cycles in which the bending effects developing in the dampers' bolt lines lead to a significant oscillation of the bolt forces which, at the peak, achieve, again, practically the initial force.

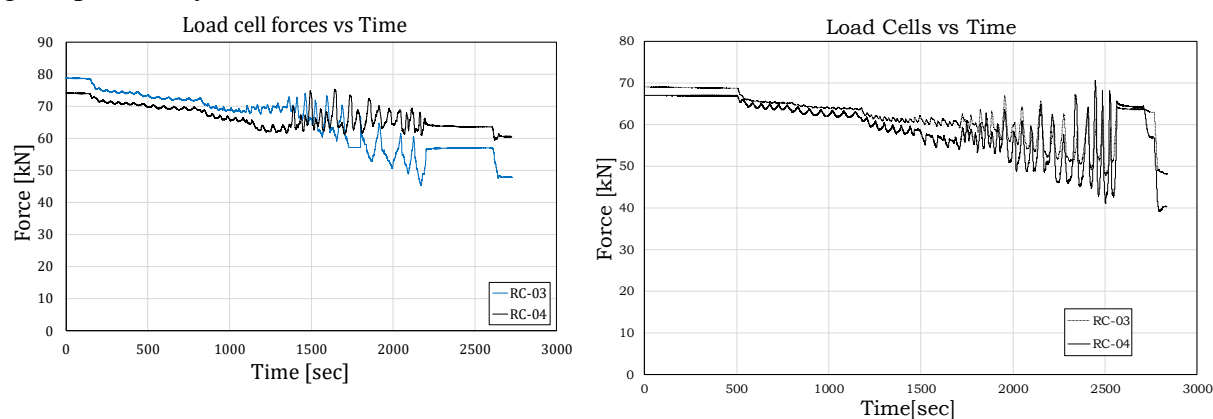


Figure 3.14 – Preload force in the bolts of the friction damper FREEDAM-CYC01 (left) and FREEDAM-CYC02 (right)

All the experimental tests responded completely in line with the expected behaviour. In all the tested cases minor yielding of T-stubs and L-stubs was observed at the stem to flange connection confirming the efficiency of the proposed design procedure. Therefore, in all the experimental tests the energy dissipation was provided only by the FREEDAM friction dampers leaving at the end of the test all the structural elements practically undamaged (Figure 3.15). Another thing that was pointed out in this experimental phase is that the Belleville disk springs did not seem to provide a substantial benefit in terms of hysteretic behaviour. This result confirms the observations already made in Chapter 2 dealing with the testing of the friction dampers.

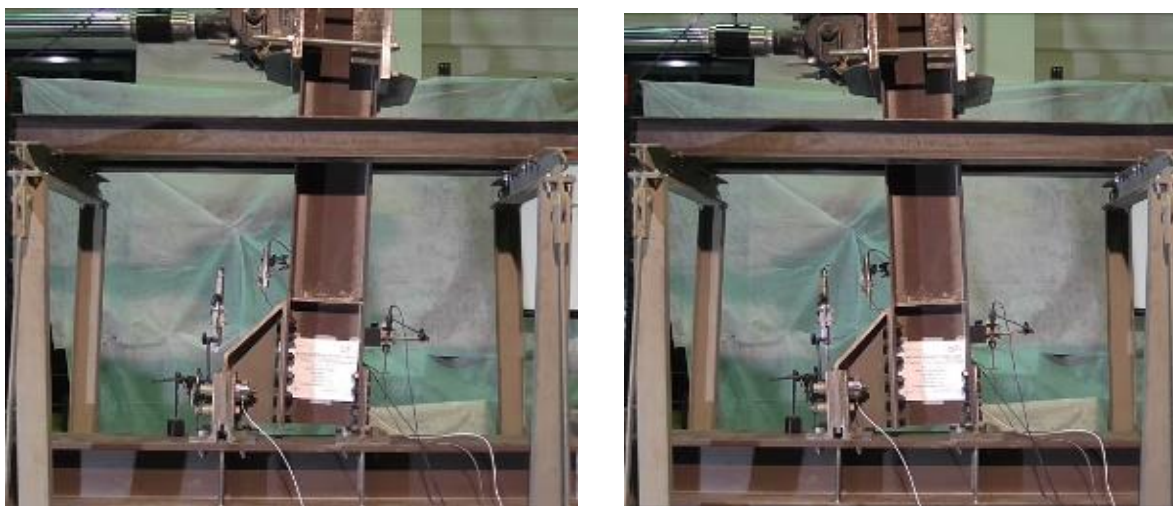


Figure 3.15 – FREEDAM-CYC02 specimen in the deformed configuration at the end of the test

In particular, regarding the comparison between the VFC configuration and the HFC configuration, a similar behaviour was observed concerning the strength degradation during the cyclic loading history. Also, the influence of the Belleville washers was negligible in both cases. However, the use of the VFC configuration provides a reduction of the asymmetry of the hysteresis loops and the improvement of their shape which is more close to the ideal rectangular shape as it is testified by the comparison between the force versus displacement curves of the friction dampers obtained for VFC configuration (Figure 3.11 left) and the HFC configuration (Figure 3.11 right). In particular, the typical shape exhibited by the hysteresis loops in the HFC configuration is due to the different pressure distribution on the friction pads occurring when the joint is under hogging moment compared to the one occurring under a sagging moment. This has been also testified by the FEM simulations presented in Chapter 4.

3.3 EXPERIMENTAL TESTS ON INTERNAL JOINTS

3.3.1 Test setup and experimental programme

Internal beam-to-column joints have been tested at the University of Coimbra. The connections tested in this experimental activity are identical to those tested at the University of Salerno as external joints. Therefore, it means that the only difference occurring in the cyclic response of the beam-to-column joints is due to the different behaviour of the panel zone in shear. In particular, under the typical seismic distribution of the bending moment transmitted by the beams, the shear force expected in the panel zone is twice the one occurring in the case of external joints. Therefore, the primary aim of this part of the experimental activity planned within the FREEDAM research project is the validation of the criteria for the evaluation of the panel zone behaviour in shear which constitute a part of the design procedure developed during the research project and presented in detail in Part II “Design Handbook”, Chapter 7.

Therefore, similarly to the experimental campaign on the external joints, four different configurations of the FREEDAM connection were tested, varying the beam and the column dimensions (IPE270/HEM220 and IPE450/HEB500) and the configuration of the friction

dampers (vertical or horizontal configuration). A total of 8 tests were carried out, as reported in Table 3.3.

Table 3.3: Experimental programme

N.	Test code	Column and beam dimensions	Type of test	of FREEDAM damper configuration	Coating material
1	IN270_CYC 1_M4_(1)	HE220M / IPE270	Cyclic	Horizontal pads	M4
2	IN270_CYC-1_M4_(2)	HE220M / IPE270	Cyclic	Horizontal pads	M4
3	IN270_CYC-2_M4_(1)	HE220M / IPE270	Cyclic	Vertical pads	M4
4	IN270_CYC-2_M4_(2)	HE220M / IPE270	Cyclic	Vertical pads	M4
5	IN450_CYC-1_M4_(1)	HE500B / IPE450	Cyclic	Horizontal pads	M4
6	IN450_CYC-1_M4_(2)	HE500B / IPE450	Cyclic	Horizontal pads	M4
7	IN450_CYC-2_M4_(1)	HE500B / IPE450	Cyclic	Vertical pads	M4
8	IN450_CYC-2_M4_(2)	HE500B / IPE450	Cyclic	Vertical pads	M4

In all the tests, the material labelled as M4 was used as the coating material of the friction pads and disk spring washers were used in the bolt assemblies of the dampers.

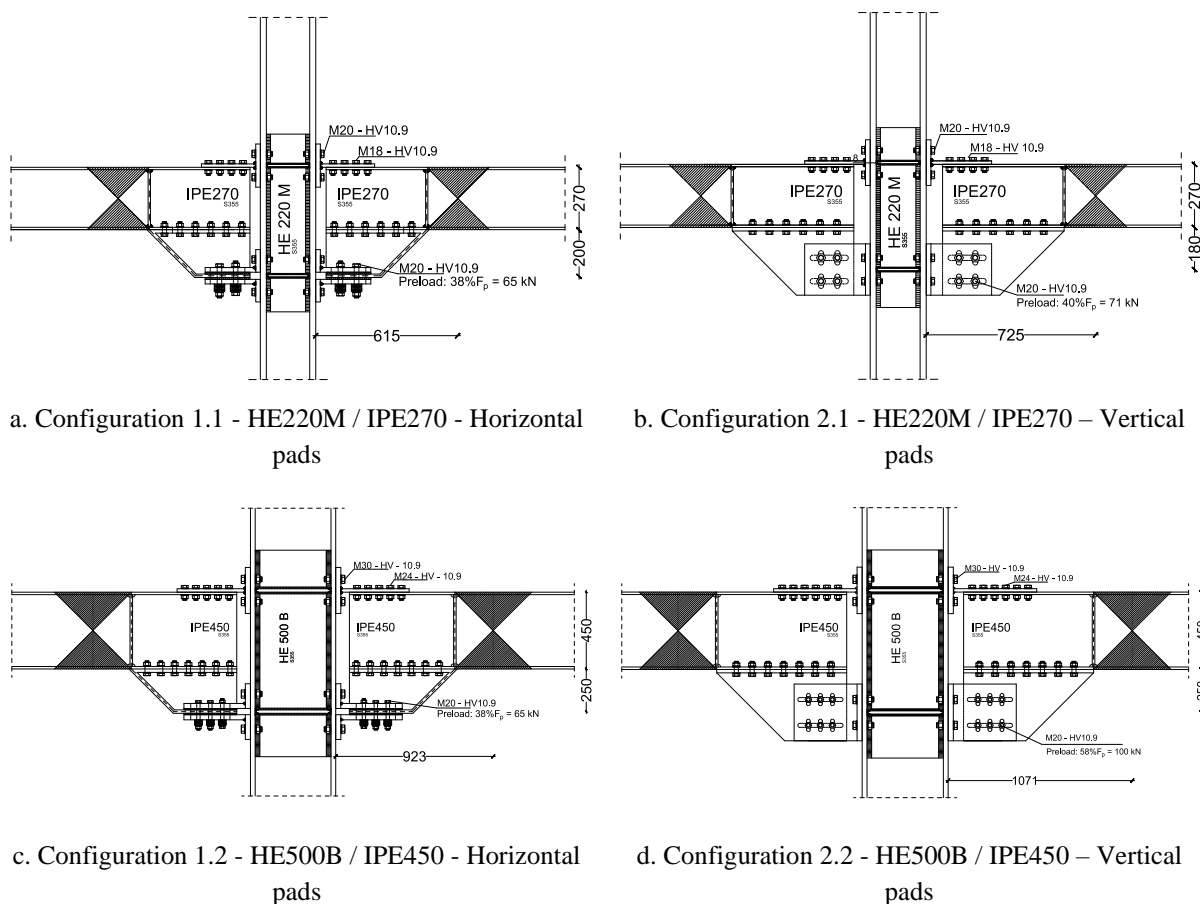


Figure 3.16 – Tested specimens (internal joints)

The bolts were preloaded using the torque method and the preload force to be applied in the bolt assemblies of the damper for each specimen was estimated based on the design procedure defined for the FREEDAM dampers developed on the basis of the experimental results presented in Chapter 2. The bolt preloading accounts for the average value of the friction coefficient and its statistical variability. The tested specimens are depicted in Figure 3.16. A scheme of the test setup is reported in Figure 3.17. The column is supported by a hinge at the bottom, while the beam ends are vertically supported allowing the lateral movement of the specimens. The cyclic load was applied to the top of the column by an actuator, following the AISC 341/2010 [37] seismic provisions, with a imposed maximum rotation equal to 50 mrad. The bending moment transmitted to the beam-to-column connections has been estimated with Eq. (3.1), multiplying the reaction at the beams ends, R (Figure 3.18), by the length between the beam constrain and the column flange (L_b in Figures 3.17 and 3.18), while the connection chord rotation has been estimated dividing the column horizontal displacement at level of the actuator, δ by the distance between the actuator and the column hinge (L_c in Figures 3.17 and 3.18).

$$M_t = R \times L_b \tag{3.1}$$

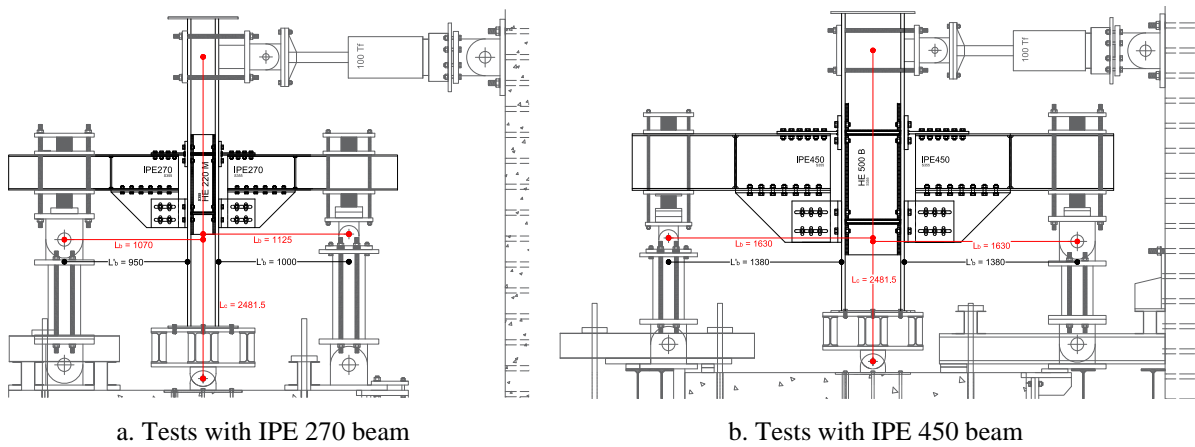


Figure 3.17 – Test layout for internal joints (dimensions in mm)

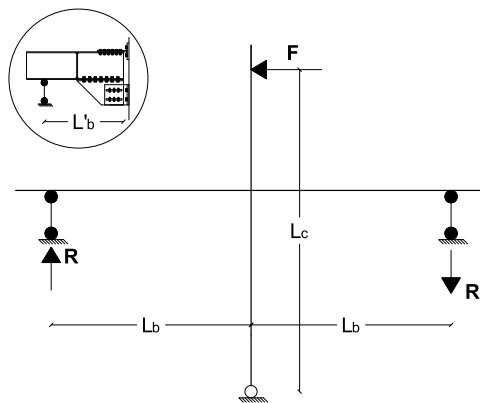


Figure 3.18 – Scheme for the calculation of the constraint reactions in the test layout

During the tests, force, displacements, deformations, torque and temperature were measured, which required the use of a significant amount of instrumentation, as exemplified in Figure 3.19 for one of the specimens. In detail, in each, the following instrumentation was used:

- 1 actuator - Force range: ± 900 kN; Displacement range: ± 150 mm; Frequency 1Hz with maximum displacement range $+7.02\text{mm}/-5.63\text{mm}$;
- 4 load cells - Maximum capacity 500kN in compression;
- 15 displacement transducers (DT in Figure 3.19) - LVDT (n.4 sensors range $\pm 25\text{mm}$; n.4 sensors range $\pm 50\text{mm}$);
- 1 static torque transducer - nominal torque 1000Nm;
- Thermocouple (TC in Figure 3.19);
- 4 annular load cells - capacity 350kN;
- 46 strain gauges, (*E* in Figure 3.19) - length 6mm, strain limit 5%.

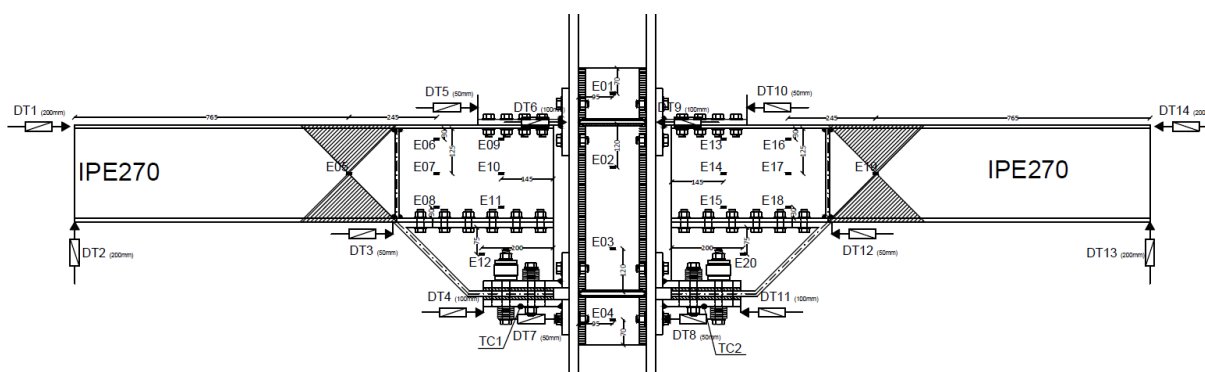
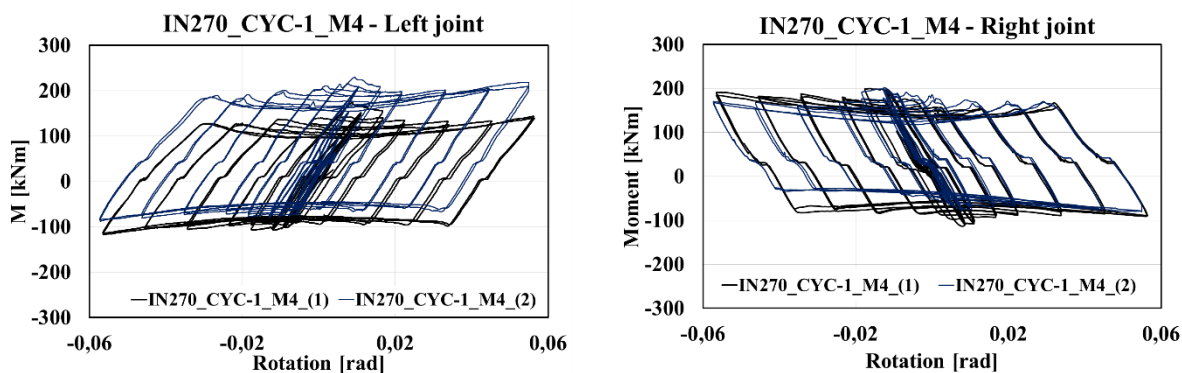


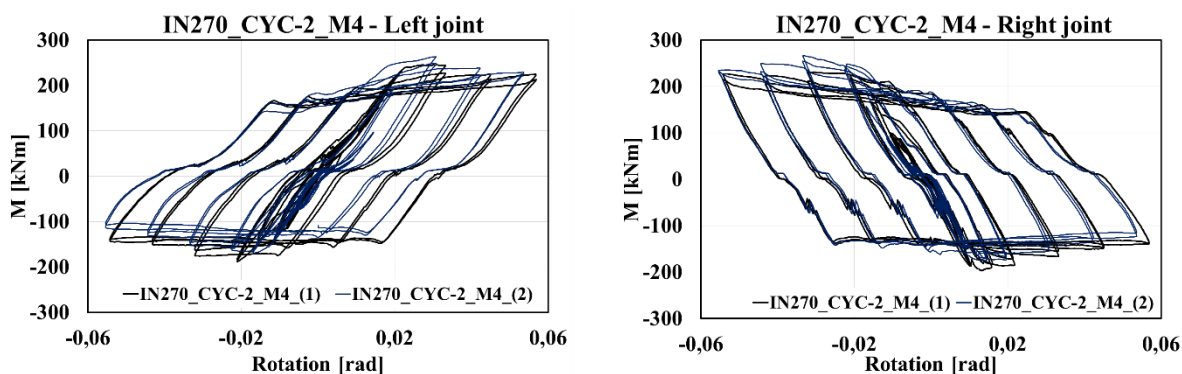
Figure 3.19 – Instrumentation

3.3.2 Results of the experimental tests

The moment-rotation curves of the different tested specimens are reported in Figure 3.20 for the specimens with IPE270 beam and Figure 3.21 for specimens with IPE450 beam, respectively. In these curves, when the positive bending moment occurs the upper part of the joint is in tension and the friction damper is in compression. Conversely, when a negative bending moment occurs the opposite situation is developed with the friction damper in tension and the bolted T-stub, connecting the top flange, in compression. In general, the results showed that these joints, independently of the beam size and the configuration of the damper, present a similar cyclic behaviour, with a rigid behaviour up to the achievement of the static friction resistance followed by quite stable hysteretic loops during the whole loading history. Besides, all the other joint components practically remained in the elastic range as exemplified for the L-stubs and T-stub components in Figure 3.22. Therefore, the use of the friction dampers is able to assure the dissipation of the energy avoiding the damage of all the other joint components. Observing the different moment-rotation curves is possible to notice some asymmetry between the response of the right and left joint due to some asymmetries of the experimental layout. In particular, it was ascertained that the rotation centres of the two pendulums located in correspondence of the beam ends were not perfectly aligned.



a. IN270_CYC 1_M4 (HE220M/ IPE270 - Horizontal pads)

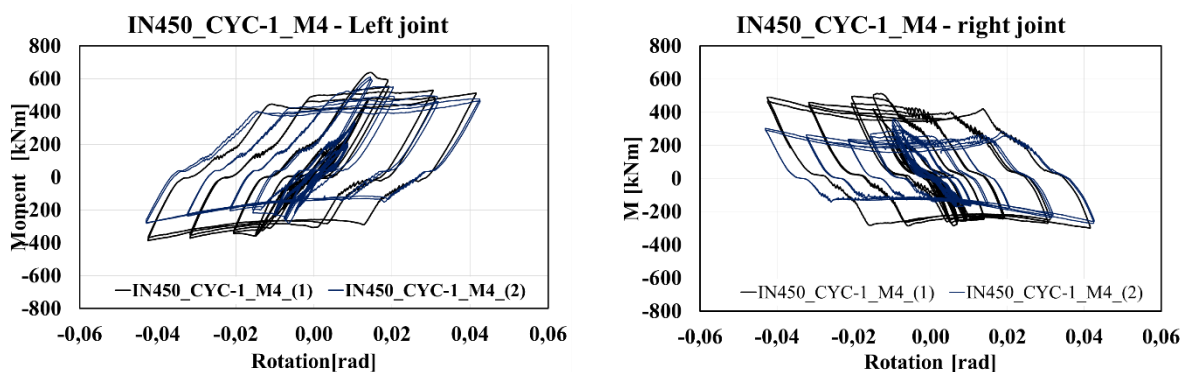


b. IN270_CYC-2_M4 (HE220M/ IPE270 - Vertical pads)

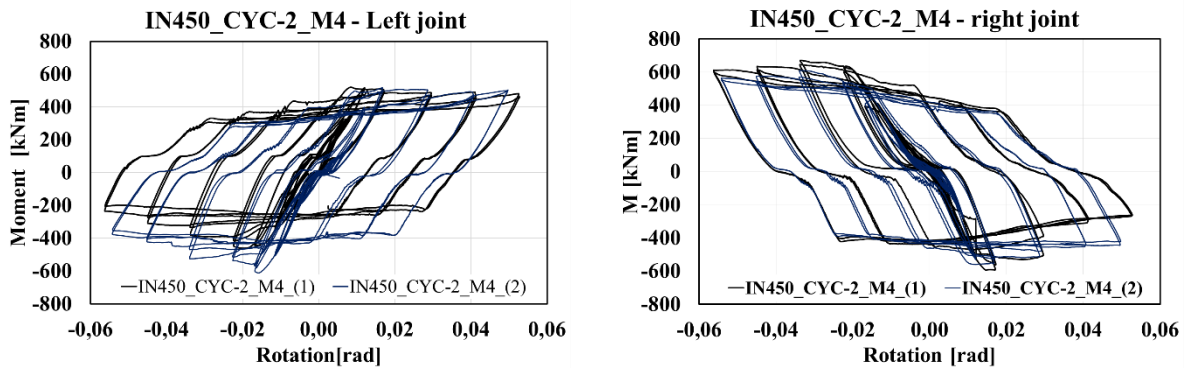
Figure 3.20 – Moment rotation curves – Specimens with smaller beam

Also, all the tested specimens exhibit an asymmetric behaviour under sagging and hogging response of the joints which is mainly due to the different deformations that the T-stub and L-stubs experience when subjected to tension compared to compression (Figure 3.23). This is usually more pronounced in the specimens with the horizontal configuration of the friction dampers as already pointed out by the experimental tests carried on on external joints.

Furthermore, the degradation of the friction resistance that is observed can be explained by the increase of the loss of preload force in the bolts during the cyclic loading history (Figure 3.24).

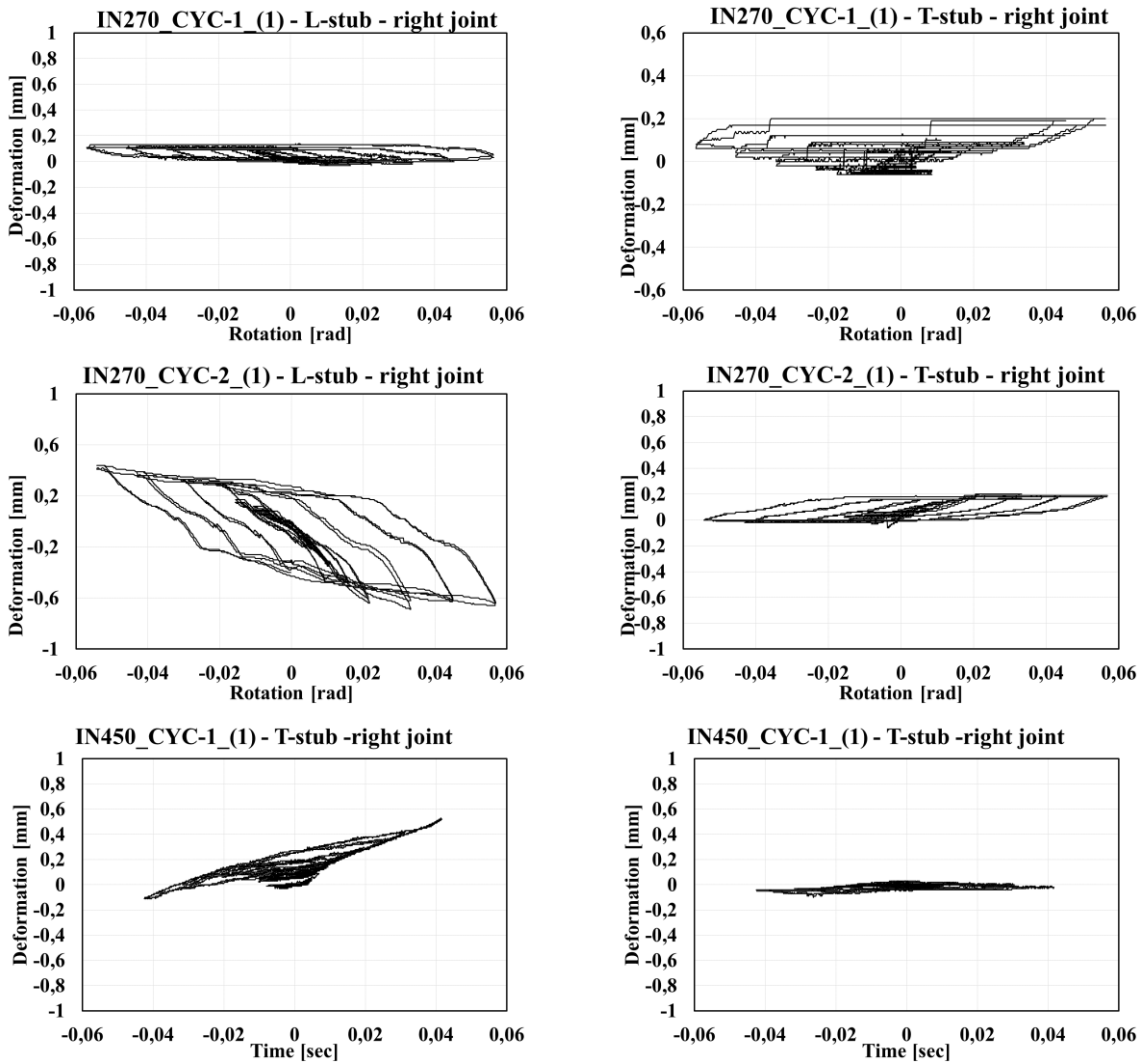


a. IN450_CYC 1_M4 (HE500B/ IPE450 - Horizontal pads)



b. IN450_CYC-2_M4 (HE500B/ IPE450 - Vertical pads)

Figure 3.21 – Moment rotation curves – Specimens with IPE 450 beam



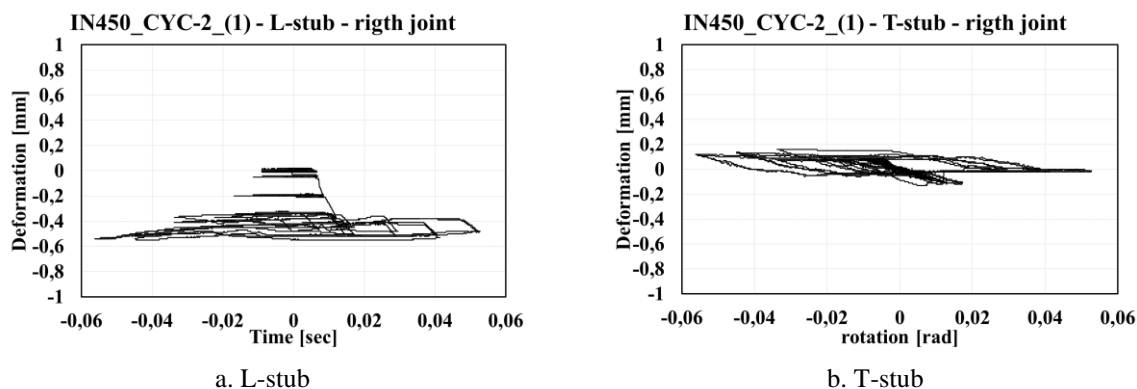


Figure 3.22 – Deformation of T-stub and L-stubs

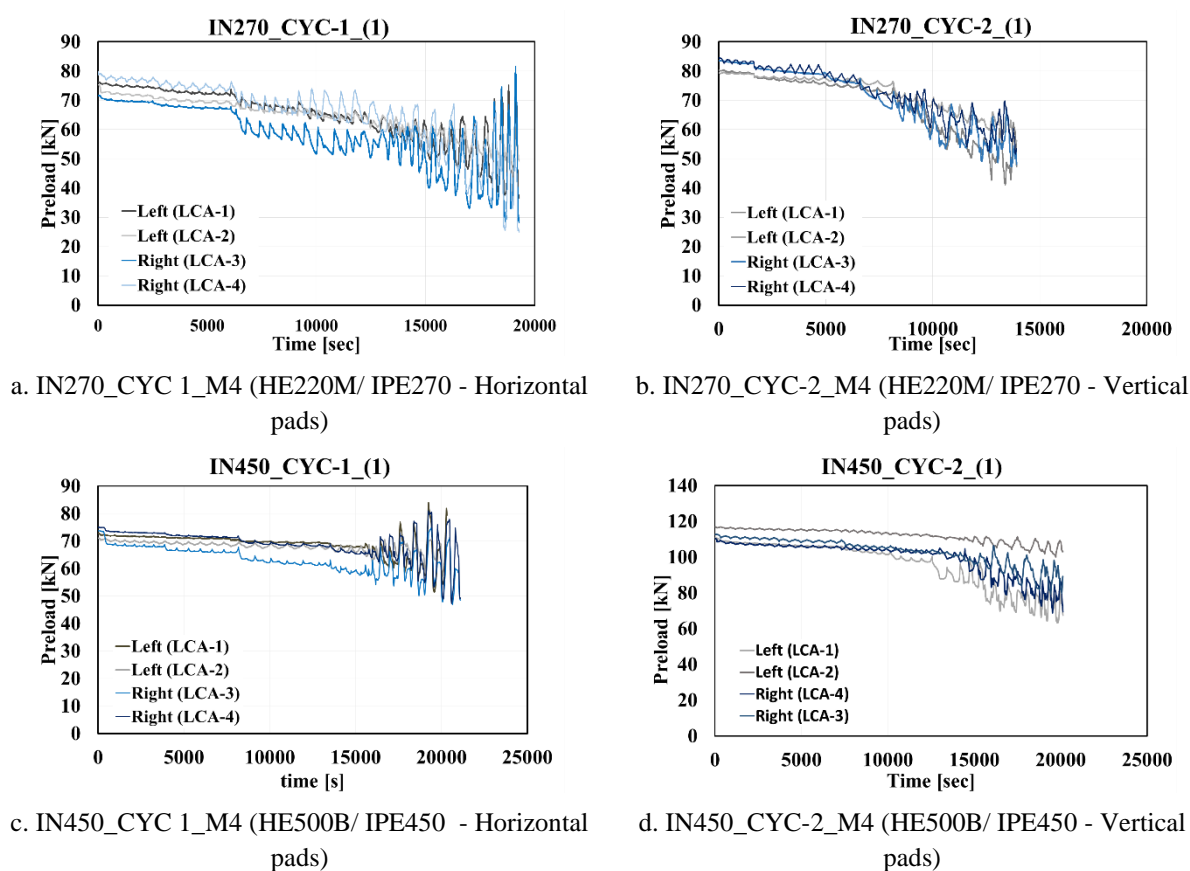


Figure 3.23 – Bolt forces

3.4 CONCLUSIONS

In this chapter, the results of the experimental programme devoted to the study of the seismic behaviour of beam-to-column connections equipped with two different configurations of friction devices have been reported. In particular, based on the main outcomes obtained in the previous tasks of the project (mechanical parameters of the friction materials, the role of the Belleville washers, influence of the loss of the bolts’ preload force), 16 beam-to-column connections have

been designed and tested at the STRENGTH Laboratory of the University of Salerno (external joints) and the University of Coimbra (internal joints).

Based on the results, the following conclusions can be drawn:

- Two different configurations have been tested: i) with the friction damper located in the horizontal plane parallel to the beam flange (HFC configuration) and ii) with the damper located to keep the friction pads aligned with the plane of the beam web, namely vertical configuration (VFC configuration). The difference from the point of view of the overall joint response is quite small, suggesting that both configurations can be effectively applied in practice. Nevertheless, the connection with the friction damper in the VFC configuration provided a more stable cyclic behaviour and lower asymmetry of the cyclic behaviour;
- In all the analyses cases the obtained behaviour was characterized by plumb hysteretic loops without any pinching, as expected, and with low degradation of energy dissipation capacity, strength and stiffness;
- The local measurements executed during the tests showed that, in agreement with the design criteria, the energy dissipation is provided only by the friction dampers, while the non-dissipative components (beam, T-stub, L-stubs) remain practically undamaged.

Therefore, the results of the whole experimental campaign constitute an effective pre-qualification of the FREEDAM beam-to-column connections and of the corresponding design criteria which will be illustrated in Part II “Design Handbook”, Chapter 7. In particular, the pre-qualified design procedure will specify all the technological details and requirements to be respected to obtain predetermined levels of performance, following the same methodology provided by the component method already codified in EC3 [38].

3.5 REFERENCES

- [1] V. Piluso, G. Rizzano: “Experimental analysis and modelling of bolted T-stubs under cyclic loads”, *Journal of Constructional Steel Research*, Vol. 64, pp. 655–669, 2008.
- [2] M. Latour, V. Piluso, G. Rizzano: “Experimental analysis of innovative dissipative bolted double split tee beam-to-column connections”, *Steel Construction*, Vol. 4, pp. 53-64, 2011.
- [3] M. Latour, V. Piluso, G. Rizzano: “Free from damage beam-to-column joints: Testing and design of DST connections with friction pads”, *Engineering Structures*, Vol. 85, pp. 219-233, 2015.
- [4] M. Latour, V. Piluso, G. Rizzano: “Experimental Analysis of Friction Materials for supplemental damping devices”. *Construction and Building Materials*, Vol.65, pp. 159-176, 2014.
- [5] M. Latour, G. Rizzano: “Monotonic Modelling, Cyclic Behaviour and Fatigue Life of Dissipative T-stubs”, ICASS 2009, Hong Kong, 2009.
- [6] M. Latour, V. Piluso, G. Rizzano: “Cyclic behaviour of Friction Dissipative Double Split Tee Connections”, STESSA 2011, Santiago de Chile, 2011.
- [7] C.E. Grigorian, T.S. Yang, E.P. Popov: “Slotted bolted connection energy dissipators”, *Earthquake Spectra*. Vol.9, No.3, pp.491-504, 1993.

-
- [8] A. Sato, K. Kimura, K. Suita, K. Inoue: “Cyclic test of high strength steel beam-to column connection composed with knee-brace damper and friction damper connected by high strength bolts”, Proceedings of the SEEBUS 2009. Kyoto, Japan, 2009.
- [9] E.M. Guneyisi, M. D’Aniello, R. Landolfo: “Seismic upgrading of steel moment-resisting frames by means of friction devices”, *Open Construction and Building Technology Journal*, Vol. 8(Suppl 1: M9), pp.289–99, 2014.
- [10] M. Taghi Nikoukala, S.R. Mirghader, K.M. Dolatshahi: “Analytical study of moment resisting frames retrofitted with shear slotted bolted connection”. *Journal of Structural Engineering*, Vol. 141, 2015:04015019.
- [11] V. Piluso, R. Montuori, M. Troisi: “Innovative structural details in MR-frames for free from damage structures”. *Mechanism Research Communications*, Vol.58, pp.146-156, 2014.
- [12] C. Christopoulos, A. Filiatrault: “Principles of Passive Supplemental Damping and Seismic Isolation”, Pavia: IUSS PRESS, 2006.
- [13] T.T. Soong, Jr B.F. Spencer: “Supplemental Energy Dissipation: State-of-the-Art and State-of-the-Practice”, *Engineering Structures*. Vol.24, pp.243-259, 2002.
- [14] G.A. MacRae, G.C. Clifton, H. Mackinven, N. Mago, J. Butterworth, S. Pampanin: “The sliding hinge joint moment connection”, *Bulletin of New Zealand society for earthquake engineering*, Vol.43, n.3, September 2010.
- [15] S. Ramhormozian, G.C. Clifton, G.A. MacRae: “The Asymmetric Friction Connection with Belleville springs in the Sliding Hinge Joint”, NZSEE Conference, 2014.
- [16] G.C. Clifton, J.W. Butterworth: “Moment-resisting steel framed seismic-resisting systems with semi-rigid connections”, 12th WCEE, Auckland, New Zealand.
- [17] G.C. Clifton, R. Zaki, J.W. Butterworth: “Damage-resistance steel framed seismic-resisting systems”, 13th WCEE, Vancouver, Canada, 2004.
- [18] J.C. Golondrino, G. MacRae, J. Chase, G. Rodgers, G.C. Clifton: “Velocity effects on the behavior of asymmetrical friction connections (AFC)”, 8th STESSA Conference, Shanghai, China, July 1-3, 2015.
- [19] H. Khoo, G.C. Clifton, J. Butterworth, G. MacRae, G. Ferguson: “Influence of steel shim hardness on the sliding hinge joint performance”, *Journal of Constructional Steel Research*, Vol.72, pp. 119-12, 2012.
- [20] S. Ramhormozian, G.C. Clifton, H. Nguyen, K. Cowle: “Determination of the required part-turn of the nut with respect to the number of free threads under the loaded face of the nut in fully tensioned high strength friction grip property class 8.8 bolts”, Steel Innovations Conference, 2015.
- [21] H. Khoo, G.C. Clifton, J. Butterworth, G. MacRae: “Experimental Study of Full-Scale Self-Centering Sliding Hinge Joint Connections with Friction Ring Springs”, *Journal of Earthquake Engineering*. September Vol. 17, pp. 972-997, 2013.
- [22] H. Khoo, G.C. Clifton, G. Macrae, S. Ramhormozian: “Proposed design models for the asymmetric friction connection”, *Earthquake Engineering & Structural Dynamics*. Vol. 44(8), pp.1309-1324, 2014.
- [23] H. Khoo, G.C. Clifton, J. Butterworth, G. MacRae, S. Gledhill, G. Sidwell: “Development of the self-centering Sliding Hinge Joint with friction ring springs”, *Journal of Constructional Steel Research*, Vol.78, pp.201-211, 2012.

-
- [24] J. Borzouie, G. MacRae, J. Chase: “Cyclic Performance of Asymmetric Friction Connections”, *The Bridge and Structural Engineer*, March 45(1), 2015.
- [25] G. Ferrante Cavallaro, A.B. Francavilla, M. Latour, V. Piluso, G. Rizzano: “Cyclic response of low yielding connections using different friction materials”, *Soil Dynamics and Earthquake Engineering*, 114, pp. 404-423, 2018.
- [26] G. Ferrante Cavallaro, A.B. Francavilla, M. Latour, V. Piluso, G. Rizzano: “Standardised friction damper bolt assemblies time-related relaxation and installed tension variability”, *Journal of Constructional Steel Research*, Vol.41, pp.66-81, 2018.
- [27] M. Latour, M. D’Aniello, M. Zimbru, G. Rizzano, V. Piluso, R. Landolfo: “Removable friction dampers for low-damage steel beam-to-column joints”, *Soil Dynamics and Earthquake Engineering*, Vol. 115, pp. 66-81, 2018.
- [28] G. Ferrante Cavallaro, A.B. Francavilla, M. Latour, V. Piluso, G. Rizzano: “Experimental behaviour of innovative thermal spray coating materials for FREEDAM joints”. *Composites Part B Engineering*, Vol. 115, pp.289-299, 2017.
- [29] M. Latour, V. Piluso, G. Rizzano: “Experimental analysis of beam-to-column joints equipped with sprayed aluminium friction dampers”, *Journal of Constructional Steel Research*, 146, pp. 33-48, 2018.
- [30] A. Lemos, L.S. da Silva, M. Latour, G. Rizzano: “Numerical modelling of innovative DST steel joint under cyclic loading”, *Archives of Civil and Mechanical Engineering*, 18 (3), pp. 687-701, 2018.
- [31] M. D’Antimo, M. Latour, G. Rizzano, J.F. Demonceau J.P. Jaspart: “Preliminary study on beam-to-column joints under impact loading”, *Open Construction and Building Technology Journal*, 12, pp. 112-123, 141, pp. 145-155, 2018.
- [32] M. Zimbru, M. D’Aniello, A. De Martino, M. Latour, G. Rizzano, V. Piluso: “Investigation on friction features of dissipative lap shear connections by means of experimental and numerical tests”, *Open Construction and Building Technology Journal*, 12, pp. 154-169, 2018.
- [33] E. Natri, M. D’Aniello, M. Zimbru, S. Streppone, R. Landolfo, R. Montuori, V. Piluso: “Seismic response of steel Moment Resisting Frames equipped with friction beam-to-column joints”, *Soil Dynamics and Earthquake Engineering*, 119, pp. 144-157, 2019.
- [34] V. Piluso, R. Montuori, E. Natri, A. Paciello: “Seismic response of MRF-CBF dual systems equipped with low damage friction connections”, *Journal of Constructional Steel Research*, 154, pp. 263-277, 2019.
- [35] F. Di Lauro, R. Montuori, E. Natri, V. Piluso: “Partial safety factors and overstrength coefficient evaluation for the design of connections equipped with friction dampers”, *Engineering Structures*, 178, pp. 645-655, 2019.
- [36] A.F. Santos, A. Santiago, G. Rizzano: “Experimental response of friction dampers under different loading rates”, *International Journal of Impact Engineering*, Vol. 132, pp.1-14, 2019.
- [37] ASCE 341-2010, *Seismic provisions for structural steel buildings*. Chicago, 2010.
- [38] CEN, 2005b. “Eurocode 3: Design of steel structures - Part 1-8: Design of joints”.

CHAPTER 4

FINITE ELEMENT MODELLING OF FREEDAM DAMPERS AND CONNECTIONS

4.1 INTRODUCTION

Steel Moment Resisting Frames (MRFs) are ductile and dissipative structural systems that can guarantee excellent seismic performance if properly designed and detailed. However, exploiting their large source of ductility implies accepting severe damage into main members to which large residual drifts are unavoidably associated. As a direct result, structures exhibiting an excellent seismic performance may require expensive refurbishment and repairing costs that might be impractical and unsustainable, thus leading to a more favourable demolition after severe earthquake.

The recent earthquakes occurred in New Zealand (e.g. starting from Christchurch 2010) clearly highlighted this issue. Therefore, research into new techniques to prevent or limit structural damage to buildings has gained relevance. The global tendency has been a shift towards the development and implementation of low damage seismic resisting systems in order to reduce the economic effects of earthquakes so that, any minor damage may be easily and cheaply repaired thus preventing the collapse of the building and guaranteeing that it quickly becomes operational. The main goal of FREEDAM project was to develop and validate novel connections equipped with friction dampers that prevent damage to the connected members and dissipate energy by means of the slippage into clamped steel elements and a friction pad.

A wide range of tests and analytical studies were carried out within the FREEDAM project and the relevant results are described in other chapters of this document (see Chapter 2 for the development of FREEDAM dampers and Chapter 3 for the development of FREEDAM connections and Chapter 6 for pseudo-dynamic seismic testing). However, based on a critical review of the state of the art the main aspects characterizing the joint performance have been identified, and in order to characterize the local response of the devices as well as its interaction with the other parts of the connection as well as the structural members a comprehensive and extensive parametric study was carried out on the basis of finite element simulations. Indeed, a wide range of studies demonstrated that finite element analyses can be effectively used to predict the nonlinear behaviour of bolted joints giving an accurate description of the loading paths in the joint components.

Therefore, within the project two different numerical programmes were performed intending, on one hand, to fully explore the behaviour of the friction interfaces and, on the other hand, analyse the results when applied to dissipative joints in order to explore their local response.

The objectives of this study are the following:

- Development of a modelling strategy to simulate complex friction problems. The proposed approach is able to describe the friction behaviour of the damper installed in the bolted connection.

- Modelling of the beam-to-column connections equipped with the friction device, subjected to monotonic and cyclic loading conditions.
- Characterizing the mechanical response at local level to develop effective design rules.

All these issues are described and discussed in this Chapter, where the results of all finite element simulations performed within FREEDAM project are summarised. The chapter is organized in three main parts, namely: 1) the description and discussion of the modelling of FREEDAM dampers and relevant features of the local behaviour; 2) the description and discussion of the seismic response of FREEDAM beam-to-column joints; 3) discussion of possible design provisions resulting from the discussion of the outcomes obtained from finite element simulations.

4.2 FE MODELLING OF FREEDAM DAMPERS

The primary objectives of finite element analyses were to evaluate the effects of the mutual interaction between bolts and the effects of the load distribution under the bolt heads.

Once validated the models against the experimental tests, parametric simulations were carried out to investigate the monotonic and cyclic performance of the lap shear specimens that were designed to test the response of friction dampers. FE simulations allowed assessing the friction coefficients of the eight different materials used as interfaces evaluating also their ability to withstand cyclic loading histories in terms of energy and strength degradation. The models were compared against the experimental results, showing their accuracy to simulate the behaviour of lap shear friction connections, showing also the influence of different modelling approaches over the simulated data.

4.2.1 Modelling assumptions

The Finite element models (FEMs) were developed using ABAQUS v.6.14 [2]. The geometries of the numerical models were nominally identical with those of the specimens tested in FREEDAM project (see Fig. 4-1). In particular, the sub-assemblies of FFD with different number of disc springs such as 9, 6, 3, and 0 were modelled, and the geometry of fixed part was not included as it has no influence on the results in order to decrease computational cost (see Figure 4-1b-i).

The solid finite element type C3D8I (an 8-node linear brick, incompatible mode) was adopted for all steel plates and high strength bolts. The choice of FE element was based on its capacity to avoid the shear-locking phenomenon that can significantly affect the initial stiffness of connection, unlike the C3D8R element.

The steel properties for plates were modelled considering the nominal elastic properties, while the non-linear behaviour was modelled by means of the von Mises yield criteria. Plastic hardening was represented using a nonlinear kinematic and isotropic hardening. Metal plasticity was considered for the coating layer M4 as well. The true stress-true strain curves adopted for material M4 and steel plates are given in Fig. 4-2.

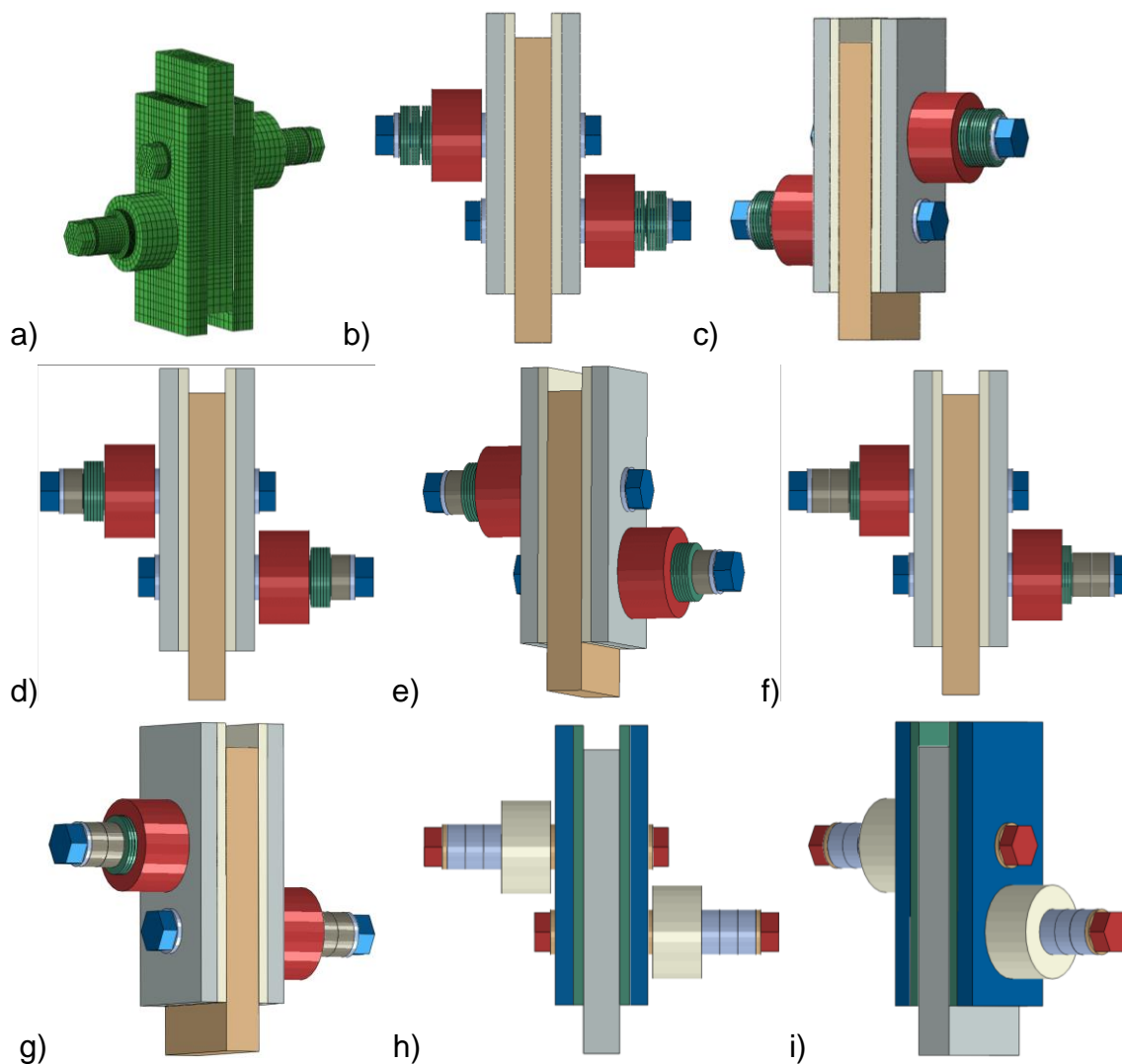
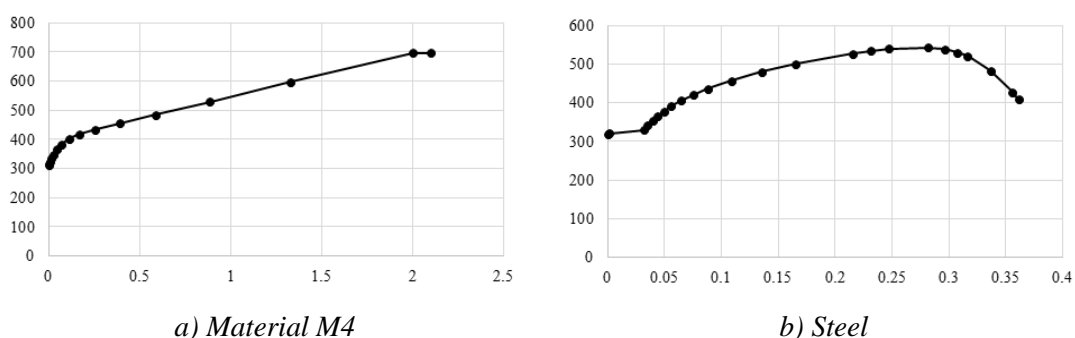


Figure 4.1 - Generated FE models of lap shear specimens: a) example of mesh; b-i) sub-assemblies with different number of disc springs



a) Material M4

b) Steel

Figure 4.2 - True stress – strain nonlinear properties

The bolts were modelled by meshing a solid cylinder having the nominal circular gross area of the bolt and the true stress – true strain curves were derived from [3, 4].

All possible interactions (bolt head to outer plate, bolt shank to corresponding bolt hole, plates in contact) are modelled by means of “Surface to Surface contact” with finite sliding formulation.

Both tangential and normal behaviour are considered, the former using a “Penalty” friction formulation together with “slip-rate-dependent data” scaled for explicit analyses, while the latter using the “Hard-Contact” formulation. “Tie” constraints were used to model the bond between the M4 coating layer and the steel shim.

The bolt clamping was modelled using the “Bolt load” feature available in the FE software and the design preload value was imposed. The clamping was applied in an individual step prior to the application of the loading protocol.

The external restraints were simulated by slaving to reference points (RP) the nodes belonging to the end portion of the internal plate of the device. The displacement history was imposed on the RP located at one end of the device. The loading protocol and number of cycles of Analyses were equal to those experimentally imposed (e.g. see Fig. 4-3).

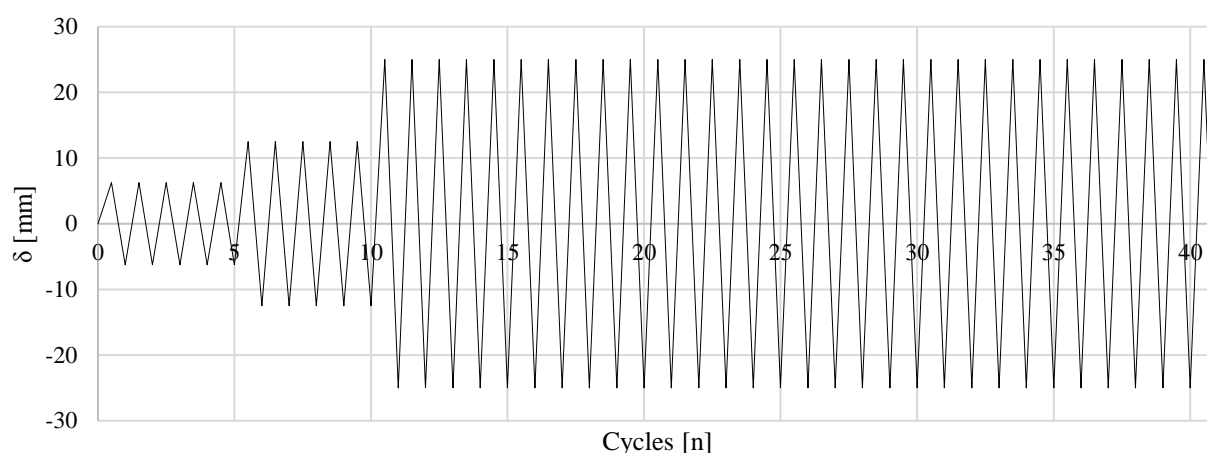


Figure 4.3 – Displacement history of series UT-NV

The experimental tests carried out in Salerno on the lap shear specimens with and without disk springs clearly highlighted the large amount of heating developed due to the friction at large cumulated displacement. Since the heat conducted by friction may influence the hysteretic behaviour of the friction joints due to thermal expansion coupled thermo-mechanical analyses have been carried out. In order to reproduce the temperature variation and propagation due to heating induced by friction, the thermal properties were also taken into account. The Specific Heat “c” was set equal to $4.52E^{+8}$ mJ/ton/°C, the Thermal Expansion “ α_L ” was assumed equal to $1.26E^{-5}$ mm/mm/°C and the Thermal Conductivity “k” equal to 48 mW/mm/ °C.

Both implicit quasi static and explicit coupled thermo-mechanical dynamic analyses were carried out in order to investigate on the computational efficiency and accuracy of these types of analysis. An example showing the difference between the type of analysis is shown in Fig. 4-4. It should be noted that both types of analysis are effective to simulate the overall behaviour of the friction connections. Generally, implicit analyses provide more reliable results than explicit ones. On the other hand, explicit analyses provide advantages in terms of computational efficiency. Table 4-1 summarizes the average computational time necessary to carry out each type of analysis. As it can be easily recognized, the implicit solver requires a heavier computational effort.

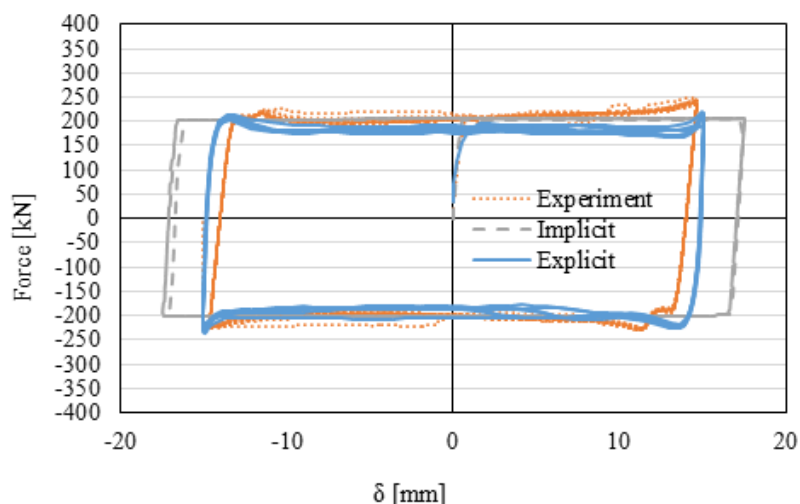


Figure 4.4 - Experimental vs both Implicit and Explicit Force-Displacement curves

Table 4.1: Comparison between implicit and explicit analysis

FE Solver	Average Duration of Analysis	Comment on Results
Implicit	24 hours	Both FE solvers are successful to demonstrate results analogous to experimental ones
Explicit	6 hours	

Table 4-2 reports the types of specimens with the corresponding number of disk springs (DS). The geometry of the fixed part of the specimens was disregarded in order to decrease computational demand, as it has no influence on the results (see Fig. 1b-i).

Table 4.2: ID of specimens with disk springs

No. of DS	M6	M4
9 DS	NV 21	NV 17
6 DS	NV 22	NV 18
3 DS	NV 23	NV 19
0 DS	NV 24	NV 20

The numerical results are discussed hereinafter on the following outputs: i) Sliding Force [kN] - Displacement [mm] / Time [s]; ii) Total Preload Magnitude [kN] - Displacement [mm]; iii) Temperature [kN] - Displacement [mm] / Time [s].

4.2.2 Validation and discussion of results

4.2.2.1 Influence of disk springs in lap shear joints with M6 friction material [NV-21-22-23-24]

Figure 4-5 summarizes the main results of the local behaviour of lap shear joints with M6 material. In particular, Fig.4-5a shows for model NV-21 that the temperature in the assembly elements (i.e. both bolts and plates) increases with cumulative sliding.

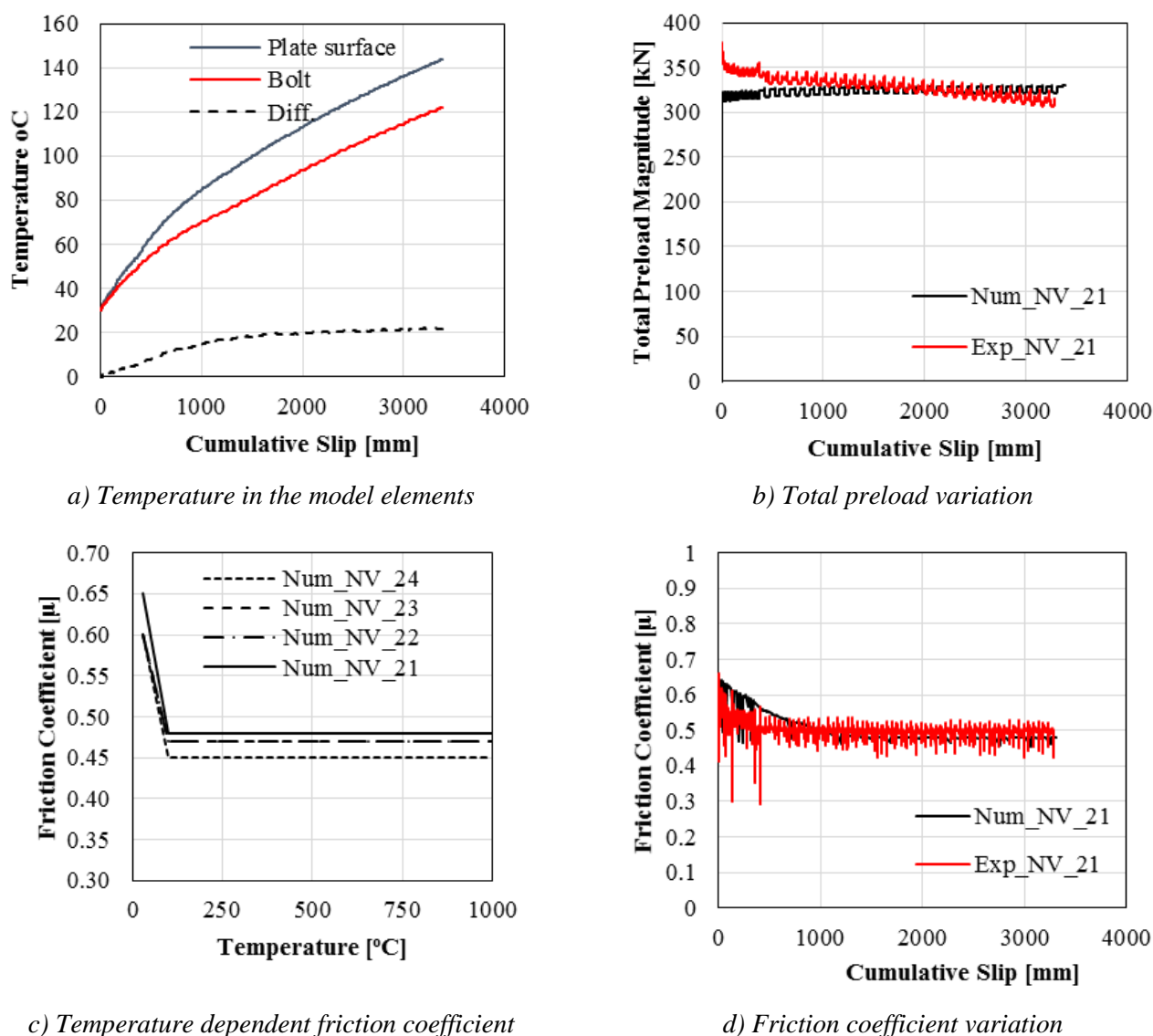


Figure 4.5 – Sliding vs displacement response of Models NV-21-22-23-24

As expected, the energy dissipated by friction is converted to thermal energy. It was observed that after 3000mm of cumulative slip, the average temperature difference between plate surface and bolt is about 15 °C to 20°C for all models. Even though thermal properties are modelled as mentioned before, it seems that the preload forces have not been affected significantly and they remain constant in the models (see Fig. 4-5b), mostly because the thermal expansion occurs in both the plates and bolts. The partial loss of friction coefficient was modelled in the FE models using temperature-dependent friction laws calibrated based on experimental results (see Fig. 4-5c). As temperature increases because of continuous sliding of plates, friction coefficient

decreases accordingly, and as possible to observe in Fig. 4-5d, the models satisfactory predict these phenomena.

Figure 4-6 shows the comparison between the experimental and numerical curves in terms of sliding force and displacement. As it can be easily observed, the FE models are fully capable to reproduce the overall hysteretic curves, thus providing accurate results.

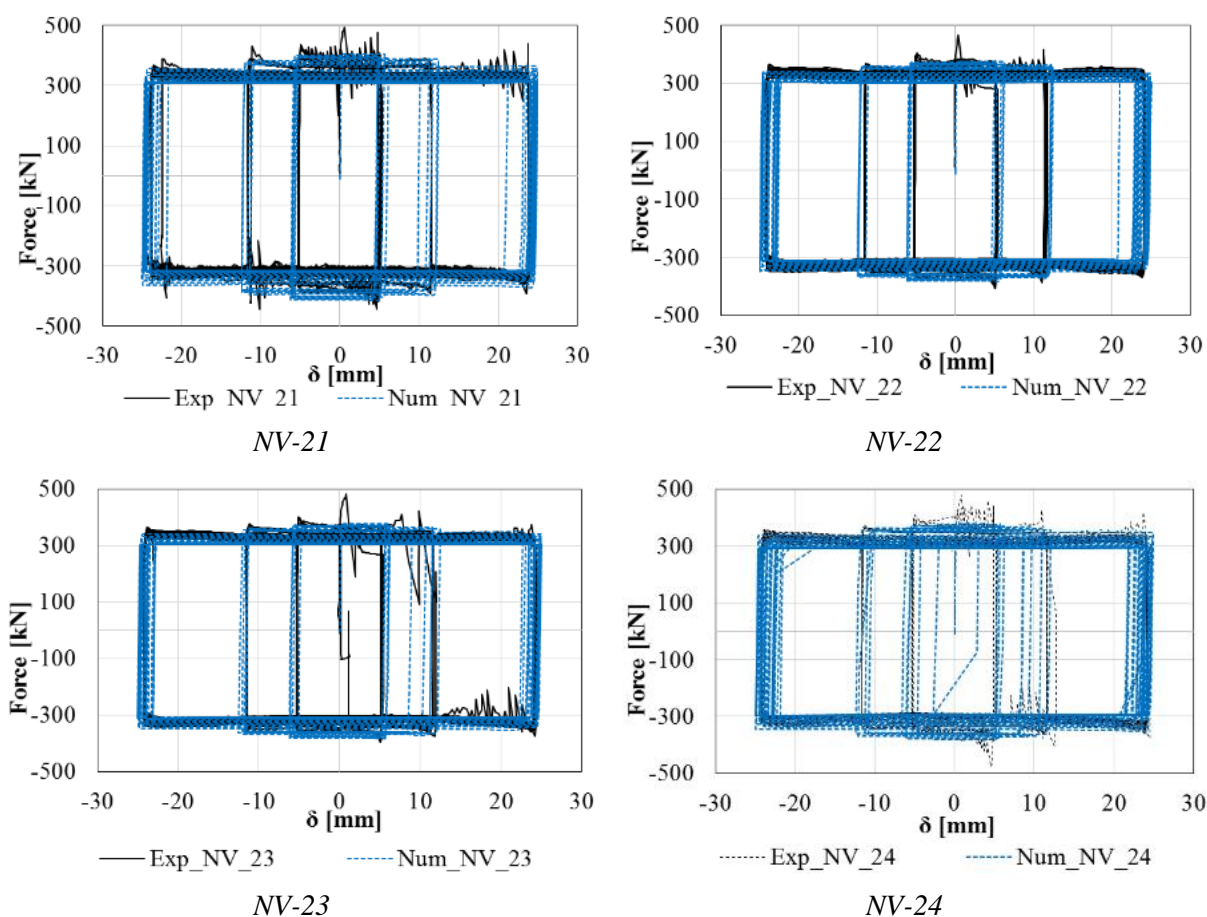
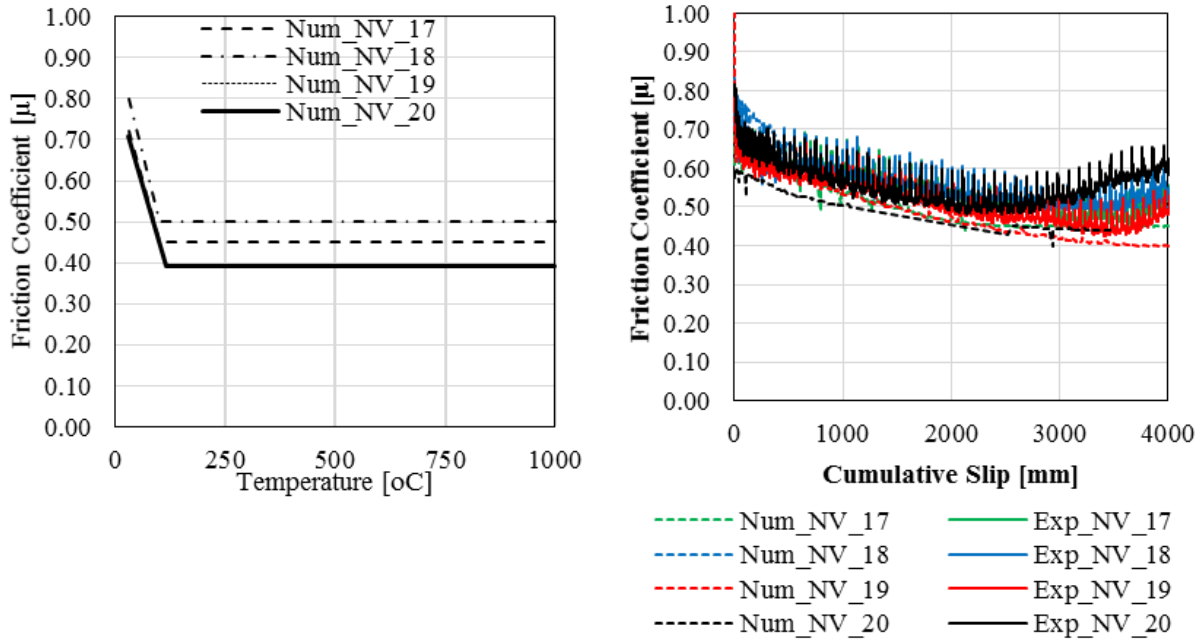


Figure 4.6 – Simulated vs test response of lap shear joints with M6 material [NV-21-22-23-24]

4.2.2.2 Influence of disk springs in lap shear joints with M4 material [NV-17-18-19-20]

As observed during the experimental tests, M4 material exhibits the greater friction degradation during the slip, thus resulting in a more complex modelling. Also in this case no significant differences in terms of loss of preload was observed between the models with varying number of DS. As temperature increases because of continuous sliding of plates, friction coefficient decreases according to given temperature-dependent input data (see Fig. 4-7a). Moreover, there is no direct relation in the number of disc springs and degradation of friction coefficients (see Fig.

The 4-7b) sliding force – displacement curves are depicted in Fig. 4-8, where it can be recognized the distinct degradation of the slip capacity cycle by cycle.



a) Temperature dependent friction coefficient

b) Friction coefficient – displacement curves

Figure 4.7 – The friction coefficient curves for lap shear joints with material M4 [NV-17-18-19-20]

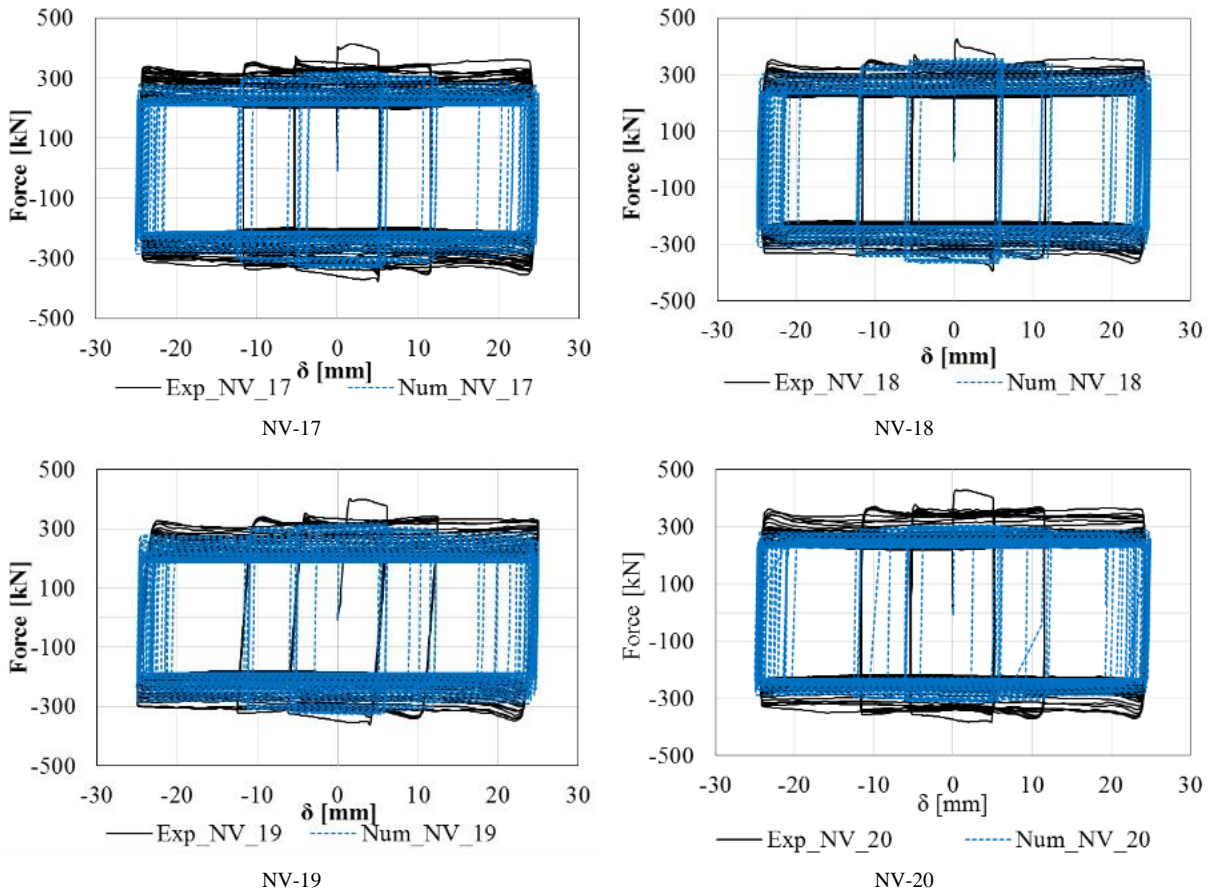


Figure 4.8 – The friction coefficient curves for lap shear joints with material M4 [NV-17-18-19-20]

4.2.2.3 Pressure Dependency of Friction Coefficients

In order to investigate pressure dependency of friction coefficients, contact area information and normal forces due to contacts for each interaction are recorded from the FE simulations. With the help of those, it is possible to establish a relation between the measured frictional force from experiment, the contact pressure and its associated area of contact by means the following expression:

$$F_f = \mu(F_{pre}) \cdot F_{pre} \approx \int_A \mu(P) \cdot P \cdot dA \approx \sum_i \mu(P_i) \cdot P_i \cdot A_i \approx \mu(F_N) \cdot F_N \quad (4.1)$$

where:

F_f = Frictional force measured during experimental test

F_{pre} = normal force measured during experimental test (pretension)

F_N = normal force obtained from FE simulation

P = contact pressure obtained from FE simulation

A = contact area obtained from FE simulation

$\mu(F_{pre})$ = friction coefficient calculated from experimental results

$\mu(F_N)$ = friction coefficient generated from relationship between experimental results and FE simulation

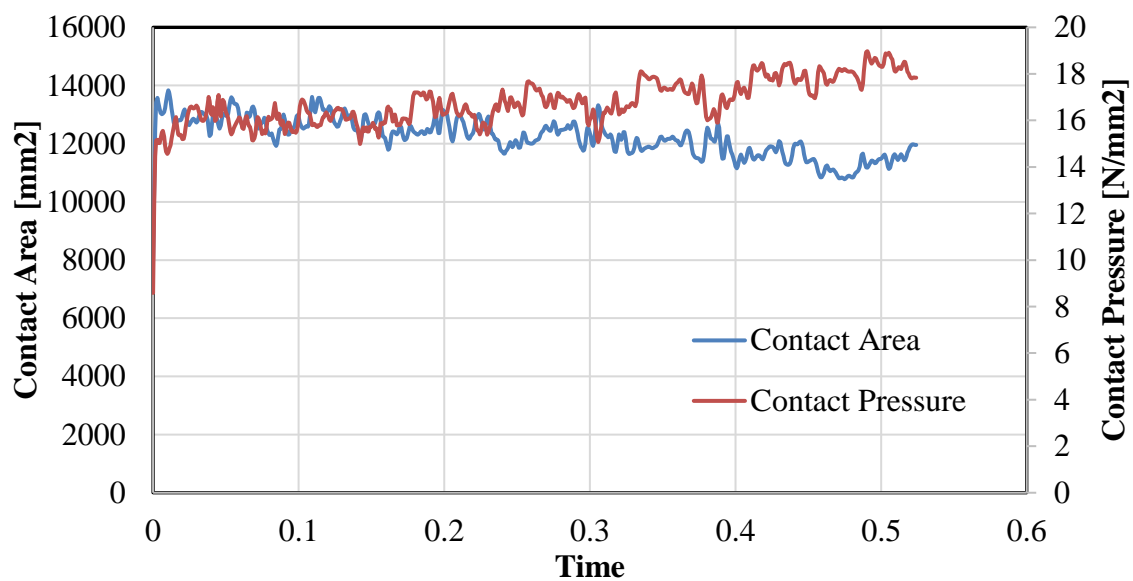


Figure 4.9 – Contact area vs. Pressure.

As it can be seen at Fig. 4.9, with the overall motion regardless of pulling out or pushing, contact area is slightly decreasing while contact pressure is increasing.

In addition to this, actually no matter what the amount of preloading magnitude is, namely contact pressure and measured contact areas are always following the same trend at the simulations of uniaxial experiments of FFD as can be seen at Fig. 4.10 and 4.11. This situation also shows that materials are rigid enough not to be affected by contact pressure. This slight decreasing of contact area might be in consequence of elastic/plastic strain of the surfaces or bending of plates in a small extent.

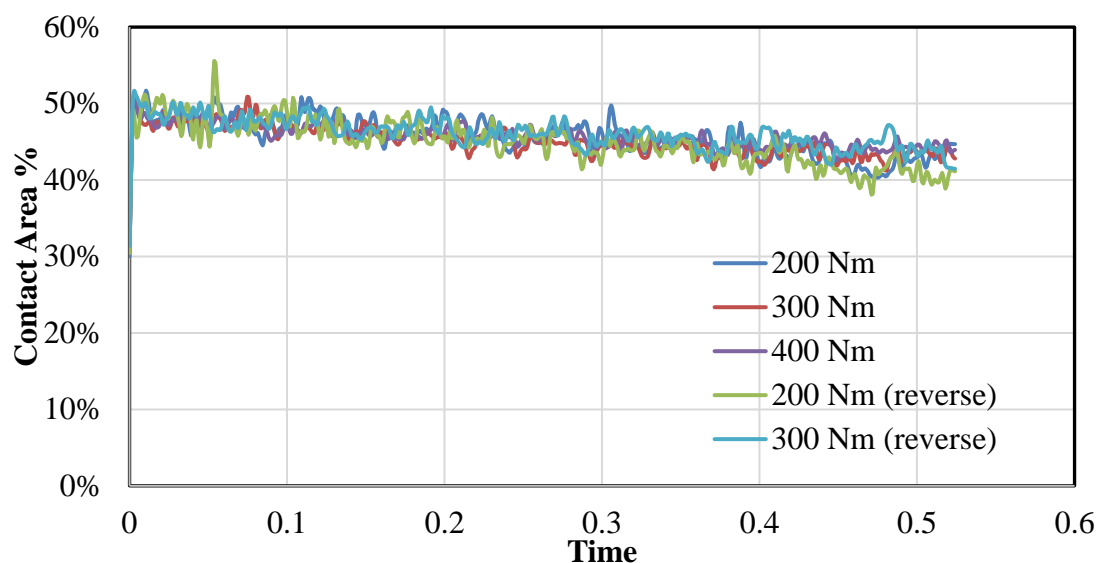


Figure 4.10 – Contact Area Percentages for Different Preload Torques.

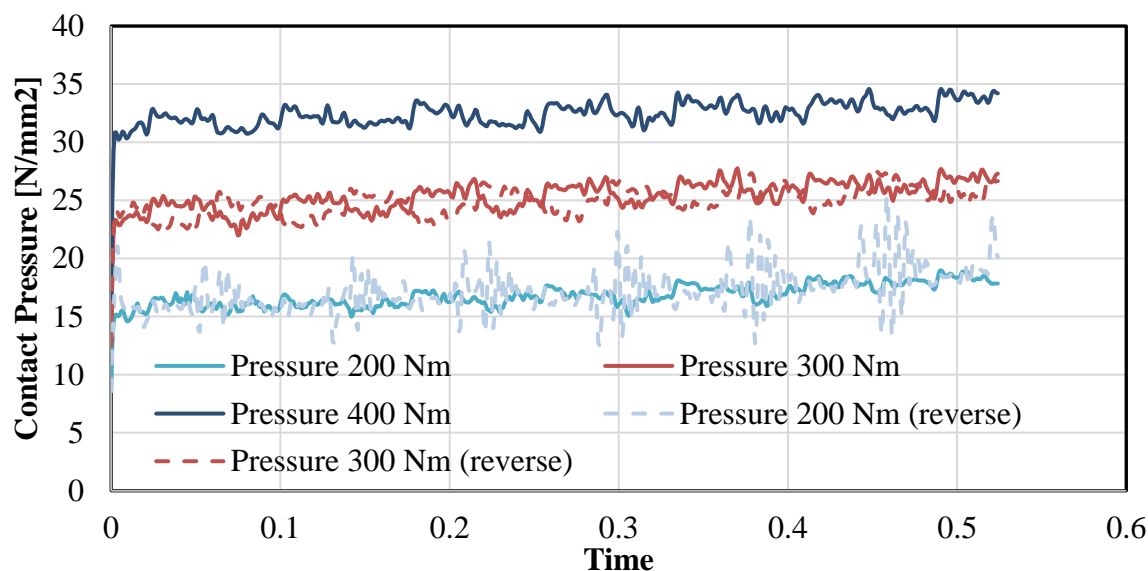


Figure 4.11 – Contact Pressures for Different Preload Torques.

However, experiments indicated that higher preload magnitudes result in lower friction coefficients because of tribological characteristic of friction layer, and also with the continuous motion, very slight degradation of friction was observable, which is might be due to losing contact area and so increase of pressure, which is also seen during analyses.

4.3 FE MODELLING OF FREEDAM CONNECTIONS

The FE analyses on FREEDAM connections were devoted to investigate the local behaviour of the assemblies in order to evaluate the effects of the transfer mechanism from the beam to the column and the local redistribution of forces and deformations within the bolts of the devices.

Once validated the models against the experimental tests, parametric simulations were carried out to investigate the monotonic and cyclic performance of the joints equipped with friction dampers.

4.3.1 Modelling assumptions

The experimental tests were used to validate the finite element (FE) models developed using Abaqus v 6.14 [2]. The quasi-static analyses were performed by employing the Dynamic Implicit solver. The geometrical characteristics of the experimental assemblies were replicated in the FE software by modelling solid parts meshed using the C3D8R finite element (an 8-node linear brick with reduced integration). Both geometrical and mechanical nonlinearities were accounted for. The experimental tests on the large beam-to-column assemblies have suffered unexpected slippage in the connections between the column and the setup and therefore, the deformability source was taken into account in the numerical model. Figure 4.12 depicts the general model shape and Figure 4.13 shows the average material properties obtained experimentally.

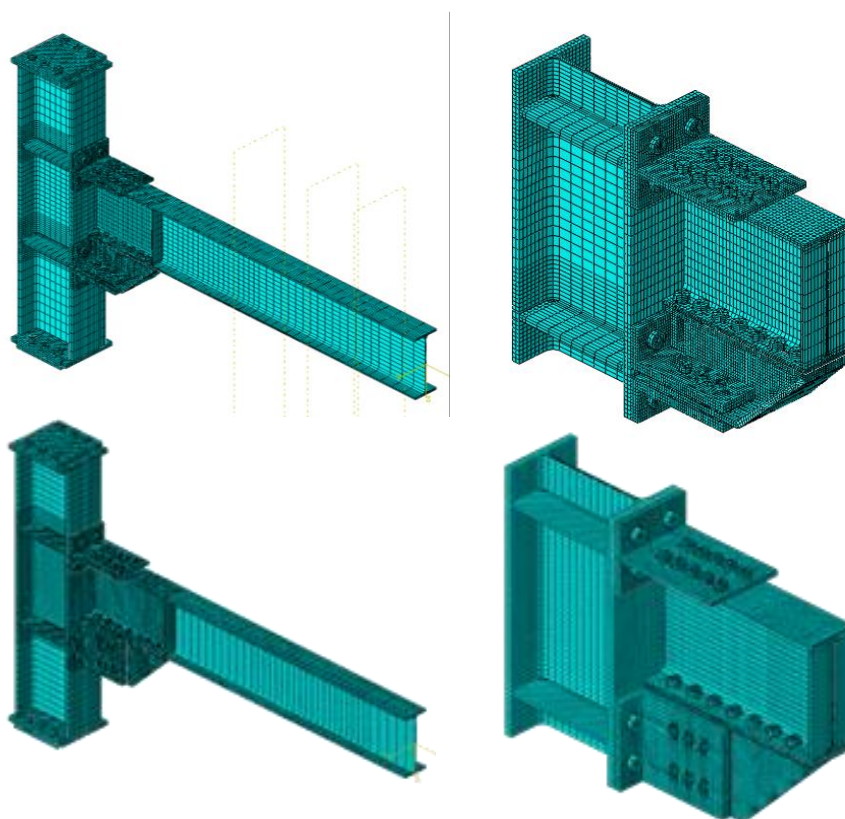
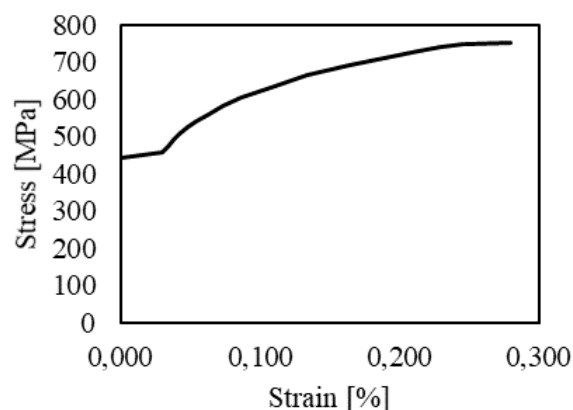


Figure 4.12 – Features of FE model of beam-to-column joints with FREEDAM dampers

The steel material properties were modelled based on the coupon tests performed in the laboratory as part of the experimental campaign, namely the yield stress was set equal to 380 MPa for beams, 427 MPa for columns and 443MPa for both L-stub and T-stubs. The elastic modulus was assumed equal to 210000MPa and Poisson's coefficient equal to 0.3.

The nonlinear branch of the constitutive law was implemented using a half cycle input method and assuming both nonlinear kinematic and isotropic plastic hardening, as described by [5-10]. The bolts were modelled as shown by [3,4].



Material properties

Figure 4.13 – average stress-strain curve of steel S355

The model parts in contact, such as the bolts and plates, were assigned with interactions modelling both the Normal Behaviour to avoid overclosure (by means of the “Hard Contact” option) and Tangential behaviour to define the relative sliding (by employing the Coulomb friction law). In addition, to simulate the partial loss of the friction coefficient due to the smoothing of the superficial roughness of the friction pad, the temperature-dependent friction laws shown in Section 1.2 was used, thus friction coefficient decreases with the increase of temperature because of continuous sliding of plates. The reference friction properties are presented in Table 4.3. The simulations shown hereinafter were performed assuming the 5% dynamic percentile was used for the numerical simulations.

Table 4.3: Friction material properties

Friction coefficient	5% Percentile	95% Percentile
	$\mu_{5\%}$	$\mu_{95\%}$
Static	0.69	0.84
Dynamic	0.53	0.65

Since no plastic deformations are expected in the welded components, tie constraints linking together surfaces in contact have been used to replicate in a simplified manner the presence of full penetration welds.

The analyses were performed considering two loading steps: (i) bolt clamping and (ii) displacement history application.

The boundary conditions of the joints have been accurately simulated to reproduce those used during the tests. In addition, the beam was laterally restrained with out-of-plane restraints located in the same sections of the experimental setup. The AISC 341 [11] loading protocol up to 5% interstorey drift ratio was applied at the beam end consistently with the test procedure.

4.3.2 Validation and discussion of results: external joints

The adopted modelling assumptions effectively simulate both the global and the local response of the tested joints, as it can be observed in Fig. 4.14 and 4.15 respectively.

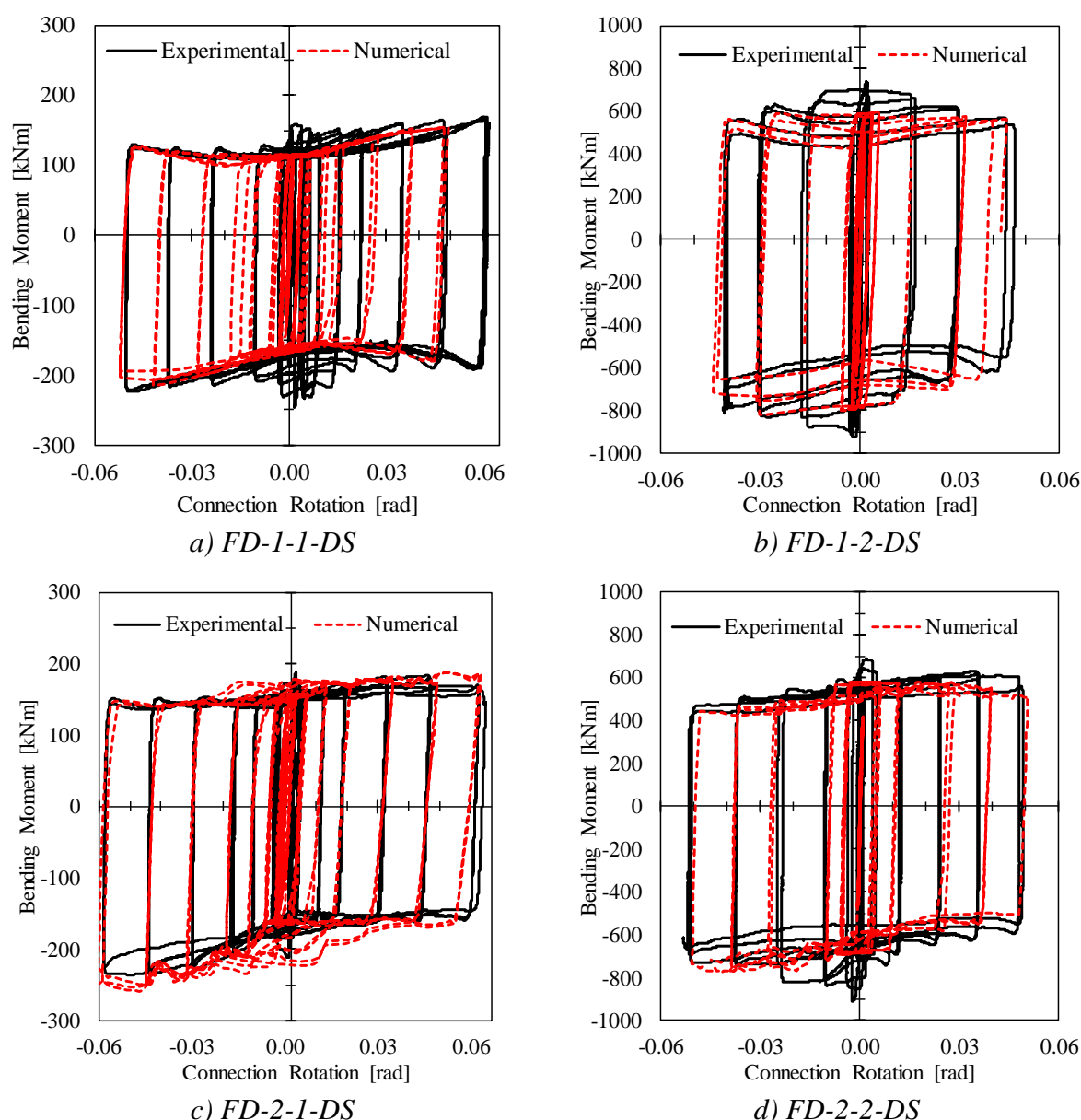


Figure 4.14 – Experimental vs numerical results in terms of Bending Moment – Connection rotation

Since the transition from the static to the dynamic friction was not modelled, the response of the joint during the initial cycles are not accurately replicated. However, this inaccuracy disappears at increasing the number of cycles.

During the experimental campaign no damage was observed in the steel elements. However, the numerical analyses show some concentrations of slight plastic damage, depicted in terms of equivalent plastic strain (PEEQ) in Fig. 4.15, at the base of the web of the upper T-stub (where the center of rotation is located), and either at the bases of the L-stubs, at the top web-flange area of the beam underneath the T-stub and in the shear bolts of the device. Furthermore, plastic deformations can be observed in the shanks of the bolts in the friction device. Indeed, the horizontal damper configuration induces shear type bending effects in the shanks with two bearing contacts in all bolts of the device. On the contrary, the bolts in the vertical damper have one bearing zone at mid-length of the clamped shank, which leads to larger local plastic strain

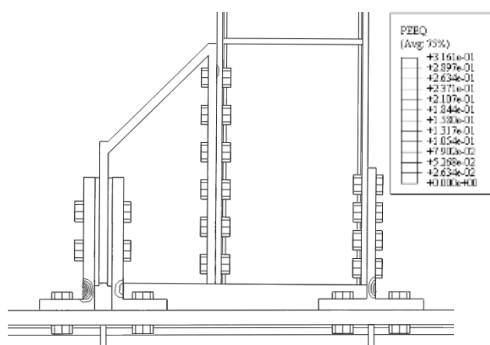
(see Fig. 4.16). In addition, in this second case the bolts close to the column face do not exhibit plastic strains.



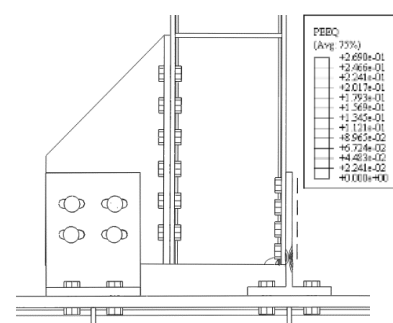
a) Experimental joint FD 1-1



b) Experimental joint FD 2-1

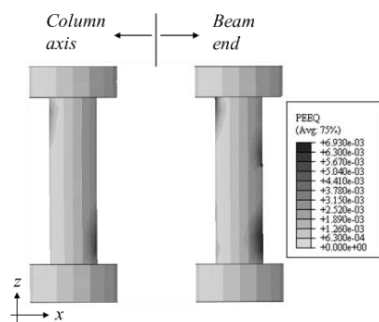


c) PEEQ distribution for model FD 1-1

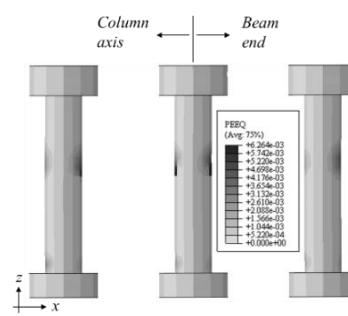


d) PEEQ distribution for model FD 2-1

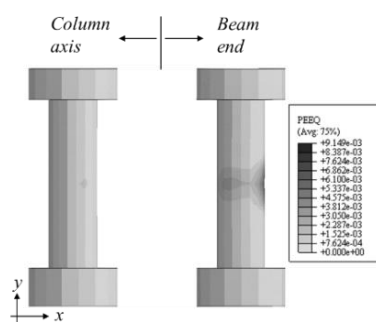
Figure 4.15 – Experimental vs. numerical models after cyclic test up to 5%



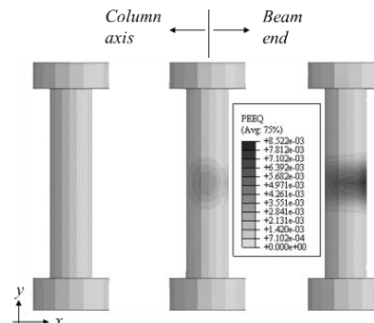
a) FD-1-1



b) FD-1-2



c) FD-2-1



d) FD-2-2

Figure 4.16 – Equivalent plastic damage (PEEQ) in the damper bolts

4.3.3 Validation and discussion of results: internal joints

Internal joints (hereinafter also referred in the plots as “X” joints) exhibit almost the same behaviour of external joints (hereinafter also referred in the plots as “T” joints), since the column web panel remains in elastic range and the non-linear mechanism develops in the Freedom dampers.

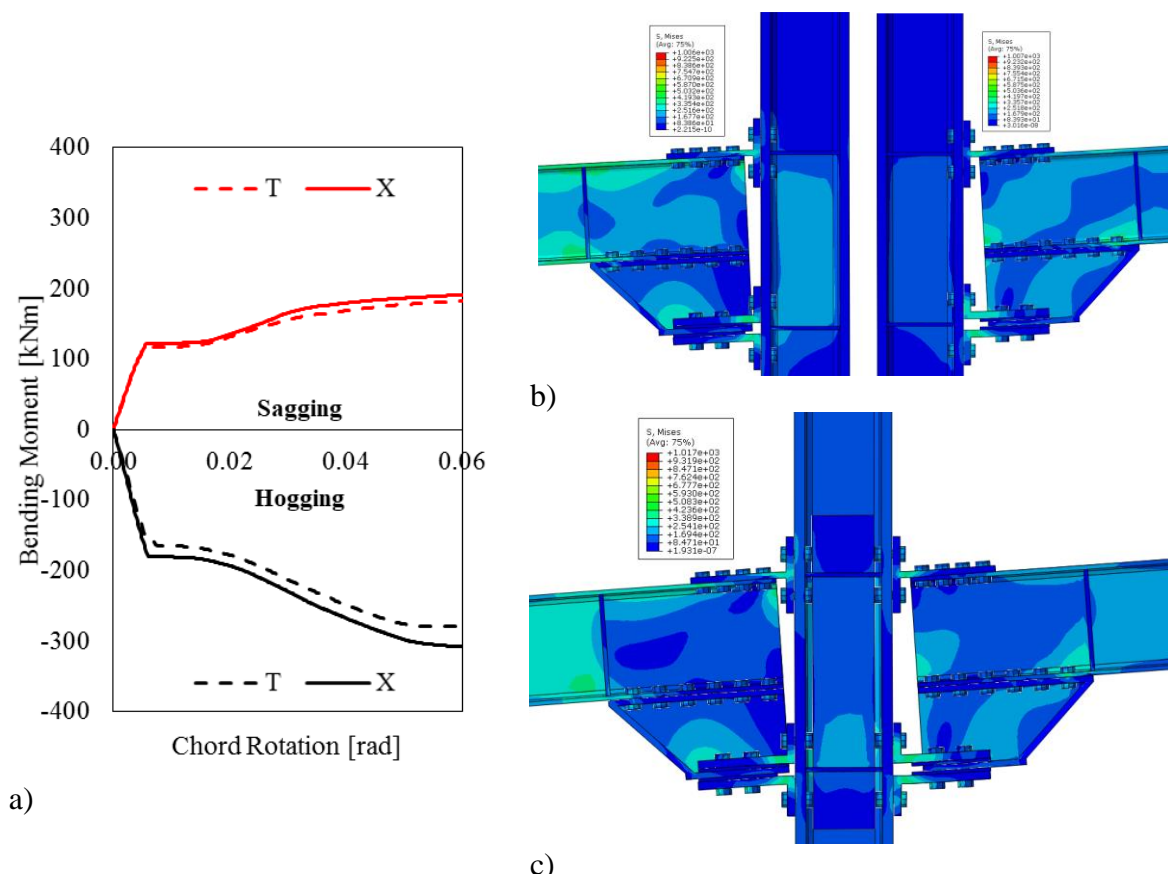


Figure 4.17 – Comparison between T and X joints with haunched damper

Therefore, for the sake of brevity, hereinafter it is simply shown the comparison between the response of T and X joints alternatively equipped with haunched (i.e. horizontal friction mechanism) and vertical rib (vertical friction mechanism) damper. Figures 4.17a and 4.18a show the moment-rotation response curves of the joints with haunched and vertical rib damper. As it can be trivially observed, the differences are negligible and are mainly due to the different overall rigidity of the column, which is stiffer in the case of internal joints, thus at the same imposed chord rotation the rotational contribution of the column is lower and the slip of the device is slightly greater as well as its corresponding reaction.

The deformed shape and the stress distributions are almost the same for both T and X joints as it can be observed comparing Figure 4.17b to 4.17c and Figure 4.18b to 4.18c for the configurations with haunched and vertical rib damper, respectively.

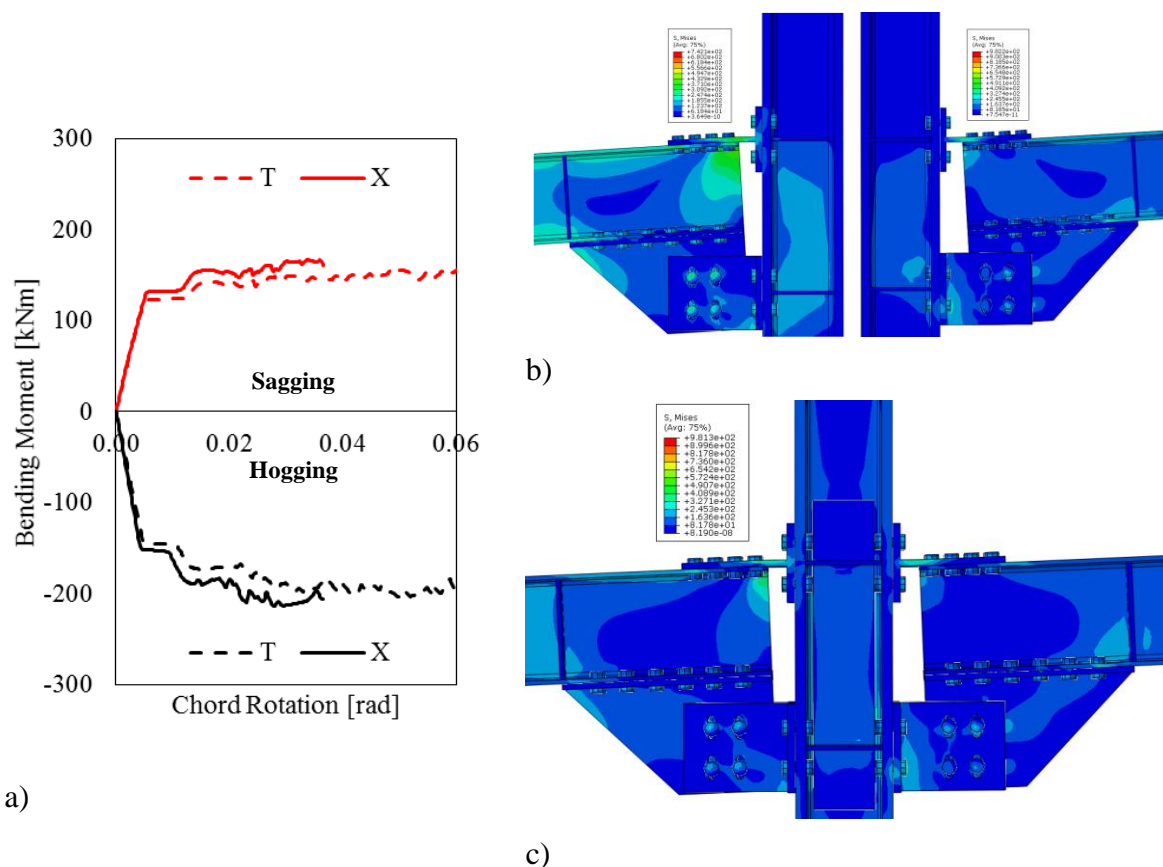


Figure 4.18 – Comparison between T and X joints with vertical rib damper

4.4 SUMMARY OF NEW INFORMATIONS FOR DESIGN PROVISIONS

4.4.1 Shear force in the T and L stub connections

By means of FEAs it was investigated the local behaviour of the FREEDAM joints in order to characterize any aspect related to the design of the connections (T-stub and L-stub) at column face is the shear check, because these elements should guarantee the resistance due to combined tensile and shear forces to avoid premature failure.

Figure 4.19 shows the distribution of shear forces at the level of the Tee and L-stubs as well as the total shear force in the section at the column face. In both tested friction device configurations, the cumulated shear in the two components (i.e. the sum of the relevant absolute values) is larger than the overall shear force (see Figure 4.19 a and c for type 1 and Figure 4.19 b and d for type 2). In order to investigate the evolution of the shear force with the connection rotation, monotonic analyses under both hogging and sagging loading conditions were alternatively performed.

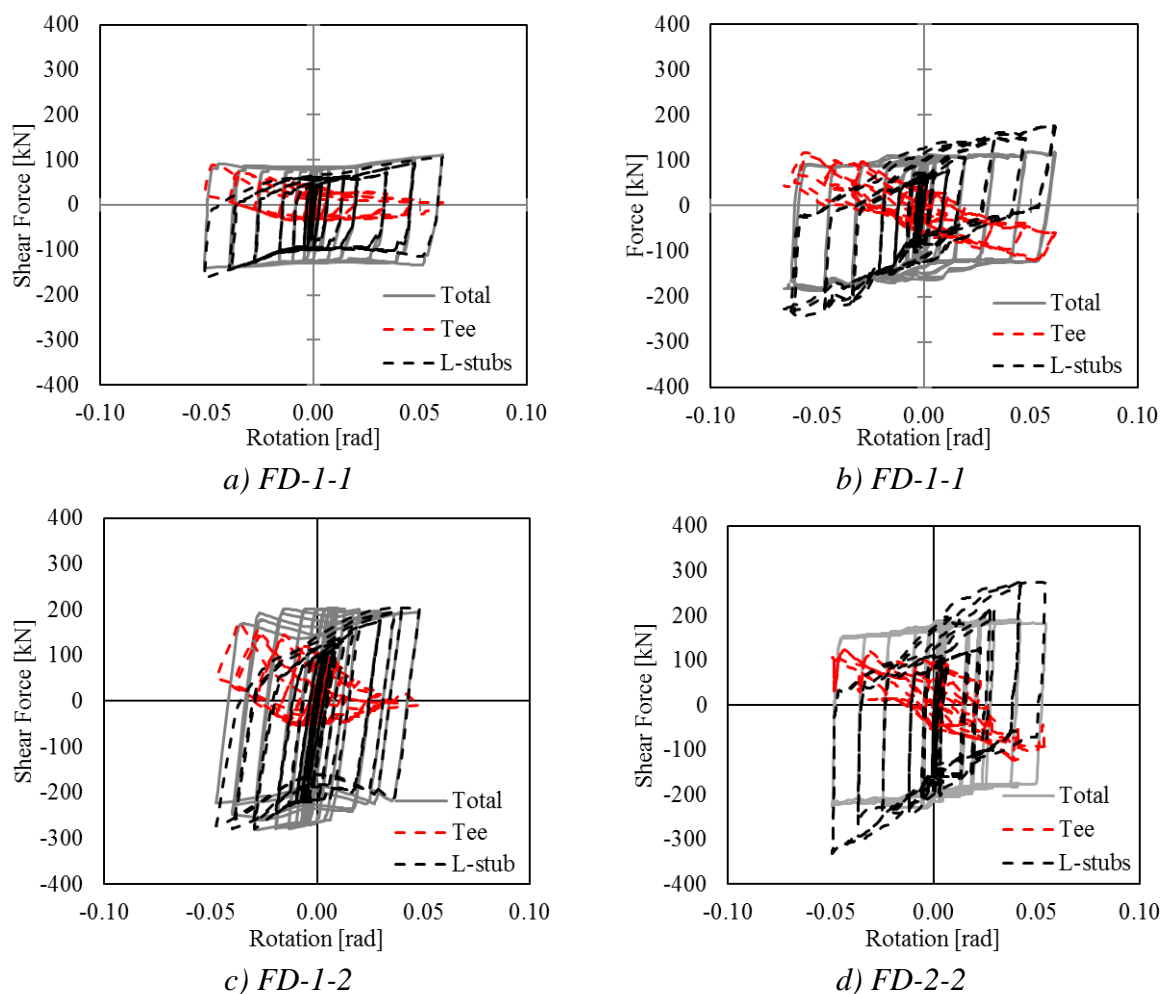


Figure 4.19 Shear force transferred by different components

The results presented in Figure 4.20 confirm the previous observations and offer insight into the magnitude of the shear transferred by each component. Indeed, for the investigated cases, the L-stubs transfer larger shear force compared to the T-stub. Configuration 1 joints are characterized by levels of maximum shear force transferred by the Tee of about 50% of the total shear, while the L-stubs reach values close to 100% of the total shear (Figure 4.20 a and c). However, while Configuration 1 components transfer shear of up to maximum total shear, Configuration 2 assemblies (Figure 4.20 b and d) exhibit the same behaviour observed cyclically i.e. the shear in the components reach values larger than the total shear, with the shear transferred by the L-stubs reaching values almost 2 times larger than the total shear for rotation values close to 0.06 rad.

The differences of shear force distributions between the 2 components is mainly due to the larger stiffness provided by the L-stubs in the vertical plane and the vertical sliding force component. Indeed, the transfer mechanism of shear force amongst the components (for comparison see Figure 4.16) is highly complex and configuration dependent. The type 1 joint (FD 1-1-DS) is characterized by same sign shear forces transferred by the L-stubs and in a smaller measure by the T-stub. On the contrary, the T-stub of FD 2-1-DS carries an opposite sign shear force, owing to the heightened level of shear force transferred by the L-stubs, in order to preserve the equilibrium at the column face. The hogging/sagging loading conditions lead to the same

distribution of forces between the components for the same configuration, with a smoother transfer of the forces under positive bending.

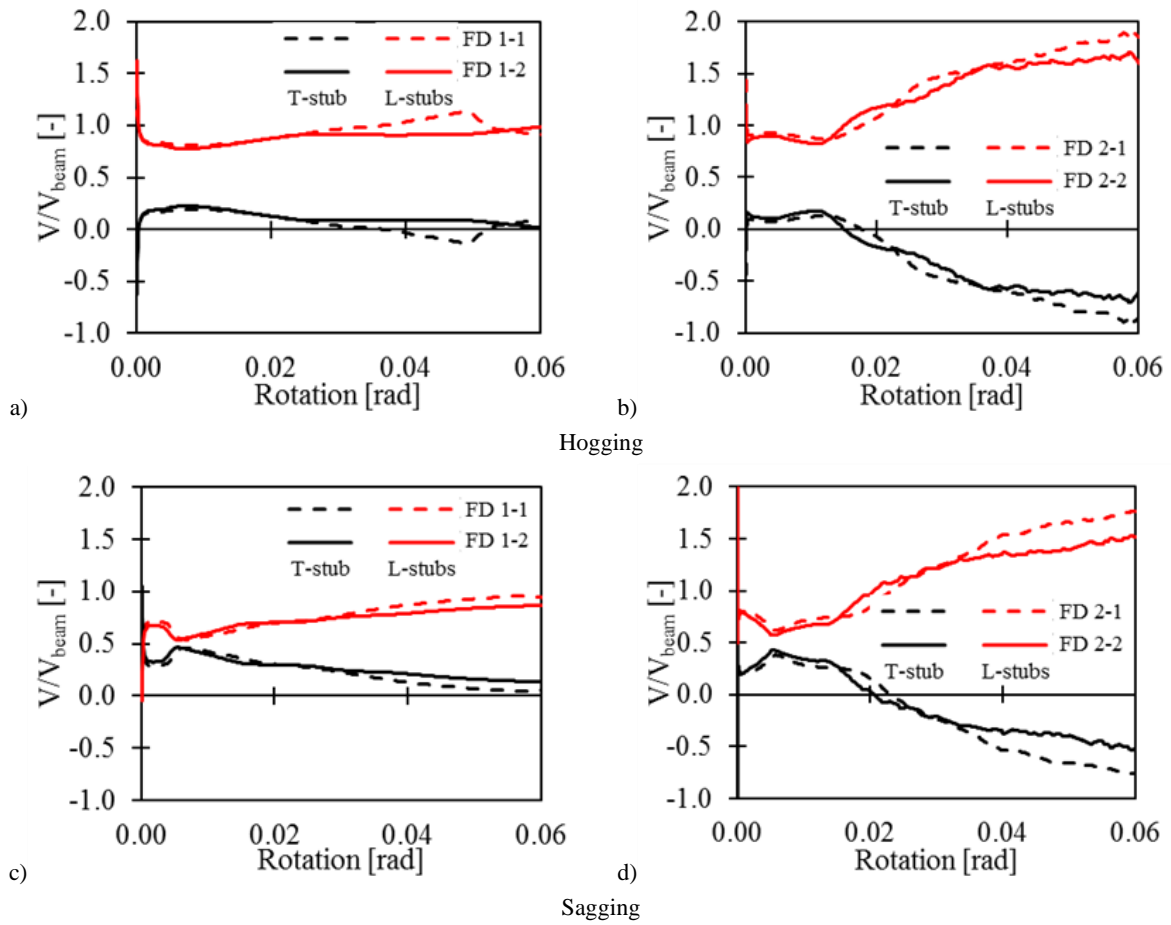


Figure 4.20 Shear force at the connection face

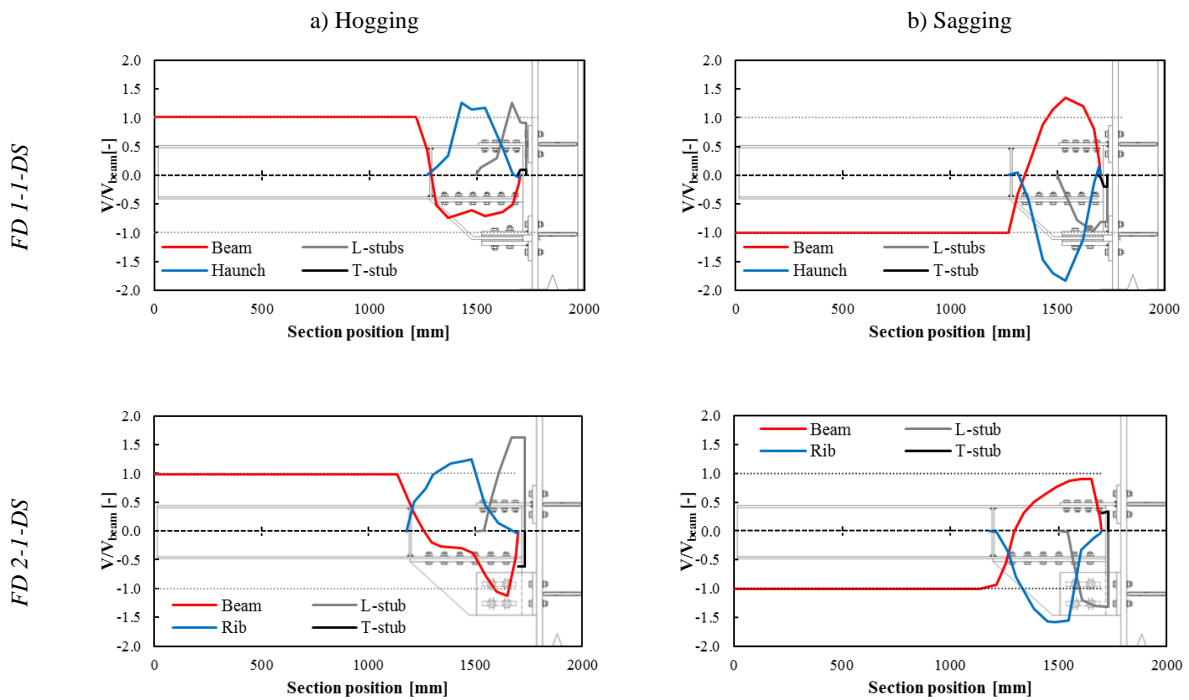


Figure 4.21 Distribution of shear in the connected elements at 0.04 rad damper rotation

In the analyses performed on the models depicting the experimental tests it was observed that small concentration of damage is located in the base of the T-stub, the L-stubs (in the case of Configuration 1), the bolts of the friction damper and in a reduced extent in the beam (the web-flange junction at the beam end immediately below the T-stub and in the slotted holes at the end of the beam-haunch connection). These results are presented in Figure 4.22 in terms of PEEQ (equivalent plastic strain) distribution on the large beam to column assemblies. As it can be observed in the legend of PEEQ that are evaluated at the rotation equal to 0.05rad, the horizontal friction damper configuration leads to larger plastic deformations in the joint elements. As a matter of fact, this result can also be observed in terms of dissipated energy, presented in Figure 4.23. Indeed, the friction energy normalized with respect to the total dissipated energy for the first configuration is smaller compared to the second configuration and the opposite is true in terms of normalized plastic energy. Although the second damper configuration leads to lower plastic damage, it is worth noting that the plastic damage is limited for both configuration, maximum plastic energy dissipation is less than 5% of the total energy dissipated at 0.05 rad.

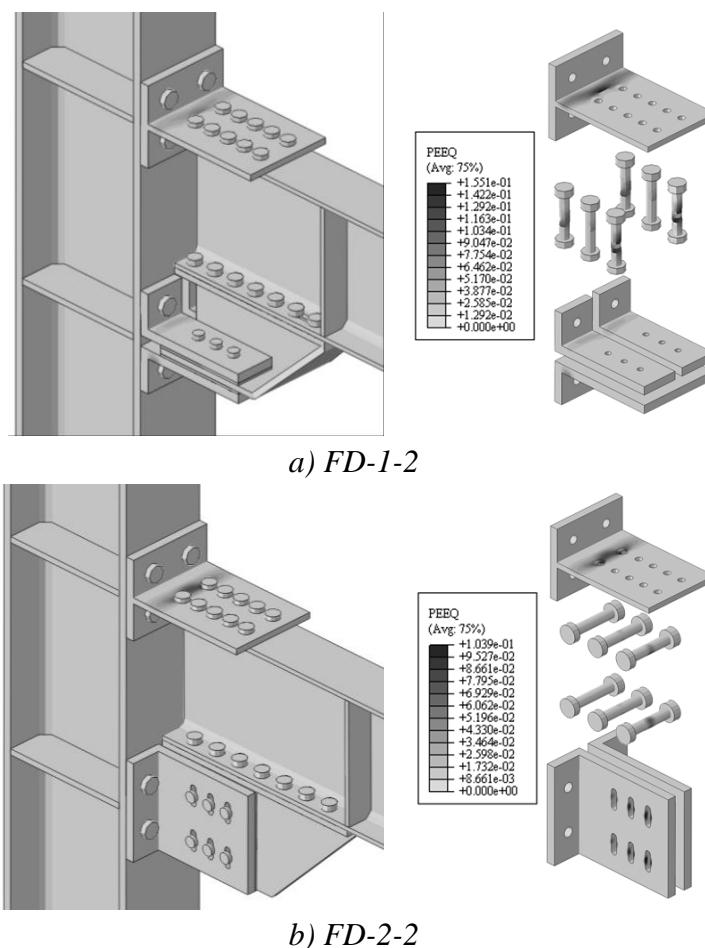


Figure 4.22 PEEQ Distribution at the end of the cyclic analysis for large joint assemblies

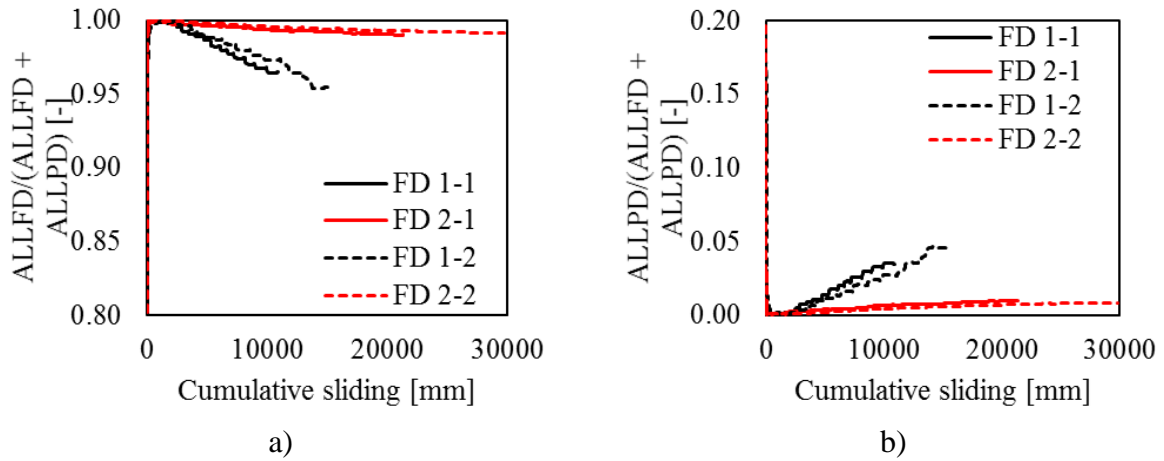


Figure 4.23 Normalised dissipated energy a) Friction energy and b) Plastic energy

4.4.2 Influence of clamping force

The experimental tests confirmed the importance of the clamping force applied to the bolts into the device. Therefore, in addition to the pre-loading force adopted in the tests (hereinafter referred as N_b), a value 50% smaller ($0.5 N_b$) and a value 50% larger ($1.5 N_b$) have been considered. It should be noted that in all cases $1.5 N_b$ is smaller than $F_{p,C}$ (which is equal to 172kN for M20 gr.10.9 bolts).

Figure 4.24 shows the comparison of the response curves for the four joints (i.e. the two joint configurations and two assemblies) Tables 4.4 and 4.5 report the numerically measured mechanical properties of the joints. The bending moments reported, $M^{(+)}$ and $M^{(-)}$, represent the bending moment at the occurrence of the sliding under sagging and hogging, respectively. Equations (4.2), (4.3) and (4.4) clarify the meaning of the mechanical parameter reported in the tables.

$$\Gamma^{(+)} = 1 + \frac{M_{0.5N_b}^{(+)} - M_{N_b}^{(+)}}{M_{N_b}^{(+)}} \quad (4.2)$$

$$\Gamma^{(-)} = 1 + \frac{M_{0.5N_b}^{(-)} - M_{N_b}^{(-)}}{M_{N_b}^{(-)}} \quad (4.3)$$

$$\Delta M^{(+/-)} / M^{(-)} = \frac{M^{(-)} - M^{(+)}}{M^{(-)}} \quad (4.4)$$

Where $\Gamma^{(+)}$ and $\Gamma^{(-)}$ represent the variation of the hogging and sagging bending moment capacity, respectively, considering alternatively the change in the clamping force from the design value N_b to $0.5 N_b$ and $1.5 N_b$; $M^{(+)}$ and $M^{(-)}$ are the sagging and hogging bending moments. The subscripts depict the analysis from which the bending moment is taken, e.g. with clamping force

equal to either $1.5 N_b$ or $0.5 N_b$; $\Delta M^{(+/-)}/M^{(-)}$ represents the difference between the hogging and sagging bending moment for each respective analysis (considering the three values for N_b).

As expected, the variation of the bending moment is proportional with the bolt pre-tension, although differently under both sagging and hogging. As reported in Tables 4.4 and 4.5, this difference is strictly related to the joint configuration and it is constant with the beam depths, clamping force, or friction coefficient. The difference is about 25% for Configuration 1 and 15% for configuration 2.

Further observation that can be made based on Figure 4.24 is that the post-yield response of joint configuration 1 differs with the size of the beam-to-column assembly and with the level of preloading (relative to the maximum preloading force). In particular, the joint with shallow beam and lower relative preloading exhibits hardening (i.e. positive post-yield stiffness), while the joint with deeper beam and higher relative preloading shows softening (i.e. negative post-yield stiffness), the latter is more evident for the lower values of clamping force. These phenomena are more pronounced under hogging bending moment. The second configuration exhibits a more linear behaviour in both examined assemblies.

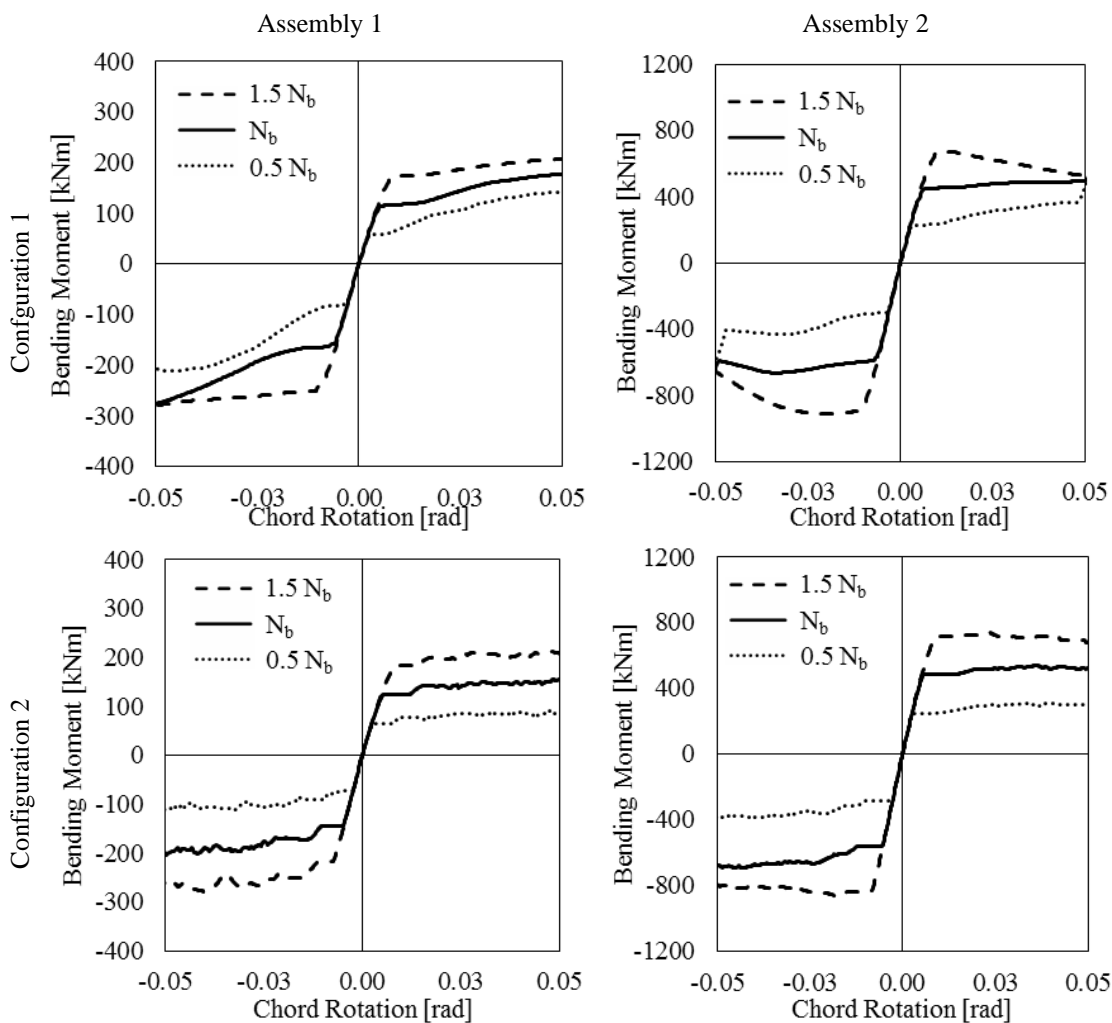


Figure 4.24 Influence of the clamping force on the bending moment capacity

The stiffness of the joint is not affected by the variation of clamping force, since it is determined by the stiffness of the other components of the joint (the connection at column face, the column web panel, etc.).

Table 4.4 Bending moments for model FD 1-2-DS considering the variation of clamping force

Clamping force	$M^{(+)}$ [kNm]	$M^{(-)}$ [kNm]	$\Gamma^{(+)}$ [-]	$\Gamma^{(-)}$ [-]	$\Delta M^{(+/-)}/M^{(-)}$ [-]
N_b	453	602	-	-	25%
$0.5N_b$	230	298	51%	50%	23%
$1.5N_b$	690	902	152%	150%	24%

Table 4.5 Bending moments for model FD 2-2-DS considering the variation of clamping force

Clamping force	$M^{(+)}$ [kNm]	$M^{(-)}$ [kNm]	$\Gamma^{(+)}$ [-]	$\Gamma^{(-)}$ [-]	$\Delta M^{(+/-)}/M^{(-)}$ [-]
N_b	484	564	-	-	14%
$0.5N_b$	250	290	52%	51%	14%
$1.5N_b$	714	838	148%	149%	15%

4.4.3 Influence of Friction Coefficient

Another important design parameter is the friction coefficient between the sliding surfaces. Therefore, in order to examine its role on the joint performance three different values of the dynamic friction coefficient μ are considered, namely the 5% percentile ($\mu_{5\%}$), the average value (μ_{avg}) set equal to 0.59, and the 95% percentile ($\mu_{95\%}$), see

Table 4.3:

Fig.4.25 depicts the numerical curves in terms of bending moment vs. chord rotation. It is possible to observe that the higher percentile of the friction coefficient values the larger is the joint capacity. This observation confirms the need to account for the variability of the friction properties of the friction pads to design the non-yielding structural members.

Similar hardening/softening behaviour can be observed for both joint configuration and, additionally, the response curves seem scaled proportionality with the friction coefficient. Tables 4.6 and 4.7 summarize the variation of the bending capacity of the FD-1-2-DS and FD-2-2-DS models analysed with larger values of friction coefficient (μ_{avg} and $\mu_{95\%}$) with respect to the design value ($\mu_{5\%}$) under hogging ($M^{(-)}$) and sagging ($M^{(+)}$) loading conditions.

Table 4.6 Bending moments for model FD 1-2 considering the friction coefficient variation

Friction coefficient	$\Delta\mu$ [-]	$M^{(+)}$ [kNm]	$M^{(-)}$ [kNm]	$\Gamma^{(+)}$ [-]	$\Gamma^{(-)}$ [-]	$\Delta M^{(+/-)}/M^{(-)}$ [-]
$\mu_{5\%}$	-	446	593	-	-	25%
μ_{avg}	110%	521	670	117%	113%	22%
$\mu_{95\%}$	117%	535	733	120%	124%	27%

Table 4.7 Bending moments for model FD 2-2 considering the friction coefficient variation

Friction coefficient	$\Delta\mu$ [-]	$M^{(+)}$ [kNm]	$M^{(-)}$ [kNm]	$\Gamma^{(+)}$ [-]	$\Gamma^{(-)}$ [-]	$\Delta M^{(+/-)}/M^{(-)}$ [-]
$\mu_{5\%}$	-	484	564	-	-	14%
μ_{avg}	110%	529	627	109%	111%	16%
$\mu_{95\%}$	117%	568	679	117%	120%	16%

The variation in the case of FD-1-2-DS differs with respect to the variation of the friction coefficient. In particular, a larger increase of bending moment can be observed for the same increase of friction coefficient. On the other side, the analyses of model FD-2-2-DS in Table 4.7 show a closer dependency of the bending capacity with the friction property randomness.

The parameter $\Delta M^{(+/-)}/M^{(-)}$, evaluated also for this set of analyses confirms the previous observation regarding the relation between the damper’s configuration and the different response under sagging and hogging conditions (values ranging around 25% for configuration 1 and 15% for configuration 2).

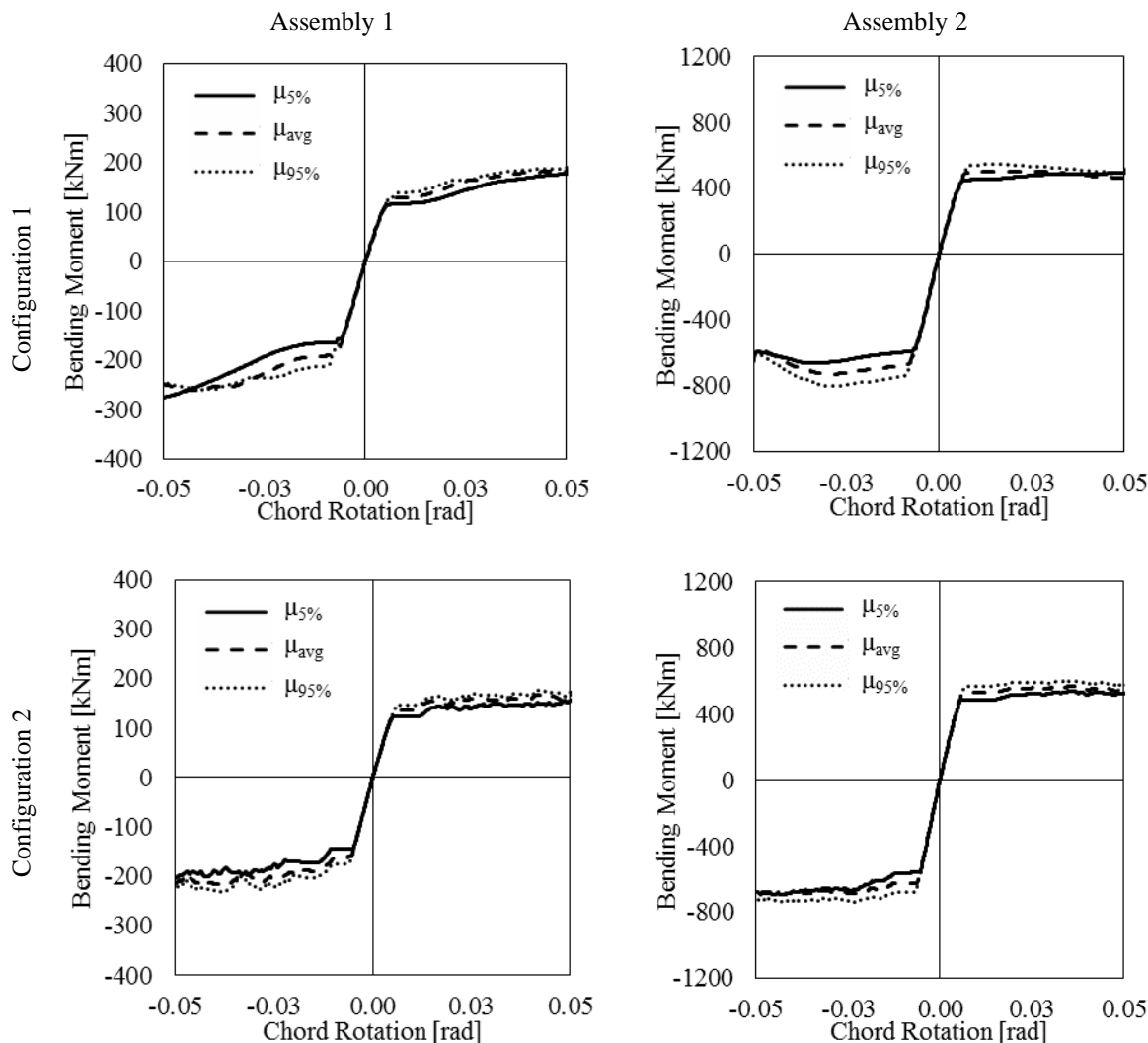


Figure 4.25 Configuration 1 vs Configuration 2

4.5 REFERENCES

- [1] Latour M., Piluso V., Rizzano G. (2014) “Experimental Analysis on Friction Materials for Supplemental Damping Devices”, *Construction and Building Materials*, 65:159-176.
- [2] Dassault Systèmes. Abaqus analysis 6.14 User’s manual. Simulia Inc.; 2015
- [3] M. D’Aniello, D. Cassiano, R. Landolfo, “Monotonic and cyclic inelastic tensile response of European preloadable GR10.9 bolt assemblies”, *Journal of Constructional Steel Research*, vol. 124, pp. 77-90, 2016.
- [4] M. D’Aniello, D. Cassiano, R. Landolfo, “Simplified criteria for finite element modelling of European preloadable bolts”, *Steel and Composite Structures*, vol. 24(6), pp. 643-658, 2017.
- [5] Cassiano D., D’Aniello M., Rebelo C., (2017) Parametric finite element analyses on flush end-plate joints under column removal. *Journal of Constructional Steel Research*, 137: 77–92.
- [6] Cassiano D., D’Aniello M., Rebelo C., (2018). Seismic behaviour of gravity load designed flush end-plate joints. *Steel and Composite Structures, An International Journal*, 26(5): 621–634. DOI: <https://doi.org/10.12989/scs.2018.26.5.621>.
- [7] D’Aniello M., Tartaglia R., Costanzo S., Landolfo R. “Seismic design of extended stiffened end-plate joints in the framework of Eurocodes”. *Journal of Constructional Steel Research*, 128, 512–527, 2017
- [8] Tartaglia R., D’Aniello M., Rassati G.A., Swanson J.A., Landolfo R. (2018). Full strength extended stiffened end-plate joints: AISC vs recent European design criteria. *Engineering Structures*, 159:155–171.
- [9] Tartaglia R., D’Aniello M., Zimbru M., Landolfo R., (2018). Finite element simulations on the ultimate response of extended stiffened end-plate joints. *Steel and Composite Structures, An International Journal* 27(6): 727-745. DOI: 10.12989/scs.2018.27.6.727.
- [10] Tartaglia R., D’Aniello M., Landolfo R., (2018). The influence of rib stiffeners on the response of extended end-plate joints. *Journal of Constructional Steel Research*, 148: 669–690.
- [11] ANSI/AISC 341-16 (2016). “Seismic Provisions for Structural Steel Buildings”. American Institute of Steel Construction.
- [12] Tartaglia R., D’Aniello M., “Nonlinear performance of extended stiffened end plate bolted beam-to-column joints subjected to column removal” *The Open Civil Engineering Journal*, 2017, 11: 369-383
- [13] D’Aniello M., Cassiano D., Landolfo R. “Monotonic and cyclic inelastic tensile response of European preloadable GR10.9 bolt assemblies”. *Journal of Constructional Steel Research*, 124: 77–90, 2016.
- [14] D’Aniello M., Cassiano D., Landolfo R., (2017) Simplified criteria for finite element modelling of European preloadable bolts. *Steel and Composite Structures, An International Journal*, 24(6): 643-658.
- [15] Zimbru M., D’Aniello M., De Martino A., Latour M., Rizzano G., Piluso V., (2018). Investigation on Friction Features of Dissipative Lap Shear Connections by Means of

Experimental and Numerical Tests. *The Open Construction and Building Technology Journal*, 12(Suppl-1, M9): 154-169.

- [16] Francavilla A.B., Latour M., Piluso V., Rizzano G. (2015). Simplified finite element analysis of bolted T-stub connection components. *Engineering Structures*, 100: 656-664

CHAPTER 5

BEHAVIOR UNDER IMPACT LOADING

5.1 INTRODUCTION

It is recognised that the behaviour of beam-to-column connection subjected to impact loads can differ from the behaviour observed under normal loading conditions [1–4]. This is mainly due to the occurrence of elevated strain rates in several components of the joints, coming from the high velocities of loading characteristic of impact loads.

Strain rate is the property that defines the strain deformation (d_ϵ) per unit of time (d_t) to which a material is subjected, d_ϵ/d_t , and it affects the stress-strain curves of the steel. In general, the strength properties increase for higher strain rates, with a more pronounced increase for steels with high ductility. For instance, for mild steel, the yield strength at elevated strain rates (approximately 600s^{-1}) can be considered 1.5 times the yield strength under static loads [5,6], while the high strength steel used in bolts, usually does not show an increase of more than 10% for the yield strength [1,7,8]. Furthermore, besides the variation of strength, a loss of ductility is normally associated with higher strain rates.

Usually, the variation in the strength properties of steel when subjected to elevated strain rates is described by the parameter *DIF* “dynamic increase factor”, given by the ratio between the strength observed when elevated strain rates are considered and the strength observed under static loads. Models to represent the dynamic increase factor of the yield strength are already available in the literature [9,10], such as, the Johnson-Cook model [9] which describes the variation of strength with strain rates as a logarithmic function.

As connections are generally constituted by the assembly of different steel grades (typically high strength steel for bolts and mild steel for plates), regarding the effects of strain rates in the global behaviour of steel connections, it is easy to understand that their dynamic response can strongly differ from the static one, depending on the strain rate properties of the materials constituting plates and bolts. In general, it is observed an increase in their elastic and ultimate resistance, while their ductility capacities tend to decrease as far as the speed of loading increases [1–4]. In this view, knowing that in a structural scale, a good local ductility of connections is quite important to allow the development of alternative load paths in structures [11,12], it is clear that the effect of strain rates has to be properly taken into consideration in the structural modelling.

In this chapter, the summary of the results and conclusions obtained during the FREEDAM project [13] is reported, concerning the behaviour of the FREEDAM connections under impact loading. For more detailed information on these results, the PhD theses of Marina D’Antimo [14] and Ana Francisca Santos [15] can be consulted.

5.2 FREEDAM DAMPERS UNDER IMPACT LOADING

5.2.1 Description of the tested specimens and experimental programme

The tested specimens shown in Figure 5.1 are similar to those used for the cyclic tests. These specimens are double shear lap connections with a couple of additional 8 mm steel plates (made of steel S275JR) coated using thermal spray (friction pads), pre-stressed with M20 bolts. Two distinct parts composed the specimen. The first is the “slip part”, in which the internal plate (made of AISI304 stainless steel) is slotted to simulate the slotted haunch flange of the FREEDAM connection. The second part is the “fixed part”, where an internal steel S275JR plate is used to connect the specimens to the testing equipment. Besides, two external steel plates with a thickness of 15 mm are placed between the bolt heads and the friction pads to reproduce the spreading effect of the bolt forces at the interface. Three different modifications from the “standard” configuration of Figure 5.1 were designed according to Eurocode 3 [16], so that different failure modes of the friction damper could be assessed (Figure 5.2).

The entire experimental programme is summarized in Table 5.1 and it is divided into three groups. In the first group (Group A), the specimen configuration *a* (Figure 5.2) was used, which has two slotted holes with a total length equal to 41 mm, internal plates with a thickness equal to 30 mm and preloaded M20 10.9 HV bolts. In Group B, bolts M20 8.8 SB were used in all eight tests. In these tests, the specimen *a* was used for the static tests while, the specimen *b* was used in the impact tests, differing from the specimen *a* in the length of the slotted hole (it has only one longer slotted hole, Figure 5.2). Finally, in Group C, the specimen *c* was used, that differs from the configuration *a* in the thickness of the internal plates (here a 10 mm thickness was adopted) so that a plate in bearing failure mode could be tested. Additionally, the width of the internal plate at the fixed part was also enlarged to assure the failure mode at the slip part of the specimen. Furthermore, the three different coatings materials selected from the results of the cyclic tests on the FREEDAM dampers, namely, M1, M4 and M6, were used in each group test. A total of 32 impact tests were performed. Furthermore, 8 quasi-static tests were carried out as well, to have a base behaviour of the specimens for comparison with the impact tests results. Before each test, the bolts were tightened using a calibrated torque wrench to introduce a preload force F_p equal to $0.5 \cdot f_{ub} \cdot A_s$ (f_{ub} is the ultimate strength of the bolt and A_s is the tensile stress area of the bolt). The magnitude of torque applied to each bolt is dependent on the design preload value F_p , the diameter of the bolt d and the bolt k -factor.

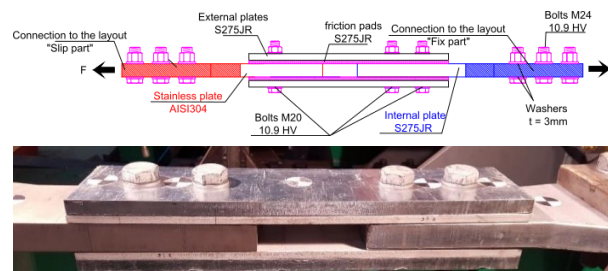


Figure 5.1 - FREEDAM specimen: Lateral view

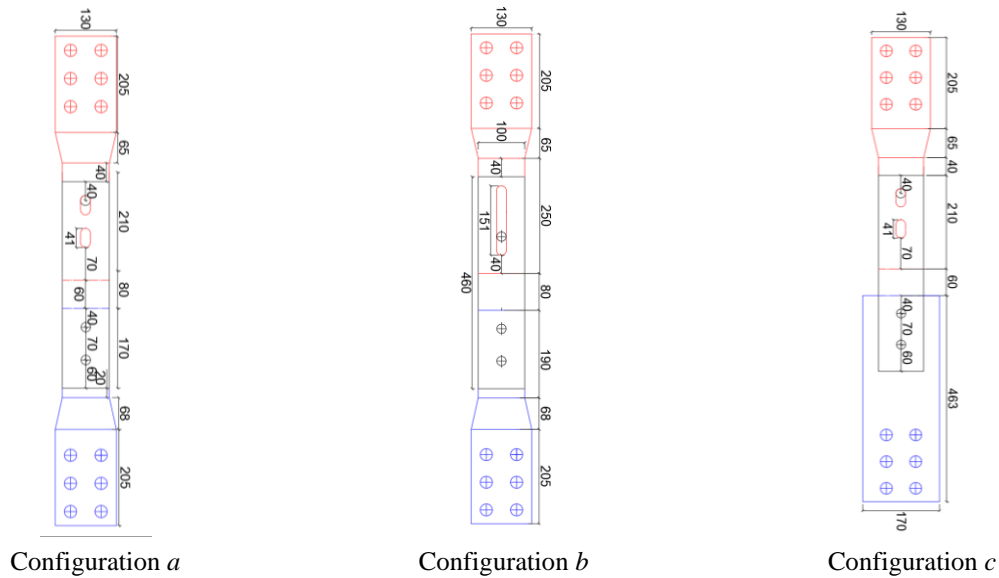


Figure 5.2 - Tested specimens: Front view (dimensions in mm).

Table 5.1 - Experimental programme

⁽¹⁾ ID	Conf.	Bolt	Preload	⁽²⁾ Test Type
Group A				
T3- M4/M1/M6-SI-30	a	M20 10.9 HV	122.5 kN	4 Impacts. 20Bar; 50Bar; 75Bar; 100Bar
T4- M1/M6- FI-30				100Bar
T8-M4/M6/M1-St.-30				Monotonic FC: 0.2kN/s
T10/11 –M4–St. 30				Monotonic DC: 0.01mm/s
Group B				
T1-M1- SI-30	b	M20 8.8 SB	98 kN	3 Impacts: 40Bar; 60Bar; 80Bar
T2-M1- FI-30				80Bar
T1-M6- SI-30				3 Impacts: 20Bar;40Bar; 60Bar
T7-M1/M6-St.-30	a			Monotonic FC: 0.2kN/s
Group C				
T5-M4- SI-10	c	M20 10.9 HV	122.5 kN	5 Impacts: 50Bar; 80Bar; 100Bar; 120Bar; 150Bar
T5-M1/M6- SI-10				3 Impacts:50 Bar; 100 Bar; 150 Bar
T9-M1-St.-10				Monotonic ⁽²⁾ FC: 0.2kN/s

⁽¹⁾ID-Test: Tn^o- X- Tt – Pt: Tn^o=Test number- X=ID Coating Material (M4, M1, M6) – Tt=Test type: Sequential (SI), Full Impact (FI), Static (St.) – Pt=Internal plate thickness [mm]

⁽²⁾FC – force control; DC- displacement control

5.2.2 Description of the test setup

The test setup used for the impact tests is schematically presented in Figure 5.3. It comprises two HEB 500 beams placed horizontally and fixed to the reaction slab of the lab. At one end, these beams are orthogonally bolted to a rigid reaction frame built from two IPE450 members whereas, at the other end, are connected to a HEB650 member. All the steel parts of the layout were made of structural steel grade S355. In this way, a very stiff structure is built, which can accommodate impacts without deformations or rotations. Furthermore, the column to which the impact force is applied (“*flying beam*”) is placed in parallel to the rigid reaction frame and it is made from a cross-section with very high stiffness (HEM340) to not suffer significant deformations when the impact force is applied. At the opposite end of the application load, this beam is restrained by a pivot. Additional details regarding the testing rig can be found in [17].

The specimen to be tested is connected to the flying beam and the reaction frame. The boundary conditions of the specimen are dependent on the type of loads to be transmitted. In this case, the specimen was connected by two hinges to transmit only tension uniaxial forces (Figure 5.3).

Two types of impact tests can be performed using this layout - full and sequential (FI or SI). In a sequential test, the same specimen is loaded and unloaded multiple times, with higher pressure in each sequence, up to failure (red lines in Figure 5.4). In this way, it is possible to determine the approximate value of pressure needed to achieve failure. Moreover, from the unloading phase of the specimen, an approximation of the elastic stiffness of the specimen can be obtained. For a full impact test, the collapse pressure from the sequential test is used.

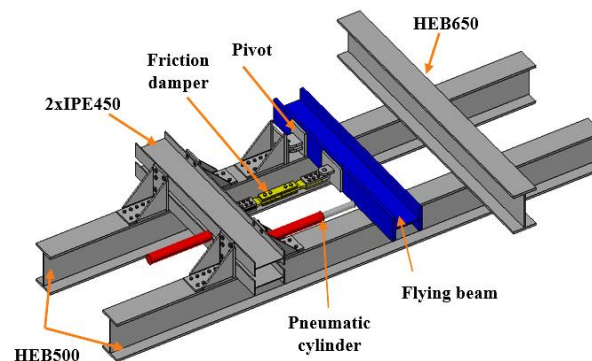


Figure 5.3 -Sketch of the experimental layout used for impact tests – Friction damper tests

For testing the specimens under impact loads, the instrumentation needed is not as simple as for the quasi-static tests due to the dynamic nature of the loads. Firstly, the inertial forces of the system can no longer be neglected and secondly, the instrumentation used has to be specific to read short-duration tests. It is then necessary to read, besides from the force and displacements, also accelerations and velocities. The force was read by a load cell, while the deformation of the specimen and “*flying beam*” was measured by laser triangulation sensors. Besides, a Photron high-speed camera was also used, which recorded the tests and provided displacements, velocities and accelerations during the tests on specific points of the specimen. Moreover, to take into account the inertial forces of the beam, two accelerometers were used to record the accelerations at the centre of mass of the “*flying beam*” a_{cm} and the point of the application force a_f .

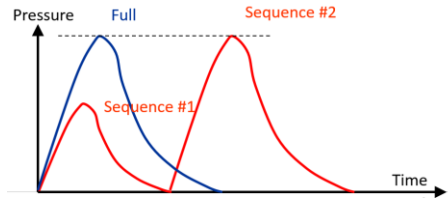


Figure 5.4 - Types of impact tests – Force history scheme

5.2.3 Results of the experimental tests

The main purpose of this experimental activity was to study the behaviour of the FREEDAM dampers under impact loading and evaluate if the strain rates generally induced by this type of loading, change significantly the reference behaviour of the same specimens observed under quasi-static loading. This evaluation was assessed using a dynamic factor “DF” (Eq. 5.1):

$$DF_{P_i} = \frac{P_{i,imp}}{P_{i,st}} \tag{5.1}$$

to which corresponds the ratio between a certain behavioural parameter (P_i) under impact loading (imp) and the same parameter under quasi-static loading (st). Five behavioural parameters were selected, namely: the static friction coefficient μ , the design and ultimate resistance (F_y and F_u), the initial elastic stiffness after the occurrence of slippage S_{ini} and the ductility capacity of the damper after the occurrence of slippage δ_u . As an example, in Figure 5.5, these behavioural parameters are reported for the tests of group A (Table 5.1), with the coating M1. Table 5.2 and Table 5.3 summarises the dynamic factors found for all the examined cases.

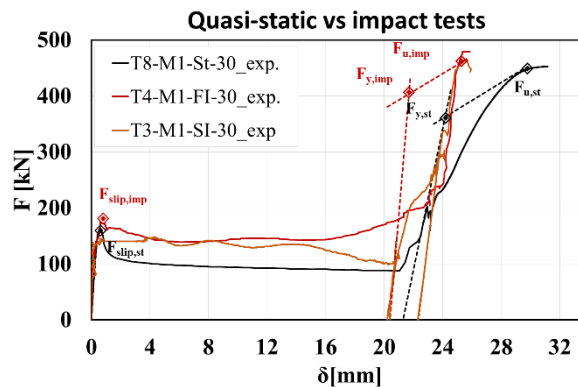


Figure 5.5 - Experimental force versus displacement curves (Group A, M1)

Based on the results, the main conclusions that can be drawn regarding the behaviour of the FREEDAM dampers are:

- An increase of the initial friction resistance was generally observed under impact loading ($DF_{friction}$ in Table 5.2). Furthermore, during the slip, a degradation of the slip force was observed in both impact and quasi-static tests (F_{slip}/F_{slip} in Table 5.2). However, independently of the coating material, this degradation was less significant in the impact tests, probably because, at high loading rates, the initial friction coefficient is closer to the kinetic coefficient. From this perspective, the application of friction dampers within connections can increase

their performance under loads rapidly applied since their friction resistance is increased by the presence of elevated strain rates.

- The elastic initial stiffness after the slip also (S) increased for higher loading rates, which was related to the increase of the strength of the materials composing the components of the friction damper.
- The influence of the loading rates on the ultimate resistance and ductility of the friction damper was more significant when the specimen failed by the plate in bearing rather than the bolt in shear (an increase of resistance of 11% vs 5% and a decrease of ductility of 50% vs 30%). This is because the stainless steel used in plates have a higher sensitivity to different strain rates than the high strength steel used in bolts [18,19].
- For the tested specimens, the failure modes observed in the static tests did not change in the presence of high loading rates. The changes in the static failure mode of connections due to impact loading are still not completely understood since it seems to depend on several aspects such as the mechanical and geometrical properties of the parts constituting a connection (as the thickness of plates and/or bolt grade), the rate of the test and the experimental boundary conditions. For example, the parametric study carried out by Ribeiro *et al.* [20] showed that the T-stub component with the increase of the loading rate, show brittle failure modes. On the other hand, other authors such as [3,4], observed always the same failure mode, independently of the plates' thickness or the applied loading rate.

Table 5.2 - Summary of the values of the friction dynamic factors and degradation of the friction resistance

Material	Bolt class	F_k/F_{slip}		DF_{frict}
		Static	Impact	
M4	10.9 HV	0.8	0.84	1.06
M1	10.9 HV	0.7	0.9	1.04
	8.8 SB	0.48	0.84	1.09
M6	10.9 HV	0.5	1.15	1.13
	8.8 SB	0.67	0.83	1.03

F_k – kinematic slip force (force at the end of slip); F_{slip} – initial slip force (see Figure 5.5)

Table 5.3. Summary of the values of the Dynamic factors after the occurrence of slippage

Parameter	DF	Group		
		A	B	C
S	DF_S	1.37	1.28	1.44
F_y	DF_y	1.08	-	1.3
F_u	DF_u	1.04	1.09	1.11
δ_u	$DF_δ$	0.72	0.57	0.44

5.2.4 Simulation of the tests' results

Following the experimental campaign described in the previous section, a numerical study has been carried out to widen the knowledge on the friction damper behaviour. At first, the model was calibrated by simulating the experimental results. After this calibration, a parametric study was performed considering: i) four internal plate thickness, namely, 8 mm, 10 mm, 15 mm and 30 mm, to activate different failure modes, ii) variation of the initial bolt preload and iii) different velocity rates.

All the numerical analyses were carried out with ABAQUS software, using the dynamic implicit solver [21] with the quasi-static procedure to capture the quasi-static behaviour and the moderate dissipation procedure to capture the dynamic behaviour of the specimens.

The model has the same geometry as the specimens experimentally tested in the previous section (Figure 5.6). No restraint was provided in the sliding plate, and on the other end, the fixed internal plate was restrained in the direction of the application of displacement. Concerning the applied loading, two subsequent steps were defined. First, the bolts were preloaded using a temperature gradient approach and then, the internal stainless plate was pulled. For the quasi-static analysis, the displacements were applied monotonically. To calibrate the dynamic numerical models, the experimental displacement-time curves were applied as a boundary condition.

The model was generated with solid element type C3D8R (first-order reduced integration continuum elements) with “Hex” element shape, allowing for non-linear geometrical and material behaviour. Normal contact conditions were introduced with “hard-contact” property allowing for separation. Concerning the tangential behaviour, different properties were assumed depending on the contact surfaces. For the parts that were not in contact with the friction shims a friction coefficient equal to 0.2 with a “penalty” formulation was assumed. For the remaining parts, the assumed value of the friction coefficient was equal to the experimental value. Furthermore, as described in the previous section, a degradation of the friction resistance is generally observed during the slip of the friction damper. This effect was considered degrading the preloading force in the bolts according to the experimental results. For the impact tests, a slip-rate dependent model has been adopted, taking into account the DF_{frict} , given in Table 5.2.

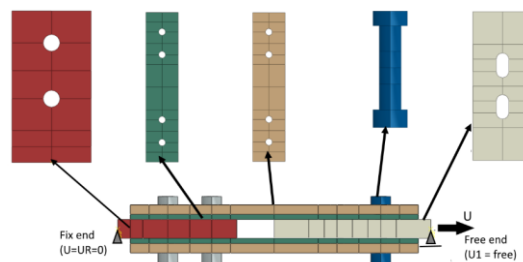


Figure 5.6 - Numerical model of friction damper: Geometry and boundary conditions

A key aspect of these numerical simulations was the characterization of the material properties of the different parts of the damper, since, to assess a full characterization of the dampers behaviour (static and dynamic), a complete characterization of materials stress-strain curves is required including damage as well as the influence of the strain rates in these curves. The damage

of the materials was included using the damage ductile model available on ABAQUS, while the Johnson cook model was used to account for the effects of the strain rates [22]

The numerical simulations were able to describe quite well the behaviour observed in the experimental tests, in terms of the force-displacement curves, as exemplified in Figure 5.7 for the tested curves shown previously.

Increasing the number of the studied parameters made possible to observe different failure modes and deformation levels of all the components of the damper, allowing the assessment of trend lines describing the effect of strain rates for a certain behavioural parameter, as reported in Figure 5.8 for the ultimate strength and deformation of the bolt and slip plate. These trend lines were then applied in an analytical model to characterize these elements [23].

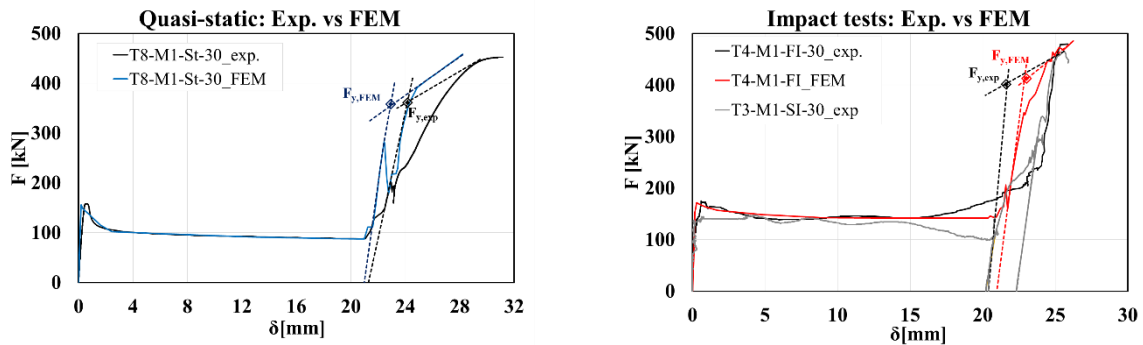


Figure 5.7- Experimental tests vs numerical simulations

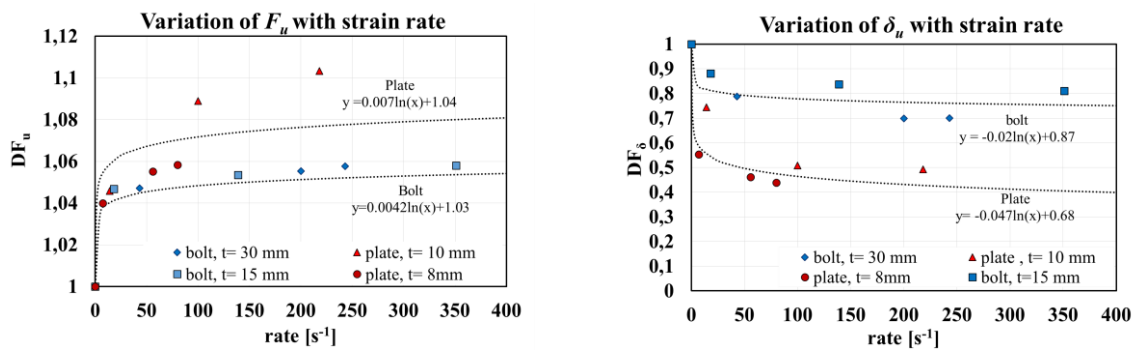


Figure 5.8 - Influence of velocity on the behaviour of the friction damper

5.2 FREEDAM connections under impact loading

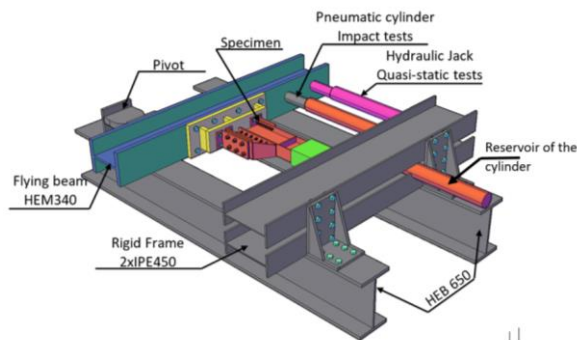
5.3.1 Typologies tested

The specimens tested at University of Coimbra and University of Liege have similar configurations, except for the columns, where HEM340 and HEB220 were used for the external and internal joints, respectively, as reported in Figure 5.9 and Figure 5.10. These specimens are a modification of a DST (Double Split Tee) joint where the bottom tee is replaced by a friction damper constituted by a couple of angles and pre-loaded friction pads, located on an additional haunch bolted to the lower flange of an IPE220 beam through M12 class 10.9HV preloaded bolts. The angles and pre-loaded friction pads composing the friction damper are connected with

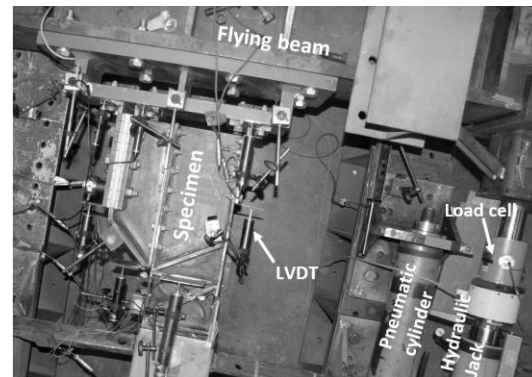
but allows the horizontal sliding (Figure 5.11). The instrumentation used was also the same as used in the experimental tests of the FREEDAM dampers (Chapter 2).

Table 5.4. Experimental programme

Test type	Quasi-static	Impact
	Monotonic:	Sequential Impact:
Loading Scheme	displacement control 0.02 mm/s	75 bar (500 mm/s); 120 bar (1000mm/s) ; 200 bar (1200mm/s)



a. 3D Drawing



b. Photo of part of the experimental setup

Figure 5.11 - Experimental layout

Results of the experimental tests

Figure 5.12 shows the experimental bending moment-rotation curves ($M-\theta$) obtained in each sequence of impact (Impact 1, Impact 2 and Impact 3) as well as the quasi-static $M-\theta$ curve.

Independently of the type of loading, the initial behaviour of the experimental curves shows that the connection response is governed by the friction damper behaviour up to the end stroke of the slots. Comparing the quasi-static with the impact response (impact 1 - #75 bar), it was observed a DF factor equal to 1.14 for the friction resistance (M_{slip} in Figure 5.12). Besides, during the slip, under quasi-static loading, there is a visible degradation of the friction resistance while, under impact loading, this value increases, which was related to the increase of the velocity through the slip [25].

After the complete slip of the friction device, additional components of the connection are activated and some non-dissipative parts of the connection start to yield. Under quasi-static loading, the collapse was achieved by the T-stub in bending with thread stripping failure in the bolts of the T-stub flange (Figure 5.13). Even though undesired, this failure mode is a typical failure for HV bolts in tension and consequently, in T-stubs with HV bolts when designed to collapse in mode 2 or 3 [1,26,27].

Concerning the impact testing, after the first impact (Impact 1 - #75bar), two additional tests were performed at higher pressures. Unfortunately, these pressures were not enough to induce the failure of the connection. However, it can be observed that after the slip, the impact behaviour follows the static one.

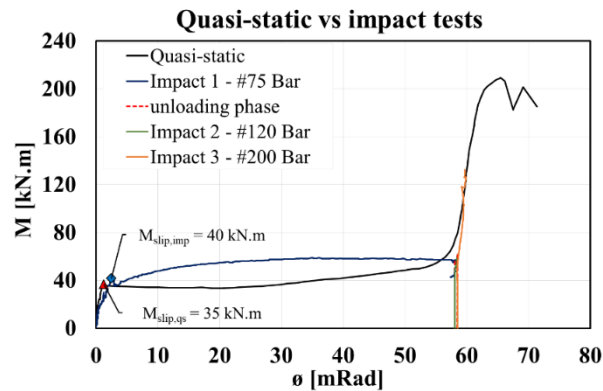


Figure 5.12 - Experimental rotational connection behaviour: quasi-static vs impact tests



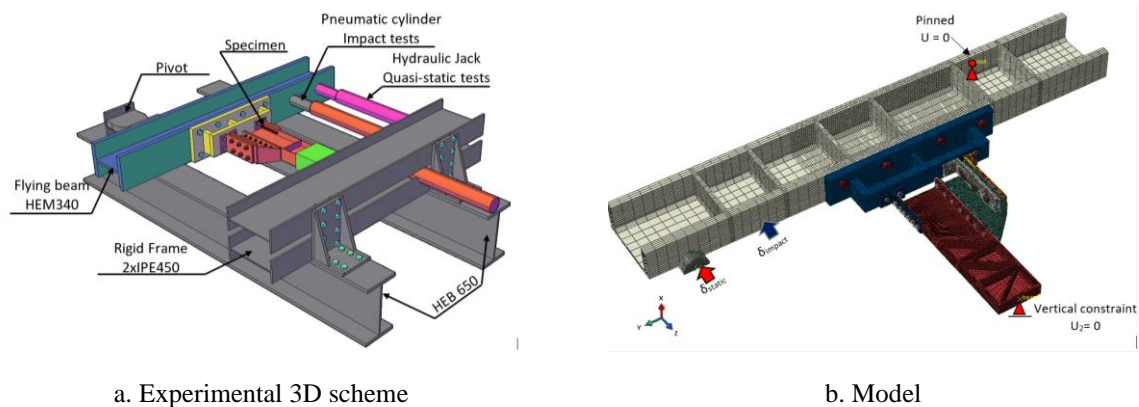
Figure 5.13 - Connection after failure: T-stub

Simulation of the tests' results

The simulations of the tests on the FREEDAM connection were carried out with ABAQUS software. To decrease the computational time, the experimental layout was simplified. Firstly, since the layout is symmetric in the XX plane, only half of the layout was modelled. Secondly, the reaction frame was omitted. Furthermore, the supports were modelled with reference points, imposing the required constraints in the zones in contact with the supports (pinned constraint and vertical constraint in Figure 5.14b), while the rod of the actuator was modelled as a solid object in which displacements in time are applied.

In total, five different parts were considered: i) HEM 340 beam “*flying beam*”; ii) the IPE 220 beam; iii) the actuator; iv) the rigid part connecting the connection to the HEM 340 beam and v) all the parts of the FREEDAM connection. All bolts were modelled as one single piece of bolt+head+nut, except the M16 HV bolts, where the transition between the smooth shank and the threads was modelled by reducing the cross-sectional area of the bolt, as suggested by Grimsno *et al.* [28] (Figure 5.15), to assess more correctly the nut stripping failure observed in the experimental test.

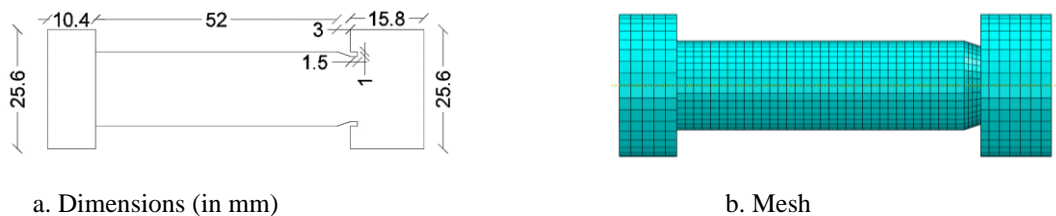
Concerning the modelling proprieties/assumptions (meshing, contact interactions, preload, material properties, etc.), the approach used for the models of the FREEDAM dampers was also used here.



a. Experimental 3D scheme

b. Model

Figure 5.14 - FEM models: Boundary conditions



a. Dimensions (in mm)

b. Mesh

Figure 5.15- M16 HV Bolt modelling

The numerical simulations were divided into two parts: first, the experimental tests were simulated (Figure 5.16) and after, a parametric study was performed, considering: i) bending direction (hogging and sagging), ii) effect of the bolt ductility by simulating the use of 2 nuts in the HV bolts and iii) the loading rate.

Based on the numerical results, the following conclusions were drawn:

- The numerical study showed that the connection behaviour under hogging and sagging bending moment is not symmetric (Figure 5.17a). This asymmetry up to the slip has been related to the higher opening of the L-stubs when compared to the T-stub opening under hogging moment [29]. After the slippage, the asymmetric behaviour is due to the different contribution of the upper and lower L-stubs, which seems to be due mainly to the deformation of the friction damper bolts in shear and at the ultimate load, which were not all in contact with both L-stubs webs. However, it was demonstrated through FE that this behaviour could be improved by avoiding the brittle nut thread stripping failure of the tee elements bolts by simulating the use of 2 nuts in these elements (Figure 5.17a).
- Regarding the dynamic behaviour of the connection, in general, it is observed that an increase of the initial friction resistance occurs with the speed of the tests ($DF_{friction}$ between 1.02 and 1.14) as well as an increase of the elastic (DF_{MRd} between 1.1 and 1.15) and ultimate resistance (DF_{Mu} between 1.05 and 1.12). Conversely, the ductility capacity decreases although not significantly ($DF_{\phi u}$ between 1.0 and 0.88). Besides, no significant changes were observed in the initial stiffness of the specimens (Figure 5.17b).

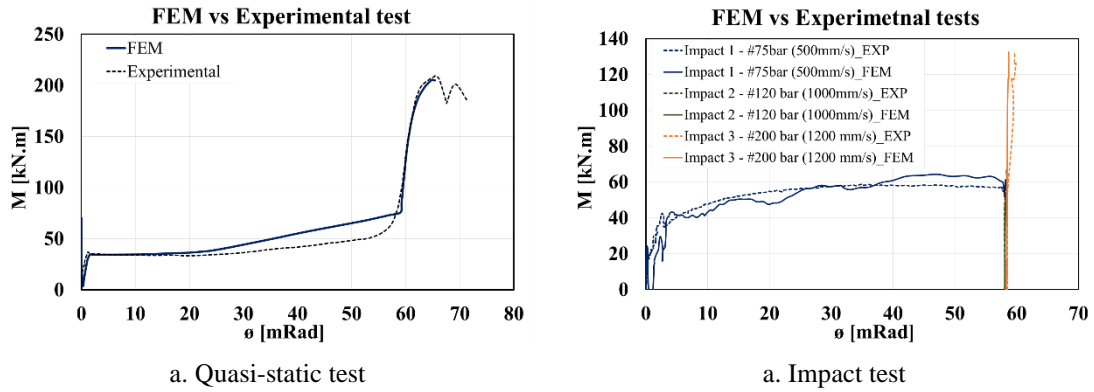


Figure 5.16 - FEM vs Experimental tests

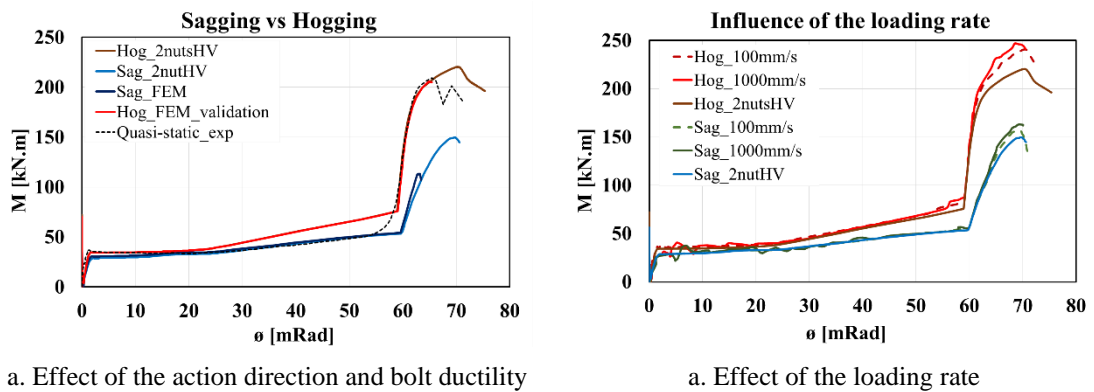


Figure 5.17 - Parametric FEM results

5.3.3 Studies on internal connections

Description of the test setup

The test campaign performed on the internal connections included a static monotonic test and drop weight tests on two different beam-to-column joint specimens equipped with Symmetrical Friction Dampers (SFDs-Figure 5.18)

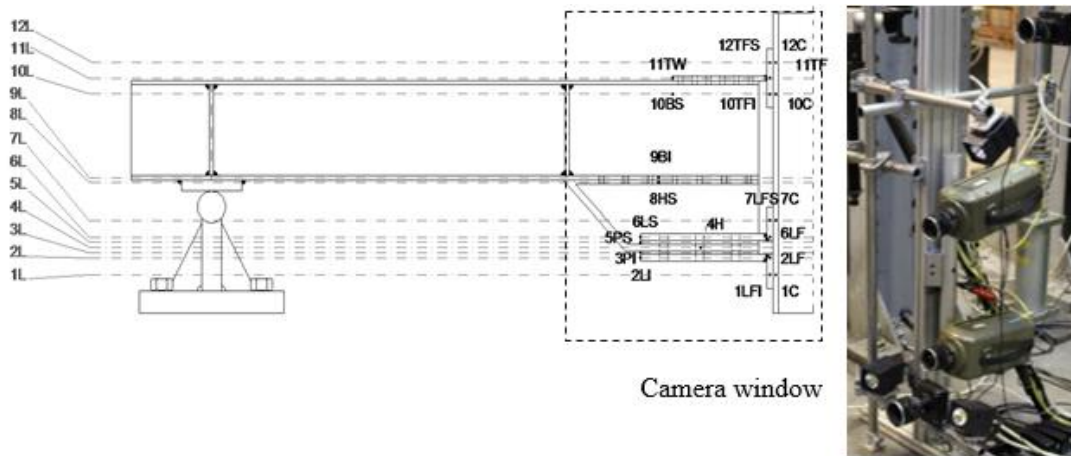


Figure 5.18 - Impact test configuration (half of the specimen) with digital image correlation measurement

The impact tests have been performed through a dropping mass, which hits the head of the column with variable speeds (Figure 5.18 and Figure 5.20). Two parameters were modified in the performed tests: the dropping height of the impacting mass fixed to a maximum of 4.1 meters from the top of the impacted column and the dropping mass weight (M1=211 kg and M2=460 kg – Figure 5.20). These parameters are fixed according to the targeted impact energy during the test. The dropping mass is connected to tubular guides (Figure 5.20), which are guiding the mass until the impact and during the rebound. All the specimens are identified with an alphanumeric tag describing the main features of the test, as reported in Figure 5.19, where the code is indicating (i) the type of test (IT for Impact Test or ST for Static Test), (ii) the joint configuration (FR for FREEDAM joint), (iii) the number of the test (01, 02, etc.), (iv) the used mass (M1 = 211kg or M2=460 kg) and (v) the dropping height (H250 means a dropping height of 250mm).

Test label example:

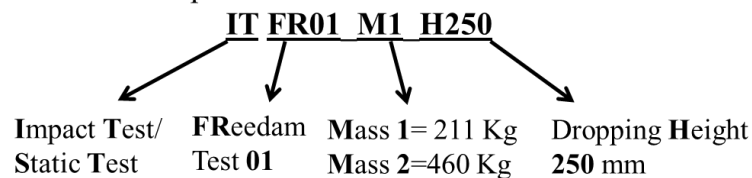


Figure 5.19 Test nomenclature

A total number of 6 impact tests were performed as reported in Table 5.5. For the mass M1, the dropping heights ranged from 250 mm to 4300 mm while, for the mass M2, the heights varied from 250 mm up to 3744 mm (maximum exploitable height considering the encumbrance of the specimen and the mass). Overall, falling speeds ranged from 2.04 m/s to 8.45 m/s. Two specimens were tested, specimen 1 was impacted 5 times, while specimen 2 was impacted one time with the maximum exploitable impact energy. A summary of the performed impact tests is provided in Table 5.5, where “1*” means a sequential impact on the same specimen.

Moreover, calibration tests on the used equipment and tensile tests on the used material were performed. The calibration tests consisted of preliminary impact tests on simply supported beams [30].

Table 5.5. Impact test labels and main properties

Impact test	Specimen	M [kg]	h [m]	v [m/s]
ITFR01-M1-H250	1	211	0.25	2.04
ITFR02-M1-H4300	1	211	4.3	8.97
ITFR03-M2-H250	1*	460	0.25	1.98
ITFR04-M2-H2000	1*	460	2	6.09
ITFR05-M2-H2500	1*	460	2.5	6.93
ITFR06-M2-H3744	2	460	3.74	8.45

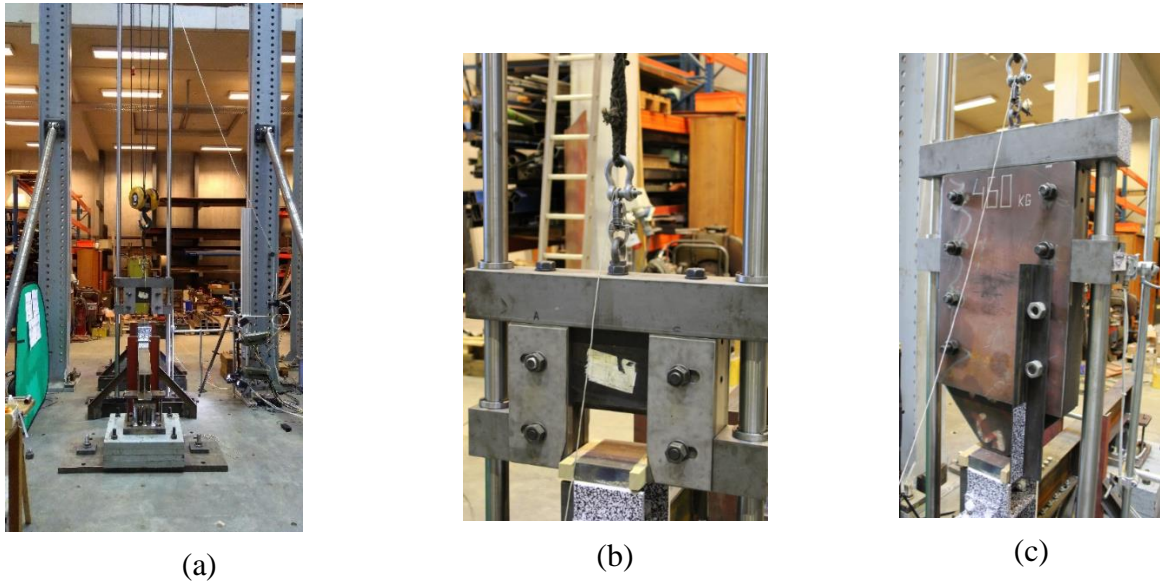


Figure 5.20 Impact test layout: Mass M1 (211kg) (b) and M2 (460 kg) (c)

All the measurements during the tests were performed using the Digital Image Correlation (DIC) technique (Figure 5.18).

Results of the experimental tests

Through the static tests, force vs. vertical displacement and moment vs. rotation curves were derived through the use of displacement and rotation transducers; these curves are reported in Figure 5.21. It can be observed that an almost perfect symmetrical behaviour of the specimen is observed, as expected. The maximum applied force was reached due to the unexpected occurrence of global out-of-plane instability of the specimen; to avoid this phenomenon during the impact test, the lateral restraints of the tested specimens were strengthened for the impact tests. These curves have been used as reference results to validate the numerical approach used later on to perform parametrical studies.

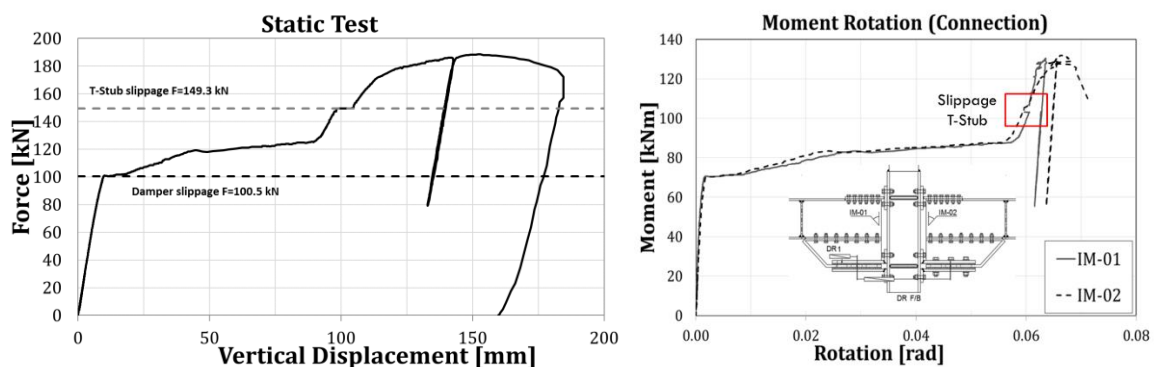


Figure 5.21 force vs. vertical displacement and moment vs. rotation curves obtained through the static test

Two impact tests were performed with the mass M1 on specimen 1: tests ITFR01-M1-H250 and ITFR02-M1-H4300 (Table 5.5). The first test was performed with a small dropping height 250 mm to remain in the elastic domain (i.e. no plasticity should be experienced in any components

of the joint) while the second one with a dropping height of 4300 mm was performed to activate plasticity in the tested specimen.

Four impact tests were performed with the mass M2: three of them (ITFR03, ITFR04 and ITFR05) on specimen 1, i.e. sequential impacts on the specimen previously tested with the mass M1 with the main objective of calibrating the testing setup with the new mass M2; the last one (ITFR06) has been performed with the maximum capacity of the system, in terms of energy and velocity, on specimen 2. Several points, belonging to the main joint components, were recorded with the cameras during the impact. Some examples are reported in *Figure 5.22* where the vertical displacement of Point 10 C (see Figure 5.18) vs time curves for the different tests are provided. The Figures are reporting a similar trend of displacement evolution in time for all the points registered.

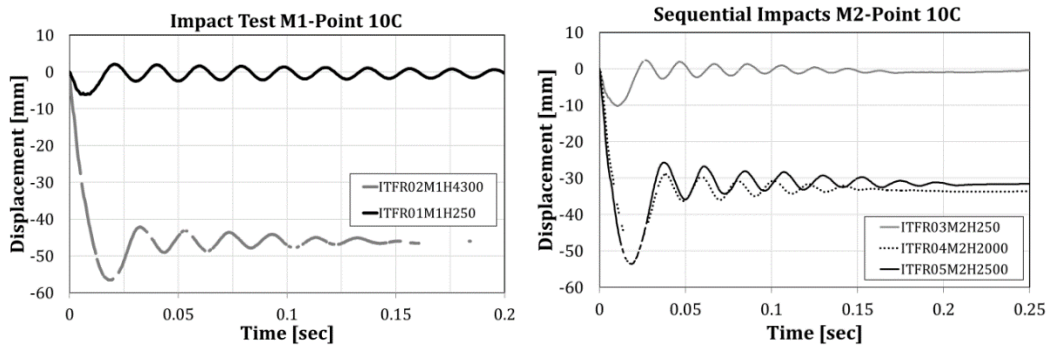


Figure 5.22 Impact test results – examples of point displacement vs. time measurements for the point 10C

In tests ITFR01-M1-H250 and ITFR03-M2-H250, everything remains elastic and the specimen does not show any permanent deformations after the tests. Test ITFR02-M1-H4300 exhibited a permanent deformation of 46.2 mm at the end of the test but the level of associated plasticity in the joint components was still limited. Indeed, the energy associated to the impact with mass M1 was not sufficient to activate plasticity in the joint components; however, the friction device exhibited a slippage of about 20 mm resulting in the above mentioned permanent deformation. Considering the total dimension of the slotted holes of 65 mm and as the bolts were placed in the centre of the slot, the bolts have reached the end stroke of the holes. The test with the maximum available energy and velocity (ITFR06) shown a slip of 24 mm of the SFD and permanent deformation of 88.5 mm (Figure 5.25).

In all the performed tests, theoretical velocities calculated for the impact ($v_{theo,imp}$ – see Eq. (5.1)) are slightly different from the one detected by the acquisition system ($v_{act,imp}$). Indeed, the real velocities are usually lower than the theoretical ones and, accordingly, the same is observed for the energies ($E_{act,imp}$ is the actual Energy and $E_{theo,imp}$ the theoretical one – see Eq. (5.2)).

$$v_{theo,imp} = \sqrt{2gh} < v_{act,imp} \quad (5.1)$$

$$E_{theo,imp} = \frac{1}{2}mv_{theo,imp}^2 < E_{act,imp} \quad (5.2)$$

where g is the gravitational acceleration, m is the weight of the dropped mass and h is the dropping height. In Table 5.6, actual and theoretical values are reported, showing that the lower

is the dropping height, the higher is the scatter. The observed difference is mainly associated with the friction developing between the dropping mass and the guiding system which is not taken into account in the theoretical estimation. However, in all the tests, the ratios between the actual velocity and the real one are close to 1, which shows a negligible influence of the friction on the real velocities. In the same table, the values of the maximum (δ_{max}) and permanent (δ_{perm}) deflections of the joint at the point 10 C are also reported. For the sequential impact (ITFR03, ITFR04 and ITFR05), the permanent displacement is referring to the previous test, the i -th maximum displacement ($\delta_{max,i}$) should be summed to the permanent displacements of all the previous impacts. It is clear that an increase of the dropping height results in an increase of the permanent deformation magnitudes.

If the impact velocity is close to the rebound one, namely the velocity when the impactor leaves the body, the impact is considered elastic. In reality, an impact is never completely elastic, part of the energy being used to deform the impacted body. The nature of the impact can be characterized by the ratio of these velocities called Coefficient of Restitution “COR” (see Eq. (5.3), given in Table 5.6. A value of this COR close to one means that the response of the specimen is mainly elastic.

$$COR = \frac{V_{reb}}{V_{theo,imp}} \leq 1 \quad (5.3)$$

The COR coefficient for the performed tests is varying from 0.58 for ITFR03 to 0.16 for ITFR02. The latter shows that increasing the energy of impact (mass weight and/or height) leads to more dissipation of energy through the activation of plastic deformations; thus, the impact becomes strongly inelastic.

Table 5.6. Impact Tests results

Impact test	h [mm]	$V_{theo,imp}$ [m/s]	$V_{act,imp}$ [m/s]	V_{reb} [m/s]	$V_{act,imp} / V_{theo,imp}$	$E_{theo,imp}$ [J]	$E_{act,imp}$ [J]	COR	δ_{max} [mm]	δ_{perm} [mm]
M1=211 kg										
ITFR01-	250	2.21	2.04	1.06	0.92	517.5	439.0	0.51	6.16	NA
ITFR02- M1-H4300	4300	9.18	8.97	1.49	0.98	8900.6	8488.6	0.16	56.5	46.2
M2=460 kg										
ITFR03-	250	2.21	1.98	1.16	0.89	1128.2	901.7	0.58	10.2	NA
ITFR04- M2-H2000	2000	6.26	6.09	1.20	0.97	9025.2	8530.3	0.19	49.3	34.8
ITFR05-M2- H2500	2500	7.00	6.93	1.13	0.99	11281.5	11045.7	0.17	53.6	31.1
ITFR06- M2-H3744	3744	8.57	8.45	1.46	0.98	16895.2	16422.6	0.17	102.6	88.5

At the end of the impact tests, the achievement of a considerable level of plasticity in the L-stub and the T-stub was detected; also, the slippage of the friction device and the consumption of the pad coating material were visible.

Due to the limitation in the laboratory facilities, the impact force was not directly registered during the tests. Accordingly, the impulse-momentum theorem and a graphic approach were used ([14] & [30]).

Table 5.7 gives a summary of the two methodologies for the maximum impact force estimation. Even though the two methodologies are only a rough estimation of the force, the experimental values of the DIFs for the impacted joint are calculated, only for inelastic impacts as the DIF has a physical meaning only in this case (reported in Table 5.7). Moreover, for the cumulative impact tests ITFR04 and ITFR05, the slippage occurred already in the previous tests, thus, the maximum displacement and the permanent deformation cannot be used for the graphic method and are not reported in the table.

However, it has to be highlighted that the DIF coefficient computed for test ITFR06 may not be accurate with this method. Indeed, Lateral Torsional Buckling (LTB) occurred during the performed static test.

Accordingly, a FEM model as presented in the next section and validated through comparisons to the experimental results is used to first check the predicted values of the forces and secondly to broaden the experimental test campaign performing parametric analyses.

Table 5.7. DIF calculation

Test	δ_{max} [mm]	δ_{perm} [mm]	$v_{act,imp}$ [m/s]	v_{reb} [m/s]	t_{pulse} [s]	F_{ST} [kN]	F_{GR} [kN]	F_{IT} [kN]	DIF_{GR}	DIF_{IT}
Mass M1										
ITFR02 M1	56.5	46.2	8.97	1.49	0.018	118.5	123.1	122.6	1.039	1.03
Mass M2										
ITFR06 M2	102.6	88.5	8.45	1.46	0.027	158.7	164.6	168.8	1.037	1.06

where M is the dropping mass; $v_{act,imp}$ is the measured velocity; v_{reb} is the measured velocity of the first bounce; t_{pulse} is the impact width pulse, F_{ST} is the equivalent static force, F_{GR} is the impact force estimated with the graphic method and F_{IT} are the maximum impact force evaluated with the impulse theorem.

Simulation of the tests' results

Modelling assumptions

A preliminary FE model of the static test was developed in ABAQUS/CAE using an implicit dynamic solver as reported in [31]. However, the model did not include the damage of the materials and, even though the implicit dynamic analyses can be used also in case of impact tests, this method is time-consuming. Accordingly, in view of optimizing the running time which is of particular interest for the parametrical studies to be conducted and to avoid convergence problems, the simulations of the impact on the FREEDAM joint have been performed using an Explicit time integration. Explicit solution methods have been developed for high-speed problems where inertia plays an important role [21]. For sake of consistency, the explicit solver is also extended to the static analysis of the specimen and compared with the experimental results.

The approach used to build a FE modelling in the explicit solver is summarised herein. Exploiting the symmetry of the system, a short column (half of an HEB 200) was connected to the beam using SHJ. At the beam extremity, a roller was placed trying to reproduce as close as possible the laboratory boundary conditions, and half of the column was modelled accounting for a vertical plane symmetry (*Figure 5.23*). Two beam sections were laterally and torsionally restrained to reproduce the restraints placed in the experimental setup.

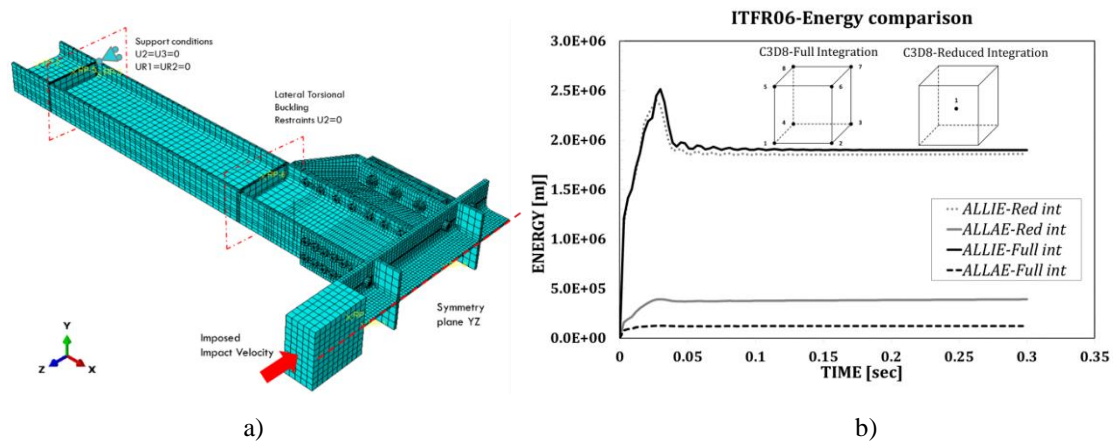


Figure 5.23. FEM detail and energy comparison

The impact has been performed by the means of a 3D discrete rigid body with isotropic inertia and it was meshed using rigid elements. Tie constraints were used to connect the stiffeners to the beam and the column. A general contact was introduced for all the elements, with a “hard contact” definition in the normal direction and a tangential behaviour with a 0.3 friction coefficient. The contact between the friction pads and the slotted haunch plate was defined as a surface-to-surface contact, with specific tangential friction and a normal behaviour following the classical Coulomb friction model. The impactor was placed directly in contact with the tested specimen, assigning to the mass the value of the initial velocities ($v_{act,imp}$ given in Table 5.6) of the real tests. C3D8 full integration was selected as the most appropriate one.

A mesh sensitivity study was also performed to select the best mesh compromise between the accuracy of the results and analysis time. Overall, the mesh is composed of 33737 elements for a total analysis time in between 20 and 48 hours for each simulation, depending also on the output requests. Moreover, two different analyses were performed: in a first analysis, the bolts were preloaded and, subsequently, a second dynamic analysis was performed and the state of deformation due to the preloading was charged as an initial condition at the beginning of the second analysis (as a predefined field). The bolts are modelled using the nominal diameter and scaling the material nominal stress as explained in [32–36]. The bolt preload is applied to the middle section of the bolt shank, using the option “Bolt Force”. Following the procedure presented in [30,37], the damping was modelled with the classical Rayleigh theory calibrating only the mass proportional coefficient ($\alpha=11$) with a damping ratio of approximately 2%.

The material models implemented in Abaqus are derived from coupon tests. The engineering curves are implemented in ABAQUS as true stress true strains curves with a Young modulus of

210 GPa and a Poisson ratio of 0.3. Ductile damage material is implemented following the procedure given by Pavlović in [38]. The damage was introduced only in the parts in which high plasticity is expected: T-Stub, L-stubs and bolts. Damage evolution can be extracted from experimental tests, using a reverse approach and calibrating the parameters by modelling the coupons tests in Abaqus [14,30]. Bolt modelling is implemented following the simplified model with an equivalent shank as explained in [36]. Since no coupon tests were performed on the bolts, reference is made to the tests reported in [32]. For dynamic loadings, the strain rate needs to be implemented in the model. From the results obtained in [30], the best way to account for strain rate in FEM modelling is using Johnson-Cook formulation. The latter has been used here.

Main results

The static test was simulated applying displacement to the column and extracting the reactions at the support (accounting for the symmetry). The behaviour of the specimen, when LTB is prevented, results in an increase of the resistance and a reduction of the ductility. Moreover, accounting for the material damages, the bolt failure can be detected by the model, which was not the case in the numerical simulation presented in [31,39], where the ductility was so overestimated. Introducing the damage and including the restraints out-of-plane to avoid the occurrence of the LTB, the dynamic simulation gives a good prediction of the maximum resistance achieved in the test. The failure is achieved at the bolt of the lower L-stub in combined shear and tension.

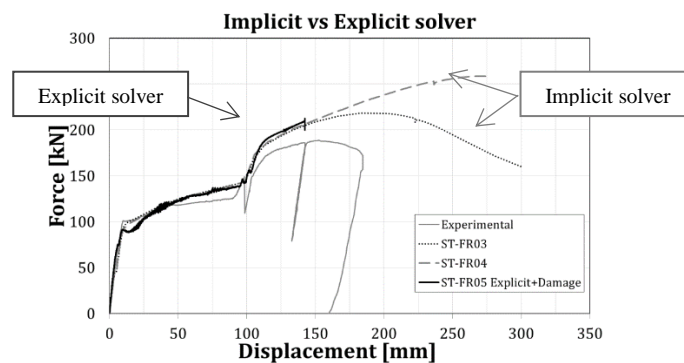


Figure 5.24. Comparison between an implicit and explicit simulation of the static test

This model has then been used to simulate the behaviour of the specimen under the impact. As shown in the comparisons presented in Figure 5.25, the developed model can catch with a good agreement the response of the joint during and after the impact.

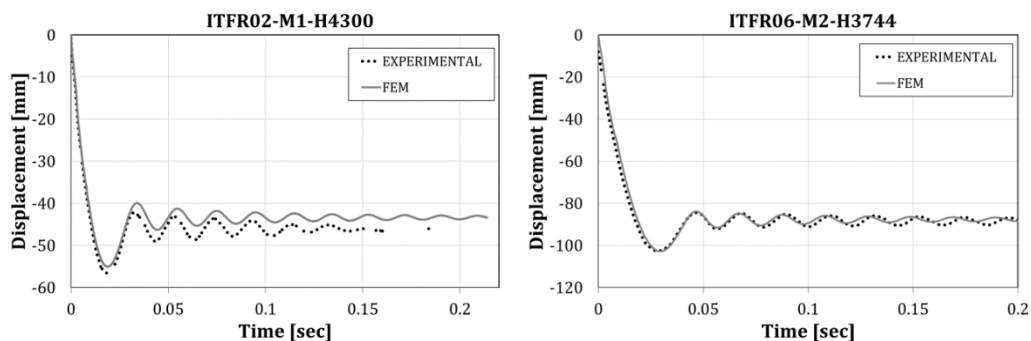


Figure 5.25 Experimental tests vs FE modelling

In *Table 5.8*, the comparison between the experimental results and the FEM analyses is reported in terms of maximum and permanent displacement (δ_{max} and δ_{perm}) with the relative errors in the prediction. Overall, the FEM seems to predict with good accuracy the two values with a maximum error of around 9% for the test ITFR01.

Table 5.8. Comparison of FEM experimental

Impact test	$\delta_{max,Exp}$ [mm]	$\delta_{perm,Exp}$ [mm]	$\delta_{max,FEM}$ [mm]	$\delta_{perm,FEM}$ [mm]	%err, δ_{max} [-]	%err, δ_{per} [-]
ITFR01-M1-H250	6.16	-	5.6	-	9.09%	-
ITFR02-M1-H4300	56.7	46.2	55.1	43.9	2.82%	4.98%
ITFR06-M2-H3744	102.6	88.5	102.8	87.8	0.19%	0.79%

Since it was not possible to record the forces associated with the impact during the experimental tests, the so-validated FEM model is a useful tool to estimate the force summing the reactions at the support points. For the calculation of the DIF from the FEM modelling, the static resistance obtained from the FEM was used ($F_{ST,FEM}$) instead of the experimental one (F_{ST}) as, for the static experimental test the lateral-torsional buckling was not prevented while it was the case for the impact tests and in the numerical simulations. *Table 5.9* gives also a comparison between the DIFs calculated with different methods. From the comparison, it seems that the impulse theorem underestimates the DIF values.

Table 5.9. Impact force estimation and DIF

Test	$\delta_{max,EX}$ [mm]	$\delta_{perm,EX}$ [mm]	$\delta_{max,FEM}$ [mm]	F_{ST} [kN]	$F_{ST,FEM}$ [kN]	$F_{DYN,FEM}$ [kN]	E_{Diss} [kNm m]	DIF_{FEM} [-]	DIF_G R [-]	DIF_{IT} [-]
ITFR02	56.5	46.2	55.1	118.5	124.9.18	136.8	4774.2	1.09	1.04	1.03
ITFR06	102.6	88.5	102.8	159.7	153.2	179.2	11234	1.14	1.04	1.06

* where $\delta_{max,EX}$ is the maximum displacement in the experimental tests; $\delta_{perm,EX}$ is the permanent deformation in the experimental tests; $\delta_{max,FEM}$ is the maximum displacement in the FEM; F_{ST} is the equivalent static force; $F_{ST,FEM}$ is the static force estimated with the FEM; $F_{DYN,FEM}$ is the force associated to impact; E_{Diss} is the dissipated energy.

With the help of the validated FE model, parametric analyses have been performed to extend the results obtained through the experimental test campaign under impact. Overall, the most important parameter influencing the joint behaviour is the impact energy but different joint behaviours can be identified when different impact masses or velocity are used. In particular, from the parametric study, the energy dissipation capacity of the joint, which is the best parameter to classify the response, is identified with the use of a parameter called Energy dissipation rate R_e [40]. Three groups of parametric analyses were performed for a total of 25 simulations:

- The first group (Group 1) investigates the influence of the impact velocity with mass weights (M1=0.106t, M2=0.23t and M3=0.3t).
- Group 2 investigates the influence of the mass weight variation on the joint response keeping constant the velocity ($V=6.26$ m/s).
- The last group (Group 3), investigates the influence of the contemporary variation of mass and velocity keeping constant the impact energy ($E_{11}=8.83E+03$ J).

The main outcomes of the conducted parametrical study can be summarised as follows:

- Increasing V or M increases R_E but, when the impact energy is constant, the joints resist better to higher velocity rather than higher masses due to strain rate effects, even though the investigated velocity range is limited due to the achievement of the bolt failure. The vertical displacement seems to be more sensitive to the drop weight than the velocity;
- There is not a clear correlation between the DIF and the velocity of rotation of the joint because many factors are contributing to a different distribution of velocity in the joint component (velocity, mass and energy of impact);
- The global DIF of the joint does not exhibit a clear correlation with the measured maximum strain rate appearing in the specimen.

5.3.4 Summary of new information for design provisions

As a general outcome of the conducted studies, it has been demonstrated that the FREEDAM connection and its friction dampers exhibit a good and ductile behaviour in case of dynamic loading and, in particular, in case of impact. Significant energy can be dissipated through the activation of the friction damper and its associated significant displacements.

Dynamic effects influence the global response of the connection. In particular, it has been demonstrated that higher resistances can be reached due to (i) an increase of the friction coefficient at the level of the friction pad and (ii) the development of strain rate effects at the level of joint components while the ductility is slightly affected.

To profit from this positive effect, it is required to ensure the activation of ductile components at failure and so, to avoid brittle failures and, in particular, the failure of the bolts in shear and/or in tension.

The design of the FREEDAM joint considering the effect of strain rates can be assessed considering the static design rules and adding the influence of the strain rates. There are some different ways to consider the strain rates within the connection behaviour. In a simplified way, the global dynamic behaviour can be obtained by multiplying the static resistance by a DIF coefficient varying from 1.0 to 1.2 and the static friction resistance (slip resistance) by 1.1. Another option is introducing the effect of strain rates individually in each component of the connection and then apply the design rules. The introduction of these effects can be done through the application of trend lines such as those reported in Figure 5.8 and can be applied for the resistance and ductility of the components. In this way, it is possible to assess analytically the global and local behaviour of these connections for different loading velocities, depending on the induced strain rates [22,25].

For more advanced investigations, the conducted studies resulted in recommendations on how to appropriately simulate numerically the behaviour of FREEDAM joints through FEM. In particular:

- The use of the Johnson-Cook behaviour law to account for strain rate effects has been validated and recommended values for its characterisation parameters are recommended in [30];
- Methods to appropriately simulate the bolt preloading has been proposed and validated;

- The procedure given by Pavlović in [38] to simulate material damages has been applied and validated – in particular, values for the parameters to be used in this procedure are proposed in [14].

5.4 REFERENCES

- [1] G. Culache, M.P. Byfield, N.S. Ferguson, A. Tyas, Robustness of Beam-to-Column End-Plate Moment Connections with Stainless Steel Bolts Subjected to High Rates of Loading, *J. Struct. Eng.* 143 (2017).
- [2] J.B. Davison, Investigation the Robustness of Steel Beam-to-column connections, in: 10th Int. Conf. Steel, Sp. Compos. Struct., North Cyprus, May, 2011.
- [3] E.L. Grimsmo, A.H. Clausen, M. Langseth, A. Aalberg, An experimental study of static and dynamic behaviour of bolted end-plate joints of steel, *Int. J. Impact Eng.* 85 (2015) 132–145.
- [4] P. Barata, A. Santiago, J.P. C. Rodrigues, C. Rigueiro, Experimental behaviour of beam - to-column steel joints subjected to impact loading, in: Eighth Int. Conf. Adv. Steel Struct., Lisbon, July, 2015.
- [5] E. Saraiva, *Variação das propriedades mecânicas do aço relacionadas com problemas de impacto em estruturas.*, University of Coimbra, 2012.
- [6] K. Vedantam, D. Bajaj, N.S. Brar, S. Hill, Johnson - Cook strength models for mild and DP 590 steels, *AIP Conf. Proc.* 845 I (2006) 775–778.
- [7] J. Ribeiro, A. Santiago, C. Rigueiro, L. Simões da Silva, Analytical model for the response of T-stub joint component under impact loading, *J. Constr. Steel Res.* 106 (2015) 23–34.
- [8] H. Fransplass, M. Langseth, O.S. Hopperstad, Tensile behaviour of threaded steel fasteners at elevated rates of strain, *Int. J. Mech. Sci.* 53 (2011) 946–57.
- [9] G. Johnson, W. Cook, A constitutive model and data for metals subjected to large strains, high strain rates and high temperatures, in: *Proc. 7th Int. Symp. Ballist.*, The Hague, The Netherlands, 1983: pp. 541–7.
- [10] J. Malvar, J. Crawford, Dynamic increase factors for steel reinforcing bars, in: *Twenty-Eighth DDESB Semin.*, Orlando, n.d. [https://doi.org/10.1061/\(ASCE\)CF.1943-5509.0000971](https://doi.org/10.1061/(ASCE)CF.1943-5509.0000971).
- [11] T. McAllister, *World Trade Center building performance study: data collection, preliminary observations and recommendations.*, Federal Emergency Management Agency, Federal Insurance and Mitigation Administration, 2002.
- [12] Arup, *Review of international research on structural robustness and disproportionate collapse*, Department for Communities and Local Government, 2011.
- [13] FREEDAM, *FREE from DAMAge Steel Connections, Final Report*, 2019.
- [14] M. D’Antimo, *Impact characterization of innovative seismically designed connections for robustness application*, 2020.
- [15] A.F. Santos, *Behaviour of friction joints under impact loads*, University of Coimbra, PhD thesis, 2019.
- [16] Eurocode 3, *Design of steel structures. Part 1.8: Design of joints*, Brussels, Belgium, 2010.
- [17] P. Barata, A. Santiago, J.P.C. Rodrigues, C. Rigueiro, Development of an experimental system to apply high rates of loading, *Int. J. Struct. Integr.* 7 (2016) 291–304.
- [18] W.-S. Lee, C.-F. Lin, Impact properties and microstructure evolution of 304L stainless

- steel, *Mater. Sci. Eng. A*. 308 (2001) 124–135.
- [19] W.E. Luecke, J.D. McColskey, C.N. McCowan, S.W. Banovic, R.J. Fields, T. Foecke, T.A. Siewert, F.W. Gayle, *Mechanical Properties of Structural Steels, Federal Building and Fire Safety Investigation of the World Trade Center Disaster, NIST NCSTAR 1-3D*, 2005.
- [20] J. Ribeiro, A. Santiago, C. Rigueiro, L.S. Da Silva, Analytical model for the response of T-stub joint component under impact loading, *J. Constr. Steel Res.* 106 (2015) 23–34.
- [21] Abaqus, *Abaqus Theory Manual*, 2011.
- [22] A.F. Santos, A. Santiago, M. Latour, G. Rizzano, Analytical assessment of the friction dampers behaviour under different loading rates, *J. Constr. Steel Res.* 158 (2019) 443–459. <https://doi.org/10.1016/j.jcsr.2019.04.005>.
- [23] A.F. Santos, A. Santiago, M. Latour, G. Rizzano, Analytical assessment of the friction dampers behaviour under different loading rates, *J. Constr. Steel Res.* 158 (2019) 443–459.
- [24] Np En 1993-1-8, Norma Portuguesa - Eurocódigo 3 - Projeto de estruturas de aço, *Inst. Port. Da Qual.* (2010) 146.
- [25] A.F. Santos, A. Santiago, M. Latour, G. Rizzano, L. Simões da Silva, Response of friction joints under different velocity rates, *J. Constr. Steel Res.* 168 (2020). <https://doi.org/10.1016/j.jcsr.2020.106004>.
- [26] M. D’Aniello, D. Cassiano, R. Landolfo, Monotonic and cyclic inelastic tensile response of European preloadable gr10 . 9 bolt assemblies, *J. Constr. Steel Res.* 124 (2016) 77–90.
- [27] E. Munoz Garcia, J. Davidson, A. Tyas, Analysis of the response of structural bolts subjected to rapid rates of loading, in: *4th Eur. Conf. Steel Compos. Struct. - EUROSTEEL*, Maastricht, The Netherlands, 2005.
- [28] E.L. Grimsmo, A.H. Clausen, A. Aalberg, M. Langseth, A numerical study of beam-to-column joints subjected to impact, *Eng. Struct.* 120 (2016) 103–115.
- [29] M. Latour, M. D’Aniello, M. Zimbru, G. Rizzano, V. Piluso, R. Landolfo, Removable friction dampers for low-damage steel beam-to-column joints, *Soil Dyn. Earthq. Eng.* 115 (2018) 66–81.
- [30] M. D’Antimo, M. Latour, J.-F. Rizzano, Gianvittorio Demonceau, Experimental and numerical assessment of steel beams under impact loadings, *J. Constr. Steel Res.* 158 (2019) 230–247. [https://doi.org/10.1061/\(asce\)st.1943-541x.0002288](https://doi.org/10.1061/(asce)st.1943-541x.0002288).
- [31] M. D’Antimo, M. Zimbru, M. D’Aniello, J.-F. Demonceau, J.-P. Jaspart, R. Landolfo, Preliminary finite element analyses on seismic resistant FREE from DAMAge beam to column joints under impact loading, 2018. <https://doi.org/10.4028/www.scientific.net/KEM.763.592>.
- [32] M.D. Aniello, D. Cassiano, R. Landolfo, Monotonic and cyclic inelastic tensile response of European preloadable gr10 . 9 bolt assemblies, *J. Constr. Steel Res.* 124 (2016) 77–90. <https://doi.org/10.1016/j.jcsr.2016.05.017>.
- [33] M. D’Aniello, R. Tartaglia, S. Costanzo, R. Landolfo, Seismic design of extended stiffened end-plate joints in the framework of Eurocodes, *J. Constr. Steel Res.* 128 (2017) 512–527. <https://doi.org/10.1016/j.jcsr.2016.09.017>.
- [34] M.D. Aniello, M. Zimbru, M. Latour, A. Francavilla, Development and validation of design criteria for free from damage steel joints, 1 (2017). <https://doi.org/10.1002/cepa.57>.
- [35] M. D’Aniello, M. Zimbru, R. Landolfo, M. Latour, G. Rizzano, V. Piluso, Finite element analyses on free from damage seismic resisting beam-to-column joints, in: *COMPDYN*

- 2017 - Proc. 6th Int. Conf. Comput. Methods Struct. Dyn. Earthq. Eng., 2017: pp. 802–814. <https://doi.org/10.7712/120117.5458.17524>.
- [36] M.D. Aniello, D. Cassiano, R. Landolfo, Simplified criteria for finite element modelling of European preloadable bolts, *Steel Compos. Struct.* 6 (2017) 643–658.
- [37] M. D’Antimo, M. Latour, J. Jaspart, J. Demonceau, Numerical and experimental investigation of simply supported steel beams under drop-weight impact tests, *Ce/Papers.* 3 (2019) 803–809. <https://doi.org/10.1002/cepa.1137>.
- [38] M.S. Pavlovic, Resistance of Bolted Shear Connectors in prefabricated steel-concrete composite decks, (2013) 1–10.
- [39] M. D’Antimo, M. Latour, G. Rizzano, J.-F. Demonceau, J.-P. Jaspart, Preliminary Study on beam-to-column joints under impact loading, *Open Constr. Build. Technol. J.* (2017).
- [40] H. Wang, B. Yang, X.H. Zhou, S.B. Kang, Numerical analyses on steel beams with fin-plate connections subjected to impact loads, *J. Constr. Steel Res.* (2016). <https://doi.org/10.1016/j.jcsr.2016.05.016>.

CHAPTER 6

SEISMIC SIMULATION BY PSEUDO-DYNAMIC TESTING

6.1 INTRODUCTION

In the previous sections the behaviour of FREEDAM connections has been described considering the experimental and numerical response of both sub-assemblies and friction dampers. In this section, considering the lack of experimental data dealing with the assessment of the behaviour of real-scale buildings with friction joints, the results of the tests on full scale structures developed during the FREEDAM project are presented. Historically, only few works have been devoted to the experimental behaviour of full-scale steel structures under seismic loading conditions. This obviously leaves some uncertainties on the range of validity of the modelling approaches usually adopted for non-linear time-history analyses. In fact, numerical models are commonly adopted, but the specialist engineer usually is not aware about the limitations concerning the range of application of the models. This because of the limited availability of full-scale experimental data to be used for the validation of the analytical approaches. Obviously, such a lack of data arises from practical limitations due to limited resources, availability of full-scale test equipment and the significant efforts needed to carry out campaigns on full-scale specimens of structures.

Within this framework, in this section the assessment of the dynamic behaviour of full-scale structures with FREEDAM connections and RBS connections are presented. To this scope, at the STRENGTH Laboratory of the University of Salerno pseudo-dynamic tests on buildings has been carried out. For the sake of clarity, it is worth highlighting that such a testing activity is a part of a wider experimental program which regards the investigation of five different connection typologies, all designed to provide a rotation capacity higher than the minimum required by Eurocode 8 for Ductility Class High (DCH): RBSs (Reduced Beam Section) connections; low-damage connections (FREEDAM type), Extended End-Plate (EEP) connections, Double-Split Tee (DST) and Double-Split X-shaped Tee (DST-X) connections. At the moment, the planned testing activity has dealt with the execution of two experimental campaigns on a full-scale two-storey steel building equipped with RBS connections, in the first campaign, and FREEDAM joints, in the second one. The main results of these pseudo-dynamic tests are reported in this section showing the benefits provided by low-damage connections in comparison with traditional strategies of conceiving beam-to-column joints.

6.2 MOCK-UP BUILDING

The mock-up is a one-bay two-storey steel structure composed of two longitudinal MRFs which are transversally braced to prevent undesired accidental torsional rotations. The longitudinal span is equal to 4 m, the transverse span is equal to 2 m and the inter-storey height is equal to 2.40 m. Since the aim of the study consists in assessing the behaviour exhibited by RBS and FREEDAM connections when belonging to a real-scale building, the mock-up was conceived to allow the

easy replacement of both the connections and the damaged column or beam ends enabling the execution of two experimental campaigns, one for each analysed connection typology (Figure 6.1). The experimental activity aims to assess the seismic response of the structure subjected to a series of seismic events using the pseudo-dynamic testing method. Through this technique, the seismic behaviour of the structure is assessed without imposing ground accelerations, but by applying, with a couple of hydraulic actuators, floor displacements evaluated solving step by step the dynamic equations of motion [1]-[3].



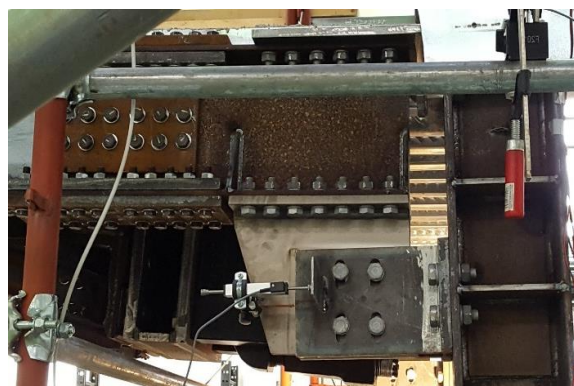
a) Mock-up with RBS connections



b) Mock-up with FREEDAM connections



c) RBS connection



d) FREEDAM connection

Figure 6.1 – The mock-up and its connections

For the sake of clarity, the main information regarding the mock-up is briefly summarized. The floors are made of HI-BOND A55 steel profiled decking which, including the reinforced concrete slab, has a total height equal to 100 mm. The deck transfers the loads to five equally spaced IPE 140 or HEB 140 secondary beams (Figure 6.2). The seismic-resistant scheme does not exhibit any composite behaviour because no shear studs have been adopted and an appropriate gap has been left between the reinforced concrete slab and the columns as suggested also by Eurocode 8. Rigid steel footings fastened with high strength dywidag bars assure the connection of the mock-up and the reaction braced frame to the strong floor of the laboratory. Furthermore, a rigid foundation diaphragm connects the steel footings of the mock-up to the base of the reaction braced frame.

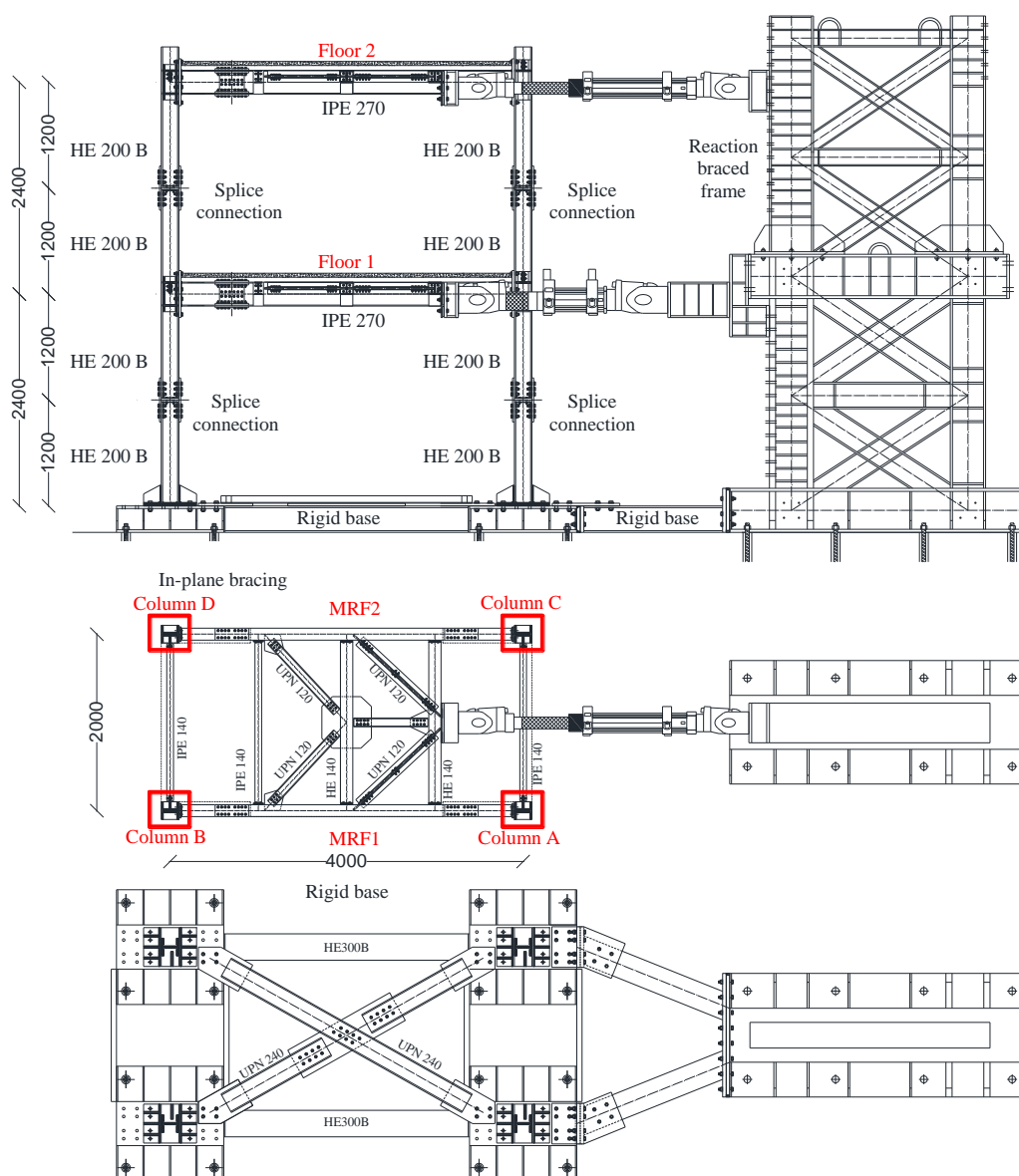
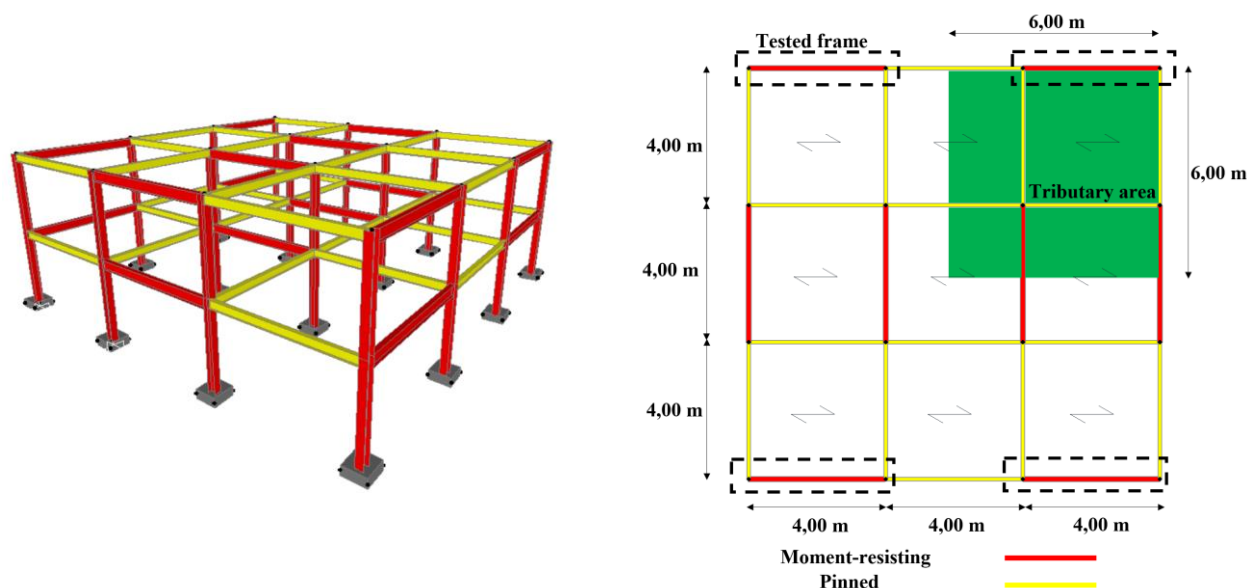


Figure 6.2 – Building mock-up (with RBS connections)

IPE 270 beams made of S275JR steel grade and HEB 200 columns made of S355JR steel grade have been adopted for the structural members. The design of the frame has been carried out according to Eurocode 8 [4], [5] provisions. Specifically, the MRFs are designed in Ductility Class High (DCH) and the structural members have been designed considering both serviceability and ultimate limit state requirements (behaviour factor equal to 6, type-1 spectrum, peak ground acceleration equal to 0.35 g and type-B soil, 1% inter-storey drifts under service conditions assuming that the partition walls do not interfere with the deformation of the main structure). The tested mock-up has been chosen so that the MRFs are representative of a reference structure characterized, for each direction, by three bays with lengths equal to 4 m (Figure 6.3). The archetype building is characterized by four MRFs in each direction, while the remaining bays are considered nominally pinned (Figure 6.3). The design values of the loads are the following: i) the dead loads are equal to 3.9 kN/m² and 3.6 kN/m² at the intermediate and at the roof level, respectively; ii) the live loads are equal to 3 kN/m² at the first level and 0.5 kN/m² at the roof level. The tributary area on each MRF corresponds to 1/4 the total floor area. The weight

of the structural members and claddings has been accounted for by increasing the masses of about 10%. In particular, the masses applied on each frame are equal to 19 tons and 14.2 tons at the first and second level, respectively.



a) 3D view of the reference structural scheme

b) Plan view and individuation of the tested frame

Figure 6.3 – Reference scheme adopted for the design of the tested MRFs

The experimental campaign carried out at the STRENGTH Laboratory of the University of Salerno belongs to a wider research program aimed at investigating the influence of different beam-to-column connections on the overall seismic behaviour of structures. For this reason, the adopted sequence of accelerograms is the same for both the completed experimental campaigns with RBS [5] and FREEDAM joints. The selected accelerograms and their amplified peak ground accelerations are reported in Table 6.1. It is worth highlighting that during the first experimental campaign, between Test 1 and Test 2 another test was performed, but it was a partial test and, for this reason, it is not reported hereinafter.

Table 6.1: Accelerograms used to perform the tests

Test n.	Accelerogram	PGA
1	Imperial Valley	1.10g
2	Spitak	0.80g
3	Artificial	0.50g
4	Santa Barbara	0.80g
5	Coalinga (partial)	0.80g

6.3 PSEUDO-DYNAMIC TESTING OF THE MOCK-UP BUILDING WITH RBS CONNECTIONS

In this section, the experimental data related to the campaign concerning the structure equipped with RBS connections are reported and discussed.

From the analysis of the experimental results, it is possible to anticipate that for all the tests the peak floor displacements and peak actuators' forces occurred in the same instants. This aspect agrees with the expected response because the structure is regular, and the first vibration mode is prominent. In Table 6.2 the main results are reported.

Table 6.2: Main experimental results (structure with RBS connections)

Imperial Valley 1.1g		Test 1	Test 2	Test 3	Test 4	Test 5	
Maximum base shear (kN)	Pull	-751	-652	-444	-586	-630	
	Push	667	670	555	592	612	
Peak first floor displacement (mm)	Pull	-78	-17	-29	-48	-47	
	Push	44	85	40	41	62	
Peak roof displacement (mm)	Pull	-150	-34	-66	-99	-94	
	Push	88	171	83	85	129	
Maximum inter-storey drift (%)	Pull	Level 1	-3.3	-0.7	-1.2	-2.0	-2.0
		Level 2	-3.0	-0.7	-1.5	-2.2	-2.0
	Push	Level 1	1.9	3.5	1.7	1.7	2.6
		Level 2	1.9	3.6	1.8	1.8	2.8

6.3.1 Imperial Valley (PGA = 1.10g)

The first test consisted of applying the ground acceleration recorded by the station located at Imperial Valley (USA) in 1979. It is important to highlight that the natural peak ground acceleration was equal to 0.37g but, in this case, an amplified PGA equal to 1.10g, about three times the real one, has been employed.

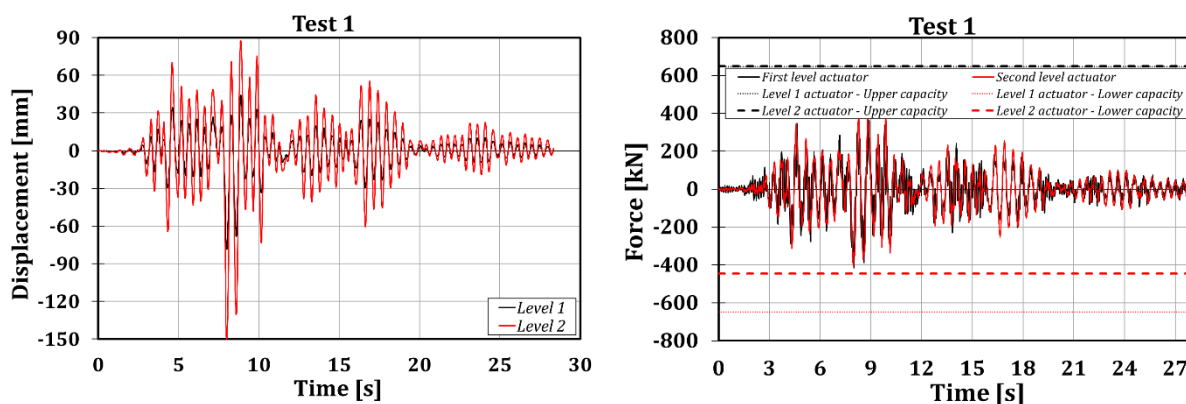


Figure 6.4 – Displacements (left) and reaction forces (right) histories for test 1

From Figure 6.4 it can be observed that the force values obtained from the actuator of the first level fluctuate more than the second level. This is mainly due to the accuracy of the force measurer installed in the MTS 243.60-02 actuator, which is characterized by a lower precision.

While the upper actuator (MTS 243.45-01) is equipped with a strain gauge load cell, the lower actuator is equipped with a differential pressure cell. The maximum base shear, peak displacements and inter-storey drifts are summarized for the two tests in Table 6.2.

It can be observed that the maximum inter-storey drift is about 3%, leading to a significant plastic engagement of the structural elements. The local measuring devices showed that both the RBS connections and the column bases underwent damage. The damage was larger for the RBS connections located at the first level and lower for the RBS connections of the second storey. The observed value of the RBSs yielding force is substantially in agreement with the design values (127.5 kNm).

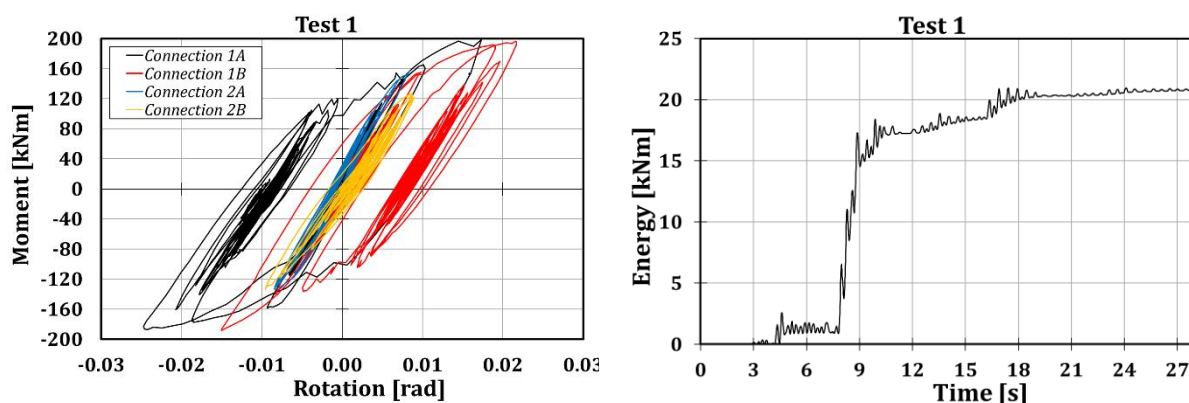


Figure 6.5 – RBSs hysteretic curves (left) and global dissipated energy (right) for Test 1 (MRF-1)

The state of damage occurring in the structure in Test 1 was due to the significant number of cycles experienced by the RBSs of the first level. This is shown by the hysteretic curves of the RBSs given in Figure 6.5 on the left. In Figure 6.5, the value of the energy dissipated by the RBSs calculated starting from the hysteretic curves is also reported on the right. It is worth observing that the RBS connections achieved a maximum local rotation slightly lower than 30 mrad, which is very close to the EC8 requirement for beam-to-column connections in DCH MRFs (35 mrad).

6.3.2 Spitak (PGA = 0.80g)

The second accelerogram was very different from the previous one because it was mainly characterized by a large amplitude peak only, while the previous one was characterized by a higher number of peaks. This feature is apparent from the results: for the Spitak earthquake, there is only one main excursion in the plastic range, characterized by an inter-storey drift of about 3.6%, while in all the other instants the structure remains practically elastic. This can be clearly understood analysing the local measurements considering, for instance, the moment-rotation response of the RBS connections (Figure 6.6). It can be noted that the moment-rotation response of the most stressed RBS connection is characterized by a peak rotation of about 30 mrad, with a bending moment at the RBS centreline equal to about 200 kNm.

It is useful to observe that this value of the peak moment is far beyond the expected value of the bending moment adopted in the design phase for the check of the connection, which was determined considering the plastic zone fully yielded and strain-hardened (140 kNm). This means that the overstrength factor equal to 1.1 suggested by EC8 is largely underestimated. In fact, in this case, the ratio between the measured bending moment and the nominal value of the

plastic resistance of the RBS is equal to about 1.6. This amount of overstrength, significantly exceeding the value given by the code provisions, is probably due to the reduction of the width-to-thickness ratio of the beam flanges in the RBS zone which practically prevent local buckling, as testified by the failure mode due to the fracture of either the flange or the weld.

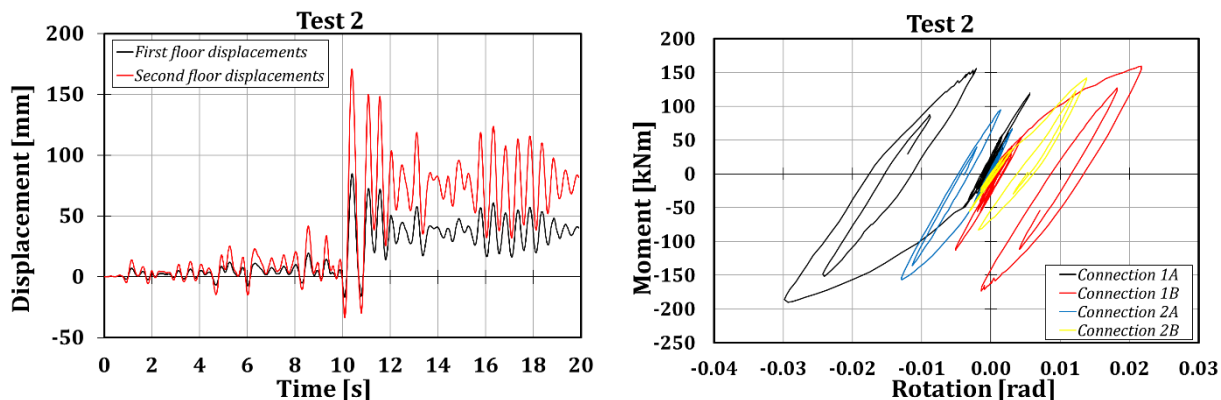


Figure 6.6 – Displacements histories (left) and moment-rotation curves (right)

6.3.3 Artificial record (PGA = 0.50g)

The third accelerogram has been artificially created by the SIMQKE tool to match the adopted design spectrum. This choice was made aiming to investigate the effects of an earthquake characterized by a high number of peaks in terms of acceleration. In this case, a peak ground acceleration (PGA) equal to 0.50g has been chosen.

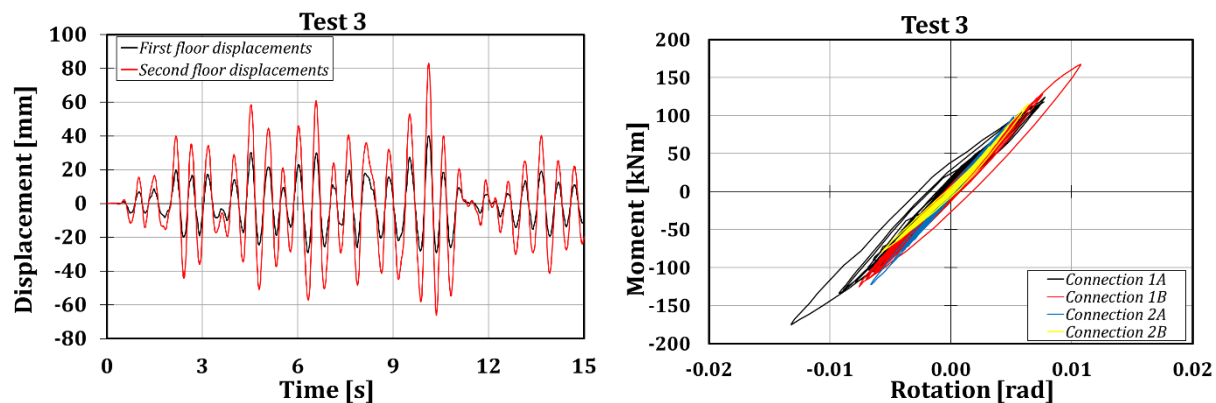


Figure 6.7 – Displacements histories (left) and moment-rotation curves (right)

During the third test, the RBS connections of the first level achieved bending moments of about 170 kNm, while at the second storey the RBS connections were only slightly damaged, experiencing maximum bending moments of 120 kNm and rotations lower than 10 mrad (Figure 6.7). The maximum base shear was equal to 555 kN and the maximum roof displacement equal to about 83 mm, leading to a maximum inter-storey drift equal to about 1.8%. In terms of moment-rotation curves, the RBS connections remained practically in the elastic range.

6.3.4 Santa Barbara (PGA = 0.80g)

Test 4 consisted of applying Santa Barbara accelerogram. This test did not show any further significant plasticization of the RBS connections and the structural behaviour remained almost in the elastic range, as it is clear observing the floor displacements and the moment-rotation

hysteretic curves reported in Figure 6.8. All the main results concerning this test are reported in Table 6.2.

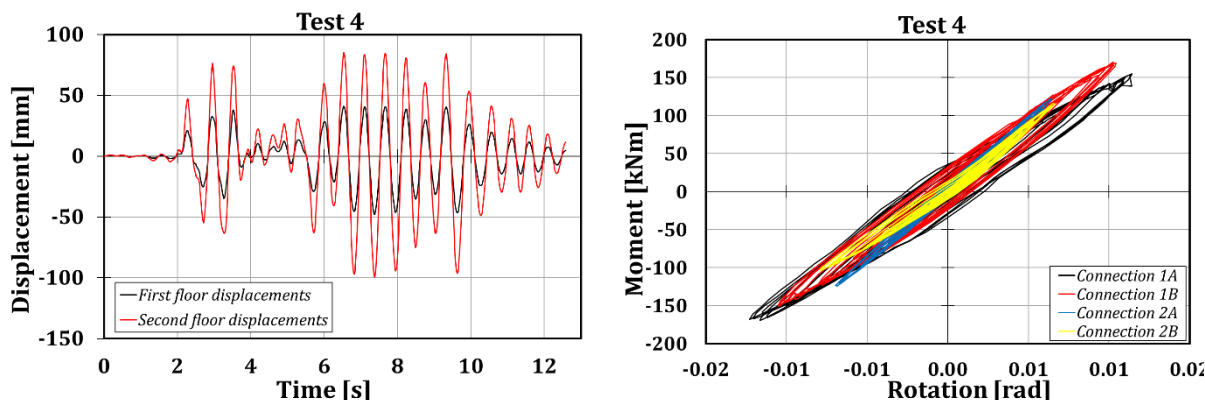
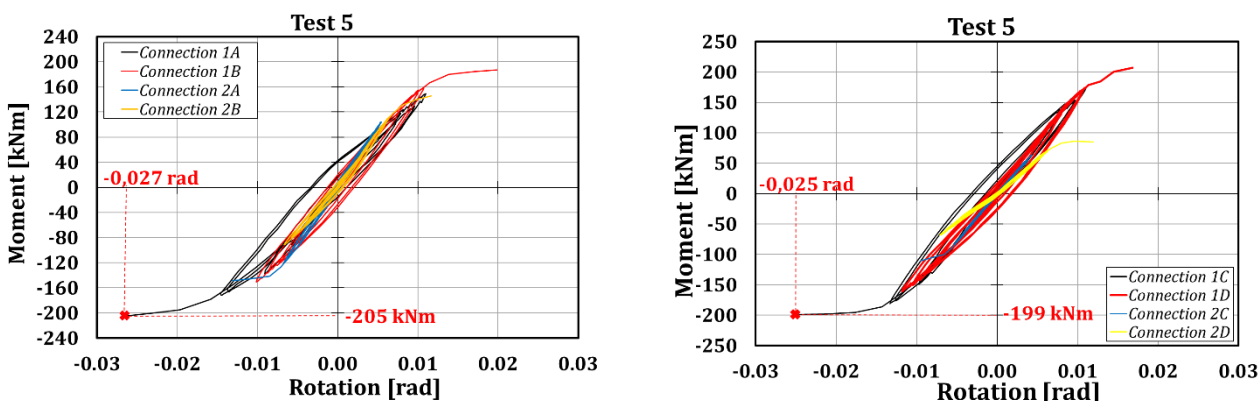


Figure 6.8 – Displacements histories (left) and moment-rotation curves (right)

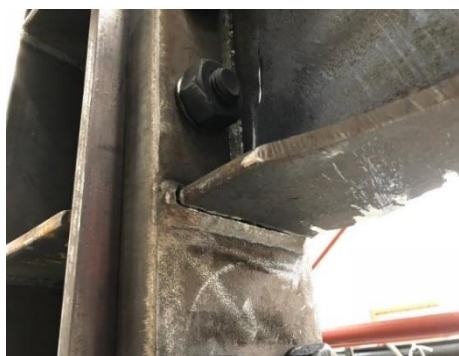
6.3.5 Coalinga (PGA = 0.80g)

The failure of the structure was achieved during Test 5. In particular, the last test was interrupted after the failure of two RBS connections located at the first storey of the building, on the two opposite frames, at the actuators’ side (Figure 6.9).



a) Test 7 – Columns A-B, 1st and 2nd storey

b) Test 7 – Columns C-D, 1st and 2nd storey



c) Failure in the welding of RBS 1A



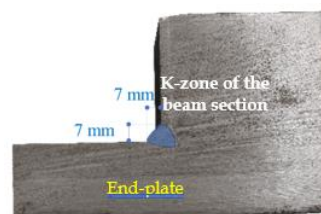
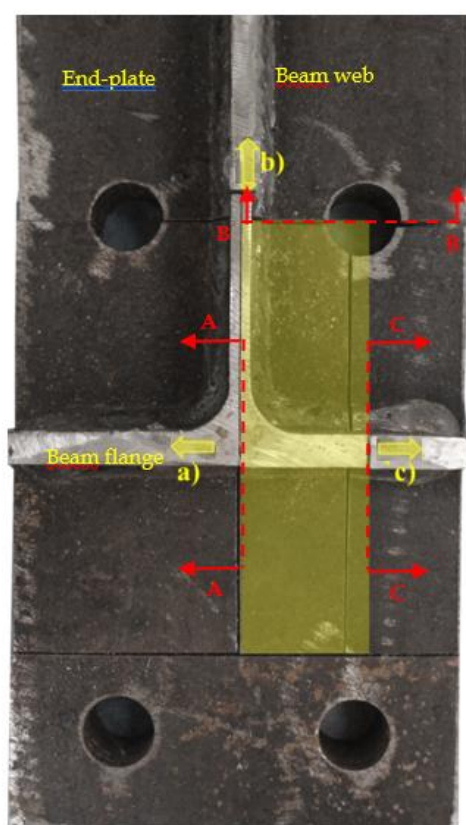
d) Failure at the centerline of RBS 1C

Figure 6.9 – Hysteretic curves of the collapsed RBSs (top) and corresponding damage patterns (bottom)

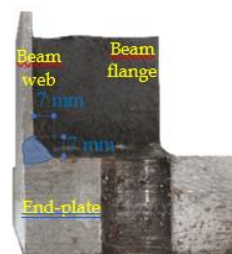
The failure was initiated by the local failure of the welding in the RBS-1A and, afterwards, also RBS-1C failed due to the redistribution of the actions which lead to a torsional moment and overload of the opposite frame. The local collapse of RBS-1A was attributed to the attainment

of the fatigue life of the welding and the unexpectedly high bending moment acting at the column flange level. It is worth to note that the bending moment at failure in RBS-1A was equal to 205 kNm. This value, as previously underlined, is bigger than the nominal resistance of the RBS of about 60% (Figure 6.9).

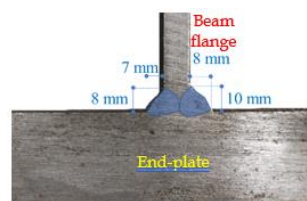
Even though the fracture of the weld connecting the beam flange to the column flange is a failure mode not expected in the case of RBS connections, it has to be considered that the loading protocol commonly adopted in the experimental analyses of the cyclic behaviour of RBS connections, typically performed on simple beam-to-column sub-assemblages, is completely different from the loading conditions occurring in the beam-to-column connections of the tested two-storey building because of the application of a series of five earthquakes. It seems that the fracture of the welds can be a consequence of the fatigue resulting from repeated earthquakes whose action overall gives rise to a high number of cycles having relatively small amplitudes, which are not able to lead to local buckling and only a few cycles with a large amplitude which did not give rise to local buckling because of the reduction of the width-to-thickness ratio of the beam flanges in the reduced section zone.



Side a): Flange weld: Partial Penetration



Side b) Web weld: Full Penetration



Side c) Flange weld: Full Penetration

Figure 6.10 – Hysteretic curves of the collapsed RBSs (top) and corresponding damage patterns

To check the accuracy of the welding detail, after the end of the test, a spare RBS already available in the laboratory and taken from the same product has been cut and inspected. The survey revealed that the full penetration butt joint detail was correctly realized and without significant defects (Figure 6.10). It is worth noting that the typology of weld detail adopted, complies with EC3 [6] and EC8 regulations and, additionally, complies with the indications

given in the AISC Steel Design Guide [7]. The beam-to-end plate welding, as recommended in the AISC Steel Design Guide, does not include access holes in the beam web to avoid the premature fracture of the beam flange due to stress concentration [8]. Therefore, as given in Figure 6.10 the beam flange was welded with 45° full penetration butt joints, making an exception for the area of the flange directly above the beam web, which was welded with a partial penetration joint on the external side and fillet welds in the roots. Since the detail complies with the code main suggestions, the obtained result confirms that the partially brittle failure must be attributed, on the one side, to the underestimation of the overstrength factors used in the design and, on the other side, to the rules adopted to design the welding details, which probably do not consider properly the fatigue life phenomena that may occur under the effect of repeated seismic events. This outcome highlights the need for further investigations devoted to the assessment of the seismic response of typical welding details under seismic actions and their low-cycle fatigue life.

Despite these considerations, it has to be observed that the tested RBS connections were subjected to a series of five destructive seismic events, which is a very severe condition normally not required by the current design practice. Therefore, even though the final collapse mode was not completely satisfactory, the behaviour of the MRFs was reasonable reliable, confirming the large energy dissipation capacity of the RBS connections.

In Figure 6.11 the floor displacements and the forces recorded by the actuators are shown. Further details can be found in Table 6.2.

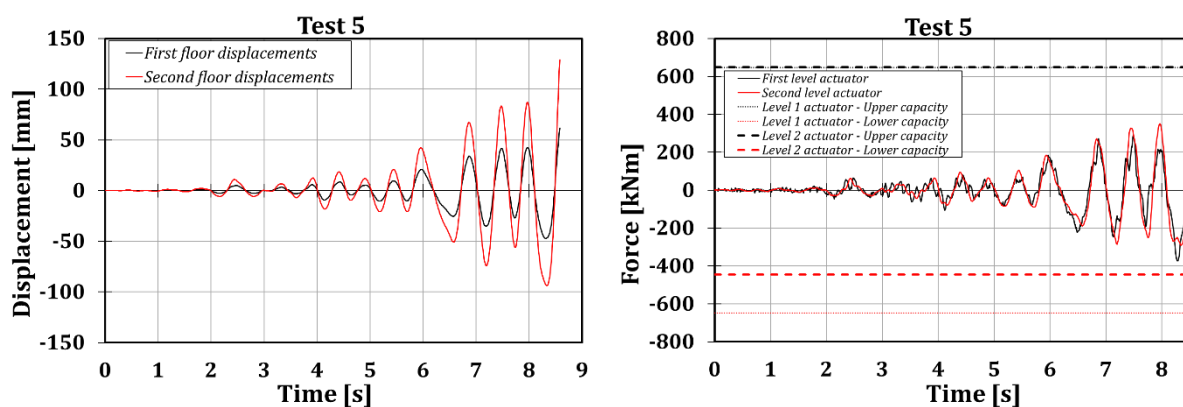


Figure 6.11 – Floor displacements (left) and actuators forces (right) of Test 5

6.4 PD TESTING OF THE MOCK-UP WITH FREEDAM CONNECTIONS

In this section, the experimental data of the campaign regarding the structure equipped with FREEDAM connections are reported and discussed. It is worth highlighting that the applied seismic inputs are the same employed in the previous campaign. Such a choice will allow comparing the seismic behaviour of the structure when equipped with the two analysed connections' typologies. In Table 6.3 the main results of the campaign are summarized.

Table 6.3: Main experimental results (structure with FREEDAM connections)

Imperial Valley 1.1g		Test 1	Test 2	Test 3	Test 4	Test 5	
Maximum base shear (kN)	Pull	-537	-447	-272	-388	-439	
	Push	477	470	347	483	495	
Peak first floor displacement (mm)	Pull	-73	-53	-41	-56	-72	
	Push	65	79	38	52	61	
Peak roof displacement (mm)	Pull	-104	-84	-75	-89	-112	
	Push	103	112	52	70	85	
Maximum inter-storey drift (%)	Pull	Level 1	-3.0	-2.2	-1.7	-2.3	-3.0
		Level 2	-1.3	-1.3	-1.4	-1.4	-1.7
	Push	Level 1	2.7	3.3	1.6	2.2	2.5
		Level 2	1.6	1.4	0.6	0.7	1.0

6.4.1 Imperial Valley (PGA = 1.10g)

The first test consisted of applying the Imperial Valley seismic input, as already done for the first experimental campaign. Unfortunately, because of technical problems that occurred with the external transducers during this test, no data about the local response of the connections are available. Therefore, it is only possible to discuss the floor displacements and the forces recorded by the actuators as depicted in Figure 6.12.

The displacements at the first and second floors achieved peak values equal to 73 and 104 mm, respectively, and the maximum base shear was equal to 537 kN (Table 6.3). It is possible to observe that the peak floor displacements and the peak reaction forces recorded by the actuators occurred at the same instants. This was expected because the structure is regular and it is characterized by the prominence of the first vibration mode. Another relevant aspect is related to the fact that the friction devices did not assure the self-recentring of the structure since residual displacements occurred at the end of the test (about 16 mm and 29 mm at the first and second floor, respectively).

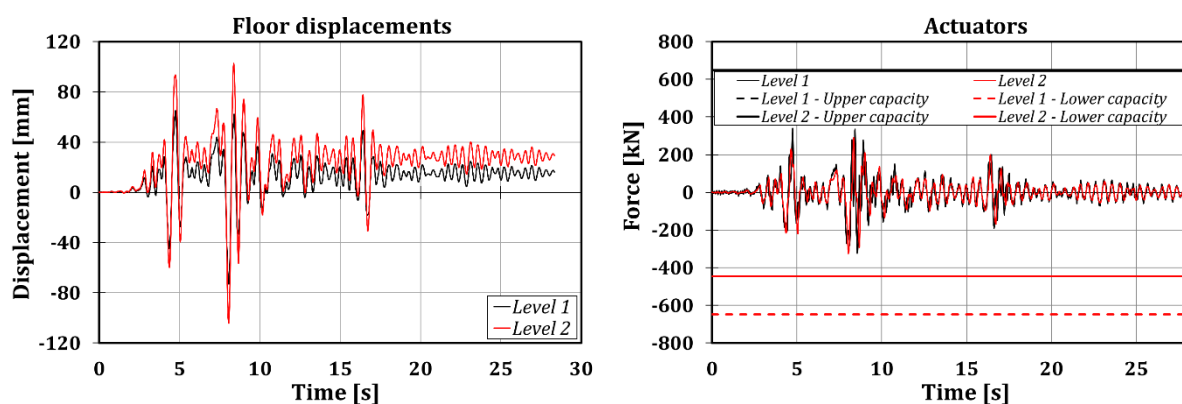


Figure 6.12 – Test 1: floor displacements (left) and reaction forces (right)

During this test, some of the friction dampers were subjected to slippage. Referring to Table 6.3, it is possible to note that the maximum inter-storey drifts achieved 3% and 1.6% at the first and

second floors, well beyond the nominal elastic limit of the structure equal to about the 1% as assumed in the design phase.

6.4.2 Spitak (PGA = 0.80g)

For the second test, the mock-up building has been subjected to the Spitak earthquake. In this case, also the experimental data referred to the behaviour exhibited by the connections are available. Regarding this accelerogram, it is worth highlighting a relevant feature: its time history is characterized by only one peak of significant amplitude, as already highlighted in the discussion of the experimental results concerning the previous experimental campaign. This aspect is reflected in the results: the mock-up experienced only one main excursion in the plastic range, as it is clear in Figure 6.13 where the results in terms of floor displacements and actuators reaction forces have been reported.

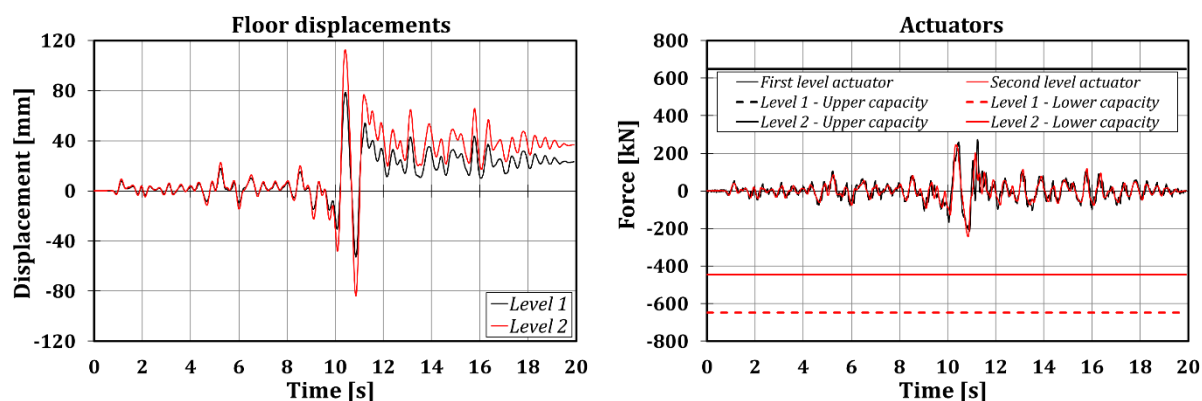


Figure 6.13 – Test 2: floor displacements (left) and reaction forces recorded by actuators (right)

Even though a maximum reduction of about 15% in terms of base shear has been observed, in comparison with Test 1, it is possible to observe a slightly larger peak roof displacement (112 mm vs 104 mm) and a maximum inter-storey drift equal to 3.3% at the first level. Moreover, in this case, the maximum inter-storey drifts are very low at the second level. In Figure 6.14 the local response in terms of hysteretic moment-rotation curves is reported. From this figure, it is possible to observe that wide and stable hysteretic rectangular-shaped moment-rotation curves were obtained, as expected.

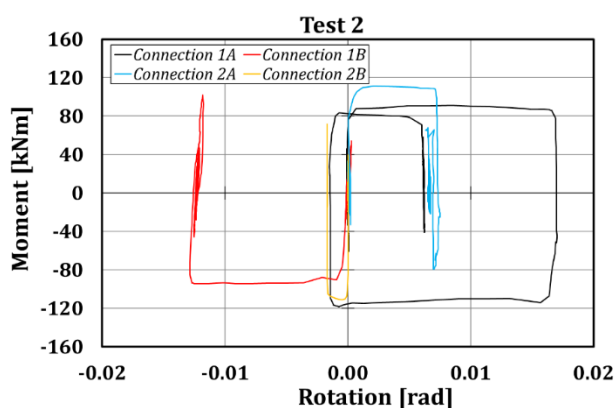


Figure 6.14 – Test 2: moment-rotation curves related to FREEDAM connections belonging to MRF-1

Nevertheless, it is possible to remark the asymmetric behaviour of the connections since the absolute values of the maximum and minimum bending moments are around 80 kNm and 120 kNm, respectively. This is in agreement with the asymmetry of the connection's behaviour already pointed out by the experimental tests on simple beam-to-column joints sub-assemblages [9], as discussed in the previous Chapter. Considering that the Spitak accelerogram is characterized by one main peak, as it was expected, it has been experimentally confirmed that the friction devices exhibit only one slipping excursion corresponding to the achievement of the PGA. The maximum rotation experienced by the connections was achieved by connection 1A and its value is about 17 mrad. The other connections achieved lower rotations. In particular, as expected, at the second level the connection rotations achieved the values of about 0.007 and 0.002 rad.

6.4.3 Artificial record (PGA = 0.50g)

With this artificially created accelerogram, that was selected for the sake of consistency with the similar structure tested in the previous experimental campaign, the MRFs remained almost in the elastic range, without additional residual displacements (Figure 6.15). The local measurements, in this test, also suggest a low plastic engagement of the structure as only connection 1A was slightly engaged in the plastic range experiencing a rotation of only 4 mrad (Figure 6.16).

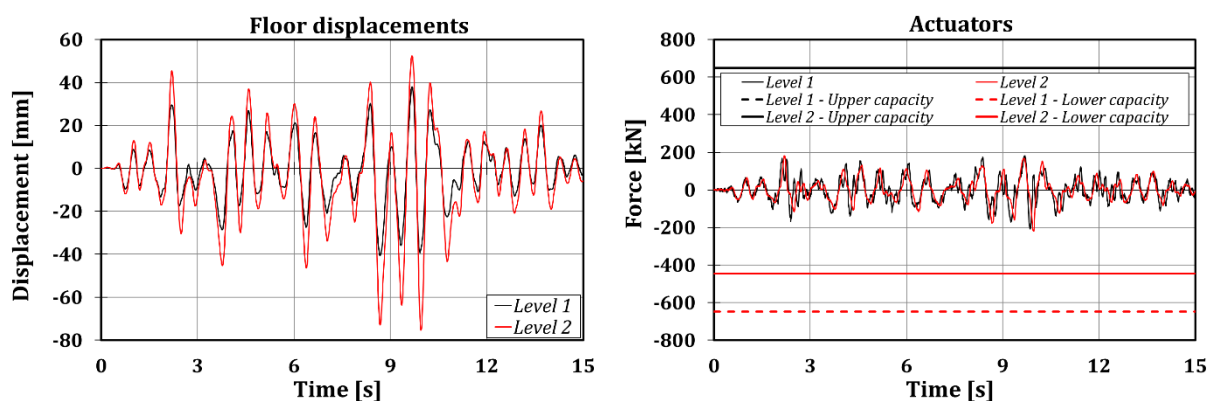


Figure 6.15 – Test 3: floor displacements (left) and reaction forces recorded by actuators (right)

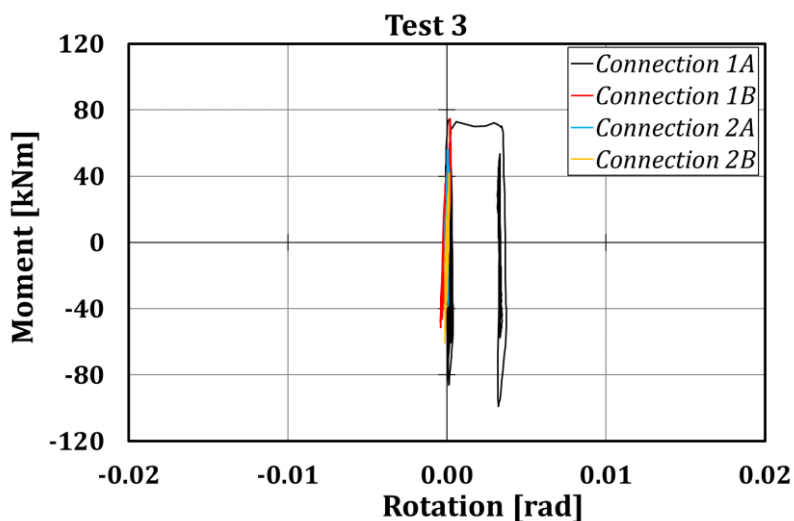


Figure 6.16 – Test 3: moment-rotation curves related to FREEDAM connections belonging to MRF-1)

6.4.4 Santa Barbara (PGA = 0.80g)

The fourth test consisted in applying the ground acceleration recorded by the station located at Santa Barbara (USA) in 1978. Even though the time history is characterized by peaks with relevant amplitude, nevertheless, the adopted peak ground acceleration (0.80g) enabled only a moderate sliding of the friction devices. The overall behaviour is not far from the features highlighted for Test 3: the floor displacements did not exceed 60 and 90 mm at the first and the second floor, respectively, inducing a maximum inter-storey drift equal to 2.3% at the first level (Figure 6.17). No residual drifts have been observed at the end of the test. Also in this case, similarly to Test 3, only connection 1A activated. Its maximum rotation was equal to 4.6 mrad (Figure 6.18).

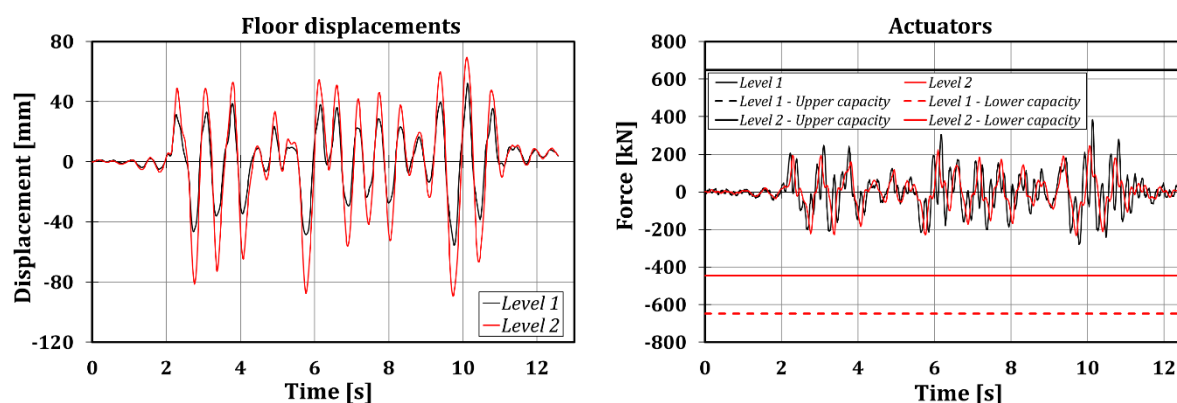


Figure 6.17 – Test 4: floor displacements (left) and reaction forces recorded by actuators (right)

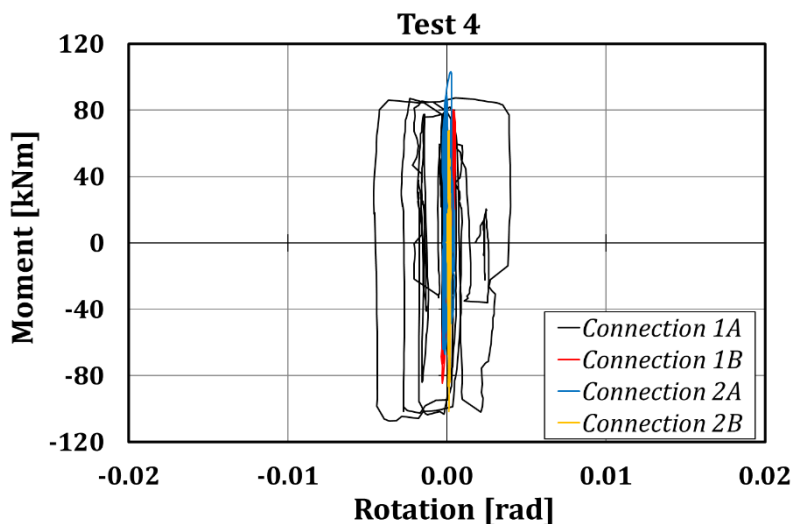


Figure 6.18 – Test 4: moment-rotation curves related to FREEDAM connections belonging to MRF-1

6.4.5 Coalinga (PGA = 0.80g)

During the last test, a higher energy dissipation occurred. This test has not been completed due to a technical problem (loss of control) giving rise to significant damage into an element connecting the mock-up and the actuator located on the first floor. This drawback happened at 8.58 seconds, the same instant at which the brittle fracture of the first RBS connection occurred in the first experimental campaign. In Figure 6.19 the displacement histories and the hysteretic curves of Test 5 are reported to corroborate the main results presented above. The maximum

floor displacement at the roof level is equal to 112 mm (the same value experienced by the structure in Test 2). The hysteretic curves are characterized by asymmetry in terms of positive and negative bending moments. Moreover, it is possible to observe that the peak moments decreased as the number of cycles increased. This is due to the reduction of the tightening torque of pre-loadable high-strength bolts caused by the consumption of the friction pads (Figure 6.20).

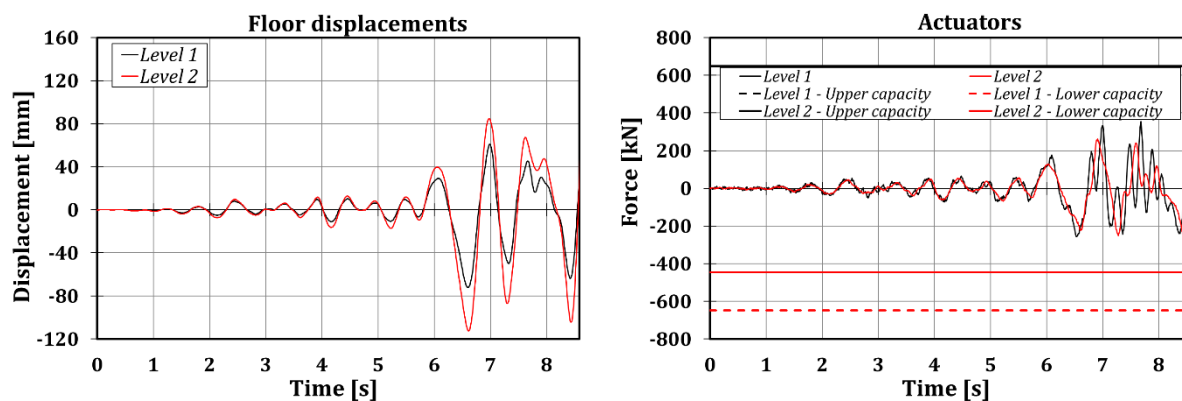


Figure 6.19 – Test 5: floor displacements (left) and reaction forces recorded by actuators (right)

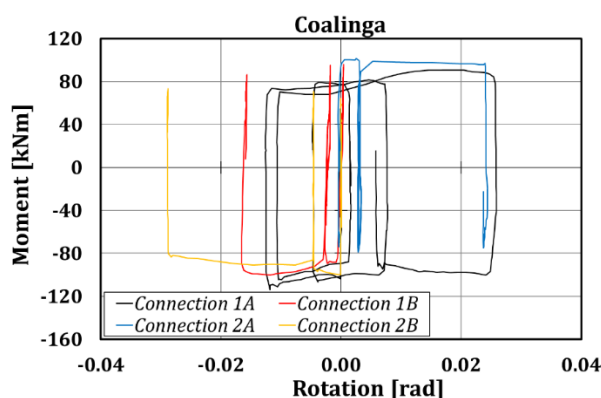


Figure 6.20 – Test 5: moment-rotation curves related to FREEDAM connections belonging to MRF-1

At the end of this second experimental campaign, no structural damage has been observed since the only elements which have contributed to dissipate the seismic input energy were the friction pads belonging to the FREEDAM connections.

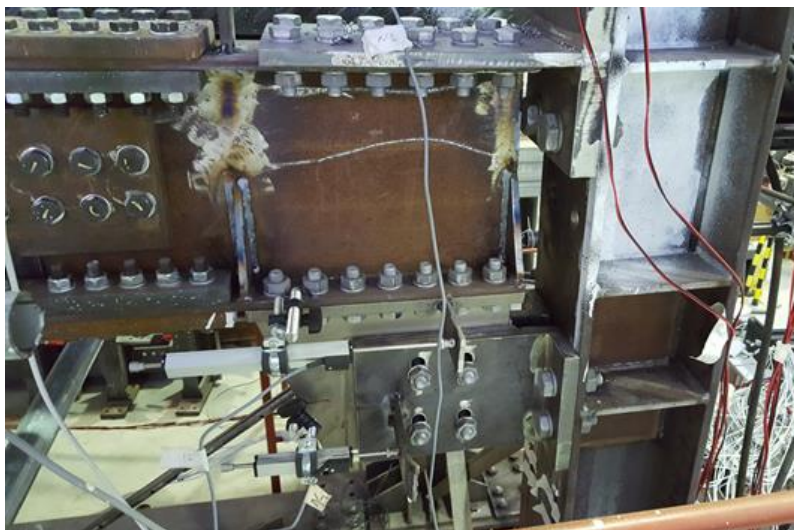


Figure 6.21 – FREEDAM connection 1A at the end of the second experimental campaign

6.5 NUMERICAL SIMULATION OF THE SEISMIC RESPONSE

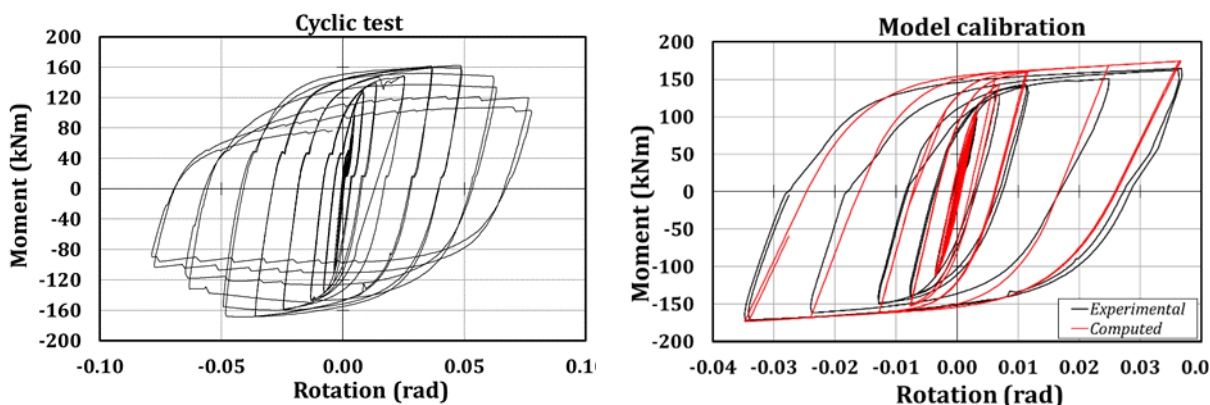
6.5.1 Structure with RBS connections

In the preliminary phase of design of the mock-up, aiming to complement the test data and to perform blind predictions of the seismic response, a non-linear 3D finite element model of the structure equipped with RBS connections was developed with the software SeismoStruct [10] (Figure 6.22). The non-linearity of the seismic response of the structure has been modelled using a mixed lumped and distributed plasticity approach. In particular, the structural elements have been modelled with inelastic force-based elements accounting for geometric and material non-linearities with a spread plasticity approach.



Figure 6.22 – 3D model of the mock-up with RBS connections

The adopted finite element is characterized by five integration sections which have been subdivided in at least 150 fibres. This subdivision is usually sufficient to assure an adequate accuracy in the calculation of the curvatures starting from the stress-strain material laws. Rigid links have been adopted to model the floor diaphragms, while lumped masses have been located at the centre of the spans. The structural detail of beam-to-column joints adopted in the mock-up was already tested in a previous work of the same authors. The specimen had a connection detail with the same RBS geometry and a similar steel grade. The results of this experimental test [11] have been employed in this work to calibrate a non-linear spring, modelling the response of the RBS connections. The moment-rotation response of the RBS tested in [11] is reported in Figure 6.23 referring to the bending moment and rotations calculated at the RBS centreline. In particular, the moment-rotation behaviour of the RBS has been modelled adopting a smooth link element [12]. This type of element is one of the more complete and complex hysteretic models available in current commercial software. Nevertheless, its main drawback is that it is based on a large number of parameters making the calibration process very complex. The calibration of these parameters was performed using the tool Multical [13] minimizing the scatter between the experimental and calibrated curve both in terms of energy dissipation and cyclic envelope. MultiCal is a tool for the calibration of hysteretic models based on genetic algorithms.



a) Cyclic response of the RBS

b) Model calibration

Figure 6.23 – Experimental and numerical moment-rotation response of the RBS

It allows finding the best combination of parameters matching the experimental response based on a set of criteria defined by the user. As far as the tests on the mock-up lead to rotation amplitudes lower than 35 mrad, the calibration procedure was applied considering the test cycles up to the amplitude of 35 mrad. This aspect is very important because the calibration of the model coefficients out of the expected range of rotations could lead to the definition of a set of parameters influenced by phenomena that do not occur at the design rotations. This is the case, for example, of the buckling phenomena observed in the test on the sub-assembly, which occurred only at rotations of about 50 mrad. The connection area has been modelled according to the approach described in Figure 6.24. Therefore, the stiffened portion of the panel zone has been modelled with rigid offsets, while the RBS non-linearity has been included in the previously calibrated spring. This non-linear spring has been located at the RBS centreline.

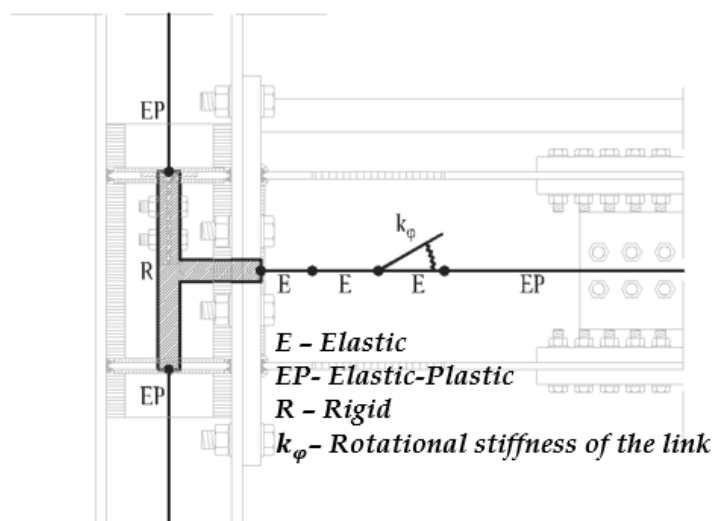


Figure 6.24 – FE model of the RBS beam-joint system

Seismic loads have been applied in terms of accelerations at the base of the frame. The time-history analyses have been performed considering a time step of 0.01 s, adopting the Hilbert-Hughes-Taylor algorithm and including a damping value equal to 1% with a Rayleigh approach as already done during the pseudo-dynamic testing.

In this section, the main comparisons between the experimental results and the numerical model are reported. In general, when compared to the five reported tests, the developed FE model seems

able to capture with a sufficient degree of accuracy the global seismic response parameters (Table 6.4). The scatters between the actual and predicted peak displacements or actual and predicted peak forces do not exceed 25%, except for the Spitak accelerogram. The lower accuracy, in this specific case, is probably due to the calibration procedure applied for the characterization of the RBSs. As explained in [13], when the accelerograms are characterized only by a few peaks, a calibration of the model parameters based only on the results of one cyclic test may lead to approximations. It was already recognized in [13] that the calibration based only on the results of one cyclic test is typically not sufficient to obtain a satisfactory prediction of the local response especially in cases where the connection experiences only a few large amplitude cycles.

Table 6.4: Experimental versus analytical comparison of base shear, floor displacements and inter-storey drift

Test	Maximum base shear (kN)		Peak first floor displacement (mm)		Peak roof displacement (mm)		Maximum interstorey drift (%)				Energy (kNm)
	Pull	Push	Pull	Push	Pull	Push	Pull (L-1)	Pull (L-2)	Push (L-1)	Push (L-2)	
1 - Real	-751	667	-79	44	-150	88	-3.27	-2.98	1.84	1.86	55.70
1 - Sim.	-656	601	-66	43	-130	84	-2.74	-3.02	1.77	1.97	50.80
1- Err. (%)	15	11	20	4	15	5	20	-1	4	-5	10
2 - Real	-652	670	-17	85	-34	171	-0.70	-0.72	3.54	3.61	33.16
2 - Sim.	-645	648	-27	74	-52	133	-1.12	-1.24	3.08	2.55	30.21
2- Err. (%)	1	3	-37	15	-36	28	-37	-42	15	42	10
3 - Real	-444	555	-29	40	-66	83	-1.22	-1.54	1.67	1.79	28.59
3 - Sim.	-477	563	-31	42	-60	88	-1.27	-1.52	1.74	1.97	15.78
3- Err. (%)	-7	-1	-4	-4	10	-6	-4	2	-4	-9	81
4 - Real	-586	592	-48	41	-99	85	-2.00	-2.16	1.71	1.84	55.63
4 - Sim.	-588	575	-47	44	-98	92	-1.95	-2.12	1.83	2.07	54.42
4- Err. (%)	0	3	2	-6	2	-8	2	2	-6	-11	2
5 - Real	-630	612	-47	62	-94	129	-1.97	-1.96	2.57	2.81	37.16
5 - Sim.	-665	555	-47	54	-81	117	-1.95	-1.62	2.26	2.63	31.12
5- Err. (%)	-5	10	1	14	15	10	1	21	14	7	19

For these cases, the calibration should be carried out considering at least the results of a cyclic test and the results of a monotonic test. Nevertheless, for all the other cases the predictions of the peak floor displacements, peak forces and peak inter-storey drifts seem rather accurate.

The table shows that the FE model provides in many cases a quite satisfactory prediction of the global response. This accurate prediction of the global response parameters does not correspond to the same level of accuracy when test data and analytical results are compared in terms of local response parameters. While the hysteretic cycles have an overall shape similar to the experimental loops, the predictions in terms of maximum/minimum rotations experienced by the

RBS connections and of peak moments at the RBS centreline are relatively more approximate (Figure 6.25).

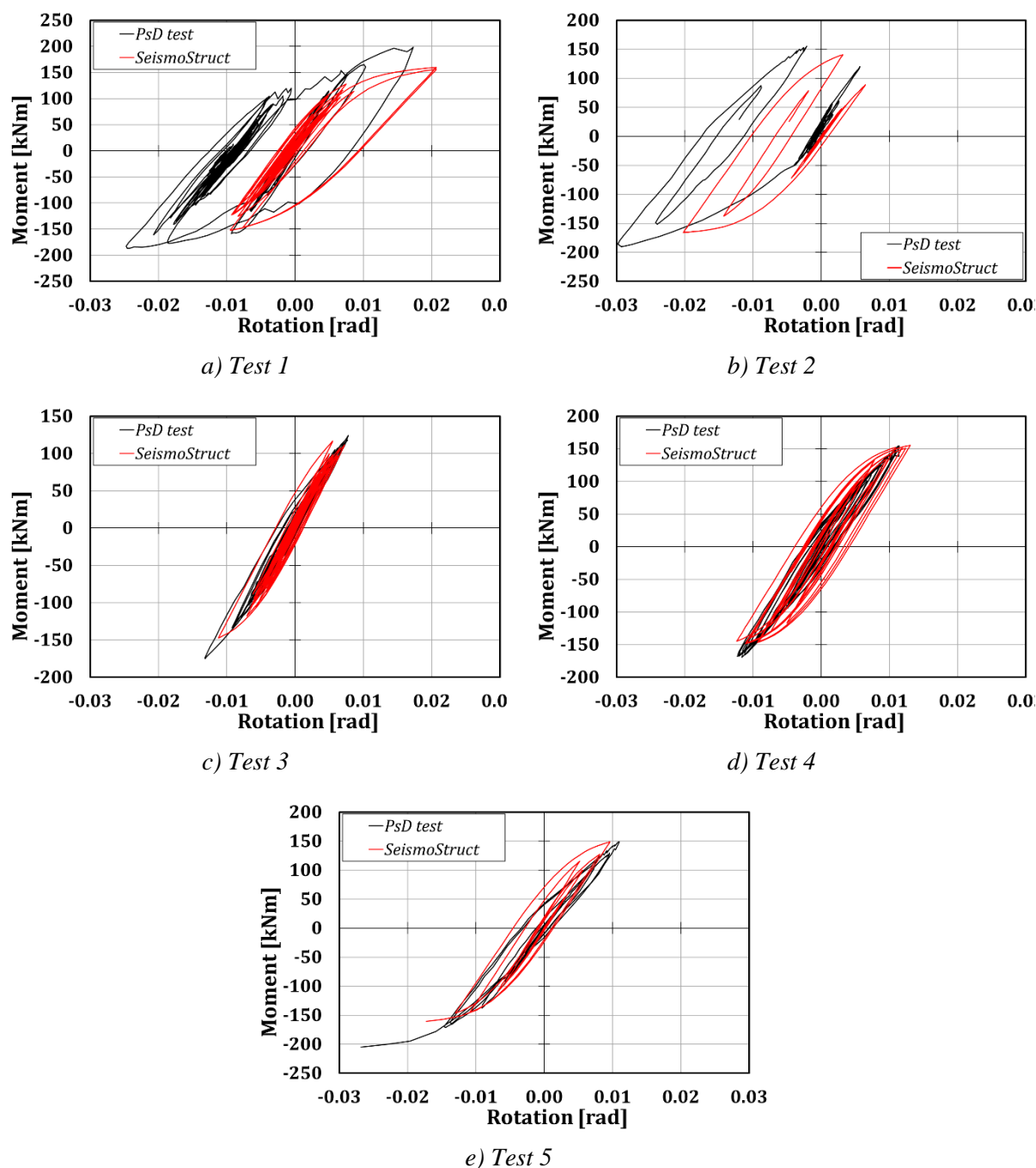


Figure 6.25 – Comparison of the hysteretic loops for RBS-1A

This comparison, for the five tests, is reported in Figure 6.25 regarding the response of connection 1A of MRF-1. The results show that the peak rotations are predicted in many cases with low accuracy, while the peak bending moments are predicted more accurately. This means that even though the spring model adopted to model the moment-rotation response of the RBS connections was calibrated starting from the results of an experimental test and employing an accurate calibration procedure, the main problem of the phenomenological models is inborn in the model typology.

While in theory such models are based on several parameters able to reproduce very accurately the experimental response of any connection type, such parameters are not directly linked to the mechanical response of the element modelled. This may lead to a discrepancy between the real and the simulated behaviour, which can be also significant in many cases. The comparisons reported in Table 6.5 show that in terms of peak rotations the errors vary from a minimum of 1% to a maximum of 62%, while in terms of peak moments, the errors vary from a minimum of 0% to a maximum of 22%. The width of the range of variation of the scatters in predicting the peak rotations, ranging between 1% and 62%, is clearly due to the fact that the parameters for modelling the cyclic behaviour of the joints are calibrated against the experimental results coming from the testing of beam-to-column sub-assemblages subjected to conventional loading protocols which can be significantly different from those occurring under real earthquakes and, even more, under the occurrence of repeated earthquakes like the sequence considered in this work. The obtained results confirm the role of paramount importance played by the loading history as already pointed out in previous works [13]. However, it is also important to point out that the scatters significantly reduce when global response parameters, such as inter-storey displacements, are of concern. This is due because local inaccuracies are averaged as soon as the number of dissipative zones increases. It is expected that in the case of structures having a greater number of storeys and bays a further improvement in the prediction of global response parameters is expected because of the high number of dissipative zones.

Table 6.5: Comparisons concerning connection 1A

Test	Rotation (rad)		Moment (kNm)		Energy (kNm)
	Maximum	Minimum	Maximum	Minimum	
1 – Real	17	-25	199	-187	10
1 – Sim.	21	-10	160	-152	7
1 – Err. (%)	19	62	-20	18	-27
2 – Real	6	-30	156	-190	4
2 – Sim.	6	-20	141	-166	3
2 – Err. (%)	15	32	-10	13	-28
3 – Real	8	-13	124	-175	3
3 – Sim.	7	-11	117	-147	2
3 – Err. (%)	-7	15	-6	16	-18
4 – Real	11	-12	155	-169	7
4 – Sim.	13	-12	155	-149	9
4 – Err. (%)	14	-1	0	12	40
5 – Real	11	-27	149	-205	6
5 – Sim.	10	-17	148	-161	4
5 – Err. (%)	-13	36	0	22	-28

From the point of view of the energy dissipation, the scatters are also significant in many cases as it is shown in Table 6.5.

6.5.2 Structure with FREEDAM connections

Referring to the structure equipped with FREEDAM connections, a non-linear 2D model of the building was developed with the software OpenSees [14] (Figure 6.26) to achieve a twofold purpose: 1) the FE model was initially developed to perform blind predictions of the seismic response of the building; 2) the FE results were aimed to check the design of the testing setup and equipment by predicting the reaction forces to be applied and verifying their compatibility with the capacities of the actuation system.

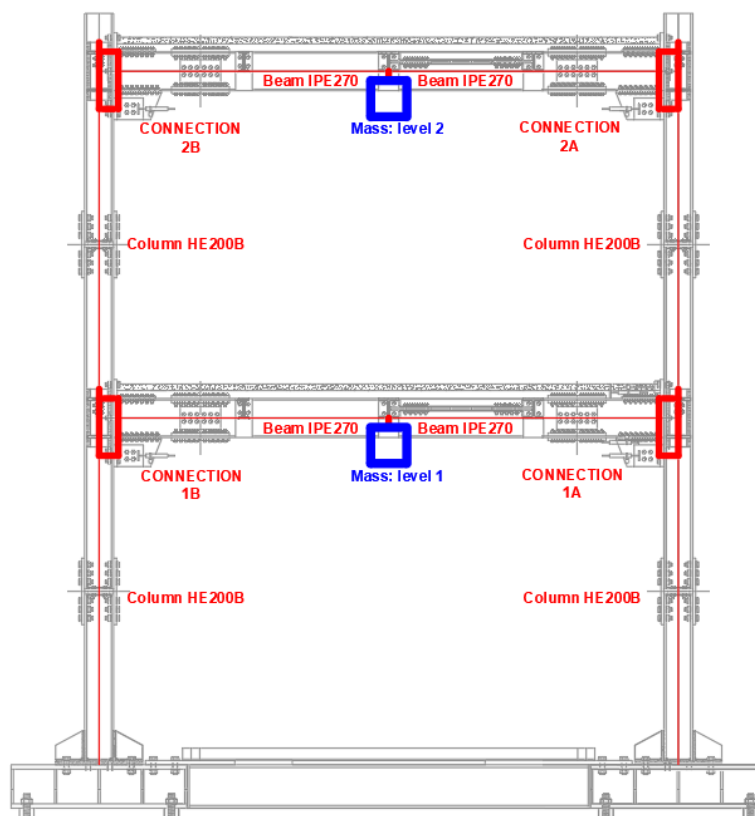


Figure 6.26 – FE model of the structure

The strategy adopted for the FE modelling has been based on the use of a mixed lumped and distributed plasticity approach. In particular, the beams and the columns have been modelled with inelastic force-based elements (*forceBeamColumn element* in OpenSees) to account for the geometric and material non-linearities with a spread plasticity approach. Each element has been characterized by five integration sections subdivided into at least 120 fibres. This ensures a good accuracy for the assessment of curvatures and internal actions starting from the knowledge of the material properties. Lumped masses have been located 65 mm below the centre of the spans to model the points of application of the inertia forces by the actuators in the testing setup.

A very refined connection modelling has been used for the connections. The model includes a hinge located at the level of the upper beam flange where the T-stub fixing the centre of rotation is located. Therefore, the model is consistent with the physical location of the centre of rotation. Besides, a *zeroLength element* endowed with a translational inelastic force-displacement law is placed at the centre-line of the friction damper (Figure 6.27).

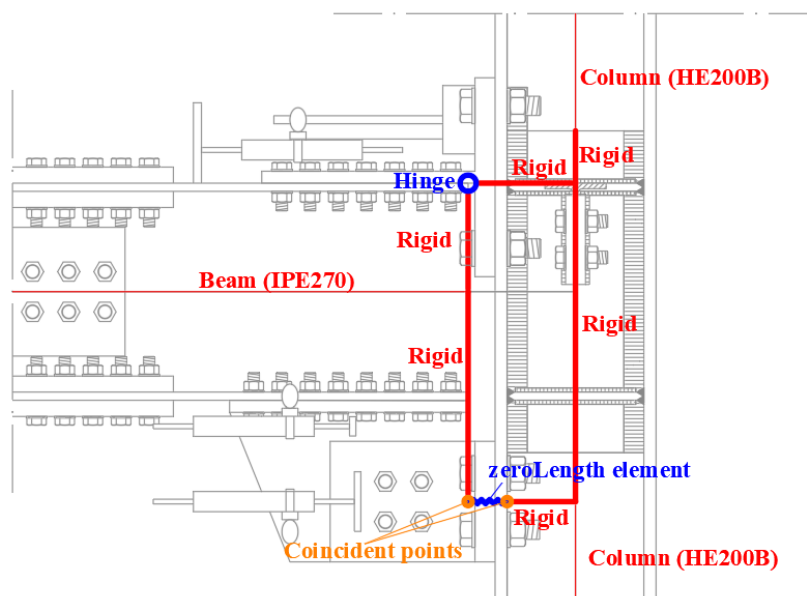


Figure 6.27 – FE model of the beam-to-column connection (refined model)

In particular, the force-displacement law of the translational spring has been provided using the *uniaxialmaterial Hysteretic* element whose input parameters are depicted in Figure 6.28; these parameters include the coordinates of six points to model the non-linear behaviour of the connection. Moreover, it is possible to model also an unloading stiffness with a ductility dependent degradation according to a factor given by $\mu^{-\beta}$.

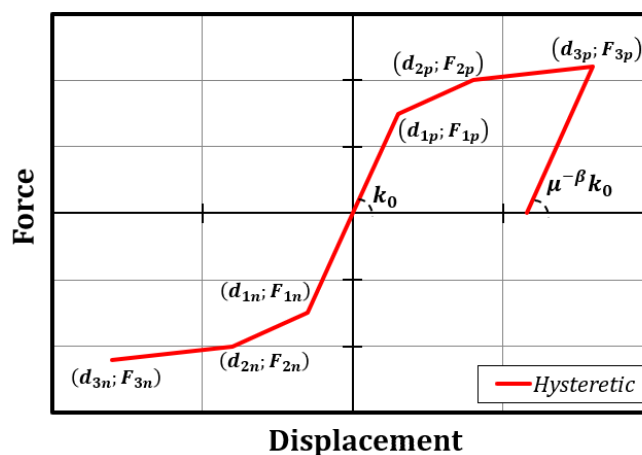


Figure 6.28 – Uniaxial Hysteretic material: parameters

Table 6.6: Uniaxial Hysteretic material: parameters

Point	d (mm)	F (kN)
3n	-170.00	-236.00
2n	-10.00	-235.00
1n	-0.02	-234.00
	0.00	0.00
1p	0.02	234.00
2p	10.00	235.00

3p 170.00 236.00

Referring to the analysed case, symmetric trilinear force-displacement law has been adopted, assuming the yielding force equal to the sliding force of the friction devices ($F_{cf,sa} = 234 \text{ kN}$), and a negligible post-elastic hardening. For the sake of clarity, the coordinates of the points have been reported in Table 6.6, while the β factor has been fixed equal to 0.

Rigid elements, as depicted in Figure 6.27, have been employed to connect the different parts of the model.

Accelerations at the base of the structure have been applied to assign the input ground motion. The adopted time-histories are characterized by a time step equal to 0.01 s. The equation of motion has been solved using the Newmark algorithm setting a damping value equal to 1% in all the tests, with a Rayleigh approach as already done during the pseudo-dynamic testing.

The proposed modelling approach of the connection has proved to be more reliable than the simple approach consisting in concentrating the flexural behaviour of the connection in a rotational spring since this solution is not able to predict the activation of the friction dampers as it happens in the pseudo-dynamic tests. The refined approach, instead, can account for the real mechanical behaviour of the joints.

The results concerning the overall building seismic response are reported in Table 6.7. The scatters in terms of peak floor displacements are lower than 25%. Moreover, as it is shown in Figure 6.29, the displacements' time-history are in phase, confirming more accurate modelling.

Table 6.7: Experimental versus numerical comparison of actuators' forces and floor displacements

Test	Actuators' forces (kN)		Peak floor displacement (mm)	
	(L-1)	(L-2)	(L-1)	(L-2)
1 - PsD	339	326	73	104
1 - Sim. 2	250	232	58	119
1 - Err. (%)	-26	-29	-21	14
2 - PsD	282	257	79	112
2 - Sim. 2	237	223	59	133
2 - Err. (%)	-16	-13	-25	18
3 - PsD	220	222	41	75
3 - Sim. 2	228	215	36	92
3 - Err. (%)	4	-3	-12	22
4 - PsD	390	255	56	89
4 - Sim. 2	240	214	43	103
4 - Err. (%)	-38	-16	-23	15
5 - PsD	340	270	72	112
5 - Sim. 2	266	242	58	126
5 - Err. (%)	-22	-10	-20	12

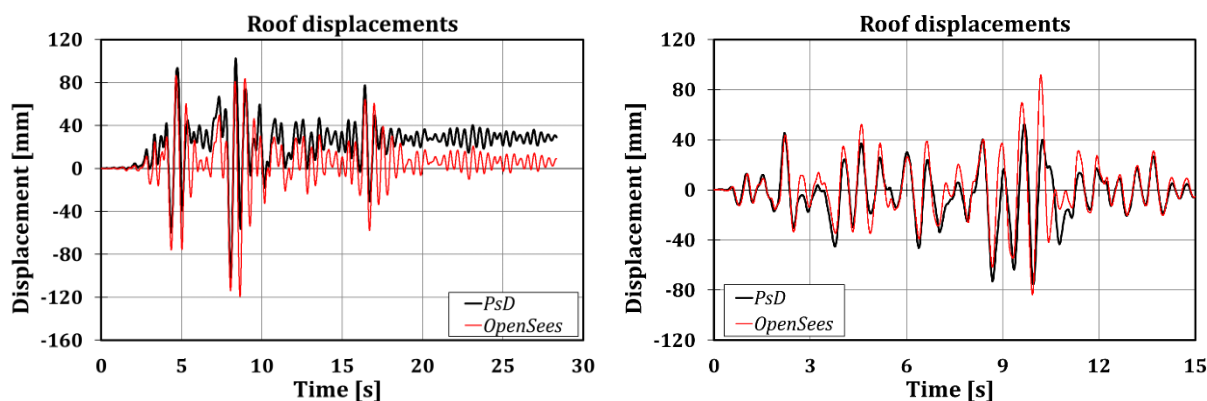


Figure 6.29 – Roof displacements: Test 1 (left) and Test 3 (right)

Furthermore, the accurate prediction of the base shear is shown in Figure 6.30.

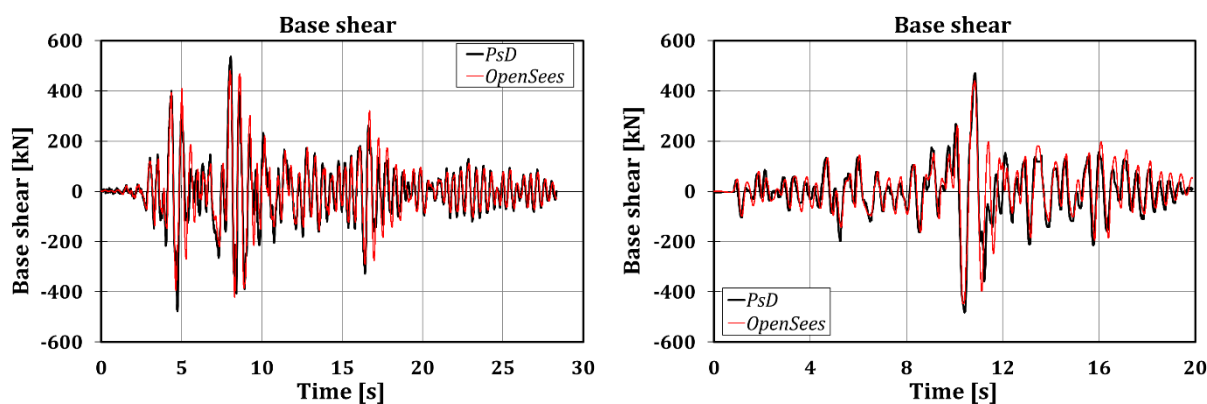


Figure 6.30 – Base: Test 1 (left) and Test 2 (right)

In Table 6.8 the comparison between experimental results and numerical simulations is presented referring to the bending moments and the rotations experienced by connection 1A. The maximum scatters in terms of bending moments vary between -14 and +28%. The main benefit provided by the use of this joint modelling approach is that the model catches the real activation of the friction dampers (Figure 6.31).

However, independently of the adopted joint modelling approach, the scatters between experimental and numerical results are not negligible testifying the difficulties in predicting the seismic non-linear response of structures due to many sources of uncertainties. In particular, in the examined case, an important influence is surely due to the random variability of the friction coefficient of the dampers and the control of the actual preloading of the bolts, both affecting the slippage resistance of the friction dampers and the time corresponding to their slippage under the seismic action.

Finally, it is important to underline that after the whole earthquake sequence the beam-to-column joints practically exhibited no damage, confirming the behaviour already exhibited by beam-to-column joints sub-assemblages during experimental tests under cyclic loading conditions [9]. They can be referred to as low-damage connections because only minor yielding occurred in the stem of the bolted T-stub close to the centre of rotation. Similar minor yielding occurred in the angles connecting the friction damper to the column flange [9]. Conversely, the same building equipped with extended end-plate connection with RBS subjected to the same earthquake sequence exhibited [5], at the end of the seismic sequence, the failure of the connection because

of the fracture of the beam flanges in the reduced beam section zone and, for some joints, because of the fracture of the welds connecting the beam to the end-plate.

Table 6.8: Experimental versus numerical comparison of connection 1A (PsD tests vs Sim. 2)

Test	Rotation (rad)	Moment (kNm)		Energy (kNm)
		Negative	Positive	
2 - PsD	17.03	118.36	90.98	4.14
2 - Sim. 2	10.52	103.50	103.93	2.15
2 - Err. (%)	-38	-13	14	-48
3 - PsD	3.74	99.24	74.11	0.34
3 - Sim. 2	0.65	85.63	103.53	0.07
3 - Err. (%)	-83	-14	40	-81
4 - PsD	4.61	107.55	87.42	2.64
4 - Sim. 2	2.53	103.60	98.49	0.26
4 - Err. (%)	-45	-4	13	-90
5 - PsD	12.58	113.82	81.36	5.69
5 - Sim. 2	7.42	103.80	103.74	1.98
5 - Err. (%)	-41	-9	28	-65

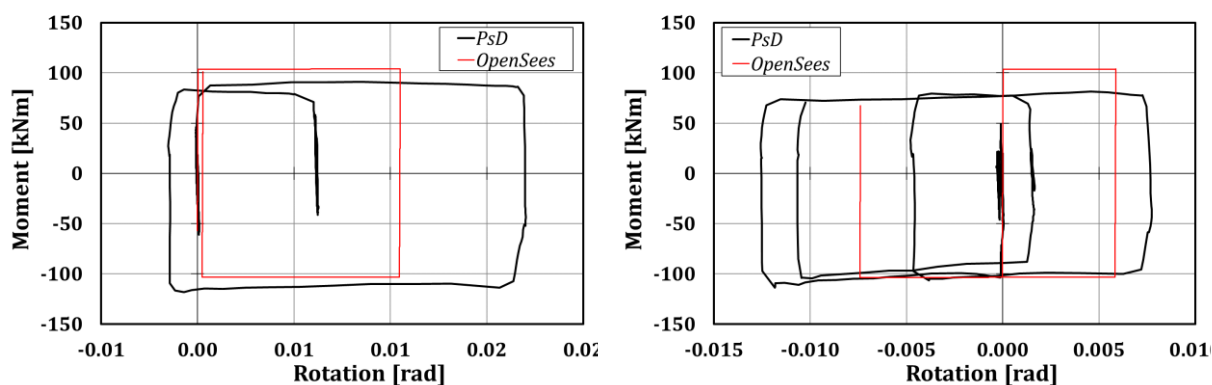


Figure 6.31 – Hysteretic curves (connection 1A): Test 2 (left) and Test 5 (right)

6.6. COMPARISON OF SEISMIC PERFORMANCES

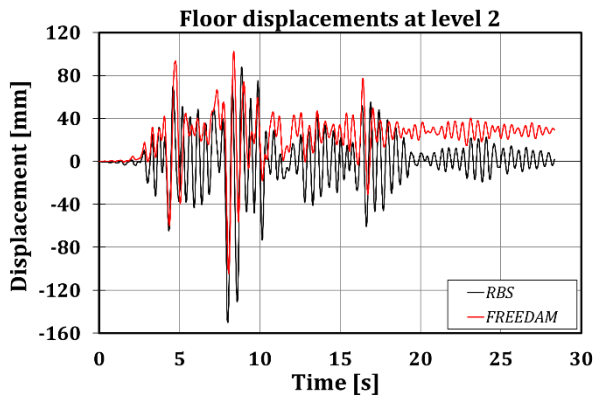
In this section, a comparison of the main results obtained by the two experimental campaigns is reported.

In Table 6.9 the floor displacements and the base shear monitored in each campaign are reported: it is possible to observe that the structure equipped with FREEDAM connections always exhibits lower base shear actions. This is due to the limited bending moments that the structure equipped with friction devices can transmit to the columns. Instead, this trend cannot be observed referring to the peak floor displacements.

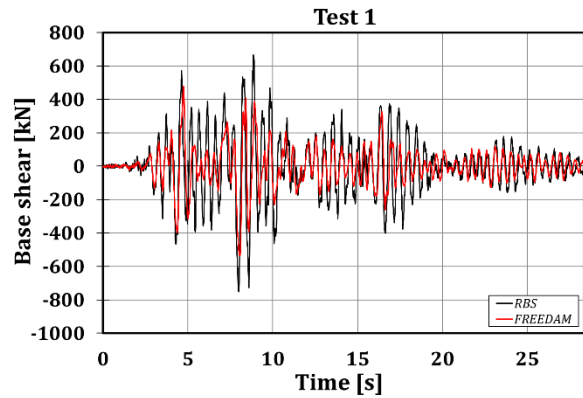
Table 6.9: Comparison between the experimental campaigns in terms of floor displacements and base shear

		Displacements (mm)				Base shear (kN)	
		Pull		Push		Pull	Push
		Level 1	Level 2	Level 1	Level 2		
Imperial Valley	RBS	-79	-150	44	88	-751.33	667.09
	FREEDAM	-73	-104	65	103	-536.88	477.20
Spitak	RBS	-17	-34	85	171	-652.47	670.44
	FREEDAM	-53	-84	79	112	-446.98	469.73
Artificial	RBS	-29	-66	40	83	-444.42	555.15
	FREEDAM	-41	-75	38	52	-271.62	346.79
Santa Barbara	RBS	-48	-99	41	85	-585.66	592.36
	FREEDAM	-56	-89	52	70	-388.06	483.42
Coalinga	RBS	-47	-94	62	129	-629.71	612.24
	FREEDAM	-72	-112	61	85	-439.24	459.37

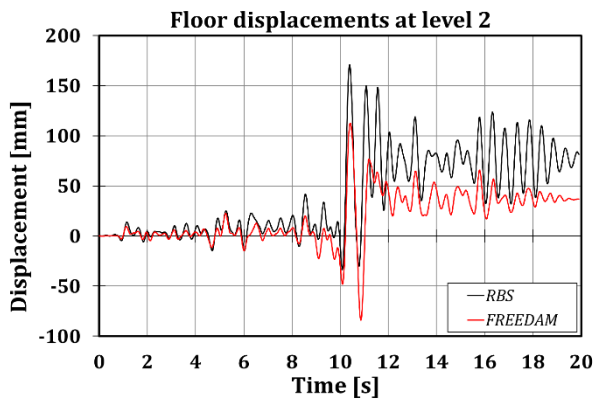
Besides, FREEDAM connections make the structural behaviour elastic between two following peaks of the input motion: this is the reason for the reduced displacement range observed, throughout the tests, in the second campaign. The last phenomenon has a general validity for all the tests, but it is reported for Test 1, 2 and 5 in Figure 6.32. Furthermore, the figures highlight that friction devices do not guarantee the self-recentring of the structure. For the sake of simplicity, the local structural behaviour exhibited by the analysed connections is reported referring to the most exploited connection for which no technical issues have occurred; the connection 1A is the chosen one, and the comparison is made referring to the Spitak and Coalinga earthquakes with PGA equal to 0.8g. The discussions for this connection and input motion are analogous for all the other ones. In Figure 6.33 it can be observed that the RBS connection is called to withstand a higher bending moment and to sustain a higher rotation demand: about 240 kNm compared to 120 kNm, and about 0,027 rad compared to 0,013 rad, respectively. Nevertheless, it can be proved that the two compared connections dissipate the same energy. This is due to the optimal way FREEDAM connection behaves, allowing at the same time, to stress the structure at low levels, and to make it stiffer, without preventing the possibility of dissipating a high amount of energy.



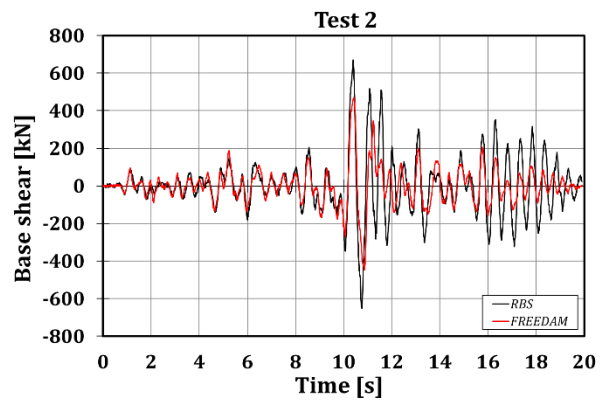
a) Test 1: second level floor displacements



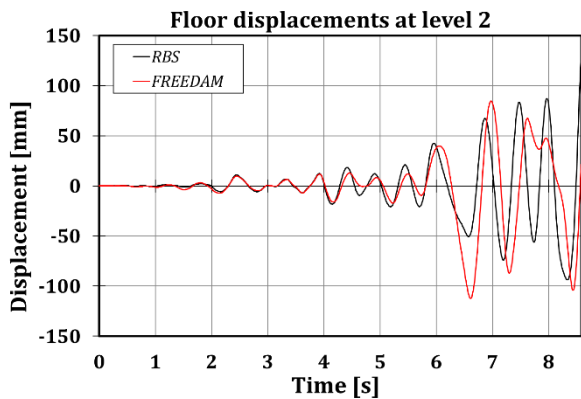
b) Test 1: base shear



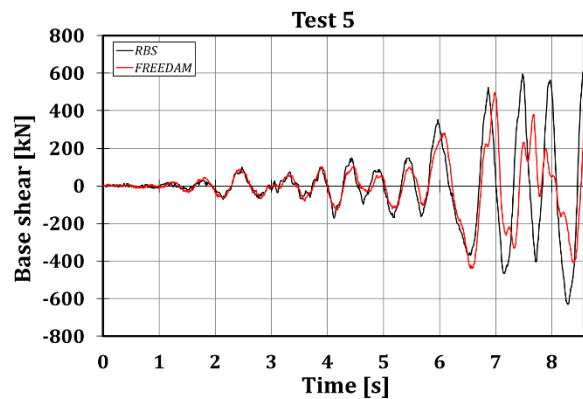
c) Test 2: second level floor displacements



d) Test 2: base shear



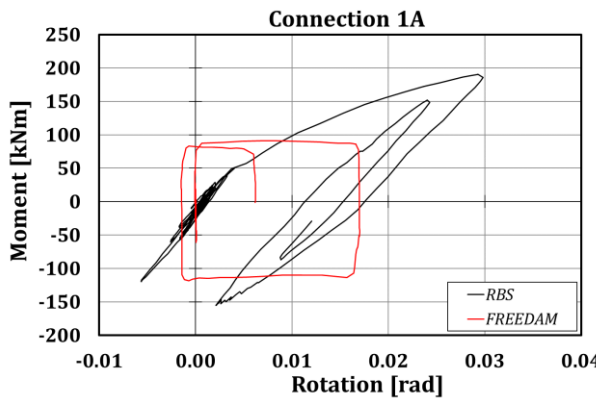
e) Test 5: second level floor displacements



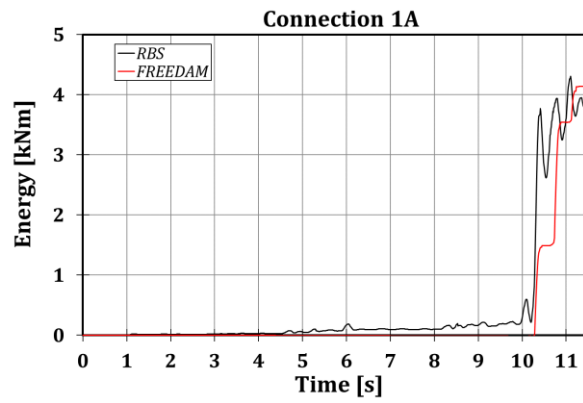
f) Test 5: base shear

Figure 6.32 – Comparison between the second level floor displacements and the base shear

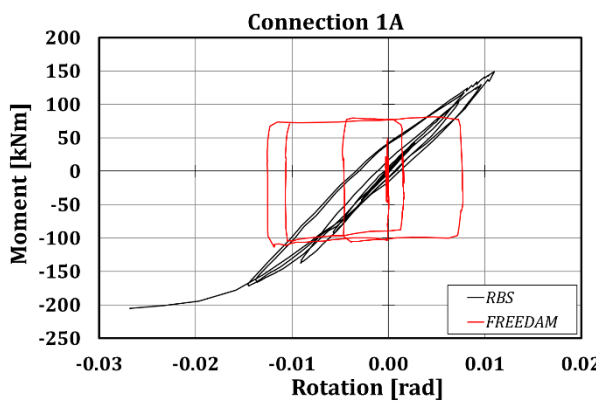
The previous statements are valid for connections belonging to the first floor, while those located at the second level, mainly show elastic behaviour and, for this reason, they are not herein reported.



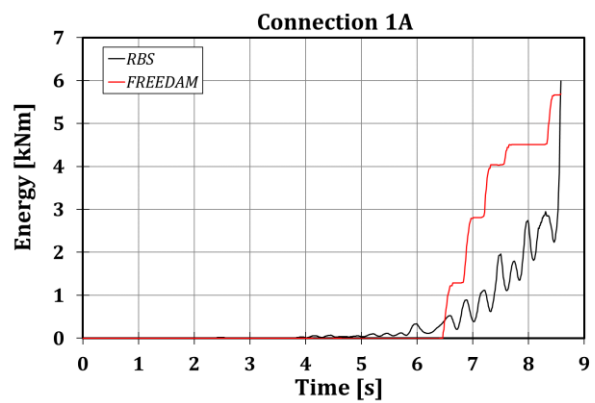
a) Test 2 – Hysteretic curves



b) Test 2 – Dissipated energy



c) Test 5 – Hysteretic curves



d) Test 5 – Dissipated energy

Figure 6.33 – Connection 1A: hysteretic curves and dissipated energy

6.7 REFERENCES

- [1] Magonette, G., Pegon, P., Buchet, P., Advanced Testing Techniques at the ELSA-JRC Reaction Wall (1998).
- [2] Molina, F. J., Buchet, Ph., Magonette, G. E., Negro, P., Bidirectional pseudodynamic technique for testing a three-storey reinforced concrete building (2004) Proc. Of 13th World Conference on Earthquake Engineering, Vancouver, Paper N., 75.
- [3] Tsai, K., Weng, Y., Lin S. L., Pseudo-dynamic test of a full-scale CFT/BRB frame (2004) 13th World Conference on Earthquake Engineering, Vancouver, Paper No. 750.
- [4] CEN (2005) EN 1998-1 Eurocode 8: Design of Structures for Earthquake Resistance. Part 1: General Rules, Seismic Actions and Rules for Buildings, CEN, European Committee for Standardization, 2005.
- [5] CEN (2005) EN 1998-3: Eurocode 8: Design of structures for earthquake resistance – Part 3: Assessment and retrofitting of buildings, CEN, European Committee for Standardization, 2005.
- [6] Di Benedetto, S., Francavilla, A.B., Latour, M., Ferrante Cavallaro, G., Piluso, V., Rizzano, G. Pseudo-dynamic testing of a full-scale two-storey steel building with RBS connections (2020) Engineering Structures, 212.
- [7] CEN [2005]: EN 1993-1-8 Eurocode 3: Design of Steel Structures. Part 1-8: Design of Joints, CEN, European Committee for Standardization, 2005.
- [8] AISC Steel Design Guide, Murray, T. M., Summer, E. A., Extended End-Plate Moment Connections. Seismic and Wind Applications, 2003.
- [9] Meng, R. L., Design of moment end-plate connections for seismic loading (1996) Ph. D. Thesis, College of Architecture and Urban Studies, The Virginia Polytechnic Institute and State University, USA.
- [10] Francavilla, A.B., Latour, M., Piluso, V., Rizzano, G., Design criteria for beam-to-column connections equipped with friction devices, Journal of Constructional Steel Research, 172 (2020) 106240.
- [11] SeismoSoft (2016). SeismoStruct 2016 – A computer program for static and dynamic analysis of framed structures.
- [12] Iannone, F., Latour, M., Piluso, V. and Rizzano, G., Experimental Analysis of Bolted Steel Beam-to-Column Connections: Component Identification (2011) J. Earthq. Eng., vol. 15, no. 2, pp. 214–244.
- [13] Sivaselvan, M. V., Reinhorn, HYSTERETIC MODELS FOR DETERIORATING INELASTIC STRUCTURES (2000) J. Eng. Mech., vol. 126, no. June, pp. 633–640.
- [14] Chisari, C., Francavilla, A. B., Latour, M., Piluso, V., Rizzano G., Amadio, C., Critical issues in parameter calibration of cyclic models for steel members (2017) Engineering Structures, vol. 132, pp. 123-138
- [15] McKenna, F., OpenSees: A Framework for Earthquake Engineering Simulation, Computing in Science and Engineering (2011) 13, 58-66.